

# A global study of tropospheric methane chemistry and emissions



**Ines Heimann**

Department of Chemistry  
University of Cambridge

This dissertation is submitted for the degree of  
*Doctor of Philosophy*

Wolfson College

April 2017



Für Mama und Papa



## **Declaration**

This dissertation is the result of my own work and includes nothing which is the outcome of work done in collaboration except as declared in the Preface and specified in the text. It is not substantially the same as any that I have submitted, or, is being concurrently submitted for a degree or diploma or other qualification at the University of Cambridge or any other University or similar institution except as declared in the Preface and specified in the text. I further state that no substantial part of my dissertation has already been submitted, or, is being concurrently submitted for any such degree, diploma or other qualification at the University of Cambridge or any other University or similar institution except as declared in the Preface and specified in the text. It does not exceed the prescribed word limit for the relevant Degree Committee (60,000 words).

Ines Heimann  
April 2017



## **Acknowledgements**

First, I would like to thank my supervisor Prof John Pyle for this PhD project, his guidance throughout my PhD, his open door and his valuable feedback. Second, I am grateful for the support I received from Drs Paul Griffiths, Nicola Warwick and Alex Archibald. Without them I would never have reached this stage of my PhD. I would like to express my thanks to Drs Tara Banerjee and Michelle Cain for their guidance in shaping the project on a day to day basis. I also owe thanks to Drs Paul Telford and Luke Abraham for providing computational support and Prof Neil Harris for his open door.

Thanks go to the numerous people who proofread this thesis and ironed out many phrasing errors.

Finally my thanks go to Jack who has been a tremendous help in all stages of this PhD. He has read each and every sentence of this thesis numerous times and his moral support never wavered.



# **A global study of tropospheric methane chemistry and emissions**

Ines Heimann

Methane is the second most important greenhouse gas after CO<sub>2</sub> and affects atmospheric temperatures directly and indirectly. Through its chemical loss in the atmosphere, methane also influences tropospheric ozone concentrations, a major air pollutant. Experiments have been performed with a chemistry-climate model investigating the effects of source and sink changes on atmospheric methane in a present day (2000) and future (2100) climate. The model setup has been altered so that methane emissions are accounted for rather than using a fixed surface concentration boundary condition. Furthermore, a new chemistry scheme has been implemented into the model in which oxidant fields are prescribed removing methane's self-feedback. This complements the existing, interactive chemistry scheme.

Interactive methane concentrations and its atmospheric lifetime were found to be slightly low biased relative to observations with a source strength of 548 Tg(CH<sub>4</sub>) yr<sup>-1</sup>, in line with recent estimates. This low bias may be linked to tropospheric ozone, NO<sub>x</sub> and CO biases in the model, all influencing the tropospheric OH radical, methane's major sink. OH was high biased relative to observational estimates, a common feature of chemistry-climate models. Methane emissions were increased to 585 Tg(CH<sub>4</sub>) yr<sup>-1</sup> with a latitudinal shift to larger tropical emissions. This increase resulted in excellent agreement between modelled and observed methane levels, both globally and in the latitudinal gradient. The 7% methane emission increase also increased tropospheric ozone levels. This highlighted methane's negative impacts on air quality, particularly important because of recent and projected methane emission increases.

Probing the sink effect on atmospheric methane levels with the new non-interactive chemistry scheme showed that reducing the OH sink strength and altering its latitudinal distribution

improved global methane levels and led to reasonable agreement with observations. However, the latitudinal gradient of non-interactive methane was overestimated suggesting that either the source or the sink distribution require adjustment. Analysis furthermore showed that a tropical shift of methane emissions only slightly improved the latitudinal gradient of non-interactive methane.

Future climate experiments were performed which show that the OH sink increase due to higher temperatures (and thus larger tropospheric water vapour content) is counteracted by projected methane emission increases. While projected CO emissions decreased to the end of the 21<sup>st</sup> century, model calculations here showed that the tropospheric CO burden increased due to chemical production during methane loss. These experiments highlighted that methane emission mitigation is not only beneficial in slowing climate warming but also in improving air quality, affecting the ozone budget.

# Table of contents

<b>List of figures</b>	<b>xv</b>
<b>List of tables</b>	<b>xix</b>
<b>Abbreviations</b>	<b>xxi</b>
<b>1 Methane in the atmosphere</b>	<b>1</b>
1.1 Atmospheric methane burden . . . . .	2
1.1.1 Recent changes in methane . . . . .	2
1.1.2 Interannual variability . . . . .	5
1.2 Methane sources . . . . .	6
1.2.1 Natural sources . . . . .	7
1.2.2 Anthropogenic sources . . . . .	9
1.2.3 Isotopic signatures . . . . .	10
1.3 Methane sinks . . . . .	13
1.3.1 The hydroxyl radical sink . . . . .	14
1.3.2 Additional sinks . . . . .	16
1.4 Methane lifetime . . . . .	17
1.5 Modelling the atmosphere . . . . .	19
1.5.1 Modelling atmospheric chemistry . . . . .	20
1.6 Summary . . . . .	23

---

1.7	Thesis outline . . . . .	23
<b>2</b>	<b>Experimental setup and model evaluation</b>	<b>25</b>
2.1	The UM-UKCA model . . . . .	25
2.1.1	Chemistry scheme . . . . .	26
2.2	Methane emissions . . . . .	28
2.2.1	Experiments . . . . .	29
2.3	Evaluation of the Base model . . . . .	31
2.3.1	Base tropospheric ozone . . . . .	31
2.3.2	Base tropospheric NO <sub>x</sub> . . . . .	37
2.3.3	Base tropospheric CO . . . . .	39
2.3.4	Base tropospheric hydroxyl radical . . . . .	46
2.3.5	Base tropospheric methane . . . . .	49
2.4	Summary . . . . .	56
<b>3</b>	<b>Non-interactive chemistry within the UM-UKCA model</b>	<b>59</b>
3.1	Model development . . . . .	60
3.1.1	Introduction . . . . .	60
3.1.2	Prescribed oxidant fields . . . . .	60
3.1.3	Non-interactive methane chemistry . . . . .	66
3.2	Evaluation of the $\Delta$ OH methane chemistry . . . . .	71
3.2.1	Tropospheric methane . . . . .	71
3.2.2	Methane oxidation . . . . .	75
3.3	Non-interactive chemistry impact on the latitudinal gradient . . . . .	77
3.4	Summary . . . . .	78
<b>4</b>	<b>Tagged methane tracer analysis</b>	<b>81</b>
4.1	Model setup . . . . .	81

---

4.1.1	Methane tracers . . . . .	81
4.1.2	Methane emissions . . . . .	82
4.2	Global methane tagged by source and region . . . . .	83
4.2.1	Zonally averaged methane tracers . . . . .	85
4.2.2	Contribution to the latitudinal gradient . . . . .	88
4.3	Optimising the latitudinal gradient . . . . .	90
4.3.1	Linear regression of the tracers . . . . .	90
4.3.2	Regression by category . . . . .	92
4.4	Summary . . . . .	96
<b>5</b>	<b>Probing the atmospheric response to methane emission changes</b>	<b>99</b>
5.1	Model setup . . . . .	100
5.1.1	Methane emissions . . . . .	100
5.2	Interactive methane . . . . .	107
5.3	Interactive hydroxyl radical . . . . .	112
5.4	Changes to ozone, carbon monoxide and nitrogen oxides . . . . .	113
5.5	Non-interactive methane . . . . .	115
5.6	Summary . . . . .	118
<b>6</b>	<b>Probing climate impacts on methane</b>	<b>121</b>
6.1	Model setup . . . . .	121
6.1.1	Emission changes . . . . .	127
6.2	Present day . . . . .	131
6.3	Temperature and water vapour changes . . . . .	131
6.4	Changes to tropospheric OH and methane . . . . .	133
6.4.1	$\Delta\text{CC}$ . . . . .	134
6.4.2	$\Delta(\text{CC}+\text{methane})$ and $\Delta(\text{CC}+\text{ems})$ . . . . .	137
6.5	Changes to other key tropospheric species . . . . .	141

---

6.5.1	$\Delta\text{CC}$ . . . . .	141
6.5.2	$\Delta(\text{CC}+\text{ems})$ and $\Delta(\text{CC}+\text{methane})$ . . . . .	144
6.6	Summary . . . . .	150
<b>7</b>	<b>Conclusions and future work</b>	<b>153</b>
7.1	Conclusions . . . . .	153
7.2	Future work . . . . .	155
	<b>References</b>	<b>159</b>
	<b>Appendix A Observations</b>	<b>175</b>
A.1	Ozone sonde data . . . . .	175
A.2	Ozone surface observations . . . . .	176
A.3	Methane and carbon monoxide surface observations . . . . .	177
A.4	$\text{NO}_x$ and CO aircraft observations . . . . .	181
	<b>Appendix B</b>	<b>185</b>

# List of figures

1.1	Atmospheric methane concentrations over the last 400,000 years. . . . .	3
1.2	Atmospheric methane concentrations over the last 10,000 years. . . . .	4
1.3	Global methane trends and growth rate from 1983 to 2014. . . . .	4
1.4	Methane trends from 2000 to 2014 as a function of latitude. . . . .	6
1.5	Histogram of isotopic data for methane sources and sinks for $\delta^{13}\text{C}$ and $\delta\text{D}$ . . . . .	12
1.6	Sources and sinks of atmospheric OH and HO <sub>2</sub> depicting the atmospheric HO <sub>x</sub> cycle. . . . .	15
1.7	Atmospheric methane oxidation to CO. . . . .	17
2.1	Global distribution of the annually summed methane emissions. . . . .	30
2.2	Modelled annual mean Base surface and zonally averaged ozone concentrations. . . . .	32
2.3	Comparison of modelled ozone with ozone sonde data. . . . .	34
2.4	Comparison of modelled surface ozone with surface observations across the Northern Hemisphere. . . . .	36
2.5	Modelled annual mean Base surface and zonally averaged NO <sub>x</sub> concentrations. . . . .	38
2.6	Modelled annual mean Base surface and zonally averaged CO concentrations. . . . .	41
2.7	Latitudinal Base CO gradient compared to observations. . . . .	42
2.8	Comparison of Base surface CO levels with surface measurements. . . . .	44
2.9	Normalised Taylor diagram comparing Base surface CO concentrations to surface measurements. . . . .	45
2.10	Seasonal variation in tropospheric Base OH concentrations and TransCom OH. . . . .	49

2.11	Modelled annual mean Base surface methane concentrations. . . . .	50
2.12	Comparison of Base surface methane levels with surface measurements. . .	51
2.13	Normalised Taylor diagram comparing Base methane concentrations to surface measurements. . . . .	52
2.14	Latitudinal Base methane gradient compared to observations. . . . .	53
2.15	Relationship between methane lifetime with respect to tropospheric OH loss and tropospheric OH concentrations for the ACCMIP models and Base. . .	55
3.1	Implementation of a prescribed oxidant field. . . . .	62
3.2	Seasonal mean zonally averaged TransCom OH concentrations. . . . .	64
3.3	Seasonal mean surface TransCom OH concentrations. . . . .	65
3.4	Global distribution of the annually summed methane emissions for eight distinct source types. . . . .	68
3.5	Latitudinal $\Delta$ OH methane gradient compared to observations. . . . .	72
3.6	Comparison of $\Delta$ OH surface methane levels with surface measurements. . .	74
3.7	Relationship between methane lifetime with respect to tropospheric OH loss and tropospheric OH concentrations for the ACCMIP models and $\Delta$ OH. . .	75
3.8	Latitudinal gradient for interactive and non-interactive Base methane. . . .	78
4.1	Map of the six subregions into which the non-interactive methane tracers are separated. . . . .	82
4.2	Annual mean zonally averaged tracer concentrations by source type and region. . .	86
4.3	Latitudinal gradient for methane concentrations separated by source type and region relative to the respective global mean concentrations. . . . .	89
4.4	Optimised latitudinal $\Delta$ OH methane gradient compared to observations. . .	93
4.5	Comparison of methane levels with surface measurements after optimisation. . .	95
5.1	Comparison of the latitudinal distribution of the $\Delta$ ems and Base methane emissions. . . . .	104

---

5.2	Comparison of the longitudinal distribution of the $\Delta$ ems and Base methane emissions. . . . .	105
5.3	Comparison of the seasonal cycle of the $\Delta$ ems and Base methane emissions.	106
5.4	Latitudinal gradient for $\Delta$ ems and Base methane compared to surface observations. . . . .	107
5.5	Comparison of Base surface methane levels with surface measurements. . .	109
5.6	Relationship between methane lifetime with respect to tropospheric OH loss and tropospheric OH concentrations for the ACCMIP models, Base and $\Delta$ ems.	111
5.7	Comparison of the zonal mean distribution and the seasonal cycle of Base OH and $\Delta$ ems OH. . . . .	113
5.8	Absolute changes in annual mean zonally averaged CO, NO <sub>x</sub> and ozone between $\Delta$ ems and Base. . . . .	115
5.9	Latitudinal gradient for $\Delta$ (ems+OH) methane and $\Delta$ OH methane compared to observations. . . . .	117
6.1	Comparison of the latitudinal distribution of the year 2100 (RCP 8.5) and Base emissions. . . . .	125
6.2	Comparison of the longitudinal distribution of the year 2100 (RCP 8.5) and Base emissions. . . . .	126
6.3	Comparison of the latitudinal distribution of the year 2100 (RCP 8.5) and Base methane emissions. . . . .	129
6.4	Comparison of the longitudinal distribution of the year 2100 (RCP 8.5) and Base methane emissions. . . . .	130
6.5	Absolute and relative changes in annual mean zonally averaged temperature ( $\Delta$ ACC – Base). . . . .	132
6.6	Absolute and relative changes in annual mean zonally averaged atmospheric water content ( $\Delta$ ACC – Base). . . . .	133
6.7	Absolute and relative changes in annual mean zonally averaged OH ( $\Delta$ ACC – Base). . . . .	134
6.8	Seasonal variation in tropospheric Base OH concentrations and $\Delta$ ACC OH. .	135

---

6.9	Absolute and relative changes in annual mean zonally averaged methane ( $\Delta\text{CC} - \text{Base}$ ). . . . .	136
6.10	Changes in annual mean zonally averaged methane concentrations under climate change after emission changes. . . . .	138
6.11	Changes in annual mean zonally averaged OH concentrations under climate change after emission changes. . . . .	139
6.12	Changes in annual mean zonally averaged CO, NO <sub>x</sub> and ozone between $\Delta\text{CC}$ and Base. . . . .	142
6.13	Changes in annual mean zonally averaged CO concentrations under climate change with changing emissions. . . . .	145
6.14	Changes in annual mean zonally averaged NO <sub>x</sub> concentrations under climate change with changing emissions. . . . .	146
6.15	Changes in annual mean zonally averaged ozone under a future climate with changing emissions. . . . .	147
6.16	Contribution to the ozone burden difference between the future climate simulations and Base. . . . .	149

# List of tables

1.1	Annual strength of methane sources and their isotopic signal. . . . .	18
2.1	Annual emissions for the year 2000. . . . .	27
2.2	Methane reactions and reaction rate constants in CheST. . . . .	28
2.3	Annual methane emissions for the year 2000. . . . .	29
2.4	Lawrence et al. [2001] analysis of annual mean air-mass-weighted tropospheric OH concentrations. . . . .	48
2.5	Lawrence et al. [2001] analysis of methane loss through reaction with OH. .	56
3.1	Lawrence et al. [2001] analysis of annual mean air-mass-weighted tropospheric OH concentrations for the $\Delta$ OH experiment. . . . .	65
3.2	Methane loss reaction rate constants with the prescribed oxidant fields in the chemistry scheme. . . . .	66
3.3	Methane emission source types that can be distinguished in the model setup and their strengths. . . . .	67
3.4	Lawrence et al. [2001] analysis of methane loss through reaction with OH. .	76
4.1	Annually summed methane emissions by source and region. . . . .	83
4.2	Absolute and relative contribution of all 33 methane tracers to the global tropospheric annual mean methane concentration. . . . .	84
4.3	Solution of the least square error optimisation for the four tracer categories.	93
4.4	Methane emission strength for the 33 tracers before and after the optimisation.	94

---

5.1	Experiments to probe the effect of changing methane emissions, OH distributions and (non-)interactive chemistry on atmospheric methane. . . . .	100
5.2	Methane emissions for the $\Delta$ ems and Base emission scenarios. . . . .	103
5.3	Comparison of key atmospheric methane variables for Base and $\Delta$ ems. . . .	110
5.4	Lawrence et al. [2001] analysis of annual mean airmass-weighted [OH]. . .	112
5.5	Comparison of key atmospheric methane variables for the $\Delta$ OH and $\Delta$ (ems+OH) experiments. . . . .	116
6.1	Summary of the four experiments probing the atmospheric response to a changing climate. . . . .	122
6.2	Annual emissions for the years 2000 and 2100 (RCP 8.5 scenario) and their differences. . . . .	124
6.3	Annual methane emissions by source type for the year 2000 and 2100 (RCP 8.5) and their differences. . . . .	128
6.4	Lawrence et al. [2001] analysis of tropospheric methane loss through the reaction with OH. . . . .	137
6.5	Tropospheric ozone burden for the four climate change experiments presented in this chapter. . . . .	148

# Abbreviations

ACCMIP	Atmospheric Chemistry and Climate Intercomparison Project
AerChemMIP	Aerosols Chemistry Modeling Intercomparison Project
AF	Africa
AS	Asia
BFGS	Broyden-Fletcher-Goldfarb-Shanno algorithm
CCM	Chemistry-climate model
CCMI	Climate Chemistry Model Initiative
CheST	UKCA chemistry scheme for the stratosphere and troposphere
CheT	UKCA chemistry scheme for the troposphere
CLASSIC	Coupled Large-scale Aerosol Simulator for Studies in Climate
CMIP5	Coupled Model Intercomparison Project Phase 5
CTM	Chemistry-transport model
DJF	December-January-February
EDGAR	Emission Database for Global Atmospheric Research
ESM	Earth system model
EU	Europe
GFED	Global Fire Emissions Database
GHG	Greenhouse gas
ITCZ	Inter tropical convergence zone
JJA	June-July-August
JULES	Joint UK Land Environment Simulator
MBL	Marine boundary layer
MCF	Methyl chloroform
MAM	March-April-May
NA	North America
NMBE	Normalised mean bias error

NOAA	National Oceanic and Atmospheric Administration
PI	Pre-industrial
ppm	Parts-per-million by volume, $10^{-6}$
ppb	Parts-per-billion by volume, $10^{-9}$
ppt	Parts-per-trillion by volume, $10^{-12}$
RMSE	Root mean square error
SA	South America
SEA	South East Asia
SON	September-October-November
SST	Sea surface temperature
TransCom	Atmospheric Tracer Transport Model Intercomparison Project
UKCA	United Kingdom Chemistry and Aerosol submodel
UM	Unified Model
US	United States of America
WETCHIMP	Wetland and wetland CH <sub>4</sub> inter-comparison of models project
$p_i$	Scaling parameter for tracer $i$
$R^2$	Coefficient of determination
$\tau$	Atmospheric lifetime
$\tau_{OH+CH_4}$	Methane lifetime with respect to tropospheric OH loss
$x_{ij}$	Modelled methane mixing ratio at location $j$ for tracer $i$
$\hat{y}$	Modelled total methane concentrations
$y$	Observed total methane concentrations
$C_2H_6$	Ethane
$C_3H_8$	Propane
$C_5H_8$	Isoprene
$CH_2O$	Formaldehyde
$CH_3$	Methyl radical
$CH_3CHO$	Acetaldehyde
$CH_3OH$	Methanol
$(CH_3)_2CO$	Acetone
$CH_3CCl_3$	Methyl chloroform
$CH_3O$	Methoxide
$CH_3O_2$	Methylperoxy radical

---

$\text{CH}_3\text{O}_2\text{H}$	Methylhydroperoxide
$\text{CH}_4$	Methane
$\text{Cl}$	Chlorine radical
$\text{CO}_2$	Carbon dioxide
$\text{H}_2\text{O}$	Water
$\text{HO}_2$	Hydroxyperoxyl radical
$\text{HO}_x$	Family of OH and $\text{HO}_2$
MCF	Methyl chloroform
$\text{NO}$	Nitric oxide
$\text{NO}_2$	Nitrogen dioxide
$\text{NO}_x$	Family of NO and $\text{NO}_2$
$\text{O}(^1\text{D})$	Singlet oxygen
$\text{O}_2$	Oxygen
$\text{O}_3$	Ozone
$\text{O}_x$	Family of O and $\text{O}_3$
OH	Hydroxyl radical



# 1 | Methane in the atmosphere

Methane ( $\text{CH}_4$ ) is the second most important directly emitted greenhouse gas (GHG) after carbon dioxide ( $\text{CO}_2$ ). While methane concentrations are significantly lower than those of  $\text{CO}_2$ , its radiative efficiency is an order of magnitude greater than that of  $\text{CO}_2$  [e.g. IPCC, 2013]. A recent study has shown that the radiative forcing of methane from 1750 to 2100 might be 25% higher than previously estimated [Etminan et al., 2016]. Furthermore, methane has a relatively short total atmospheric lifetime of  $9.1 \pm 0.9$  years [Dlugokencky et al., 2011; Prather et al., 2012]. Methane thus presents a large potential for climate mitigation strategies as any changes in methane emissions would have near immediate atmospheric effects. Reducing methane emissions may therefore leave time to implement  $\text{CO}_2$  mitigation policies. With current available technologies, a 40% cut in methane emissions may not be difficult to achieve and would lead to large changes in radiative forcing [Montzka et al., 2011a].

In addition to its direct contribution to the greenhouse effect, chemical loss of methane affects the abundance of tropospheric ozone ( $\text{O}_3$ ) and stratospheric water vapour. Both contribute to the total radiative forcing themselves [Dlugokencky et al., 2011; Myhre et al., 2016]. Furthermore, tropospheric ozone negatively impacts air quality [e.g. WHO, 2003] and is susceptible to climate and emission changes [e.g. Stevenson et al., 2013; Voulgarakis et al., 2013; Banerjee et al., 2016]. It has been shown that methane strongly affects tropospheric ozone abundance [e.g. Morgenstern et al., 2013] so that mitigating methane emission reduces both climate warming and tropospheric ozone abundance [e.g. Fiore et al., 2002].

This thesis aims to further the current understanding of atmospheric methane. Using a chemistry-climate model with a newly developed addition to its chemistry scheme, the sensitivity of tropospheric methane to changes in both methane emissions and sinks is explored. The thesis concludes with a study of future chemistry-climate interactions focussing on the impacts of methane changes on tropospheric composition.

An overview of the atmospheric methane burden is given in section 1.1, highlighting global changes in atmospheric methane over the recent past. This is followed by a description of methane sources (section 1.2) and sinks (section 1.3) including the source and sink effects on the methane isotopes. The concept of the atmospheric (methane) lifetime is introduced in section 1.4. An overview of global chemistry models is presented (section 1.5) outlining different implementations relevant for methane chemistry. The introduction concludes with a brief summary (section 1.6) before the thesis outline is given in section 1.7.

## 1.1 Atmospheric methane burden

The atmospheric methane burden has changed significantly over the past millennia. Ice core analysis has shown that methane increased to 700 ppb (parts-per-billion,  $10^{-9}$ , note that this refers to the volume mixing ratio throughout this thesis) in the warm interglacial from around 350 ppb during cold glacial periods (Figure 1.1). This has been mainly attributed to increases in wetland emissions [Dlugokencky et al., 2011; Wolff, 2014] with a contribution from reduced atmospheric oxidative capacity [Ciais et al., 2013]. Current analysis is focused on whether methane reacted to higher temperatures, thus being an indicator of climate change, or whether it forced temperatures to rise and therefore initiated climate change. Resolution of this question is however difficult due to accurate timing of ice core data and the synchronicity of global warming and changes in atmospheric chemistry [Wolff, 2014].

### 1.1.1 Recent changes in methane

Pre-industrial (PI, before 1750) methane levels were stable at around 700 ppb from about 1000 A.D. [Etheridge et al., 1998] (Figure 1.2). Since the beginning of the 20<sup>th</sup> century global methane concentrations have increased and the latitudinal gradient steepened with higher concentrations in the Northern Hemisphere [Dlugokencky et al., 1994b; Etheridge et al., 1998]. The growth rate peaked in 1991 at  $17 \text{ ppb yr}^{-1}$  when concentrations reached twice their PI levels [Etheridge et al., 1998; Dlugokencky et al., 2011; Kirschke et al., 2013]. Present methane levels are the highest levels observed in history [e.g. Montzka et al., 2011a; Ghosh et al., 2015] (Figure 1.2), and continue to rise (Figure 1.3 (a)).

The methane growth rate slowed at the beginning of the 21<sup>st</sup> century resulting in relatively constant atmospheric methane levels suggesting that sinks and sources were in balance during this time [Dlugokencky et al., 2003] (Figure 1.3). Isotopic analysis of the stable

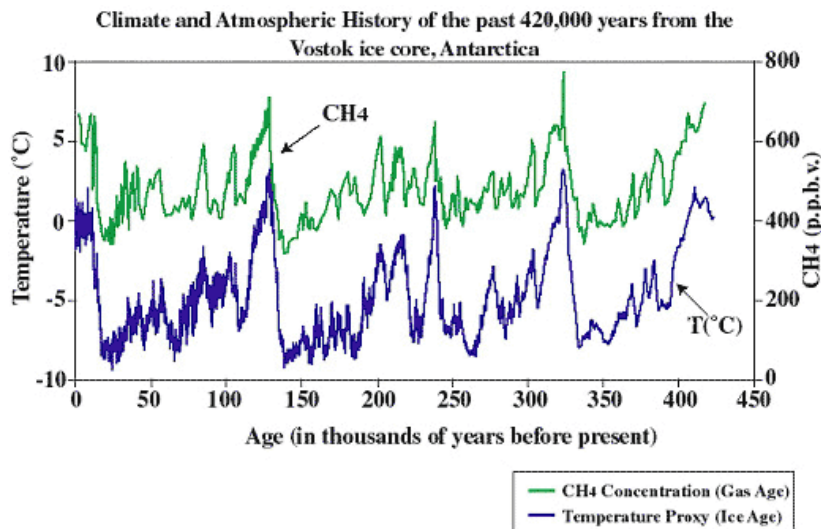


**Fig. 1.1** Atmospheric methane concentrations over the last 400,000 years showing the correlation between temperature (blue, °C) and methane (green, ppb). Figure from [https://www.giss.nasa.gov/research/features/200409\\_methane/](https://www.giss.nasa.gov/research/features/200409_methane/) [Petit et al., 1999].

global methane concentrations between 2000 and 2005 is ambiguous but suggests that fossil fuel emissions were near constant or decreasing at that time coinciding with increasing or near constant microbial emissions [Kirschke et al., 2013]. McNorton et al. [2016a] showed that interannual variability in global mean hydroxyl radical (OH) concentrations and thus in atmospheric methane loss may have also contributed to the stable methane concentrations between 2000 and 2005. The changes in these decadal methane growth rates are difficult to attribute to source changes partly due to the lack of detailed observations [Ciais et al., 2013; Kirschke et al., 2013].

In 2006 the methane growth restarted, the cause of which is currently under investigation (Figure 1.3). Increases in fossil fuel exploitation have been reported since 2006. However, these estimates lead to an overestimation of modelled methane compared to observations [Bergamaschi et al., 2013; Kirschke et al., 2013]. This highlights that either inventories suggest too large emissions or the temperature and precipitation dependence of modelled wetland emissions is too sensitive [Kirschke et al., 2013; Schwietzke et al., 2016]. Analysis of the isotopic composition of atmospheric methane furthermore shows a recent shift to lighter atmospheric methane. This can be attributed to increases in biogenic emissions, mainly from the tropical regions, as noted by Nisbet et al. [2016] and Schaefer et al. [2016]. Changes in global OH concentration may have also contributed to the renewed increase in the variability of methane [e.g. Rigby et al., 2008; Montzka et al., 2011a; Kirschke et al., 2013; Ciais et al., 2013].

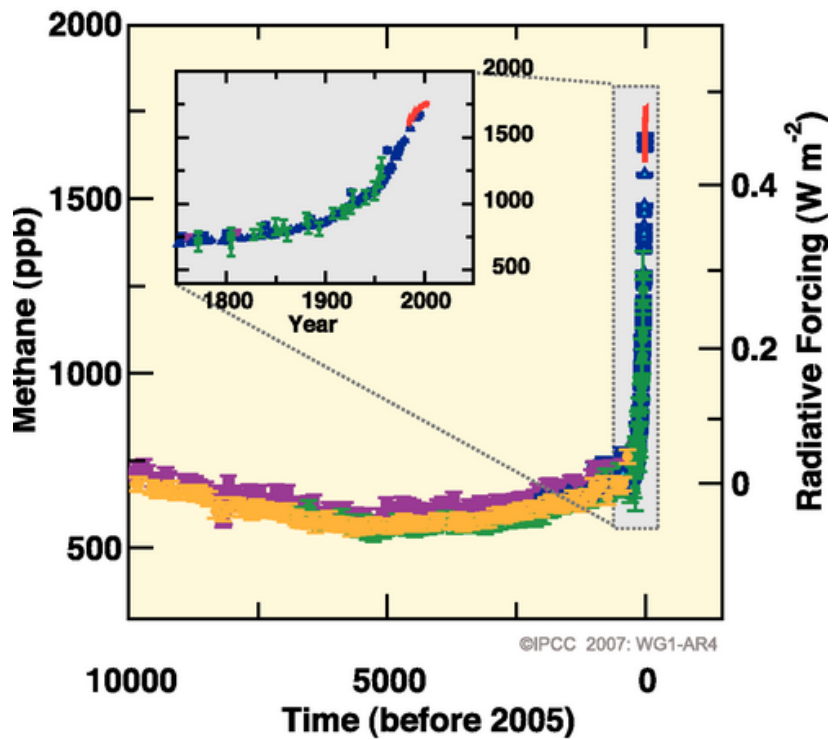


Fig. 1.2 Atmospheric methane concentrations over the last 10,000 years. Figure from Solomon et al. [2007].

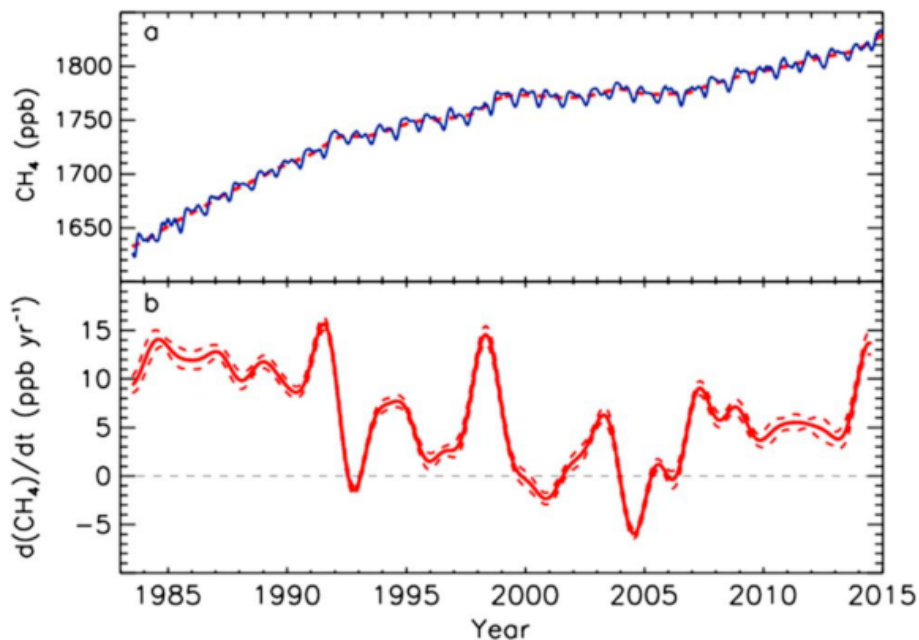


Fig. 1.3 Global monthly (blue) and annually averaged (red) methane (a, ppb) and methane growth rate (b, ppb yr<sup>-1</sup>) from 1983 to 2014. Figure from Nisbet et al. [2016].

### 1.1.2 Interannual variability

Figure 1.3 (b) shows the large interannual variability of methane concentrations, suggesting the sensitivity of (natural) methane emissions to environmental factors such as temperature, precipitation and meteorology [Warwick et al., 2002; Bloom et al., 2010; O'Connor et al., 2010; Melton et al., 2013]. In 1991, a sharp increase in methane growth rate was followed by a strong decrease. This can be attributed to the eruption of Mt. Pinatubo which initially reduced tropospheric photolysis rates by emitting sulphur dioxide into the stratosphere and increasing aerosol abundance there [e.g. McCormick and Veiga, 1992; Ehhalt et al., 2001; Bândă et al., 2016]. As a result, OH concentrations, the major methane sink (see section 1.3), were lower and methane levels augmented [e.g. Dlugokencky et al., 1996, 1998; Ehhalt et al., 2001; Lelieveld et al., 2006]. This was immediately followed by cooling due to reduced solar influx dampening the wetland source strength, both in the tropics (~70%) and the high latitudes [e.g. Dlugokencky et al., 1996; Kirschke et al., 2013; Bândă et al., 2016]. Modelling studies indicate that stratospheric ozone depletion following the eruption increased tropospheric OH levels further reducing methane levels [Bekki et al., 1994]. Isoprene emissions were also proposed to have decreased following the eruption causing decreases in tropospheric OH abundance of similar magnitude to the proposed changes in wetland emissions or biomass burning [Telford et al., 2011]. Additionally, the collapse of the former Soviet Union in 1991 was followed by a reduction in fugitive fossil fuel emissions [e.g. Dlugokencky et al., 1994a; Kirschke et al., 2013].

Another example of large interannual variability is evident around the years 1997 and 1998. These were marked by surface dryness and increased temperatures associated with a strong El Niño [e.g. McNorton et al., 2016b; Nisbet et al., 2016]. An increased number of wild fires were observed together with an initial reduction in Northern Hemispheric wetland methane emissions followed by a tropical emission increase [Bousquet et al., 2006; van der Werf et al., 2006]. Other El Niño events such as the one during 2006 show similar effects [Worden et al., 2013].

Figure 1.4 shows the latitudinal distribution of the methane growth rate as a function of time since 2000. Again, large interannual variability is evident, especially in the northern mid-latitudes in 2003 and 2004. The methane increase in 2006 is strongest in the high northern latitudes. This is likely caused by wetland emission increases due to higher temperatures in the Arctic [Kay et al., 2008; Nisbet et al., 2016]. Methane increases in the subsequent years span the entire globe.

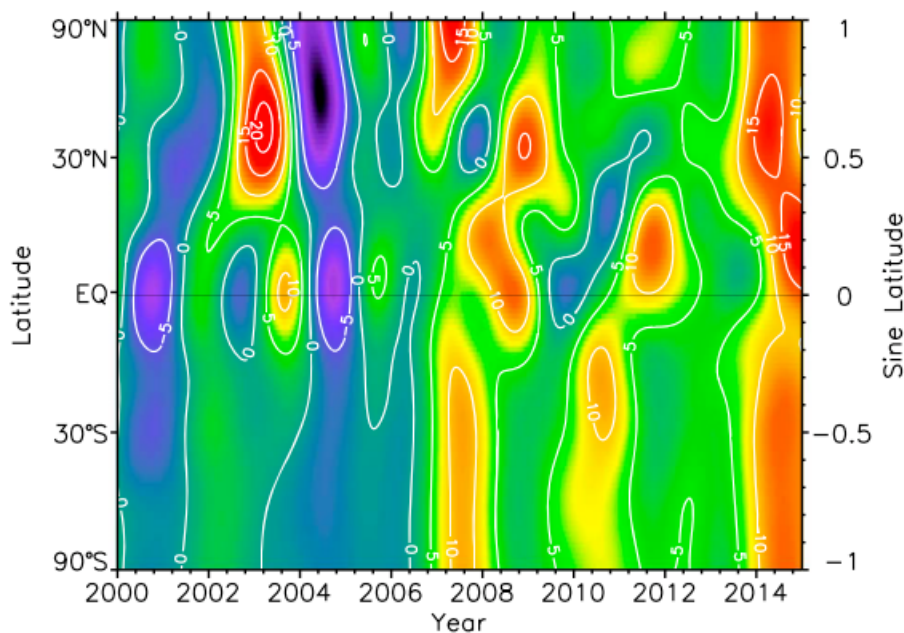


**Fig. 1.4** Latitudinal distribution of the methane growth rate from 2000 to 2014. Warm colours indicate increases while cold colours indicate decreases in the rate. Figure from Nisbet et al. [2016].

The inability to diagnose specific changes and drivers for atmospheric events shows the limitations of current measurement networks and of available climate models [Montzka et al., 2011a]. The general overview given in this section has highlighted the complexity of understanding atmospheric methane trends and their drivers. Further research is therefore necessary to fully understand the observed trends. This thesis attempts to isolate the effects of different drivers on atmospheric methane by exploring steady-state, present day atmospheric methane concentrations such as those observed at the beginning of the 21<sup>st</sup> century. This is important to advance understanding of those processes controlling methane in order to understand future methane emissions and their impacts.

## 1.2 Methane sources

This section gives an overview of methane sources and the associated uncertainty in the source strengths. The work of this thesis aims to show the sensitivity of modelled methane to the source distribution and global strength for which it is important to have an overview of the current understanding of methane sources. Total global methane emissions for the beginning of the 21<sup>st</sup> century are estimated between 526 and 569 Tg(CH<sub>4</sub>) yr<sup>-1</sup> with very large

uncertainties in the relative strength of individual sources due to few studies and observations [Dlugokencky et al., 2011; Ciais et al., 2013; Saunio et al., 2016]. Approximately 50 to 65% of methane emissions are of anthropogenic origin [Ciais et al., 2013; Kirschke et al., 2013; Saunio et al., 2016].

### 1.2.1 Natural sources

The total amount of natural methane sources can be approximated using the PI source strength, estimated as  $202 \pm 35 \text{ Tg}(\text{CH}_4) \text{ yr}^{-1}$  [Ciais et al., 2013]. The main natural source are wetlands, the largest single source of all methane sources and the main driver of the year-to-year variability in atmospheric methane abundance. They also have the highest absolute source strength uncertainty [O'Connor et al., 2010; Dlugokencky et al., 2011; Ciais et al., 2013; Kirschke et al., 2013].

#### Wetlands

The wetland global source strength is estimated as between 177 and 284  $\text{Tg}(\text{CH}_4) \text{ yr}^{-1}$  [Ciais et al., 2013]. Even with the high uncertainty in the total wetland source strength and uncertainty on their long-term trends, interannual variations are more robustly estimated with similar year-to-year trends in different studies. Most studies agree on an increasing wetland source since the 1990s [Kirschke et al., 2013]. Wetlands are thought to be the dominant source of interannual source variability, which is greatest in the tropics [Bousquet et al., 2006; Ringeval et al., 2010].

Wetlands are anaerobic environments where methanogenic microbes generate methane from organic matter during their metabolism. More methane is produced at higher temperatures, with a high water table and large substrate availability. Acidic soils reduce methane production. Methane is transported into the atmosphere via diffusion, ebullition and vascular plants [Christensen et al., 2003; O'Connor et al., 2010].

Depending on the water table height, aerobic soils may be found on top of the saturated layer. These are inhabited by methanotrophs which metabolise methane to  $\text{CO}_2$ . Thus, the water table height defines the depth of the anaerobic and aerobic layer and hence whether methane production or consumption dominates [O'Connor et al., 2010].

Wetlands are mainly found in the tropics, and at high northern latitudes (boreal regions). Their exact geographical distribution is however uncertain and likely to vary interannually

[Melton et al., 2013]. Tropical wetlands are thought to be most sensitive to water table height changes, while boreal wetlands are highly influenced by temperature variations [Bloom et al., 2010; Ringeval et al., 2010]. A recent study has shown that different ecosystems show similar temperature dependencies for their methane flux. This highlights the important effect of climate change and increasing temperatures on wetland emissions [Yvon-Durocher et al., 2014]. Furthermore, methane emissions from wetlands are stimulated by higher CO<sub>2</sub> concentrations [van Groenigen et al., 2011]. As emissions are highly sensitive to wetland extent these uncertainties in the driving factors of wetlands present a challenge for analysis and the modelling community [Kirschke et al., 2013].

Wetlands are thought to have been one of the key drivers in climate changes in the past. Changes in isotopic composition towards the lighter isotopes during warmer periods indicate an increased biogenic source strength [Kaplan, 2002; Dlugokencky et al., 2011]. However, it is still highly uncertain how wetlands will react to future climate change. Under warmer and wetter climates, wetlands are expected to release more methane [Montzka et al., 2011a] as higher temperatures and increased CO<sub>2</sub> increase the efficiency of methanogenic activity. Increased temperature may however also result in drier soils, shifting the balance between methanogens and methanotrophs in favour of methane consumption [Montzka et al., 2011a].

Currently, Arctic wetlands contribute with 15 to 50 Tg(CH<sub>4</sub>) yr<sup>-1</sup>, i.e. 2% to 10%, to global methane emissions [Bloom et al., 2010; Ciais et al., 2013]. Changes in precipitation and permafrost thawing will further influence the water table and methane production in the Arctic which is globally the most sensitive region to climate change [O'Connor et al., 2010]. Current judgement suggests that methane released in the Arctic region will increase and create a positive feedback effect. This is expected to be moderate on shorter time scales (centuries) but to play a more significant role over the millennia [Montzka et al., 2011a; Ciais et al., 2013].

### **Other natural sources**

Other natural sources are estimated to contribute 61 to 200 Tg(CH<sub>4</sub>) yr<sup>-1</sup> to total global methane emissions [Ciais et al., 2013].

**Geological sources** have an estimated source strength of  $55 \pm 11$  Tg(CH<sub>4</sub>) yr<sup>-1</sup>, accounting for 30% of the total methane source, with the largest contribution from terrestrial and marine seepages. Mud volcanoes, hydrates and geothermal and volcanic areas contribute less than 10 Tg(CH<sub>4</sub>) yr<sup>-1</sup> each [Etiope et al., 2008].

The source strength of **hydrates** is especially poorly constrained as their location is difficult to assess. Furthermore, different clathrates vary with respect to the water-to-methane ratio. It is therefore difficult to estimate the quantity of emitted methane, with currently a value of  $5 \text{ Tg}(\text{CH}_4) \text{ yr}^{-1}$  used as a placeholder [Cicerone and Oremland, 1988]. Hydrates are stable under low temperatures and high pressures and can be found in deep permafrost, on continental margins in marine sediments (below 500 m) and also on unstable continental slopes [O'Connor et al., 2010]. There are known hydrate sources in the Arctic along the continental shelf [e.g. Westbrook et al., 2009; Shakhova et al., 2010, 2013]. Current understanding is that released methane is more likely to be oxidised within the water column than to reach the atmosphere [e.g. Fisher et al., 2011; Berchet et al., 2015; Pisso et al., 2016]. As the Arctic is more sensitive to climate change than other regions destabilisation of hydrates and release of methane into the atmosphere may become significant [Westbrook et al., 2009; O'Connor et al., 2010; Fisher et al., 2011].

Other natural sources have small source strengths with **oceans** and **termites** responsible for between 10 and 20  $\text{Tg}(\text{CH}_4) \text{ yr}^{-1}$  each. Both **wild fires** and **wild ruminant animals** contribute  $5 \text{ Tg}(\text{CH}_4) \text{ yr}^{-1}$ . Their corresponding anthropogenic source analogues have much larger strengths.

### 1.2.2 Anthropogenic sources

Total anthropogenic emissions contribute  $354 \pm 45 \text{ Tg}(\text{CH}_4) \text{ yr}^{-1}$  to the global methane source strength, i.e. 50 to 65% [Ciais et al., 2013]. Most of the anthropogenic sources are found in the Northern Hemisphere which explains the increased interhemispheric gradient since PI times [Etheridge et al., 1998; Ciais et al., 2013].

The largest anthropogenic contribution to methane emissions is **agriculture** and **waste** management. Approximately 187 to 224  $\text{Tg}(\text{CH}_4) \text{ yr}^{-1}$  result from rice agriculture, animal domestication and waste deposits [Ciais et al., 2013]. Methane generated from these sources is of biogenic origin from methanogens.

Between 85 and 105  $\text{Tg}(\text{CH}_4) \text{ yr}^{-1}$  is estimated to originate from the **fossil fuel** industry. A large component is from fugitive emissions with 90% of the leaking gas being methane. These leaks together with natural geological leaks are estimated to contribute up to 30% to the total global methane flux [Ciais et al., 2013].

**Biomass burning** releases about 32 to 39  $\text{Tg}(\text{CH}_4) \text{ yr}^{-1}$  [Ciais et al., 2013]. Interannual variability can be observed due to this source's sensitivity to high temperatures. It is however

small (3% to 15% of total interannual variability) and mostly constrained to years with a high number of fire events [Bousquet et al., 2006; Bloom et al., 2010].

### 1.2.3 Isotopic signatures

Methane can be composed of different stable isotopes, namely  $^{12}\text{C}$ ,  $^{13}\text{C}$  and  $^1\text{H}$ ,  $^2\text{H}$  ( $^2\text{H} = \text{D}$ ). The isotopic ratios  $\delta^{13}\text{C}$  and  $\delta\text{D}$  are defined relative to standards, the Vienna Pee Dee Belemnite and the Vienna Standard Mean Ocean Water, respectively [Craig, 1957]. They are calculated via the equations 1.1 and 1.2 and expressed in per mill, ‰.

$$\delta^{13}\text{C} = \left[ \frac{^{13}\text{C}/^{12}\text{C}_{\text{sample}}}{^{13}\text{C}/^{12}\text{C}_{\text{standard}}} - 1 \right] \times 1000 \quad (1.1)$$

$$\delta\text{D} = \left[ \frac{\text{D}/\text{H}_{\text{sample}}}{\text{D}/\text{H}_{\text{standard}}} - 1 \right] \times 1000 \quad (1.2)$$

Generally, methane formed at higher temperatures is enriched in the heavier isotopes ( $^{13}\text{C}$  and D) while the lighter isotopes ( $^{12}\text{C}$  and  $^1\text{H}$ ) are favoured in biological processes [Cicerone and Oremland, 1988]. Methane sinks usually kinetically favour the lighter isotopes  $^{12}\text{C}$  and  $^1\text{H}$  [e.g. Allan et al., 2005]. When taking into account this fractionation by the sinks (section 1.3), observed methane concentrations can be separated from background air (typical values of  $\delta^{13}\text{C} = -47\text{‰}$  and  $\delta\text{D} = -86\text{‰}$ ) and attributed to its source [Cicerone and Oremland, 1988; Dlugokencky et al., 2011]. Isotopic analysis of the atmospheric methane budget therefore proves to be useful in terms of constraining methane emissions.

Emissions from reservoirs formed through geological processes (over a long timescale) such as fossil fuels are called *thermogenic emissions* due to the production of heat during their formation. Thermogenic emissions generally have a  $\delta^{13}\text{C}$  signature of -25 to -55‰ ranging around the isotopic composition of background air. Methane is also emitted during incomplete combustion during (wild)fires of biomass and soil carbon or fuel combustion. These *pyrogenic emissions* are the richest in  $^{13}\text{C}$  with an average  $\delta^{13}\text{C}$  signature of -13 to -25‰. Methanogenic microbes in anaerobic environments such as wetlands, rice paddies and ruminant digestive systems or waste deposits generate methane as a metabolic byproduct. These *biogenic emissions* are the poorest in  $^{13}\text{C}$  of all three source categories with an average  $\delta^{13}\text{C}$  signal of -55 to -70‰, thus lighter than background air [Cicerone and Oremland, 1988; Dlugokencky et al., 2011; Kirschke et al., 2013].

Figure 1.5 illustrates how the combined isotopic analysis may be used to distinguish methane sources and sinks. The relative source strength is shown as a function of isotopic signature. Additionally the fractionation due to sink reactions is incorporated (see section 1.3 for more details).

While the work in this thesis does not include isotopic information it lays the the ground work to include these features in future experiments. Isotopes are a useful constraint on methane sources and sinks and can help reduce uncertainties [e.g. Allan et al., 2001b; Warwick et al., 2016]. Modelling studies are crucial to reduce current uncertainty in the isotopic signal for different sources and to determine the cause for the recent increase in atmospheric methane concentrations [Nisbet et al., 2016; Schaefer et al., 2016].

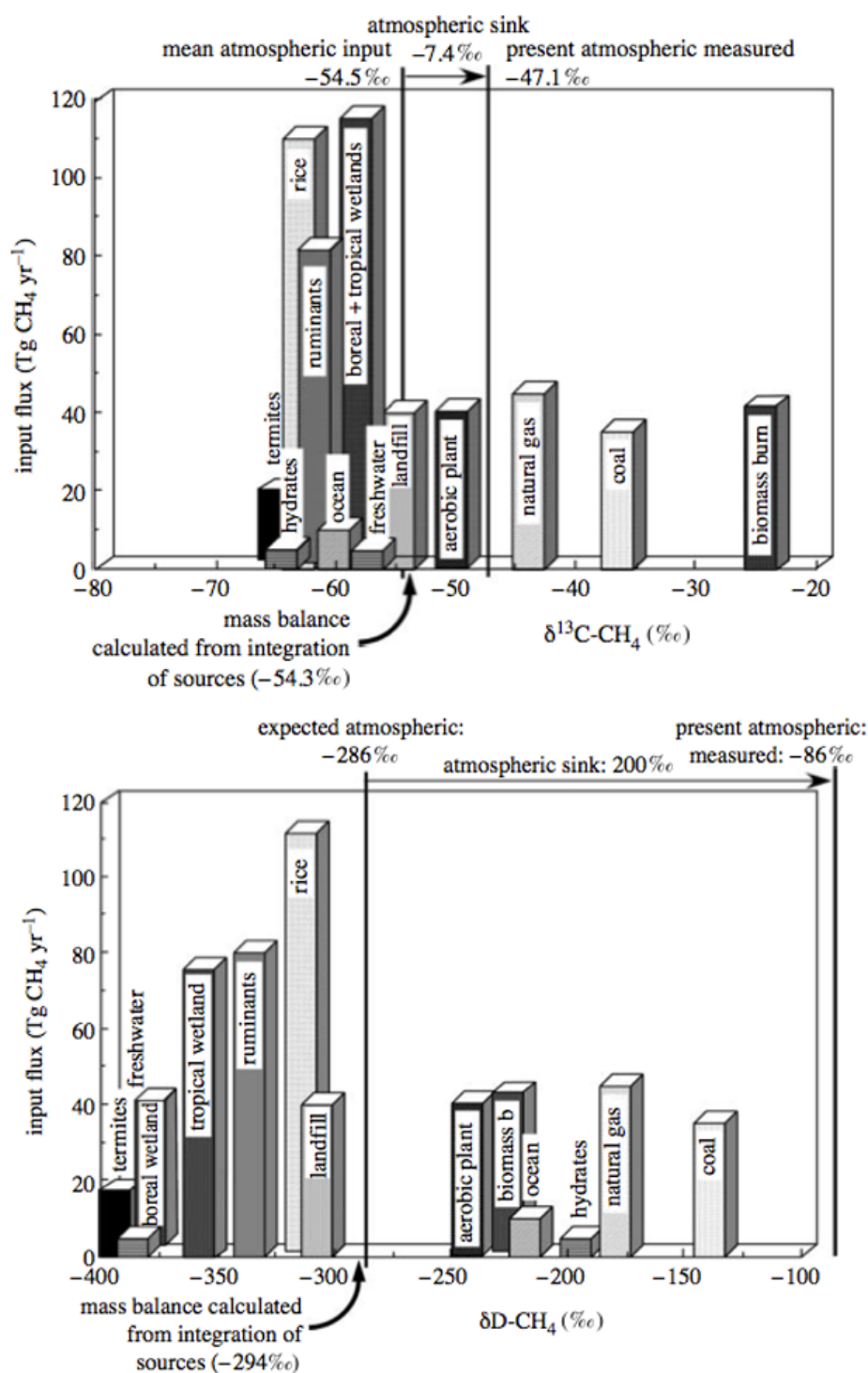


**Fig. 1.5** Histogram of isotopic data for methane sources and sinks for  $\delta^{13}\text{C}$  (top) and  $\delta\text{D}$  (bottom). Isotopic background measurements as well as integrated source signals are indicated by vertical lines. Figure from Whiticar and Schaefer [2007].

## 1.3 Methane sinks

Methane is mostly (90%) removed from the atmosphere via chemical reaction with OH, linking the methane burden to ozone and water vapour concentrations both in the troposphere and stratosphere. The remaining 10% of atmospheric methane sink is distributed between oxidation by methanotrophs in aerobic soils, stratospheric loss via reaction with chlorine and singlet oxygen radicals and destruction via chlorine radicals in the marine boundary layer (MBL) [Allan et al., 2005; Rigby et al., 2008; Ciais et al., 2013; Kirschke et al., 2013].

There is only a small imbalance between methane production and consumption with a loss flux of  $542 \pm 56 \text{ Tg}(\text{CH}_4) \text{ yr}^{-1}$  [Ciais et al., 2013] of which 90% is due to the reaction chain with OH. The OH radicals determine the oxidising capacity of the atmosphere and are responsible for the majority of hydrocarbon oxidation. Approximately 70% of the tropospheric OH reacts with CO and the remaining 30% oxidises methane. Thus, changes in the emissions of CO and other non-methane hydrocarbons can strongly influence the OH abundance and hence methane. Additionally, a strong positive feedback exists between methane and its abundance via OH chemistry. Increases in methane lead to a reduction in OH which further leads to increases in methane and a longer lifetime [e.g. Ehhalt et al., 2001; Montzka et al., 2011b].

Chemical reaction rates are not identical for the different methane isotopomers due to their mass difference, with lighter isotopomers reacting faster than their heavier analogues [e.g. Saueressig et al., 2001]. This leads to an increase in  $^{13}\text{CH}_4$  with time, leading to higher  $^{13}\text{CH}_4$  abundance in the Southern Hemisphere, where sources are less present. This effect is known as isotopic fractionation and the Kinetic Isotope Effect  $\epsilon$  is defined in equation 1.3. The loss rate of methane depends on a rate coefficient  $k_X^Y$ , where Y represents the isotope, and the concentrations of both the sink X and of methane (equation 1.4).

$$\epsilon = \frac{k_X^{13}}{k_X^{12}} \quad (1.3)$$

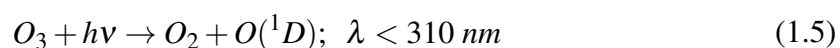
$$\text{loss rate} = k_X^Y [X] [\text{CH}_4] \quad (1.4)$$

### 1.3.1 The hydroxyl radical sink

The methane sink via reaction with OH is largest in the tropics (80%) where the OH photochemical production dominates [e.g. Bloss et al., 2005; Bousquet et al., 2006]. Thus, there is a geographical distance between the methane sources and the main sink with meteorology strongly influencing annual changes in methane loss [Warwick et al., 2002]. Analysis has shown that a 1% variation in the OH sink may change the global methane burden by up to 5 Tg(CH<sub>4</sub>) (0.3% of 1750 ppb background) [Kirschke et al., 2013]. Aerosols and trace gas emissions are the cause of at least 50% of the variability of the methane loss due to OH [Kirschke et al., 2013]. Measurements of OH are difficult and its short lifetime causes large geographical differences on short distances. Differences exist in the estimates of interannual OH variability, ranging from near zero to below 10%, leading to uncertainty about the significance and strength of this variability [e.g. Bousquet et al., 2005, 2006; Bloom et al., 2010; McNorton et al., 2016a].

Global tropospheric OH can be estimated from measurements of methyl chloroform (MCF, CH<sub>3</sub>CCl<sub>3</sub>). MCF itself is predominantly lost through reaction with OH. MCF emissions are well constrained (close to zero) since its inclusion in the Montreal Protocol [Bousquet et al., 2005; Prinn et al., 2005] so that observed changes in MCF are dominated by the chemical loss rather than by emission events [Spivakovsky et al., 2000]. MCF measurements suggest that OH is evenly distributed in the Northern and Southern Hemisphere or with slightly higher Southern Hemisphere concentrations [Prinn et al., 2001; Patra et al., 2014]. The tropospheric OH abundance has been inferred from MCF measurements at  $9.4 \pm 1.3 \times 10^5$  molecules cm<sup>-3</sup> [Prinn et al., 2001]. This thesis aims to study the effect of different OH distributions and strengths on global methane levels.

OH is produced via the reaction of water (H<sub>2</sub>O) with singlet oxygen (O(<sup>1</sup>D)), produced through photolysis of ozone at wavelengths  $\lambda \leq 310$  nm (reactions 1.5 and 1.6). OH and the hydroxyperoxyl radical (HO<sub>2</sub>) are in rapid equilibrium and together form the family HO<sub>x</sub>.



OH and HO<sub>2</sub> interconvert via reaction with nitric oxide (NO) and ozone (Figure 1.6) thus coupling methane chemistry to other chemical cycles in the atmosphere.

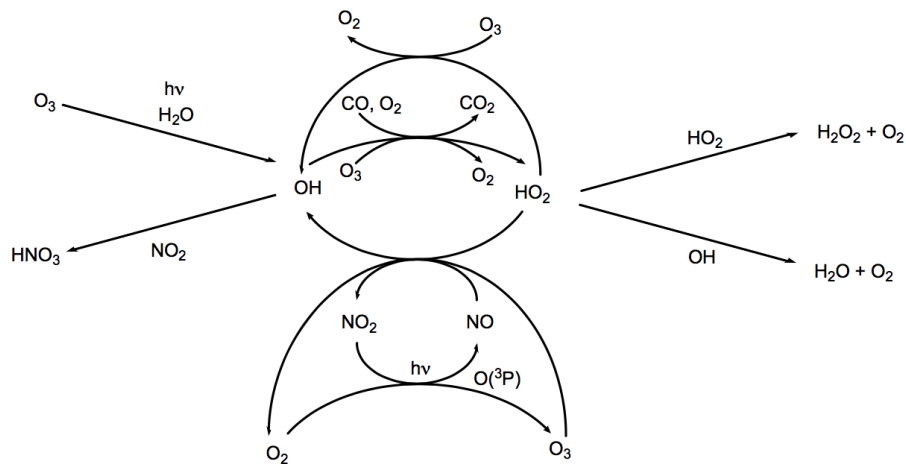


**Fig. 1.6** Sources and sinks of atmospheric OH and HO<sub>2</sub> depicting the atmospheric HO<sub>x</sub> cycle.

Methane oxidation is initiated by reaction with OH. This reaction forms the methyl radical (CH<sub>3</sub>) which goes on to form the methylperoxy radical (CH<sub>3</sub>O<sub>2</sub>) in the presence of oxygen (O<sub>2</sub>).

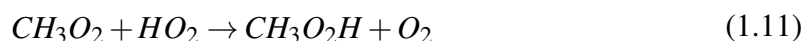


The CH<sub>3</sub>O<sub>2</sub> radical can then undergo different removal pathways depending on the atmospheric conditions. In the presence of NO the peroxy radical is reduced to methoxide (CH<sub>3</sub>O) while forming nitrogen dioxide (NO<sub>2</sub>) (reaction 1.9). Methoxide reacts with oxygen to form formaldehyde (CH<sub>2</sub>O) which is the first stable compound in the methane oxidation sequence (reaction 1.10).

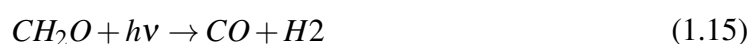


Alternatively, the CH<sub>3</sub>O<sub>2</sub> radical reacts with HO<sub>2</sub> to form methylhydroperoxide (CH<sub>3</sub>O<sub>2</sub>H) (reaction 1.11) which photolyses or reacts with OH to form methoxide and then CH<sub>2</sub>O

(reaction 1.10). The methylperoxy radical can also react with itself forming formaldehyde and methanol ( $\text{CH}_3\text{OH}$ ) which is rained out (reaction 1.12).



$\text{CH}_2\text{O}$  forms CO through photolysis or reaction with OH in the presence of oxygen (reactions 1.13 to 1.16) which is further oxidised with OH to  $\text{CO}_2$ .



The reaction chain discussed above is represented in Figure 1.7 which highlights the many branches of the seemingly simple methane oxidation. Both Figures 1.6 and 1.7 show that methane is strongly coupled to other atmospheric chemistry species and cycles via their impact on tropospheric OH. Increases in CO and other species oxidised by OH reduce the OH sink strength and can thus increase methane concentrations. In contrast, species that produce OH, such as ozone and, indirectly,  $\text{NO}_x$  (NO and  $\text{NO}_2$ ), strengthen the methane sink and thus reduce methane concentrations.

Methane can act as an ozone precursor in the presence of  $\text{NO}_x$  directly and following oxidation of methane-sourced CO [e.g. Monks et al., 2015]. Thus, methane has impacts on tropospheric air quality through its chemistry as well as indirectly through its effect on atmospheric temperatures [e.g. Fiore et al., 2002].

### 1.3.2 Additional sinks

Approximately 4% of global methane is converted to  $\text{CO}_2$  by **methanotrophic bacteria** in the soil [e.g. Stevenson et al., 2006; Dlugokencky et al., 2011] with an estimated strength of 9 to 47  $\text{Tg}(\text{CH}_4) \text{ yr}^{-1}$  [Ciais et al., 2013]. Matthey et al. [2013] showed that methanotropic

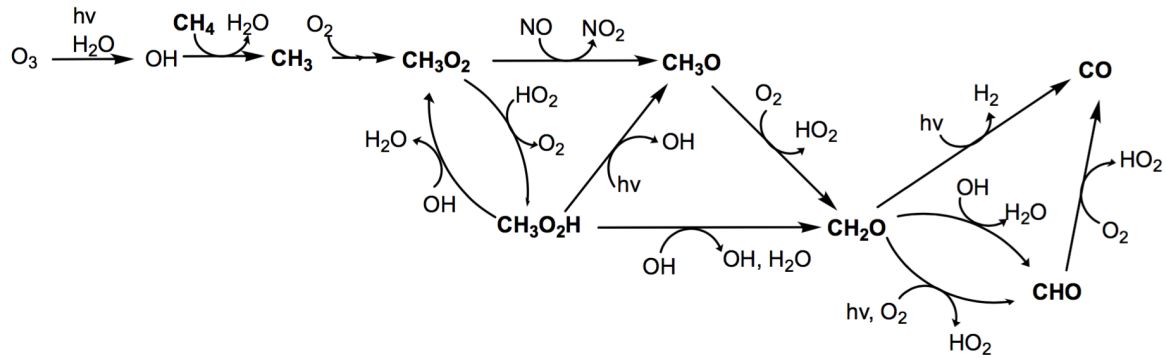


Fig. 1.7 Atmospheric methane oxidation to CO.

oxidation in regions with karst topography may also contribute to this soil sink. The remaining 6% is lost to the **stratosphere** where methane reacts with  $O(^1D)$  and chlorine radicals (Cl) [e.g. Stevenson et al., 2006] or is removed in the **marine boundary layer** (MBL) via reactions with Cl. The significance of this latter sink is still debated [Ciais et al., 2013] but analysis has suggested that the MBL sink via Cl can explain the observed isotopic sink fractionation in the Southern Hemisphere [e.g. Allan et al., 2005, 2007]. This is of particular importance when constraining emission strengths with isotopic source signatures.

Table 1.1 summarises the source and sink strengths presented in this section combined with their typical isotopic signature. Results chapters in this thesis will use the information given in these sections to establish a source map for the model experiments performed here.

## 1.4 Methane lifetime

Methane has a relatively short atmospheric lifetime which means that source or sink changes have near immediate effects on atmospheric levels. The atmospheric lifetime of a compound describes its removal time from the atmosphere [Cracknell, 1994]. When a compound is in steady state, its atmospheric lifetime  $\tau$  is defined as shown in equation 1.17.

$$\tau = \frac{\text{average global abundance}}{\text{annual total loss}} = \frac{\text{average global abundance}}{\text{annual total sources}} \quad (1.17)$$

Methane has many different loss processes (see section 1.3 above) which act in different regions of the atmosphere. Partial lifetimes can be calculated for the individual loss processes, the inverse sum of which equals to the inverse total lifetime (equation 1.18).

**Table 1.1** Annual strength of methane sources in  $Tg(CH_4) yr^{-1}$  as presented in Ciais et al. [2013]. Isotopic data is compiled from Whiticar and Schaefer [2007]. Note that the global budget has been recently revised slightly upwards [Saunio et al., 2016].

Source	Strength $Tg(CH_4) yr^{-1}$	$\delta^{13}C$ ‰	$\delta D$ ‰
Natural			
Wetlands	177 – 284		
boreal (bogs, tundra)		-62.0	-380
tropical (swamps)		-58.9	-360
Termites	2 – 22	-63.0	-390
Freshwater	8 – 73	-53.8	-385
Gas hydrates	2 – 9	-62.5	-190
Geological	33 – 75	-41.8	-200
Anthropogenic			
Fossil fuels	85 – 105		
Coal and industry		-37.0	-140
Gas		-44.0	-180
Ruminants (incl. wild ruminants)	87 – 94	-60.5	-320
Rice agriculture	33 – 40	-63.0	-320
Waste	67 – 90	-55.0	-310
Biomass burning (incl. wild fires and biofuels)	32 – 39	-24.6	-225
Sinks			
OH	454 – 617	7.4	200
Stratospheric loss	40*		
Cl	13 – 37		
Methanotrophic oxidation	9 – 47		

\* from Stevenson et al. [2006]

$$\frac{1}{\tau} = \sum \frac{1}{\tau_{partial}} = \sum \frac{annual\ partial\ loss}{average\ global\ abundance} \quad (1.18)$$

The annual partial loss is integrated over the domain in which the loss process takes place. This relationship between the abundance, atmospheric loss and sources can in principle be used to estimate one of the variables. As large uncertainties are associated with methane emissions (see section 1.2 above), the methane lifetime could theoretically be used to constrain the source estimate. Methane is lost from the atmosphere mainly through tropospheric OH (90%, see above) but stratospheric and tropospheric chlorine and soil uptake also contribute. The total atmospheric methane lifetime is  $9.1 \pm 0.9$  years [Prather et al., 2012]; the lifetime

with respect to tropospheric OH is  $11.2 \pm 1.3$  years while stratospheric loss, tropospheric chlorine and the soil sink have lifetimes of 120 years, 200 years and 150 years, respectively [Prather et al., 2012].

It is common to (only) report the methane lifetime with respect to its loss by reaction with OH,  $\tau_{OH+CH_4}$  (equation 1.19). A global OH distribution is however difficult to determine directly because of the short atmospheric lifetime of OH (see above, section 1.3) [e.g. Prinn et al., 1995; Montzka et al., 2000; Prinn and Huang, 2001; Krol and Lelieveld, 2003].

$$\tau_{OH+CH_4} = \frac{\text{average global } CH_4 \text{ abundance}}{\text{annual tropospheric OH loss}} \quad (1.19)$$

As outlined above, methyl chloroform measurements can be used to estimate tropospheric OH. As observed changes in MCF are dominated by the chemical loss with OH the MCF lifetime can be estimated from observations, analysing the decline in MCF abundance. This estimate is used in inversion studies which allow the OH distribution to be calculated. The inferred OH field can then be used to estimate the methane lifetime against tropospheric OH loss [e.g. Montzka et al., 2000; Krol and Lelieveld, 2003].

Throughout the thesis the methane lifetime against tropospheric OH loss,  $\tau_{OH+CH_4}$ , is compared to other modelling studies such as the Atmospheric Chemistry and Climate Intercomparison Project (see below, section 1.5.1) and the observational estimate in order to assess the model's ability at representing methane chemistry.

## 1.5 Modelling the atmosphere

Understanding atmospheric methane is crucial for mitigating climate change and improving air quality. Models are vital tools in developing that understanding. They are used to simulate atmospheric processes and to study how environmental events are linked. Not all models simulate atmospheric chemistry but only those that do are discussed here. Two model families exist which can resolve atmospheric chemistry are briefly introduced next.

In global chemistry-climate models (CCMs) atmospheric composition is coupled to the radiation/dynamics. Changes in composition can thus impact the climate (temperature, dynamics, radiation etc.) and climate can impact on composition. The chemistry in CCMs is generally fully interactive meaning that oxidant levels, such as OH concentrations, are a result of the chemistry simulated in the model. This type of model can be used to study the current,

past and future atmosphere. The model in this thesis is a fully interactive chemistry-climate model which resolves tropospheric and stratospheric chemistry.

Global chemistry-transport models (CTMs) prescribe dynamical fields. These are often provided from weather forecasting models or a free running parent model. The dynamics are not simulated within the model therefore no two-way coupling to the composition can be achieved with CTMs, the major difference to CCMs. In general, CTMs are computationally less expensive than CCMs (at the same resolution) as the underlying dynamics do not need to be simulated. This also means that CTMs then have more resources available for more complex chemistry schemes compared to CCMs which often need to reduce the number of reactions [e.g. Zhang, 2008]. Composition differences between CTMs and CCMs have been attributed to the missing feedbacks between the dynamics and other processes suggesting that CCMs are ultimately more suited to study atmospheric processes [e.g. Zhang, 2008].

### 1.5.1 Modelling atmospheric chemistry

This thesis will focus on assessing atmospheric methane for which chemistry is important. Thus, the next paragraphs briefly outline different modelling approaches to atmospheric chemistry. The treatment of methane in these chemistry schemes will be highlighted.

#### Non-interactive chemistry

The simplest form of chemistry modelling is by imposing atmospheric oxidant fields (e.g. OH) in the model. These oxidant fields are independent of the subsequent modelled chemistry thus only reactions relevant to the scientific question need to be simulated. This often reduces computational expense as the number of simulated processes is smaller. If modelling methane is the only objective, then only one continuity equation – for methane – needs to be solved if the oxidants are specified. Models participating in the atmospheric tracer and transport intercomparison project for methane (TransCom-CH<sub>4</sub> [Patra et al., 2011]) used such a non-interactive chemistry scheme. The project aimed to investigate the link between methane chemistry, emissions and transport. Methane emissions in addition to the oxidant fields (OH, O(<sup>1</sup>D), Cl) and methane loss rates were identical for all models participating in this project. Thus, the differences arising in global methane concentrations could be linked to atmospheric transport processes. Furthermore, different emission scenarios were simulated with the aim to improve understanding of the effect of the emission distribution on global methane levels.

The results of this intercomparison project show that the stratosphere-troposphere exchange plays a large role in the global methane budget and that the interannual methane variability is strongly linked to the interannual variations of methane emissions.

Prescribing oxidant fields also removes the chemical feedback of methane on itself. The strength of this feedback is estimated to be of maximum 10% of the total methane budget [Fung et al., 1991]. Once this feedback is ignored, methane chemistry is linear and it is thus possible to simulate multiple methane tracers in parallel. This is often referred to as ‘tagging’ as tracers can be ‘labelled’ according to their origin. An example is the recent work by Warwick et al. [2016] where methane was tagged by source type and isotopic signature. This allowed detailed analysis of the contribution of individual source types to Arctic methane concentrations. In their paper, Warwick et al. [2016] have shown that delaying Arctic wetland emissions by one month can lead to improved representation of the seasonal cycle of methane in this region. Allan et al. [e.g. 2001a] used a linear, non-interactive chemistry setup to show that a MBL chlorine sink can explain observed seasonality in methane isotopes.

### **Interactive chemistry**

Alternatively, atmospheric chemistry can be modelled interactively which means that the chemical production and loss of atmospheric oxidants is also simulated by the chemistry scheme. Interactive chemistry schemes have been used to study many different aspects of the atmosphere including, for instance, stratospheric ozone recovery [e.g. Lamarque et al., 2013], tropospheric ozone chemistry [e.g. Stevenson et al., 2006; Wild, 2007; Stevenson et al., 2013], isoprene [e.g. Archibald et al., 2011], lightning [e.g. Banerjee et al., 2014] and aerosol chemistry. Differences arise for instance from variations in the dominant reaction cycles for tropospheric and stratospheric chemistry [e.g. Morgenstern et al., 2009; O’Connor et al., 2014]. Furthermore, chemistry schemes, even those representing the same part of the atmosphere, vary in the number of reactions included as more reactions demand more computational time per time step. Very detailed chemistry schemes are therefore currently not suitable for global studies for extensive (e.g. millennia) time studies.

### **Atmospheric Chemistry and Climate Intercomparison Project (ACCMIP)**

A recent intercomparison project, the Atmospheric Chemistry and Climate Intercomparison Project (ACCMIP), targeted the “driving forces of climate change” and aimed to document atmospheric composition changes and their effect on radiative forcing [Lamarque et al., 2013]. An ensemble of 16 models, differing in resolution, cloud and radiation interaction

as well as chemistry schemes was used to analyse long-term composition changes between 1850 and 2100. This project provided a framework for modelling studies by outlining harmonised emissions and external forcings. Studies have looked at past and future ozone [Stevenson et al., 2013; Young et al., 2013], OH and methane [Naik et al., 2013; Voulgarakis et al., 2013] from these ACCMIP simulations. Furthermore the data are a useful benchmark for subsequent modelling studies such as the Climate Chemistry Model Initiative (CCMI, <http://www.igacproject.org/CCMI>) and the Aerosols Chemistry Modeling Intercomparison Project (AerChemMIP, <https://cmip.ucar.edu/aer-chem-mip>).

As done in many interactive chemistry schemes, most ACCMIP models prescribe methane concentrations at the surface, i.e. impose a concentration boundary condition. For four models methane is prescribed throughout the atmosphere while one/two models use methane emissions for the historical/future simulations. Prescribing methane concentrations reduces spin-up period to months and keeps the models at stable methane levels [e.g. Stevenson et al., 2013]. While methane concentrations are prescribed, chemical processing is allowed throughout the entire rest of the model, however, the chemistry does not feed back onto methane levels.

The prescribed levels vary around 1750 ppb for present day levels, based on recommendations from Meinshausen et al. [2011]. Individual models use different approaches to prescribe methane, ranging from one value over the entire globe to an applied latitudinal gradient. The different way of prescribing does not seem to influence the methane abundance [Naik et al., 2013].

As for other chemistry-climate models, the ACCMIP multi-model mean methane lifetime with respect to tropospheric OH loss is  $9.3 \pm 0.9$  years, lower than observation-based estimates [Voulgarakis et al., 2013]. The range in modelled methane lifetime is likely linked to the different modelled trends in OH, one major uncertainty in atmospheric science. Furthermore, most models suggest higher OH concentrations in the Northern Hemisphere which is in contradiction to OH estimates from MCF measurements (see above, Prinn et al. [2005]; Patra et al. [2014]). Improving the understanding of methane source and sink processes is therefore necessary to reproduce observational estimates for methane and other compounds with chemistry models.

Prescribing surface methane concentrations effectively overwrites any feedback of the chemistry scheme on methane [e.g. Stevenson et al., 2006; Banerjee et al., 2014]. Data from most ACCMIP models can therefore not fully assess the methane impact on tropospheric composition. In subsequent chapters the data from the ACCMIP intercomparison project will

be used for comparison purposes and to highlight differences likely arising from methane chemistry differences.

## 1.6 Summary

In this introduction, a brief overview of the current understanding of atmospheric methane was given. It was shown that atmospheric methane concentrations were seemingly at steady-state at the beginning of the 21<sup>st</sup> century before continuing to rise in 2006. The recent increase has been attributed to biogenic emission increases, identified by isotopic measurements of methane. The concept of the atmospheric lifetime was introduced and it was explained how methane's lifetime is estimated from methyl chloroform measurements.

Methane emissions and their isotopic signatures were discussed highlighting the uncertainty in the absolute source fluxes. This was followed by a brief introduction of atmospheric methane chemistry which highlighted how methane is coupled to other atmospheric species, such as CO, ozone and NO<sub>x</sub> via its major sink, the hydroxyl radical. An outline was given of modelling studies looking at methane. Both non-interactive and interactive chemistry schemes were introduced and their differences summarised.

In this thesis experiments with both interactive and non-interactive chemistry schemes are performed. A CCM is driven by a flux boundary condition so that chemical feedbacks on the methane abundance and other species are included. The next section outlines the chapters of this thesis highlighting their scientific aims.

## 1.7 Thesis outline

**Chapter 2** forms the thesis backbone, upon which all following experiments are based. The Base model, a fully interactive stratosphere and troposphere resolving chemistry-climate model, is introduced. This chapter aims to identify the biases of those chemical species of importance for methane chemistry.

In **chapter 3** a newly developed non-interactive chemistry scheme is incorporated into the Base model. The effects of altering the chemical oxidant fields on atmospheric methane are analysed.

**Chapter 4** exploits the linearity of methane chemistry in the non-interactive chemistry scheme. A local optimisation method is used to establish a revised methane emission map.

The methane emission strength and its geographical distribution are altered in the experiments presented in **chapter 5**. The effect on atmospheric methane is explored highlighting the sensitivity of atmospheric methane to small emission changes.

The last result chapter, **chapter 6**, then explores the interactions between a future climate scenario (temperatures and emissions) and atmospheric methane. Influences on other species such as OH, ozone, CO and NO<sub>x</sub> are highlighted.

The thesis concludes with **chapter 7** which brings together all findings and outlines possible avenues of future work.

## **2 | Experimental setup and model evaluation**

This chapter introduces the MetOffice's Unified Model (UM) coupled with the United Kingdom Chemistry and Aerosol submodel (UKCA), commonly abbreviated to UM-UKCA. UM-UKCA is a general circulation model, which calculates the meteorology within the dynamical core and is thus not driven by observed meteorological fields. The UM contains representations of large-scale advection, convective transport and boundary layer mixing of both chemical and aerosol tracers. All experiments in this thesis are based on the model setup described in this chapter. It seeks to present the Base model which is further developed and explored in the following chapters.

After a brief model description in section 2.1, section 2.2 details the methane emissions used for the Base model setup and introduces the experiment explored in this chapter. This is followed by a model performance evaluation for key species in methane chemistry, such as ozone, carbon monoxide, nitrogen oxides, the hydroxyl radical and methane itself, in section 2.3. Modelled data are compared to observations, described in Appendix A, and published model experiments to highlight both good agreements and any biases. Finally, section 2.4 summarises the results and identifies questions which are explored in the later chapters.

### **2.1 The UM-UKCA model**

UKCA is coupled to version 7.3 of the HadGEM3-A model in climate-mode [Hewitt et al., 2011]. It was used in the atmosphere-only set-up at N48L60 resolution (3.75° longitude by 2.5° latitude). The 60 hybrid-height levels extend up to 84 km, resolving the stratosphere.

The dynamical core is described by Davies et al. [2005] with the specific configuration explained in Hewitt et al. [2011]. The advection is semi-Lagrangian with a 20 minute dynamical time-step [O'Connor et al., 2014].

Because this version of the model is not coupled to an ocean, it is driven with observed sea surface temperatures (SST) and sea ice extent [Rayner et al., 2003]. The **Base** experiment presented in this chapter simulates the present day, with SST and sea ice extent fields taken for the year 2000.

### 2.1.1 Chemistry scheme

Photolysis, chemical reactions and the emissions and deposition of species are treated within the UKCA chemistry module, coupled to the UM advection scheme for transport. The chemistry module is called every third model time-step (i.e. every hour) via the Newton-Raphson integrator within the ASAD chemical solver [Carver et al., 1997].

The model includes both extensive tropospheric [O'Connor et al., 2014] and stratospheric [Morgenstern et al., 2009] chemistry – referred to as ‘CheST’ [Banerjee et al., 2014, 2016]. A total of 71 tracers (75 species) react in 56 photolysis, 200 bimolecular, 24 termolecular and 5 heterogeneous reactions. Note that ‘tracers’ are chemical molecules that are moved by the dynamical core while ‘species’ are only used within the chemistry scheme. These include the  $O_x$  (O and  $O_3$ ),  $HO_x$  and  $NO_x$  chemical cycles and the oxidation of CO, ethane, propane, and isoprene [Archibald et al., 2011], stratospheric chlorine and bromine chemistry, including heterogeneous processes on polar stratospheric clouds and liquid sulphate aerosols. Details of the methane chemistry included in CheST are given in section 2.1.1.

Both dry and wet deposition are parameterised within UKCA. The dry deposition is parameterised interactively following Wesely [1989], occurring in all boundary layer levels for 36 species. The wet deposition is coupled with the vertical transport in convective clouds and linked to the rainout for 29 species [Giannakopoulos et al., 1999].

Photolysis rates are calculated interactively by the Fast-JX scheme (as implemented by Telford et al. [2013]) and ozone is coupled interactively between chemistry and radiation. Methane, nitrous oxide, chlorofluorocarbons and similar gases (e.g. hydrochlorofluorocarbons) use a prescribed mixing ratio in the radiation code. Aerosols are calculated with the Coupled Large-scale Aerosol Simulator for Studies in Climate (CLASSIC) aerosol scheme [Appendix A in Bellouin et al., 2011b]. Uniform mixing ratios are assumed for  $H_2$  (34.528

ppb) and  $\text{CO}_2$  according to the simulated climate, year 2000 for the Base experiment, and are not influenced by the chemistry scheme.

Ten species (see Table 2.1 for their strengths) are emitted in the lowest model level in addition to multi-level aircraft  $\text{NO}_x$  emissions. These are updated every five days from ancillary files. Lightning  $\text{NO}_x$  emissions are calculated interactively in the model according to Price and Rind [1994]. Both anthropogenic and natural emissions are included. Anthropogenic emissions are taken from the MACCity emission dataset (an extension of the ACCMIP historical emissions dataset) for the year 2000 [Lamarque et al., 2010]. Biogenic emissions are included following Guenther et al. [1995]. Section 2.2 details explicitly how the methane emissions for this thesis's setup are compiled. Nitrous oxide ( $\text{N}_2\text{O}$ ) and halogen-containing species are prescribed using uniform surface concentrations, effectively fixing their tropospheric abundance.

**Table 2.1** Annual emissions for the year 2000 as implemented into the model taken from Fung et al. [1991]; Guenther et al. [1995]; Lamarque et al. [2010]; van der Werf et al. [2010]; EDGAR [EC-JRC/PBL, 2011]; Melton et al. [2013] (see text for more details).

Species		Emissions	
Nitrogen oxides	$\text{NO}_x$	138	$\text{Tg}(\text{NO}_2) \text{ yr}^{-1}$
Methane	$\text{CH}_4$	548	$\text{Tg}(\text{CH}_4) \text{ yr}^{-1}$
Carbon monoxide	$\text{CO}$	1113	$\text{Tg}(\text{CO}) \text{ yr}^{-1}$
Formaldehyde	$\text{CH}_2\text{O}$	9	$\text{Tg}(\text{CH}_2\text{O}) \text{ yr}^{-1}$
Ethane	$\text{C}_2\text{H}_6$	27	$\text{Tg}(\text{C}_2\text{H}_6) \text{ yr}^{-1}$
Propane	$\text{C}_3\text{H}_8$	14	$\text{Tg}(\text{C}_3\text{H}_8) \text{ yr}^{-1}$
Acetone	$(\text{CH}_3)_2\text{CO}$	46	$\text{Tg}((\text{CH}_3)_2\text{CO}) \text{ yr}^{-1}$
Acetaldehyde	$\text{CH}_3\text{CHO}$	9	$\text{Tg}(\text{CH}_3\text{CHO}) \text{ yr}^{-1}$
Isoprene	$\text{C}_5\text{H}_8$	573	$\text{Tg}(\text{C}) \text{ yr}^{-1}$
Methanol	$\text{CH}_3\text{OH}$	121	$\text{Tg}(\text{C}) \text{ yr}^{-1}$

### Interactive methane chemistry

In the atmosphere, methane is oxidised by OH, Cl and  $\text{O}(^1\text{D})$  and undergoes photolysis. Table 2.2 summarises the reaction rates and products as implemented in CheST.

Stratospheric water vapour is not calculated interactively in the chemistry scheme. Instead, stratospheric water vapour production is parameterised, assuming a uniform distribution ( $\text{H}_2\text{O} + 2 \text{CH}_4 = 6.03 \text{ ppm}$ ) [Morgenstern et al., 2009].

**Table 2.2** Methane reactions and reaction rate constants ( $\text{molecules}^{-1} \text{ cm}^3 \text{ s}^{-1}$ ) in CheST. The reaction rate constants are taken from Sander et al. [2011].

Type	Reactants	Products	Reaction rate constants
Methane loss	$\text{CH}_4 + \text{OH}$	$\text{CH}_3\text{O}_2 + \text{H}_2\text{O}$	$2.45 \times 10^{-12} \exp(-1775 \text{ T}^{-1})$
	$\text{CH}_4 + \text{Cl}$	$\text{CH}_2\text{O} + \text{H}_2$	$7.30 \times 10^{-12} \exp(-1280 \text{ T}^{-1})$
	$\text{CH}_4 + \text{O}(^1\text{D})$	$\text{CH}_2\text{O} + \text{H}_2$	$9.00 \times 10^{-12}$
	$\text{CH}_4 + \text{O}(^1\text{D})$	$\text{CH}_2\text{O} + 2 \text{HO}_2$	$3.45 \times 10^{-11}$
	$\text{CH}_4 + \text{O}(^1\text{D})$	$\text{CH}_3\text{O}_2 + \text{OH}$	$1.31 \times 10^{-10}$
	$\text{CH}_4$ photolysis	$\text{CH}_3\text{O}_2 + \text{H}$	calculated interactively
Methane production	$\text{CH}_3\text{CHO}$ photolysis	$\text{CH}_4 + \text{CO}$	calculated interactively

## 2.2 Methane emissions

Methane emissions for the Base experiment are compiled from a range of sources to a sum total of  $548 \text{ Tg}(\text{CH}_4) \text{ yr}^{-1}$ . A detailed breakdown is given in Table 2.3.

Anthropogenic emissions, namely coal, gas, rice, animals, waste and others, are taken from the Emission Database for Global Atmospheric Research (EDGAR [EC-JRC/PBL, 2011]), amounting to  $324 \text{ Tg}(\text{CH}_4) \text{ yr}^{-1}$  or 56% of total methane emissions. The “other anthropogenic emissions” combine methane emissions from transportation and energy production. A seasonal variation is applied to the fossil fuels coal and gas which has been shown to improve comparison to observational data [Gurney et al., 2005].

Seasonally varying biomass burning emissions are taken from the Global Fire Emissions Database (GFED) 3.1 [van der Werf et al., 2010] but scaled to  $35 \text{ Tg}(\text{CH}_4) \text{ yr}^{-1}$  to match recent estimates [Kirschke et al., 2013].

The wetland emissions used for the experiments in this thesis originate from the TransCom- $\text{CH}_4$  project [Patra et al., 2010]. Their geographical distribution and their seasonal cycle is based on the NASA Goddard Institute of Space Studies inventory [Fung et al., 1991] but the individual wetland emissions types (bogs, swamps and tundra) have been scaled as stated in Patra et al. [2010] to a global flux of  $149 \text{ Tg}(\text{CH}_4) \text{ yr}^{-1}$ . Then, the global wetland emission flux has been uniformly increased to the average wetland emission flux estimated in the wetland and wetland  $\text{CH}_4$  inter-comparison of models project (WETCHIMP), giving total wetland emissions of  $190 \text{ Tg}(\text{CH}_4) \text{ yr}^{-1}$  [Melton et al., 2013].

Hydrate ( $6 \text{ Tg}(\text{CH}_4) \text{ yr}^{-1}$ ) and termite ( $20 \text{ Tg}(\text{CH}_4) \text{ yr}^{-1}$ ) emissions are seasonally invariant and distributed according to Fung et al. [1991]. Soil oxidation ( $25 \text{ Tg}(\text{CH}_4) \text{ yr}^{-1}$ ) is included as a negative emission (no seasonal cycle) [Fung et al., 1991].

**Table 2.3** Annual methane emissions in  $\text{Tg}(\text{CH}_4) \text{ yr}^{-1}$  for the year 2000 as implemented into the model, taken from Fung et al. [1991]; Guenther et al. [1995]; Lamarque et al. [2010]; van der Werf et al. [2010]; EDGAR [EC-JRC/PBL, 2011]; Melton et al. [2013] (see text for more details).

Emissions	Source strength ( $\text{Tg}(\text{CH}_4) \text{ yr}^{-1}$ )
Anthropogenic	
Coal	63
Gas	40
Rice	34
Animals	97
Waste	58
Other anthropogenic	30
Biomass burning	35
Biogenic	
Wetlands	190
Termites	20
Hydrates	6
Soil sink	-25
Total	548

The global distribution of annually summed methane emissions can be seen in Figure 2.1. Emissions are large over South America, particularly around  $60^\circ\text{W}$ , Europe ( $10^\circ\text{E} - 60^\circ\text{E}$ ) and East Asia ( $100^\circ\text{E} - 130^\circ\text{E}$ ). Little methane is emitted south of  $30^\circ\text{S}$  with more methane being emitted in the northern extra-tropics than in the tropics. Emissions from South America are mainly due to wetland emissions while anthropogenic emissions are the largest contributors in Europe and East Asia (see chapter 3, section 3.1.3 for more details).

### 2.2.1 Experiments

The present day climate is simulated with prescribed SST and sea ice fields, emissions as outlined above, and concentration boundary conditions for the year 2000. For the remainder of the thesis this experiment will be referenced as the ‘Base’ experiment. The model is spun up to equilibrium (50 model years, tested by fitting an exponential curve to modelled

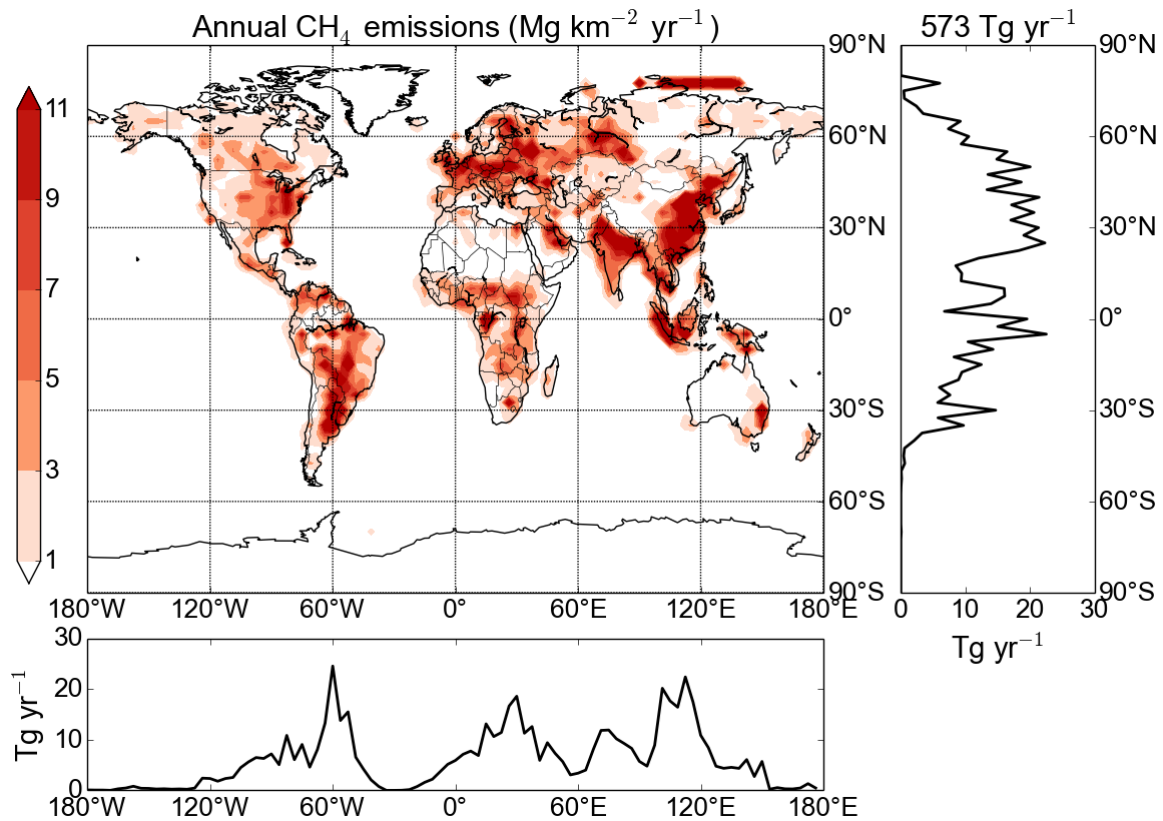


**Fig. 2.1** Global distribution of the annually summed methane emissions ( $\text{Mg}(\text{CH}_4) \text{ km}^{-2} \text{ yr}^{-1}$ ) implemented into the model. The emissions are summed over latitudinal bands of  $2.5^\circ$  and longitudinal bands of  $3.75^\circ$ .

methane) and then run for a further 10 years. The model data presented represents the average of these last 10 model years.

The Base model will be compared with data and published model studies in section 2.3.

The inclusion of methane emissions in the Base setup is the only difference to the model used for the Base experiment described in Banerjee et al. [2014, 2016]. That model applied a methane lower boundary condition (1.75 ppm) effectively fixing tropospheric methane concentrations instead of methane emissions, a common practice for chemistry-climate models (CCMs). That year 2000 experiment will be called ‘Base(lbc)’ hereafter and used for model comparison.

The Base experiment is also compared to the model presented in O’Connor et al. [2014], a HadGEM2-UKCA model at higher horizontal resolution than the model presented here but with a lower vertical resolution and tropospheric chemistry only (referred to as ‘CheT’).

## 2.3 Evaluation of the Base model

This section briefly evaluates key chemical features of the Base experiment, comparing modelled data to observations and published model data. In each section, modelled surface concentrations and the zonally averaged picture will be discussed before evaluating the model results against published data. As this thesis studies tropospheric methane, an understanding of the key chemical species affecting methane is necessary to set the scene and draw valid conclusions from the model used in this analysis.

With 90% of methane being lost through reaction with OH, analysis of those species affecting the tropospheric oxidative capacity is necessary to highlight any model biases. Holmes et al. [2013] showed that the variability in methane lifetime depends strongly on ozone, biomass burning (CO) and lightning NO<sub>x</sub>. Therefore, section 2.3.1 discusses ozone, photolysis of which produces OH, followed by NO<sub>x</sub>, an ozone precursor, and CO, a major OH sink, in section 2.3.2 and section 2.3.3, respectively. Then tropospheric OH is evaluated in detail in section 2.3.4 which finally leads to methane being discussed in section 2.3.5.

### 2.3.1 Base tropospheric ozone

Modelled annual mean surface ozone (Figure 2.2 (a)) is globally inhomogeneous and generally low in the Southern Hemisphere. Enhanced ozone concentration can be noted in the Northern Hemisphere between 30°N and 60°N with hotspots over Saudi Arabia, India, the Mediterranean and the South-West US. December-January-February (DJF) surface ozone concentrations are the lowest globally and June-July-August (JJA) the highest. Surface ozone concentrations in JJA exceed 60 ppb in many areas on the northern landmasses, especially those of a high population density (not shown).

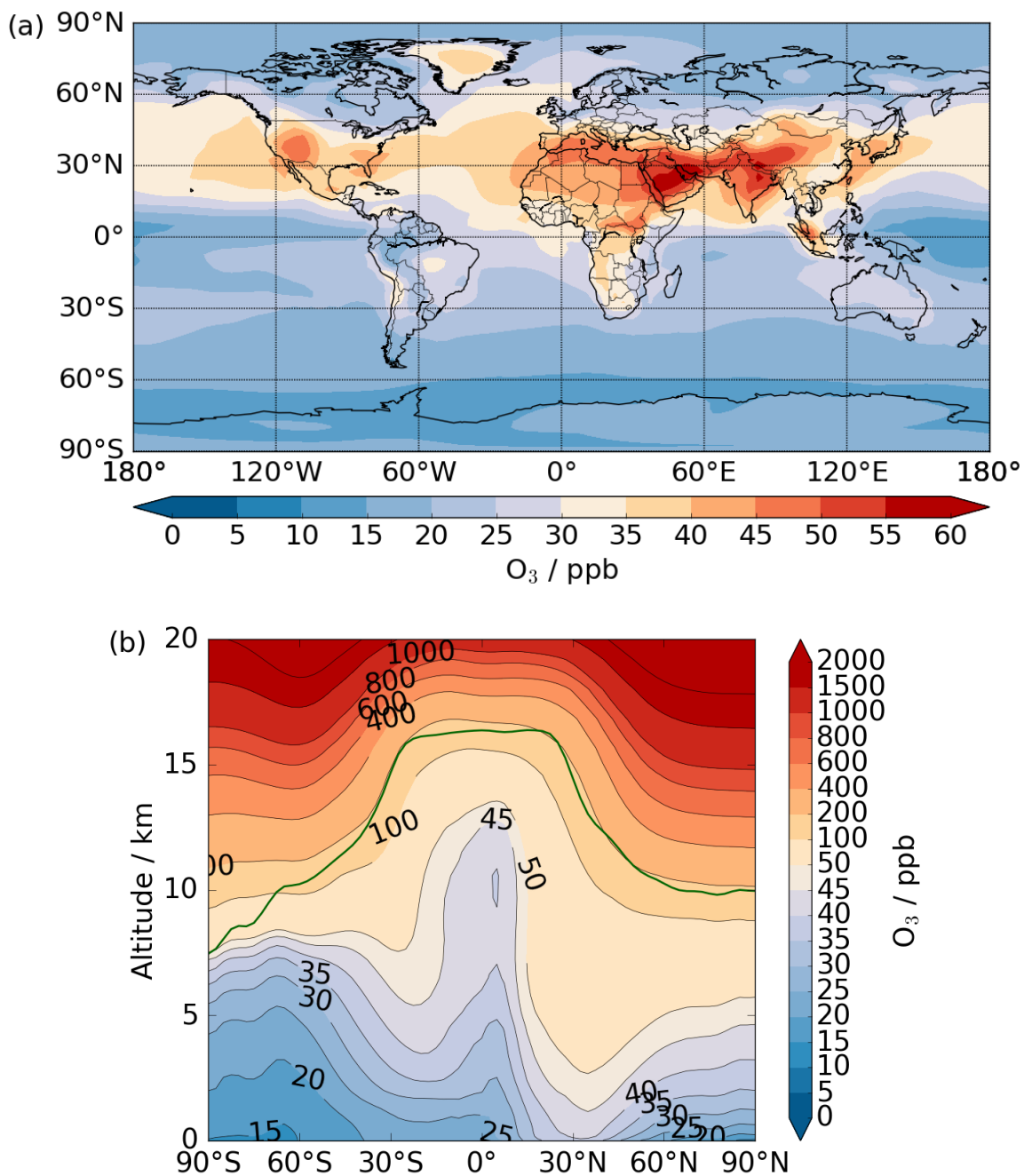


Fig. 2.2 Modelled annual mean Base (a) surface and (b) zonally averaged ozone concentrations (ppb).

Modelled annual mean zonally averaged ozone (Figure 2.2 (b)) shows that ozone is lowest at the surface and increases with altitude. The pattern shows asymmetry around the equator with less ozone in the Southern Hemisphere. A distinct updraft of low ozone concentrations can be seen around the tropics where ozone is as low as 40 ppb at 10 km altitude. At the same time downward transport of higher ozone concentrations from above can be noted at 30°N and 30°S. These patterns reflect the general atmospheric circulation patterns such as the Brewer-Dobson circulation in the stratosphere which moves tropical air upwards and then polewards and down [Brewer, 1949]. Lower surface ozone concentrations and enhanced tropical ozone updraft are apparent during DJF, a pattern reversed in JJA (not shown).

### Comparison to ozone sonde data

Figure 2.3 compares modelled ozone to ozone sonde data (see Appendix A.1, Tilmes et al. [2012]) at four pressure heights, namely surface (900 hPa), lower troposphere (700 hPa), mid troposphere (500 hPa) and upper troposphere (250 hPa).

Ozone is generally low biased in the extra tropics and high biased in the tropics with larger biases at the surface than in the middle and upper troposphere. The interquartile range of the normalised mean bias errors (NMBE, difference between model and observation mean normalised by observations) is smaller than  $\pm 10\%$  for the northern mid-latitudes while the NMBE is slightly more negative at high northern latitudes (particularly at the surface). Southern Hemispheric ozone, particularly at the South Pole with a NMBE around 40%, is low biased throughout the troposphere. Tropical ozone is biased high throughout the troposphere, with a large NMBE range throughout the year spanning across zero indicating that the modelled seasonal cycle does not match well with observations. Ozone high biases in the tropics may lead to increased OH production in this region which will be explored in more detail in section 2.3.4.

Modelled ozone compares less well to the ozone sondes than the ACCMIP models discussed in Young et al. [2013] with greater biases for the model presented here at nearly all locations and altitudes. In the tropics Base NMBE is not only greater but also positive while the ACCMIP models are low biased relative to observations. A reverse pattern can be noted in the Northern Hemisphere. OH differences between the model presented here and the ACCMIP models may well result from these ozone differences (section 2.3.4).

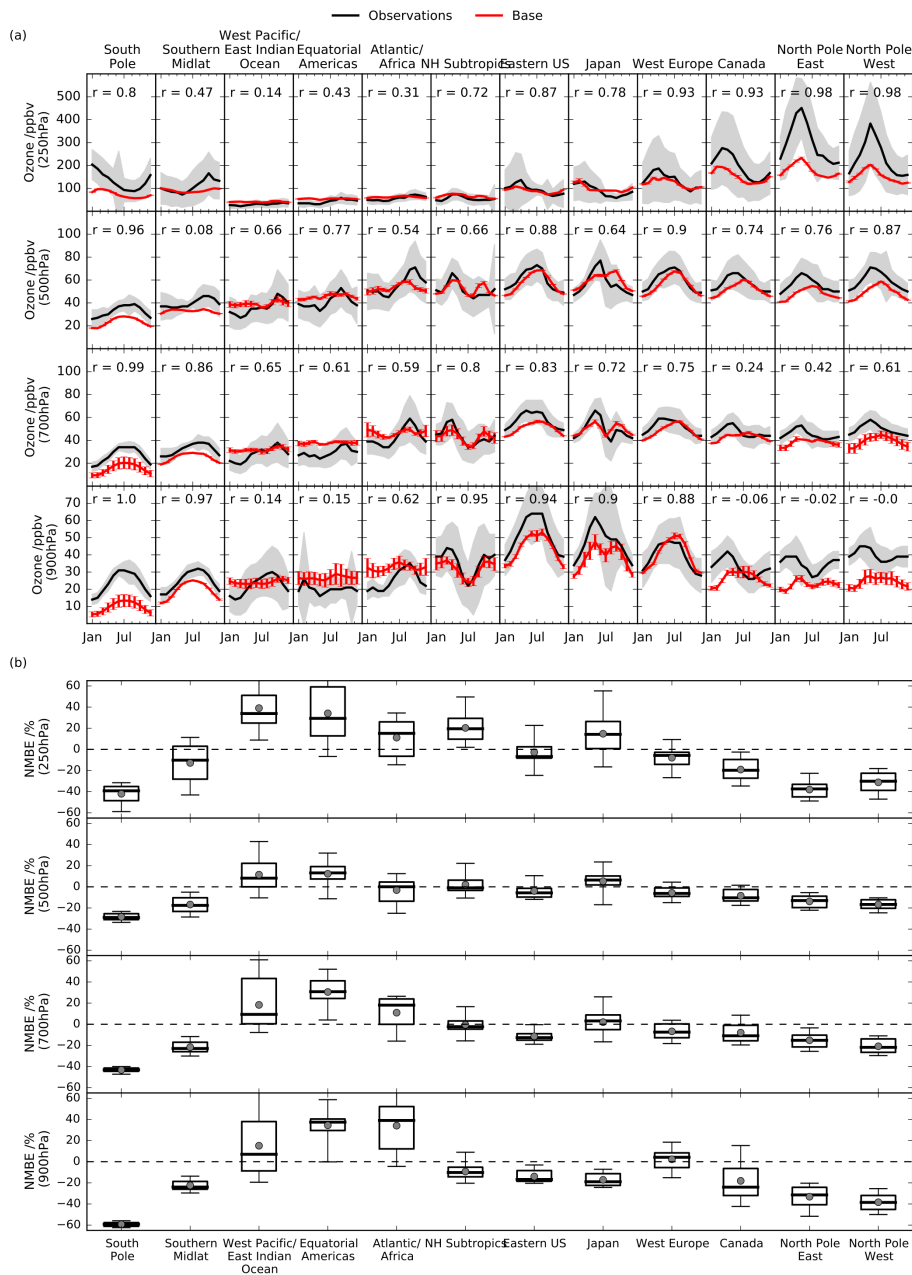


**Fig. 2.3** Comparison of modelled ozone with ozone sonde data (ppb) compiled by Tilmes et al. [2012] over twelve regions at four altitudes. (a) Modelled ozone concentrations in red, observational data in black; error bars and shading represent the  $1\sigma$  interval and indicate spatial variability over each region. The inset in each plot states the Pearson correlation coefficient,  $r$ , between modelled data and observations. (b) Normalised mean bias error for each region at each altitude.

Comparing Base to Base(lbc), the inclusion of methane emissions ( $548 \text{ Tg}(\text{CH}_4) \text{ yr}^{-1}$ ) instead of a methane lower boundary condition (1.75 ppm) results in lower tropospheric ozone by about 5%, apart from the tropical middle to upper troposphere where a 5% increase in ozone can be noted (not shown). This is likely linked to the lower methane burden and thus lower ozone production in the Base experiment presented here.

### **Comparison to ozone surface observations**

Comparison of modelled surface ozone to Northern Hemispheric surface observations (Figure 2.4, see Appendix A.2 for observation details) confirms that modelled ozone is slightly low biased relative to observations but that the seasonal behaviour is, by and large, well captured. Winter ozone is underestimated in some regions which may point to increased  $\text{NO}_x$  titration, the removal of ozone through NO in regions with high  $\text{NO}_x$  concentrations.

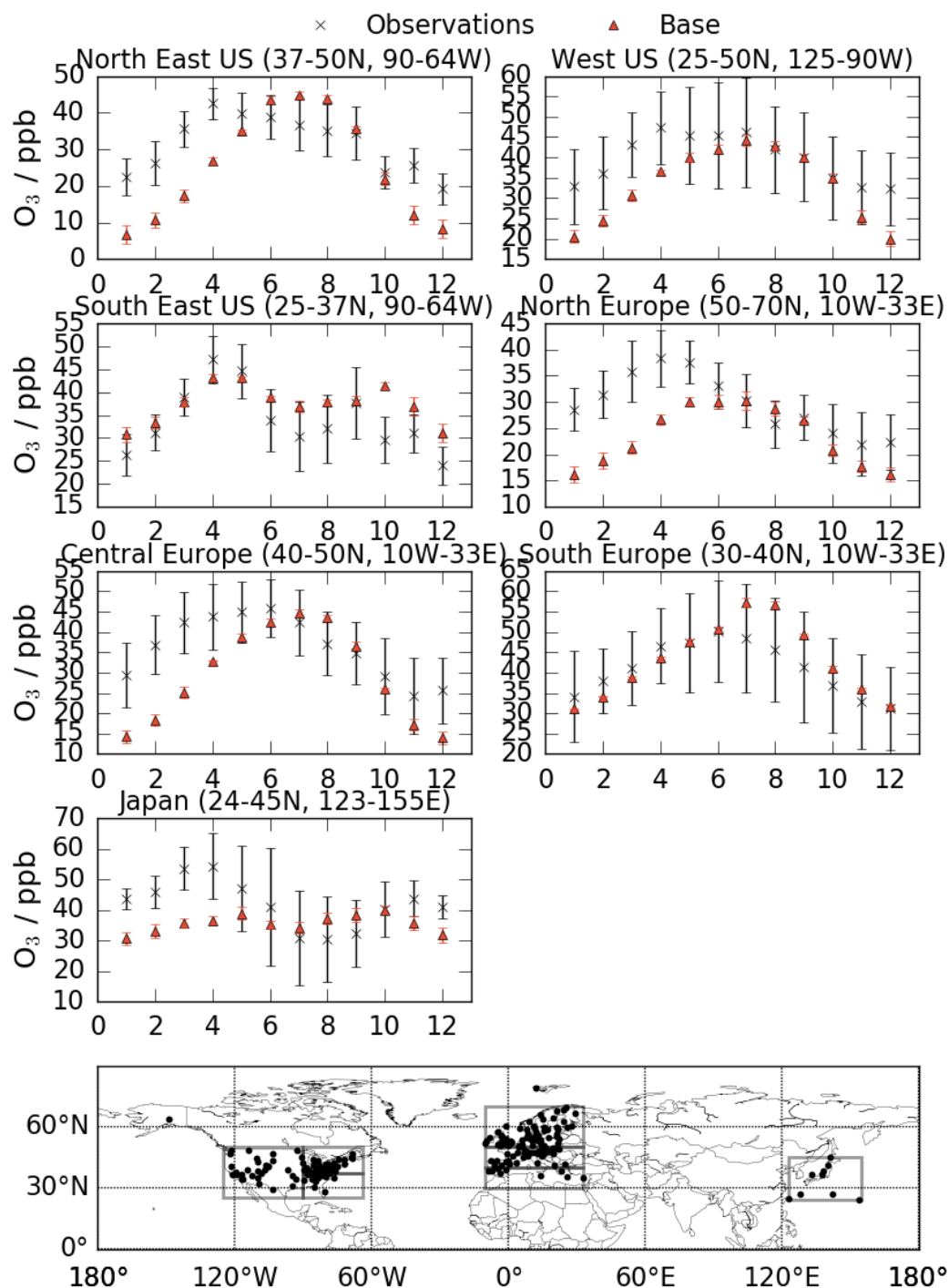


**Fig. 2.4** Comparison of modelled surface ozone with surface observations (ppb) in seven regions across the Northern Hemisphere. Observational data is shown in black (cross), Base ozone is averaged across each region (red, triangle up). Error bars represent the  $1\sigma$  interval and indicate the spatial variability across the regions. Note the different scales for the individual plots. The bottom panel shows the measurement locations and the regions over which the data and observations are averaged.

This section has shown that the general distribution of ozone in the model is reasonable when compared to observations and other models. High biases in tropical ozone have been noted which will affect OH concentrations as ozone is the main precursor for this tropospheric oxidant. Low biases in Northern Hemispheric surface ozone may be linked to high NO<sub>x</sub> titration in these polluted regions. Studies have repeatedly stressed that the drivers of tropospheric ozone and intermodel differences are not yet fully understood [Young et al., 2013; Wild, 2007]. Improving the Base ozone may improve tropospheric OH and methane concentrations but their strong coupling through tropospheric chemistry makes it unlikely that ‘fixing’ modelled ozone automatically leads to good methane representation. Modelled NO<sub>x</sub> is discussed in the next section as it is an important ozone precursor (photolysis of NO<sub>2</sub> in the presence of O<sub>2</sub>) and as such influences tropospheric OH.

### 2.3.2 Base tropospheric NO<sub>x</sub>

Modelled annual mean surface NO<sub>x</sub> (Figure 2.5 (a)) is globally inhomogeneous and strongly influenced by local emissions due to its short lifetime of NO<sub>x</sub> (one day in the lower troposphere, Ehhalt et al. [2001]). NO<sub>x</sub> is generally lower over the oceans (10 – 50 ppt) than over land, though shipping routes cause local elevation in NO<sub>x</sub> concentrations over some oceans. NO<sub>x</sub> levels are highest over heavily industrialised regions such as North America, Europe/Russia and China, where NO<sub>x</sub> concentrations exceed 2 ppb in the annual mean. Northern Hemispheric surface NO<sub>x</sub> is higher in DJF than in JJA while the regional pattern remains the same. NO<sub>x</sub> levels in the tropics and the Southern Hemisphere show less seasonal variation, apart from Africa.

Modelled annual mean zonally averaged NO<sub>x</sub> (Figure 2.5 (b)) is low in the troposphere (10 – 40 ppt) and its distribution is asymmetrical around the equator. NO<sub>x</sub> levels are higher in the Northern Hemisphere, especially at the surface with sharp decreases into the free troposphere. As most NO<sub>x</sub> emissions sources are located between 30°N and 60°N, this region has the highest surface NO<sub>x</sub> concentrations. NO<sub>x</sub> concentrations increase in the tropical upper troposphere and into the stratosphere.

The geographical pattern of modelled zonally averaged NO<sub>x</sub> compares well to Base(lbc). Tropospheric NO<sub>x</sub> concentrations are lower (5% average) in Base in most parts of the troposphere. Only in the (southern) upper tropical troposphere do Base NO<sub>x</sub> exceed those of Base(lbc) by ca. 30%. This pattern is consistent with the ozone differences between the two models.

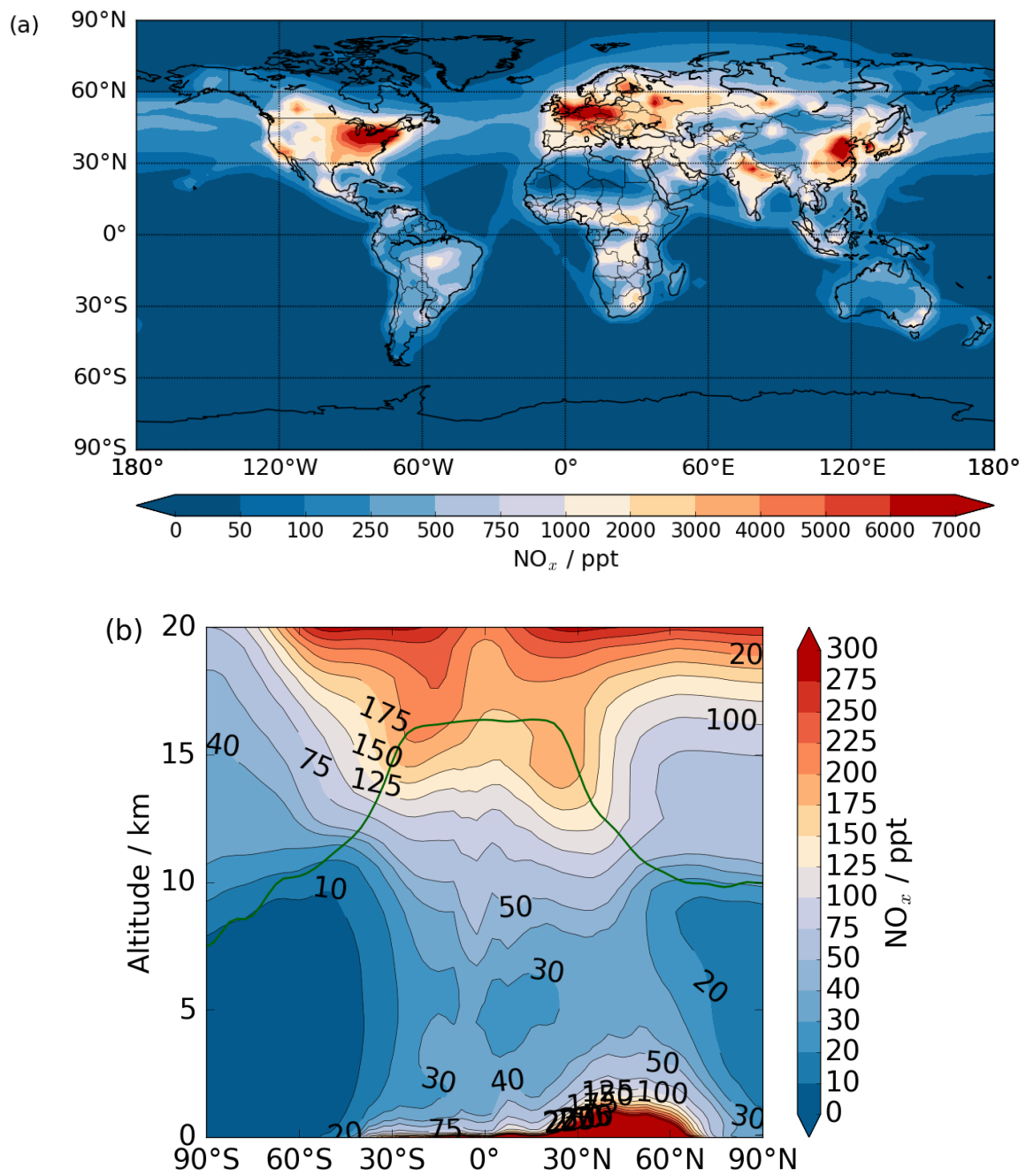


**Fig. 2.5** Modelled annual mean Base (a) surface and (b) zonally averaged NO<sub>x</sub> concentrations (ppt).

### Comparison to aircraft observations

Modelled free tropospheric  $\text{NO}_x$  levels are in general agreement with aircraft observations (see Appendix A.4, Emmons et al. [2000]); all vertical profile plots can be found in Appendix B (Figure B.1). Both the modelled and observational vertical profiles are “C-shaped”, but this is often more pronounced in the model. Repeatedly, modelled surface  $\text{NO}_x$  levels are high biased relative to observations by hundreds of ppt. This may indicate that  $\text{NO}_x$  has too long a lifetime in CheST or that the boundary layer mixing is not sufficient to disperse and remove emissions. The high surface  $\text{NO}_x$  levels can explain the surface ozone low bias in polluted regions, as seen above, through enhanced ozone titration.

Hence, modelled  $\text{NO}_x$  levels agree well with other model studies and the vertical distribution of  $\text{NO}_x$  is in broad agreement with aircraft measurements. This is important as  $\text{NO}_x$  is an ozone precursor and as such influences tropospheric OH levels.

### 2.3.3 Base tropospheric CO

Figure 2.6 (a) shows a large North-South gradient in modelled annual mean surface CO with generally lower concentrations over the oceans in the Southern Hemisphere. Northern Hemispheric CO concentrations are larger, especially over the landmasses which can be linked to anthropogenic emission hotspots (China, India, Indonesia, North-East of North America and Europe) and extensive biomass burning emissions (Africa and South America). The pattern of annual mean surface CO compares well to the CheT model presented in O’Connor et al. [2014]. This increases confidence in the spatial variability of Northern Hemispheric CO concentrations which is found in multiple modelling studies [O’Connor et al., 2014].

A hemispheric gradient can be noted in the annual mean zonally averaged CO concentrations (Figure 2.6 (b)) with higher CO levels in the Northern Hemisphere. The vertical distribution in the Southern Hemisphere is more uniform. CO concentrations maximise and minimise in DJF and JJA, respectively with larger seasonal variations in CO in the Northern Hemisphere close to the surface (not shown). The seasonality in CO can be explained both through the seasonally varying CO emissions in tropical regions (biomass burning) and the variation in the tropospheric OH sink. Additionally, CO is produced in the atmospheric loss process of methane, another influencing factor for seasonal changes. CO concentrations fall

sharply into the stratosphere, reaching concentrations below 20 ppb above 10 km and 17 km in the extra tropics and the tropics, respectively.

Studies [e.g. Naik et al., 2013; Strode et al., 2015] have found that modelled CO is often low biased relative to observations which has implications for the tropospheric OH distribution. Low CO concentrations may lead to higher OH abundance which further reduces CO concentrations. This may especially be of importance when evaluating the North-South gradient of the modelled OH field (section 2.3.4).

### **Comparison to aircraft observations**

In order to analyse the vertical distribution, modelled CO is compared to aircraft observations (see Appendix A.4, Emmons et al. [2000]). The vertical profile plots can be found in Appendix B (Figure B.2). These observations covered the 1980s and 1990s while the Base experiment models the year 2000. Higher CO emissions in the 2000s [Lamarque et al., 2010] are expected to lead to high biases in modelled CO. Surprisingly, modelled CO is low biased throughout the troposphere relative to these aircraft observations in large parts of the Northern Hemisphere, regions especially affected by emissions changes. Tropical regions show good agreement both in absolute concentrations and in the vertical distribution shape. These results suggest that Northern Hemispheric CO emissions are too low and/or chemical CO loss in the model is too high. Note that the Northern Hemispheric ozone low bias seen above does not support an overly strong OH sink in this region as ozone is an OH precursor.

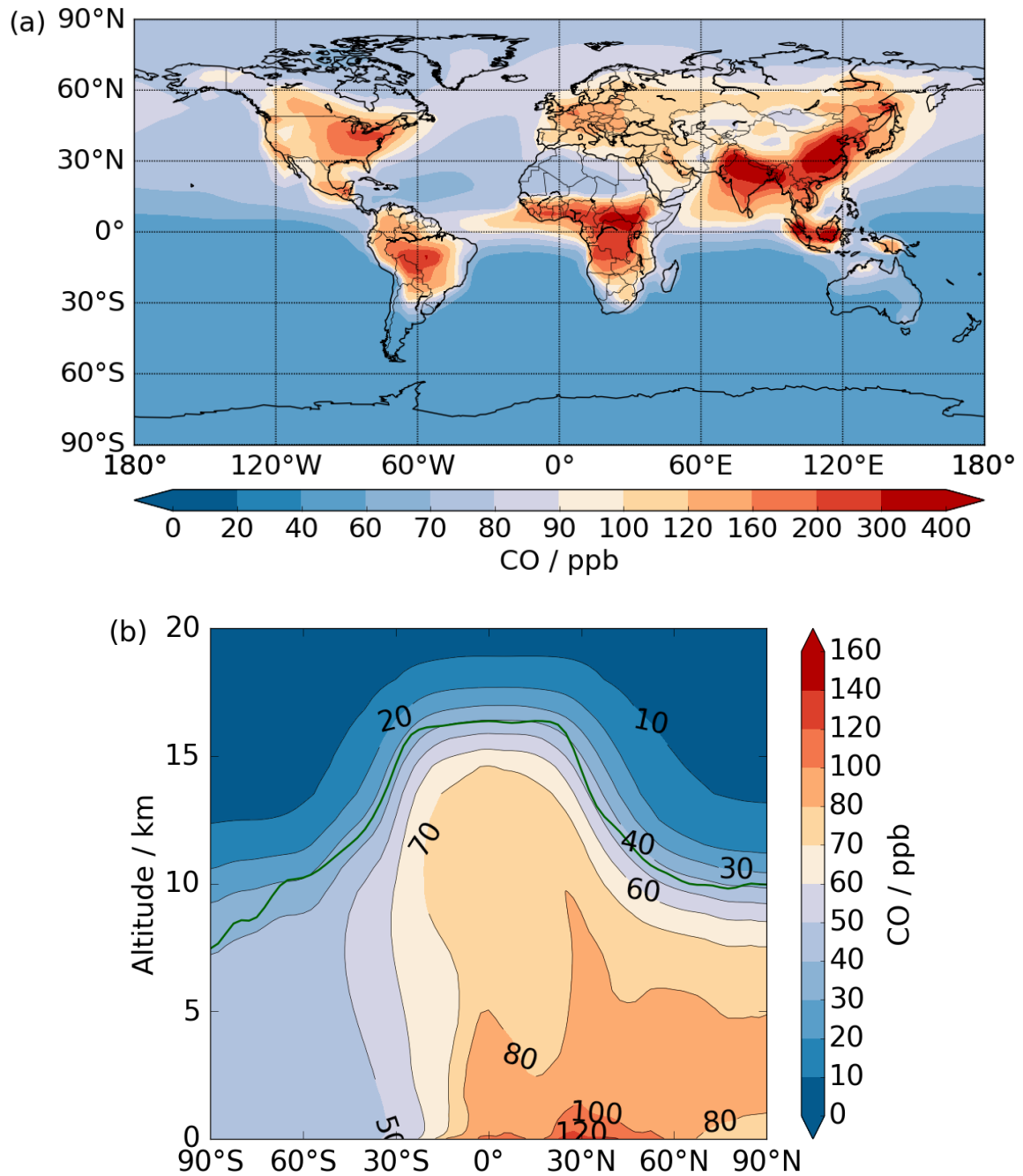


**Fig. 2.6** Modelled annual mean Base (a) surface and (b) zonally averaged CO concentrations (ppb).

### Comparison to surface observations

As CO influences OH and thus indirectly methane and methane lifetime, modelled CO is evaluated against surface flask measurements from the National Oceanic and Atmospheric Administration (NOAA), averaged between January 2000 and December 2005, (see Appendix A.3, Dlugokencky et al. [2016]). This comparison suggests that CO is globally low biased by 20 ppb on average. The modelled seasonal cycle matches the observed cycle better than the absolute concentration which can be seen in the correlation between modelled and observed CO. However, at most stations, the modelled seasonal amplitude is considerably smaller than that of observed CO. Figure 2.7 shows that the model's latitudinal CO gradient is too shallow, with increasing low bias with northerly latitude.

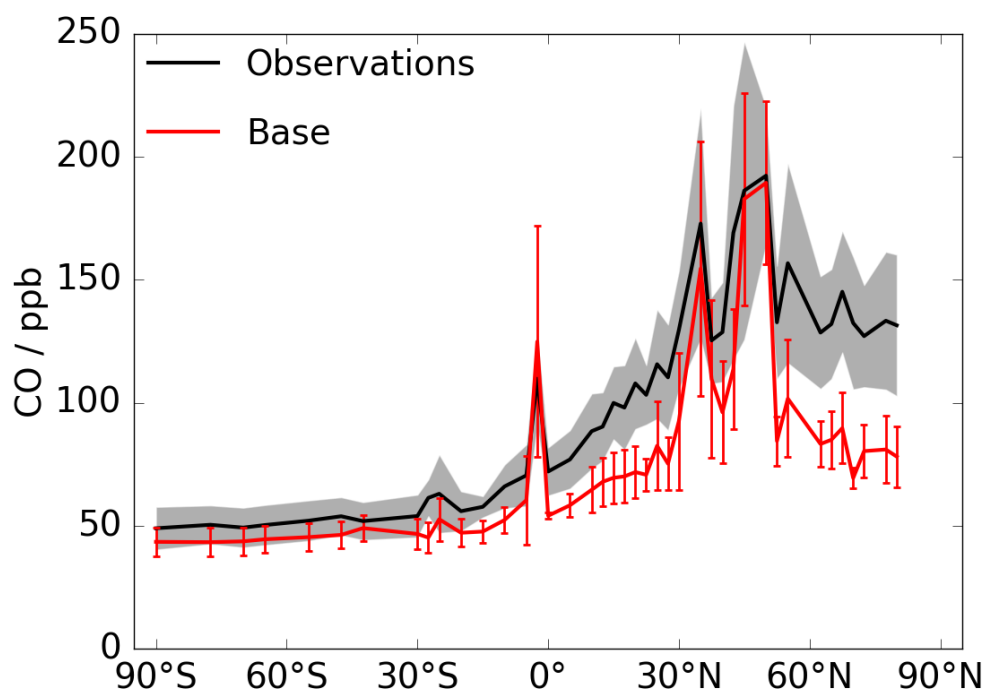


**Fig. 2.7** Latitudinal Base CO gradient (red) compared to observations [Dlugokencky et al., 2016] (black) in ppb. The observations are averaged between January 2000 and December 2005. Error bars and shading represent the  $1\sigma$  interval and indicate temporal and spatial variability at each latitude.

Figure 2.8 gives an example of the seasonal cycle comparing modelled CO concentrations with NOAA surface flask measurements [Dlugokencky et al., 2016]. In general, Southern Hemispheric CO stations correlate well with observations with only small low biases. Correlation decreases and the low bias increases into the Northern Hemisphere where the model

agrees better with observations over North America than over Asia. Over Europe and in the high northern latitudes the low bias relative to observations is even greater. As the low bias of the model is more pronounced in winter than in summer the bias may likely be caused by unrepresented seasonal changes in anthropogenic CO emissions.

The normalised Taylor diagram (Figure 2.9, Taylor [2001]) summarises the statistical match between modelled CO and all available NOAA surface flask measurements. The standard deviation is shown by the radial distance from the origin. The standard deviation from the observations at any station are normalised to 1 (depicted by the star on the x-axis). The radial distance from the reference point (normalised observed standard deviation on the x-axis) shows the root mean square error between the model and the observations. The correlation between the model and observations is shown in the azimuthal position. Southern Hemispheric stations correlate, in general, better with observations than Northern Hemispheric stations. Southern Hemispheric CO is more influenced by the sink due to the long distance from emissions. As no seasonal change in anthropogenic CO emissions is implemented in the model, this may explain the poorer correlation between model and observations in the Northern Hemisphere. It can furthermore be noted that the majority of the more northerly stations exhibit a larger normalised root mean square error (RMSE, centralised difference to the reference point on the x-axis). Additionally, stations in the Arctic circle (Barrow, Summit, Alert, and Ny-Alesund) have very similar statistical patterns suggesting that the biases towards observations are not due to local effects but represent a wider phenomenon.

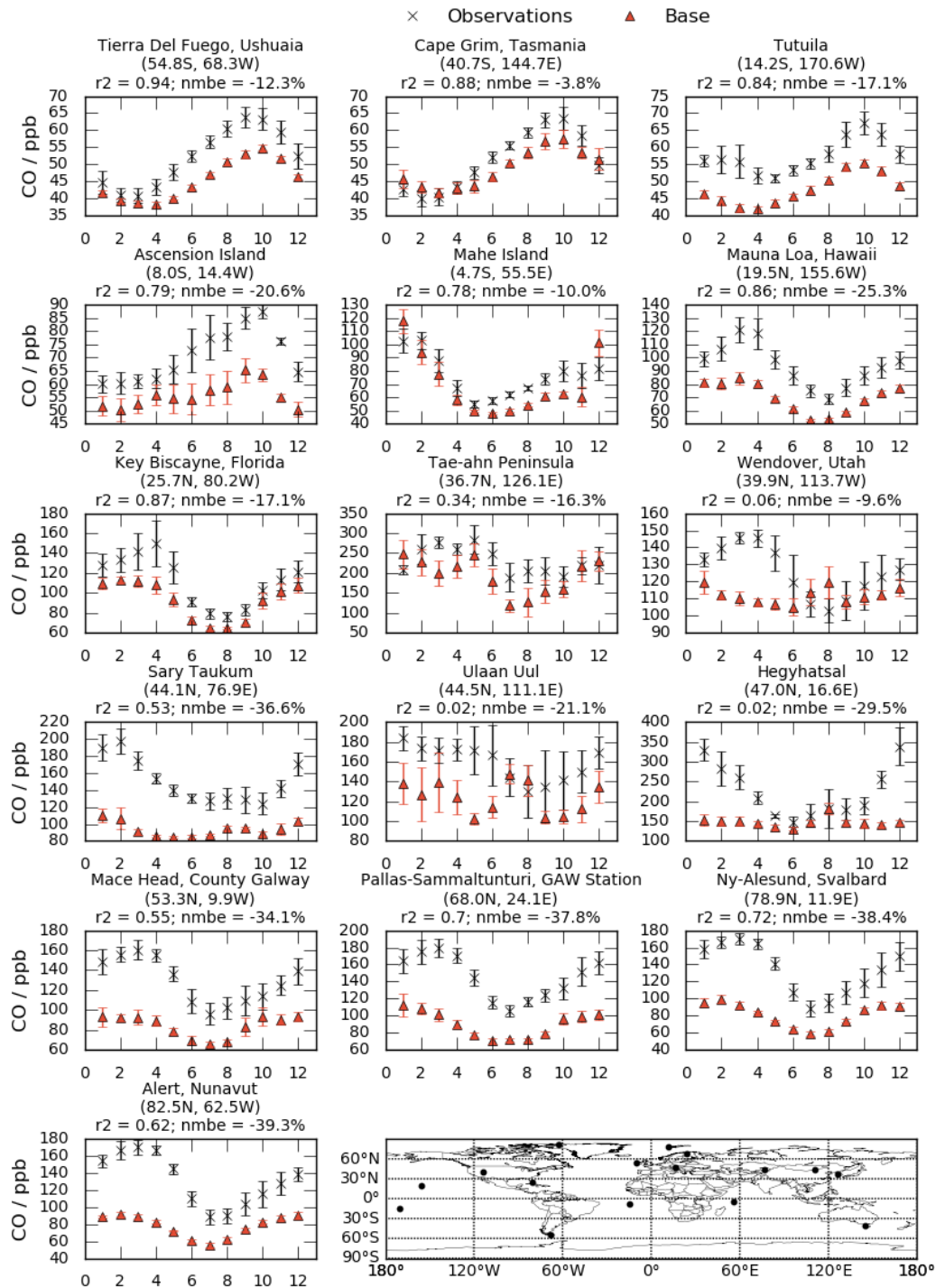
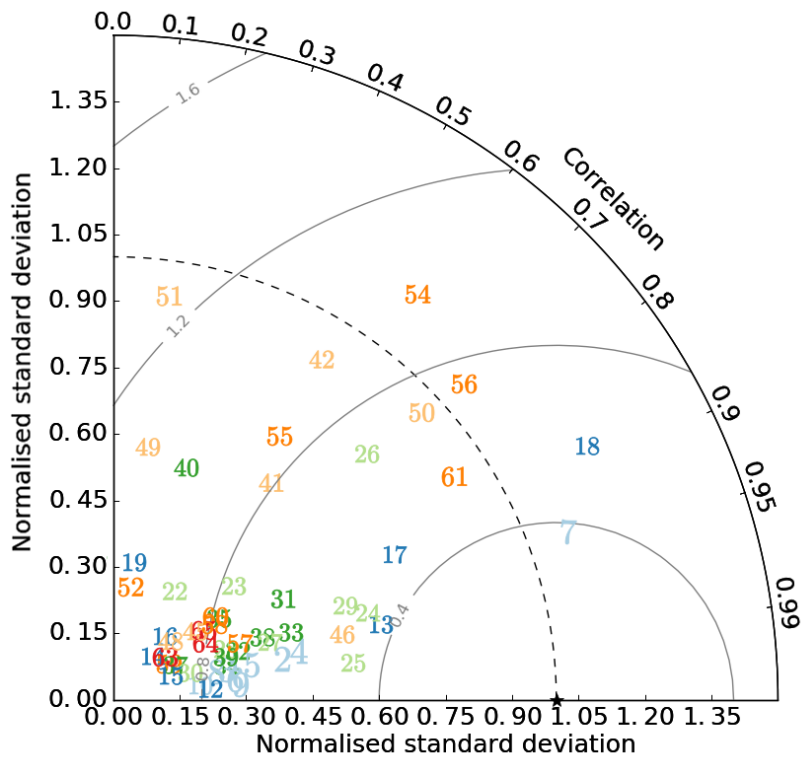


**Fig. 2.8** Comparison of Base surface CO levels with surface measurements (ppb) [Dlugokencky et al., 2016]. The observations are averaged between January 2000 and December 2005. Error bars represent the  $1\sigma$  interval and indicate temporal variability at each station. The map shows the measurement site locations used in this comparison.



★	–	17	asc	34	mid	50	kzd
1	spo	18	sey	35	izo	51	uum
2	hba	19	pocs05	36	wis	52	hun
3	syo	20	mkn	37	pocn30	53	lef
4	psa	21	bkt	38	bmw	54	oxk
5	tdf	22	chr	39	bme	55	shm
6	crz	23	pocn05	40	wlg	56	mhd
7	cgo	24	pocn10	41	tap	57	bal
8	bhd	25	gmi	42	sgp	58	cba
9	pocs30	26	rpb	43	pta	59	ice
10	eic	27	pocn15	44	uta	60	stm
11	nmb	28	kum	45	azr	61	pal
12	pocs25	29	mlo	46	thd	62	brw
13	pocs20	30	pocn20	47	nwr	63	sum
14	pocs15	31	ask	48	bsc	64	zep
15	smo	32	pocn25	49	kzm	65	alt
16	pocs10	33	key				

**Fig. 2.9** Normalised Taylor diagram comparing Base surface CO concentrations to NOAA surface flask measurements averaged between January 2000 and December 2005 [Dlugokencky et al., 2016]. The station identifiers are given in the legend, ordered from south to north (see Table A.3 in the Appendix for full station information). The larger numbers are further north.

In summary, modelled CO concentrations are higher in the Northern than in the Southern Hemisphere due to the mainly Northern Hemispheric CO emissions. However, comparison with aircraft and surface observations indicates that modelled CO is low biased relative to observations. Furthermore, the modelled hemispheric gradient appears too weak as the model low bias increases with increasing northerly latitude. This points to an overly strong tropospheric sink for CO and/or too little CO emissions. The low methane burden for this experiment (section 2.3.5) leads to less CO production, further contributing to the model's low bias.

### 2.3.4 Base tropospheric hydroxyl radical

This section analyses the tropospheric OH concentrations and compares the Base experiment to published studies, drawing both on information from other chemistry-climate simulations and OH distributions inferred from methyl chloroform measurements. The previous sections have highlighted the following results from the Base integration for key species affecting OH:

- Tropical ozone is high biased. As the tropics are a region of high solar flux this may result in increased (tropical) OH production.
- Extra-tropical ozone is low biased at the surface, potentially due to high surface NO<sub>x</sub> levels leading to ozone titration. OH production at the surface in the mid-latitudes may thus be underestimated.
- Extra-tropical free tropospheric ozone and NO<sub>x</sub> agree well with observations. OH production in these regions is expected to match estimates.
- CO is globally low biased, but more so in the Northern Hemisphere. This low bias is likely linked to either a strong tropospheric sink, i.e. OH, and/or insufficient emissions.

The modelled OH field has an airmass-weighted tropospheric OH mean of  $12.4 \times 10^5$  molecules cm<sup>-3</sup> and lies at the upper end of the ACCMIP multi-model mean ( $11.12 \pm 1.6 \times 10^5$  molecules cm<sup>-3</sup> [Naik et al., 2013]). It is noticeably higher than the OH climatology ( $10.4 \times 10^5$  molecules cm<sup>-3</sup>) suggested by Spivakovsky et al. [2000] which is based on ozone, ozone precursor, hydrocarbon and cloud coverage observations. Analysis of MCF measurements lead to the airmass-weighted global tropospheric OH estimate of  $9.4 \pm 1.3 \times 10^5$  molecules cm<sup>-3</sup> [Prinn et al., 2001].

In addition to the high bias of the global mean, the modelled OH field has a large North-South gradient (with the North:South ratio being 1.31). This gradient lies at the upper end of the ACCMIP multi-model mean and is not supported by estimates based on MCF observations which suggest a ratio around unity, however with large uncertainties [e.g. Montzka et al., 2000; Lawrence et al., 2001; Prinn and Huang, 2001; Patra et al., 2014]. This model high bias in global mean OH and the North-South gradient is expected after the analysis presented in the sections above, especially given the low bias in tropospheric CO [e.g. Montzka et al., 2000; Lawrence et al., 2001; Naik et al., 2013; Patra et al., 2014; Strode et al., 2015].

The modelled Base OH field has been analysed in greater detail using the tropospheric subsections suggested by Lawrence et al. [2001]. The values can be found in Table 2.4 (first row). It becomes apparent that the interactively calculated OH, in addition to having higher concentration in the Northern Hemisphere, peaks at lower tropical altitudes than the Spivakovsky OH climatology (last row). Compare, for instance, in the southern tropics (30°S to 0°) the Base decrease from 18.7 (below 750 hPa) to 16.7 x 10<sup>5</sup> molecules cm<sup>-3</sup> (between 500 and 750 hPa) with the increase from 14.4 to 20.0 x 10<sup>5</sup> molecules cm<sup>-3</sup> for Spivakovsky. Furthermore, changing from a methane lower boundary condition (Base(lbc), second row) to the emissions used in this setup results in a general increase in OH throughout the troposphere while the distribution remains reasonably similar. This change in OH concentration can be linked to differences in methane abundance (see section 2.3.5, next). Base OH is quite comparable to the ACCMIP multi-model mean (third row, Naik et al. [2013]) although with somewhat higher concentrations in the lower troposphere and lower concentrations in the upper troposphere.

Figure 2.10 shows the seasonal variation of tropospheric mean OH concentrations for the Base and the OH field specified in the TransCom studies [Patra et al., 2011; Hossaini et al., 2016b], referenced as ‘TransCom OH’. TransCom is an international model intercomparison exercise in which the same, specified oxidant fields was used by all participating models [e.g. Patra et al., 2011]. The modelled global mean Base OH field has a seasonal amplitude of 3.71 x 10<sup>5</sup> molecules cm<sup>-3</sup> (30% of its annual mean), nearly twice as large as the amplitude of the TransCom OH field, with a global mean of 10.4 x 10<sup>5</sup> molecules cm<sup>-3</sup> and a North-South gradient of 1.01 (see chapter 3, section 3.1.2 for more details).

It is apparent that the global (solid lines) Base OH concentrations (red) are greater throughout the year and that they maximise earlier than the TransCom OH (black). Both OH fields have similar magnitude and seasonal cycle in the Southern Hemisphere (dotted lines) while Base OH concentrations are greater and more varied compared to TransCom

**Table 2.4** Lawrence et al. [2001] analysis of annual mean airmass-weighted tropospheric OH concentrations ( $10^5$  molecules  $\text{cm}^{-3}$ ). First row: OH from Base; second row: OH from Base(lbc); third row: ACCMIP multi-model mean for year 2000 [Naik et al., 2013]; fourth row: Spivakovsky OH field as presented in Lawrence et al. [2001].

Altitude	Model	90°S – 30°S	30°S – 0°	0° – 30°N	30°N – 90°N
500 – 250 hPa	Base	5.0	12.0	13.2	8.3
	Base(lbc)	4.4	9.8	11.8	7.8
	ACCMIP	5.17±1.7	12.15±3.1	13.49±3.1	7.58±1.7
	Spivakovsky	6.4	14.3	13.6	6.4
750 – 500 hPa	Base	5.3	16.9	18.8	10.5
	Base(lbc)	4.8	14.8	17.3	9.8
	ACCMIP	5.71±1.5	15.00±2.5	17.09±2.7	9.06±1.7
	Spivakovsky	7.2	20.0	19.9	8.8
Surface – 750 hPa	Base	6.0	18.9	22.4	12.8
	Base(lbc)	5.5	17.2	20.8	12.2
	ACCMIP	5.77±1.3	15.26±2.9	18.51±3.6	10.15±2.0
	Spivakovsky	4.7	14.4	15.2	7.6

OH in the Northern Hemisphere (dashed lines). These differences suggest that the biases are associated with landmass emissions such as CO and  $\text{NO}_x$  and highlight the sensitivity of OH to biases in other chemical species such as CO (see above discussion). The TransCom OH field will be used in subsequent chapters to investigate the sink strength influence on atmospheric methane.

### Comparison to Base(lbc)

The Base(lbc) experiment exhibits an annual mean airmass-weighted tropospheric OH concentration of  $11.2 \times 10^5$  molecules  $\text{cm}^{-3}$  which is  $1.2 \times 10^5$  molecules  $\text{cm}^{-3}$  or 10% smaller than the Base OH presented here. As seen in Table 2.4, Base(lbc) OH is lower everywhere in the troposphere with larger differences in the tropics. Furthermore, this difference can be noted throughout the year with Base(lbc) always being lower than Base. These OH differences will have implications for methane and the methane lifetime.

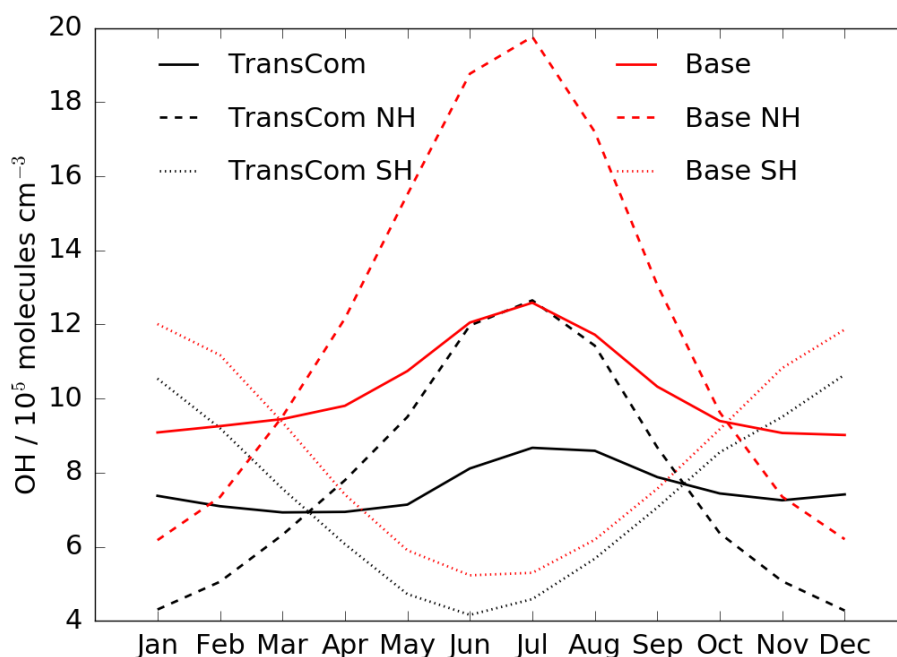


**Fig. 2.10** Seasonal variation in tropospheric Base OH concentrations ( $10^5 \text{ molecules cm}^{-3}$ ) in red and TransCom OH in black. The solid lines represent global, dotted lines Southern Hemispheric (SH) and dashed lines Northern Hemispheric (NH) OH concentrations.

### 2.3.5 Base tropospheric methane

Annual mean Base surface methane (Figure 2.11) is highest over emission areas and lower over the oceans. Southern Hemispheric methane background over the oceans is as low as 1500 – 1550 ppb which gradually increases to 1700 – 1750 ppb in the Arctic. Due to strong circumpolar winds in the Arctic, methane emitted from this region are quickly dispersed around polar latitudes leading to the elevated methane concentrations there. These emissions include hydrates from the East Siberian Shelf, boreal wetlands and Russian Siberian gas fields. Methane concentration hotspots are also located over South America due to wetland emissions; over central Africa, a region of intense biomass burning; North India with large rice paddies and industrialised regions such as the Chinese coast, Europe and Western USA.

Annual mean surface methane is calculated in the model grid boxes of NOAA surface measurement stations (Dlugokencky et al. [2016], see Appendix A.3 for more details). Modelled surface methane averages to 1620 ppb which is low biased by 160 ppb (9%) compared to NOAA surface measurements, averaged between January 2000 and December

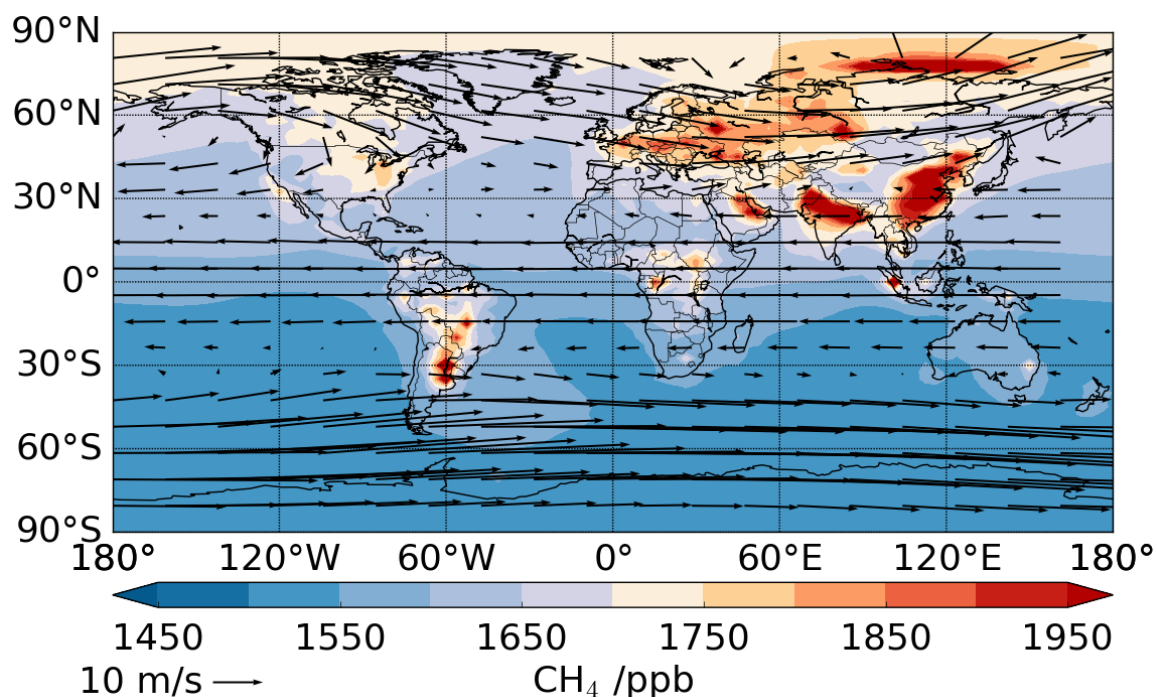
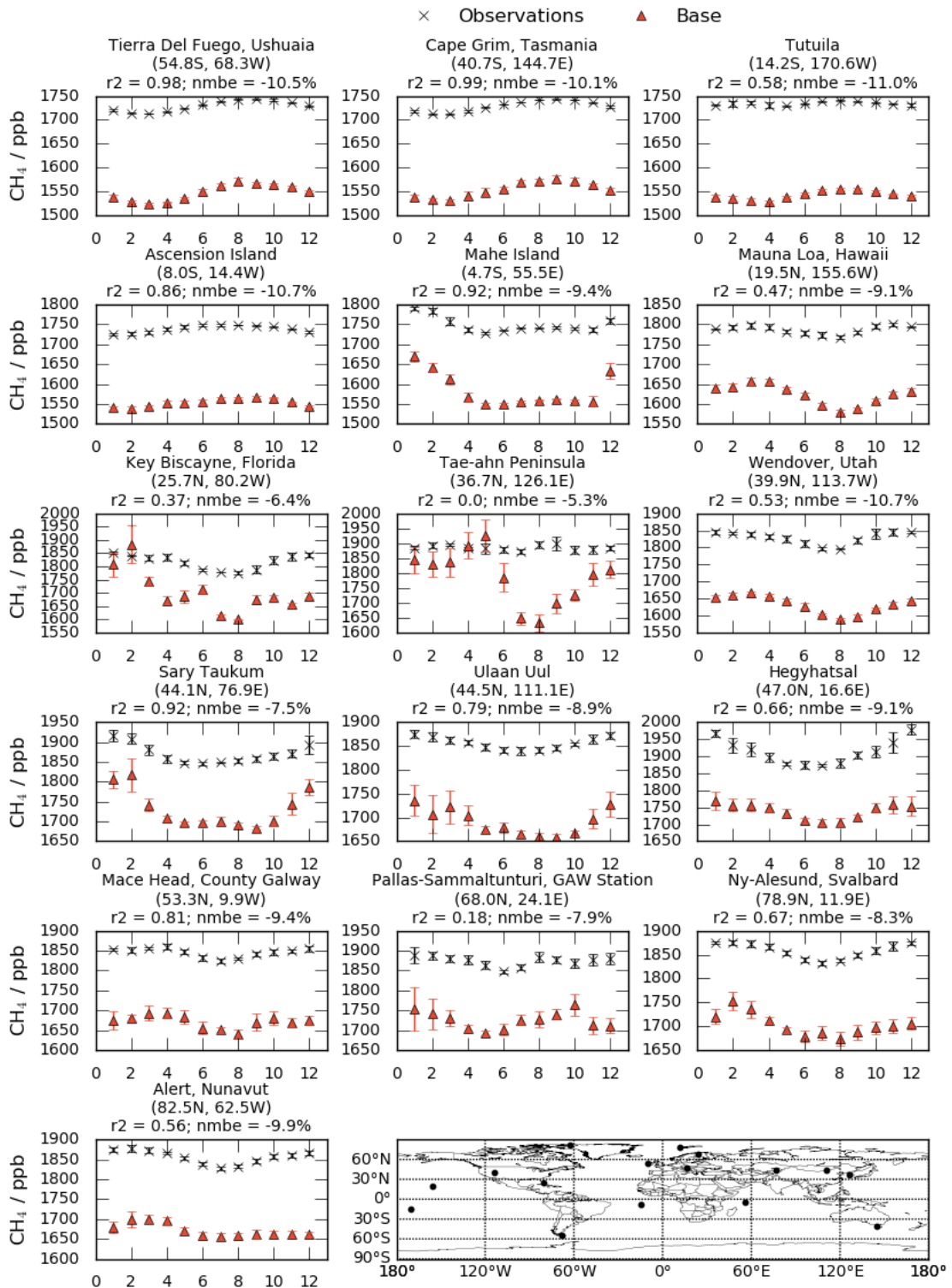


Fig. 2.11 Modelled annual mean Base surface methane concentrations (ppb). Annual mean surface wind direction and strength is overlain by arrows.

2005 (1780 ppb). This suggests that either the tropospheric methane sink (mainly OH) is too strong (see previous section 2.3.4) or the methane emissions are too low. Note that Dalsøren et al. [2016] also reported a methane low bias in their study which they corrected by scaling the modelled global methane field to match observational estimates.

Figure 2.12 gives an example of the seasonal cycle comparing modelled methane concentrations to NOAA surface flask measurements [Dlugokencky et al., 2016]. The model is low biased against observations globally but more so in the Southern than in the Northern Hemisphere. The seasonal cycle is matched well in the Southern Hemisphere (apart from Tutuila), expressed in high  $R^2$  (coefficient of determination) values ( $R^2 > 0.8$ ). Correlation between observations and modelled methane ranges between 0.37 and 0.53 over North America and is higher over Europe ( $R^2 = 0.66 - 0.81$ ) with similar NMBE over both continents. The seasonal pattern at Ulaan Uul and Sary Taukum agrees well with observations in the Northern Hemisphere ( $R^2 = 0.79$  and  $0.92$ , respectively) while the Tae-ahn Peninsula shows no correlation but the overall smallest NMBE of the stations presented here. In summary, the different stations have similar correlations with CO (section 2.3.3) and methane suggesting that chemical loss and transport are the main drivers for the mismatch in seasonal cycle.



**Fig. 2.12** Comparison of Base surface methane levels with surface measurements (ppb) [Dlugokencky et al., 2016]. The observations are between January 2000 and December 2005. Note the different scale for the individual graphs. The map shows the measurement site locations used in this comparison.

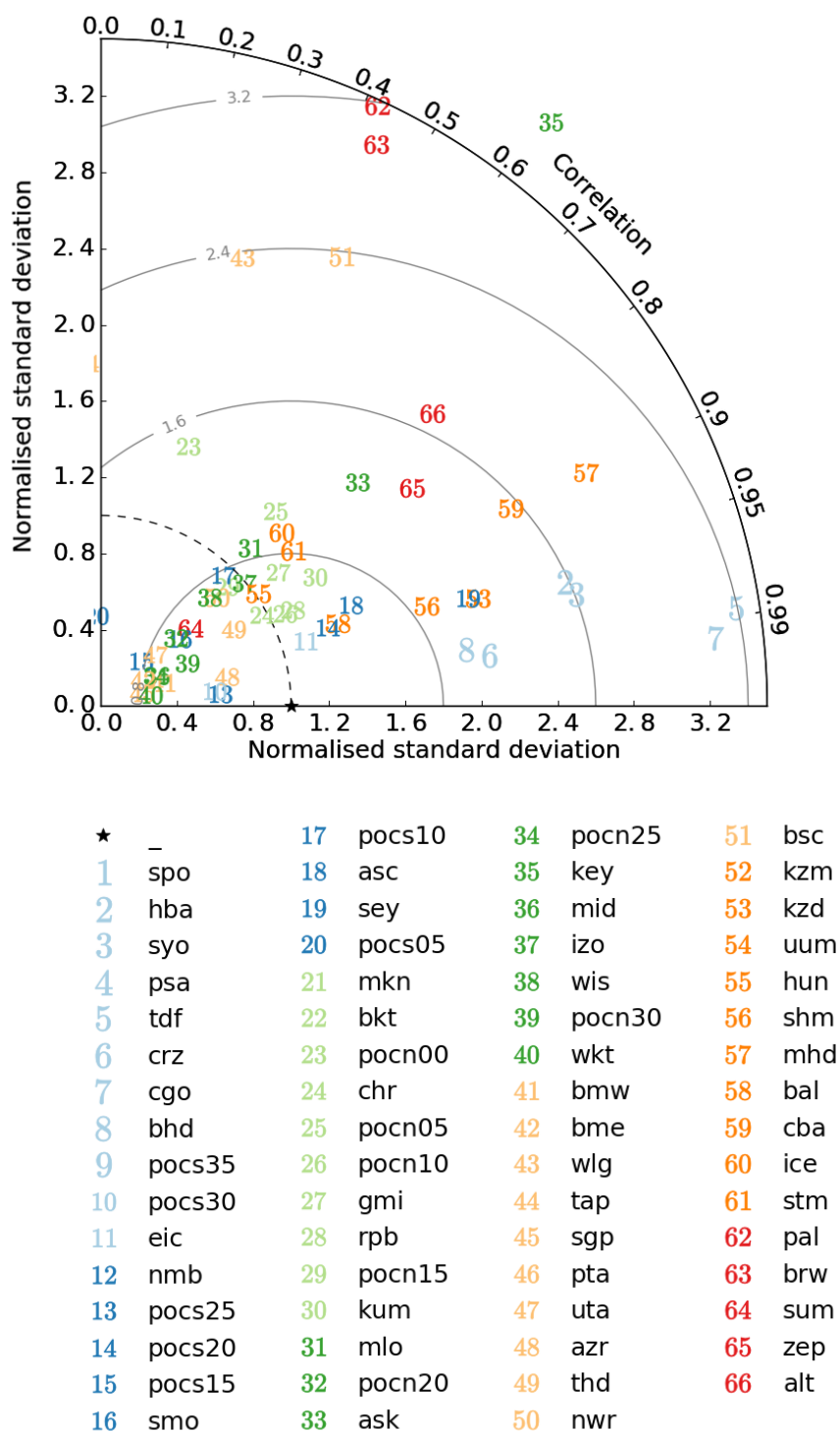


**Fig. 2.13** Normalised Taylor diagram comparing Base methane concentrations to NOAA surface flask measurements [Dlugokencky et al., 2016]. The observations are averaged between January 2000 and December 2005. The station identifiers are given in the legend, ordered from south to north (see Table A.3 for full station information). The larger numbers are further north.

The Taylor diagram (Figure 2.13) indicates that, in contrast to CO (Figure 2.9), no general statement can be made for methane comparison. The normalised standard deviations of the interactive methane concentrations representing variations in methane concentrations at the different stations scatter around the observed values. Furthermore, modelled methane variations at stations in both hemispheres deviate from those observed by a factor of two or more. The normalised RMSE for methane is also larger than for CO, however, most modelled methane lies within a distance of one normalised RMSE. Large statistical differences for stations in the Arctic circle (Barrow, Summit, Alert, and Ny-Alesund) can be noted suggesting that the biases towards observations there are likely due to local effects such as emissions.

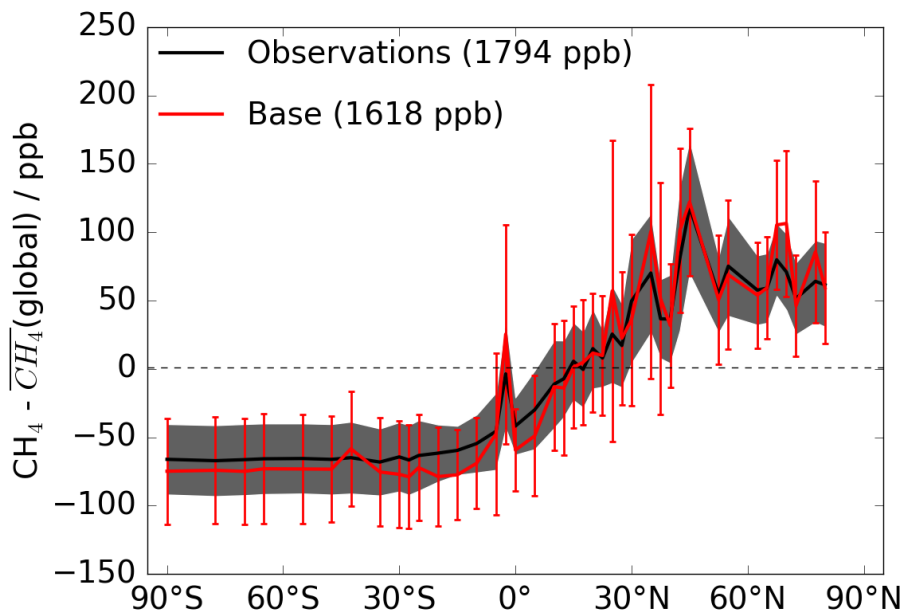


**Fig. 2.14** Latitudinal Base methane gradient (red) compared to observations [Dlugokencky et al., 2016] (black), relative to surface mean (ppb). The observations are averaged between January 2000 and December 2005. Error bars and shading represent the  $1\sigma$  interval and indicate temporal and spatial variability at each latitude.

The latitudinal gradient in modelled methane concentrations shows a hemispheric gradient of 104 ppb (Figure 2.14). This gradient matches observations very well (95 ppb) suggesting a globally uniform change to sources and/or sinks may be required to improve absolute interactive methane concentrations. The latitudinal gradient throughout this thesis is calculated as the difference between averaged Northern and Southern Hemispheric concentrations, sampled in the model grid boxes closest to NOAA surface measurement stations.

Seasonal changes in methane concentrations, denoted in the spread in Figure 2.14, are larger than observed with  $63 \pm 32$  ppb and  $38 \pm 15$  ppb for the model and measurements, respectively. The modelled concentrations also show inter-annual variability twice those observed which may be due to the fact that no clean sector sampling has been applied to the modelled concentrations (a factor influencing model-observation mismatches as noted in Warwick et al. [2002] and Warwick [2003]).

The latitudinal gradient propagates through the troposphere as methane is well mixed, decreasing into the stratosphere. Stratospheric methane is symmetric around the equator and follows the shape of the tropopause, i.e. at a given altitude methane concentrations are lower at the poles than in the tropics.

### **Comparison to Base(lbc)**

The inclusion of emissions changes the methane representation drastically when compared to a globally fixed lower boundary condition (1.75 ppm). It is thus unsurprising that large differences can be noted when Base is compared to Base(lbc): the former exhibits a methane latitudinal gradient while the latter shows globally uniform methane concentrations. Surface methane in the high northern latitudes agrees well between the two models. However, the absence of a latitudinal gradient in Base(lbc) causes the tropospheric concentrations of the two models to diverge with more southerly latitudes. Their differences maximise to 200 ppb at the South Pole. The Base stratospheric methane is more than 300 ppb smaller than Base(lbc), exceeding 100% difference at the Poles at 20 km altitude.

### **Methane lifetime**

Base methane has a lifetime with respect to tropospheric loss via reaction with OH of 8.2 years. It lies at the lower end of the ACCMIP multi-model estimate ( $9.3 \pm 0.9$  years [Voulgarakis et al., 2013]) and does not overlap with observational estimates ( $11.2 \pm 1.3$  years [Prather et al., 2012]), a recurring feature of chemistry-climate models [e.g. Naik et al., 2013]. This suggests that tropospheric methane loss with OH is too large in Base which may point to too strong an OH field (as discussed above).

A linear relationship between the methane lifetime and the annual mean tropospheric OH concentration can be established for all ACCMIP models ( $R^2 = 0.93$ ), see Figure 2.15. Note that most ACCMIP models show methane lifetimes and tropospheric OH concentrations

that do not overlap with observational estimates (denoted in dotted black lines on the figure). Both Base and Base(lbc) lifetimes lie within the 95% confidence interval of the established linear relationship.

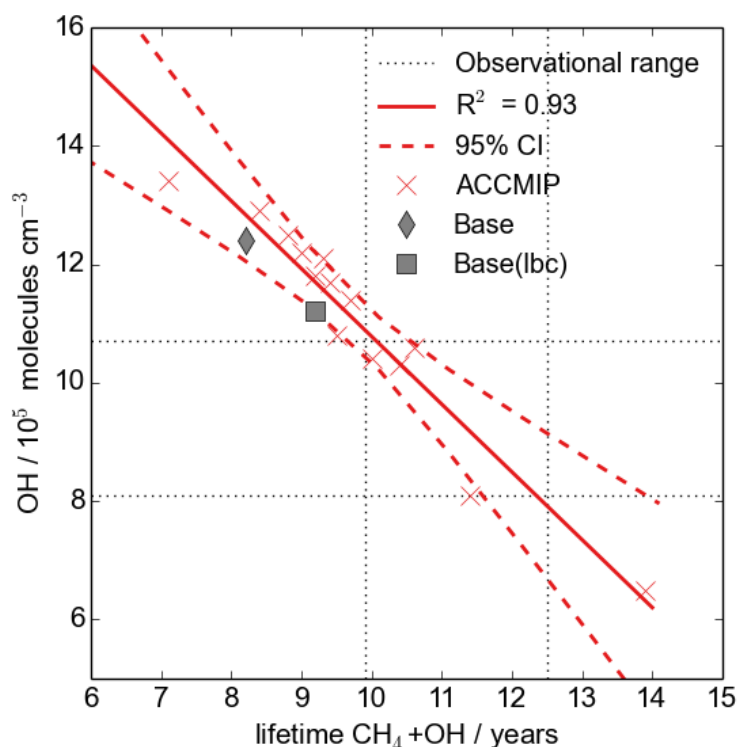


**Fig. 2.15** Relationship between methane lifetime with respect to tropospheric OH loss (years) and tropospheric OH concentrations ( $10^5$  molecules  $\text{cm}^{-3}$ ) for the ACCMIP models [Voulgarakis et al., 2013] (red crosses), Base (grey diamond) and Base(lbc) (grey square). The observational estimates for the methane lifetime [Prather et al., 2012] and the global mean OH concentrations [Prinn et al., 2001] are indicated by the black dotted lines.

The methane lifetime presented here is 1 year or 10% shorter than for the Base(lbc) experiment. The discrepancy can be explained through differences in the respective OH fields (section 2.3.4) and the methane burdens which amount to 4325 Tg(CH<sub>4</sub>) in Base and 4827 Tg(CH<sub>4</sub>) in Base(lbc), a 10% difference. It should be noted that the flux through the reaction of methane and OH is similar for the two experiment, 526 Tg(CH<sub>4</sub>) yr<sup>-1</sup> and 523 Tg(CH<sub>4</sub>) yr<sup>-1</sup> for Base and Base(lbc), respectively, despite their different methane burdens. The relative methane loss reaction is thus smaller in Base(lbc) resulting in a longer methane lifetime in this experiment.

Table 2.5 compares the relative reaction flux of methane and OH in tropospheric subregions as suggested by Lawrence et al. [2001]. Most methane is oxidised in the tropics, especially below 500 hPa. Overall the model presented here compares well with Base(lbc) with small local differences (second row). Compared to the ACCMIP multi-model mean [Voulgarakis et al., 2013] (last row), the two UM-UKCA experiments show a slight shift of methane oxidation to lower tropical altitudes while the extra-tropical fluxes are similar. The ACCMIP multi-model mean suggests a higher proportional flux in the upper troposphere and a less pronounced difference between the lower and middle troposphere compared to the UM-UKCA experiments. This is consistent with OH differences.

**Table 2.5** Lawrence et al. [2001] analysis of methane loss through reaction with OH. Values are given as percentage of global tropospheric methane loss. First row: Base; second row: Base(lbc); third row: ACCMIP multi-model mean for 2000 [Voulgarakis et al., 2013]

Altitude	Model	90°S – 30°S	30°S – 30°N	30°N – 90°N
500	Base	1.2	9.7	2.6
– 250	Base(lbc)	1.2	9.4	2.6
hPa	ACCMIP	1.5	11.4	2.3
750	Base	2.4	23.0	6.6
– 500	Base(lbc)	2.5	22.4	6.5
hPa	ACCMIP	3.2	25.5	5.8
Surface	Base	3.8	40.7	10.0
– 750	Base(lbc)	4.0	41.3	10.0
hPa	ACCMIP	4.5	37.6	8.5

## 2.4 Summary

This chapter has described the model setup for the Base experiment on which the remaining experiments of this thesis are based. The first section included an overview of the key features included in the chemical module UKCA. Then, the key chemical species influencing and influenced by atmospheric methane chemistry were evaluated and compared to measurements and other models.

Base ozone concentrations were high biased in the tropics and low biased elsewhere compared to observations. Modelled  $\text{NO}_x$  agreed reasonably well with observations in the free troposphere with large regional differences. Surface  $\text{NO}_x$  concentrations were high biased likely causing the ozone low bias noted in these regions. Modelled CO concentrations were

low biased throughout the troposphere and the modelled seasonal cycle of CO concentrations is shallower than observed.

These factors led to a high tropospheric OH field which lay at the upper end of ACCMIP estimates in terms of concentrations and the field's North-South gradient. The Base OH field was larger than suggested by estimates based on MCF observations, a reoccurring feature of CCMs. This low bias of 160 ppb was reasonably small (9%) in relative terms and could be linked to this high OH field and/or emission misrepresentation. The methane lifetime with respect to tropospheric OH lay at the lower end of the ACCMIP multi-model estimate and was short relative to the observational based estimate. This was likely linked to the low atmospheric methane abundance and the high OH field. The methane seasonal cycle showed mixed agreement with observations.

Even though model biases have been highlighted in this chapter it is worth noting that the coupled system of methane, OH, ozone and other species is difficult to stabilise and that models show a range of estimates. In the study by Dalsøren et al. [2016], for instance, modelled methane was scaled to match observations before further analysis. Improving the Base model's ozone and CO concentrations will hopefully improve tropospheric OH and methane estimates but is unlikely to lead to excellent representation of methane.

As noted before, the methane low bias may be caused by an overly strong tropospheric sink or insufficient methane emissions. The subsequent chapters will explore these effects in detail. The next chapter will introduce a new model configuration developed as part of this thesis. It uses prescribed oxidant fields which removes chemical feedbacks and renders atmospheric methane chemistry linear. A published tropospheric oxidant field based on observations (the TransCom adaptation [Patra et al., 2011] of the Spivakovsky et al. [2000] OH field) is implemented in this model setup allowing methane differences arising from chemical loss to be analysed (chapter 3). In chapter 4, the linearity of the methane chemistry in the prescribed chemistry scheme is used in order to improve the methane emission distribution. Chapter 5 then analyses the impact of a different methane emission distribution and source strength on global methane and its latitudinal gradient (both the interactive and non-interactive part). In chapter 6 results are presented that study the climate and future emission impact on methane levels.



### 3 | **Non-interactive chemistry within the UM-UKCA model**

The previous chapter introduced the UM-UKCA model with resolved stratospheric and tropospheric chemistry and analysis was presented evaluating this Base model against observations. Low biases in the modelled methane concentrations (9%) relative to observations were highlighted. This underestimation may be caused by underestimated methane emissions and/or overestimated atmospheric methane loss. In the next chapters these two processes will be explored in more detail. In addition to the low biases in modelled methane, the previous chapter has highlighted high biases in interactively modelled OH. These biases were accompanied by biases in CO, ozone and NO<sub>x</sub> which all influence (and are influenced by) the tropospheric oxidising capacity. The methane bias in Base may thus have been caused by the chemistry modelled with UM-UKCA. This will be explored in this chapter. The effect of methane emission changes on the atmospheric abundance will be studied in chapters 4 and 5.

In order to impose a different chemical oxidant field in the model, the CheST chemistry scheme in the UM-UKCA model has been extended. The new scheme, in which the oxidant fields are prescribed and not calculated interactively, will be introduced in section 3.1. In section 3.2, methane modelled with this new setup will be evaluated against observations and results from the Base model.

With the use of prescribed oxidant fields, the chemical feedback of methane on itself is removed. This self-feedback causes methane concentrations to increase more than suggested by a simple mass-balance from an emission increase [e.g Isaksen and Hov, 1987; Prather, 1994, 1996; Fuglestedt et al., 1999]. The question arises whether ignoring this feedback poses a problem in model evaluation. Section 3.3 how the non-interactive chemistry scheme affects the modelled latitudinal methane gradient. The chapter concludes in section 3.4.

## 3.1 Model development

### 3.1.1 Introduction

The previous chapter has highlighted low biases in modelled methane and high biases in interactively modelled OH. In addition biases in CO, ozone and NO<sub>x</sub> were noted. The methane bias in Base may thus be caused by the chemistry modelled with UM-UKCA. In order to probe the effect of the chemistry on methane, the UKCA submodel was modified, allowing the use of prescribed oxidant fields in addition to, and without interacting with, the standard CheST chemistry scheme.

The use of imposed oxidant fields simplifies methane studies by removing the necessity to simulate all species involved in the production and loss of atmospheric OH. Prescribing oxidant fields removes any chemical (self-)feedback of species on the oxidant field, resulting in linear methane chemistry [e.g. Fung et al., 1991]. This means that the total atmospheric field for methane (and species with similar chemistry) can be constructed from individual tracers (equation 3.1, [e.g. Warwick et al., 2006, 2016]). The number of tracers can be adapted to study aims and is limited solely by computational cost and effectiveness.

$$[CH_4]_{total} = \sum [CH_4]_{tracer} \quad (3.1)$$

These different methane tracers are independent of one another due to the chemistry linearity. This means that the tracers can be scaled retrospectively without necessitating further model simulations, i.e. if the modelled total atmospheric methane is biased relative to observations, altering the individual tracer strength can lead to improvements. This setup therefore allows multiple emission scenarios to be studied with one simulation. This aspect will be explored in more detail in the next chapter.

### 3.1.2 Prescribed oxidant fields

The newly developed chemistry scheme prescribes oxidant fields for the hydroxyl radical (OH), chlorine (Cl) and singlet oxygen (O(<sup>1</sup>D)), discussed later in this section. These fields are held in a multi-level ancillary file in molecules cm<sup>-3</sup>. Using the UKCA framework, the three oxidant fields are defined as a constant three-dimensional species with a 12 month seasonality [Carver et al., 1997]. The prescribed oxidant fields are passed through the

chemical subroutines within the UKCA modules to allow for chemistry calculations in the relevant subroutines.

The oxidant fields are implemented as a monthly mean field, averaged over all time steps with linear interpolation between the months, and are updated every 5 days. With this implementation no diurnal oxidant variation is achieved in the model resulting in the chemistry being active at night. In the ‘real’ world, oxidation (through OH) likely only occurs during the day. The next section tests, theoretically, whether this way of implementing the prescribed oxidant fields into the model induces oxidation biases in the model.

### Implementation of the prescribed oxidant fields

To investigate the effect of the oxidant field setup described above, two theoretical oxidant fields, OH in this example, are analysed as shown in Figure 3.1. In Scenario A, OH is constant throughout the day ( $[OH]_{const}$ ), in Scenario B, OH has a simplified diurnal profile where OH concentrations are zero until 6:00 hours, increase linearly until 12:00 hours to  $[OH]_{max}$  and then decrease linearly to be zero from 18:00 hours. The total daily OH abundance for the two fields, that is the integral of OH over the day, is identical. This results in  $[OH]_{const} = \frac{1}{4}[OH]_{max}$ . OH and the other oxidants are imposed in the model following Scenario A while Scenario B is a simplified approximation of the real world.

For Scenario A, the change of OH with time can be expressed as

$$[OH(t)] = [OH]_{const} \quad (3.2)$$

The equivalent for Scenario B equates to

$$[OH(t)] = \begin{cases} \frac{1}{6}[OH]_{max}(t - 6) & \text{for } 6 \leq t \leq 12 \\ \frac{1}{6}[OH]_{max}(18 - t) & \text{for } 12 \leq t \leq 18 \\ 0 & \text{for } t \leq 6 \text{ and } t \geq 18 \end{cases} \quad (3.3)$$

Calculating the change in methane due to OH can be described as

$$\Delta CH_4 = \int \frac{d(CH_4)}{dt} dt = \int k[CH_4][OH(t)] dt \quad (3.4)$$

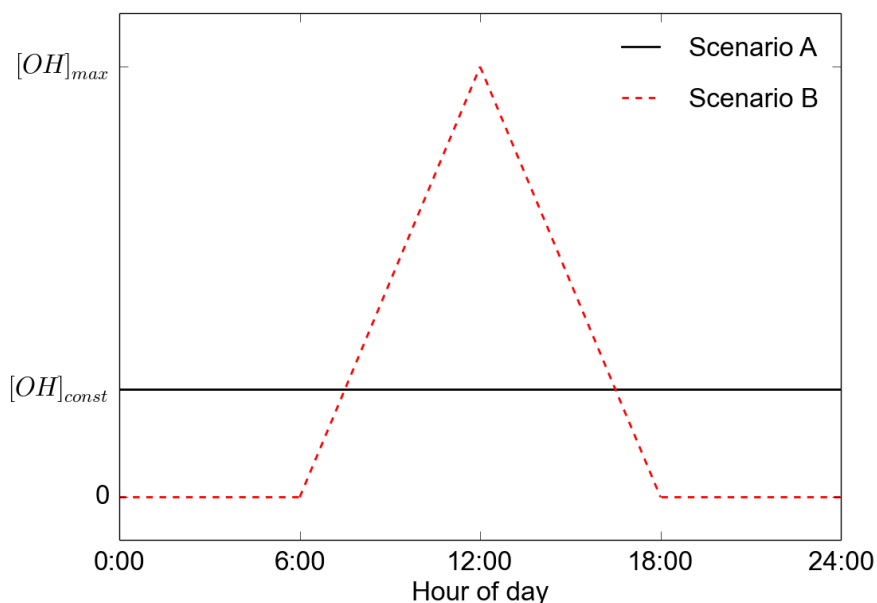


**Fig. 3.1** Implementation of a prescribed oxidant field. Scenario A tests the implementation as a monthly mean OH value with no diurnal variation, Scenario B tests the implementation with a simplified diurnal variation in OH. Total daily OH abundance is identical for both scenarios.

Note that the integral in this equation is for a 24 hour period with  $k$  representing the rate constant for the reaction between methane and OH throughout the whole period. Equation 3.4 further assumes that methane concentrations show no diurnal variation. This assumption holds as methane emissions themselves show no diurnal pattern due to their implementation (in most cases, probably a good assumption). Thus  $\Delta CH_4$  can be simplified to

$$\Delta CH_4 = \int \frac{d(CH_4)}{dt} dt = k[CH_4] \int [OH(t)] dt \quad (3.5)$$

The solution of this function for one day is  $\Delta CH_4 = 6k[CH_4][OH]_{max}$  for both Scenarios A and B. Implementing a monthly mean oxidation field therefore does not induce an oxidation bias.

It should be noted that the diurnal variation of boundary layer height with constant methane emissions throughout the day will lead to a build up of methane concentrations during the night in the shallow boundary layer.

### Description of the prescribed oxidant fields

All prescribed oxidant fields are identical to those used in the TransCom-CH<sub>4</sub> [Patra et al., 2011] and TransCom-VSLS [Hossaini et al., 2016b] projects. These fields were chosen because of their previous use in model intercomparisons. As such they allow for comparability between studies and are well accepted and trusted in the community. Furthermore, their use in the TransCom studies meant the fields were readily available for implementation.

As OH is the major chemical sink for methane, this thesis concentrates on this field. The tropospheric OH component originates from a study by Spivakovsky et al. [2000] who used a photochemical model to calculate OH from observations of ozone, water vapour, nitrogen oxides (NO<sub>2</sub>, NO, N<sub>2</sub>O, NO<sub>3</sub>, HNO<sub>2</sub>, HNO<sub>4</sub>), CO, hydrocarbons, temperature, and cloud optical depth which was then optimised against methyl chloroform (MCF) measurements. This OH field was scaled (reduction by 8%) for the TransCom project following further optimisation against the observed MCF decline in the early 2000s [Huijnen et al., 2010; Patra et al., 2011] which is the configuration used in this thesis's experimental setup and referenced as 'TransCom OH' here.

The prescribed OH field has an annual airmass-weighted global tropospheric mean of  $10.4 \times 10^5$  molecules cm<sup>-3</sup> with a seasonal amplitude of  $2.04 \times 10^5$  molecules cm<sup>-3</sup> (20% of annual mean). It was shown in chapter 2 that the seasonal amplitude of the TransCom OH field is slightly more pronounced in the Northern than in the Southern Hemisphere (Figure 2.10). Global mean TransCom OH remains relatively constant between November and May, reaching a maximum in August. The two hemispheres contain approximately equal amounts of OH (North-South gradient of 1.01) with maximum OH in the lower to middle tropical troposphere (Figure 3.2). As seen before, OH varies across the seasons with slightly higher OH concentration in the summer hemisphere. The TransCom OH field remains relatively constant through the year however, as shown in the previous chapter.

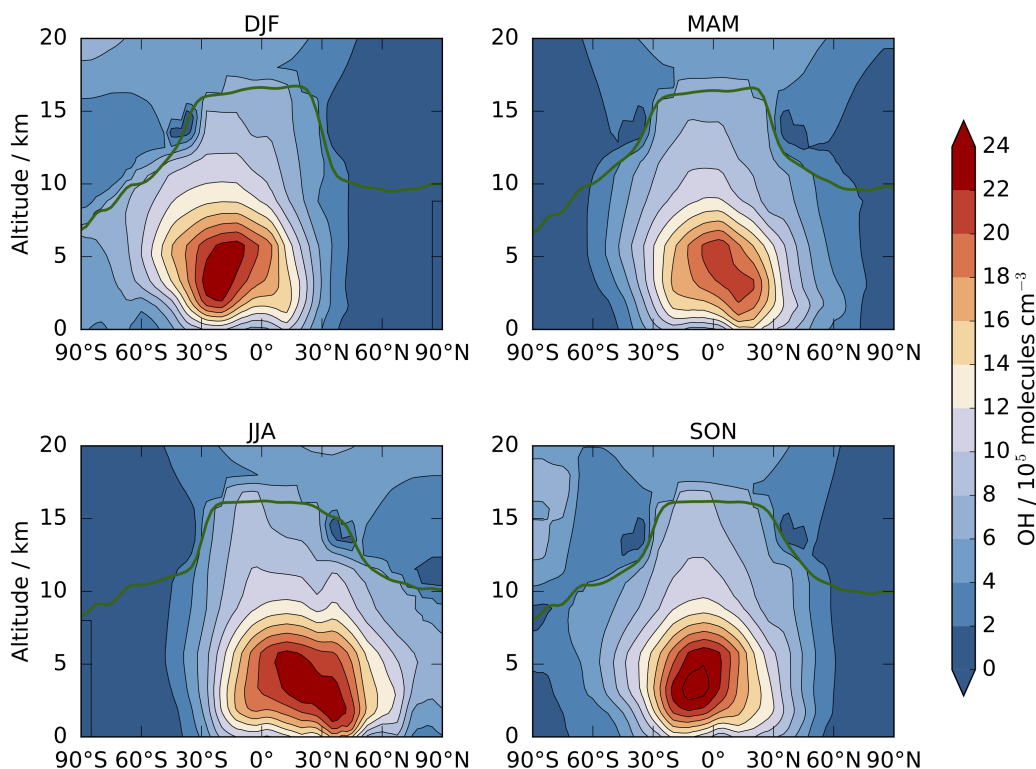


**Fig. 3.2** Seasonal mean zonally averaged TransCom OH concentrations ( $10^5$  molecules  $\text{cm}^{-3}$ ) for December-January-February (DJF), March-April-May (MAM), June-July-August (JJA) and September-October-November (SON).

Figure 3.3 shows surface (lowest five model layers) OH concentrations for the different seasons. The shift of maximum OH concentrations towards the summer hemisphere is apparent as well as the absence of OH in the polar winter. OH concentrations are highest over the land masses where  $\text{NO}_x$  and ozone increase OH production.

Table 3.1 summarises tropospheric OH abundance in twelve subregions, showing the TransCom OH field, the original Spivakovsky field and the difference between the two. The table highlights that the scaling of the OH field is larger in the Northern Hemisphere and that the surface values are, on average, least affected by the optimisation performed by Huijnen et al. [2010]. The last row of each subregion in Table 3.1 repeats the OH abundance for the Base experiment presented in chapter 2. The TransCom OH maximises at higher altitudes in the tropics compared to the Base model presented in chapter 2.

The stratospheric OH originates from a 2-dimensional model as do the fields for atmospheric Cl and  $\text{O}(^1\text{D})$  [Patra et al., 2011; Hossaini et al., 2016b].

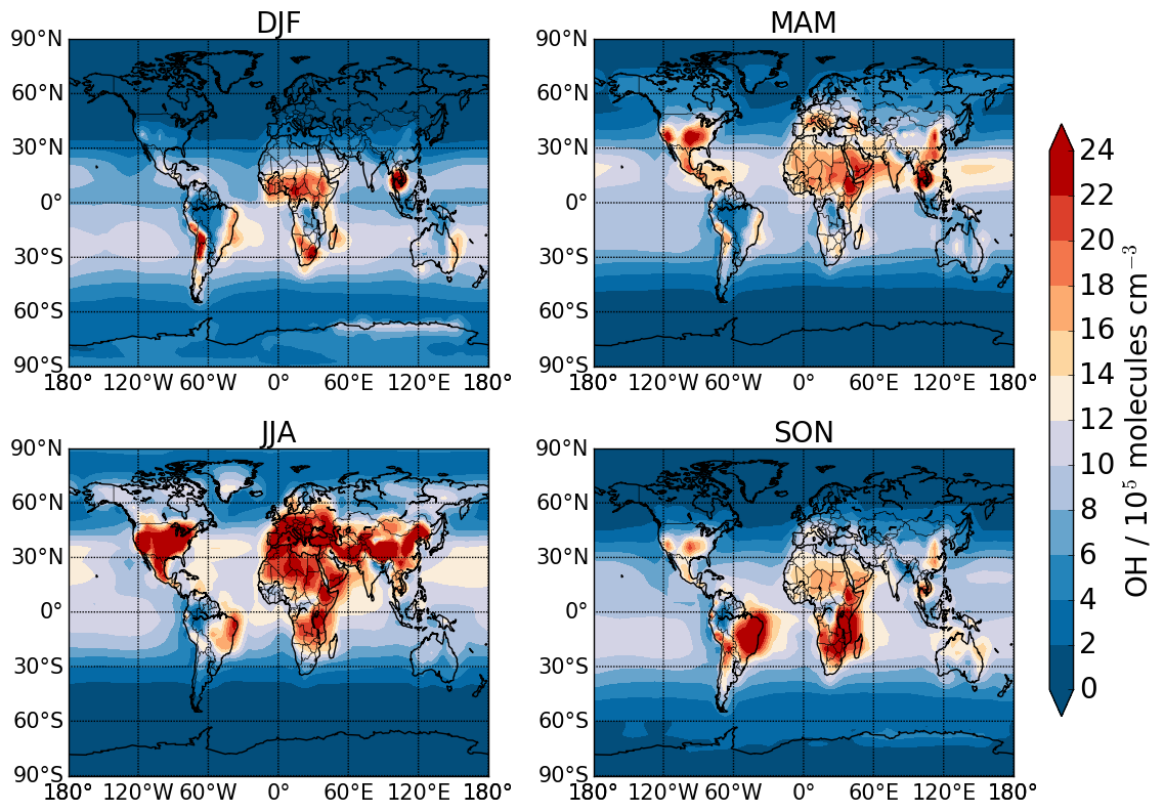


**Fig. 3.3** Seasonal mean surface TransCom OH concentrations ( $10^5$  molecules  $\text{cm}^{-3}$ ) for DJF, MAM, JJA and SON.

**Table 3.1** Lawrence et al. [2001] analysis of annual mean airmass-weighted tropospheric OH concentrations ( $10^5$  molecules  $\text{cm}^{-3}$ ). First row: TransCom OH field implemented into the model [Patra et al., 2011]; second row: Spivakovsky OH field as presented in Lawrence et al. [2001]; third row: percentage difference between the TransCom and the Spivakovsky OH fields; Fourth row: Base OH discussed in chapter 2.

Altitude	Model	90°S – 30°S	30°S – 0°	0° – 30°N	30°N – 90°N
500 – 250 hPa	TransCom	6.3	13.2	11.9	5.8
	Spivakovsky	6.4	14.3	13.6	6.4
	% difference	-1.6%	-7.7%	-12.5%	-9.4%
	Base	5.0	12.0	13.2	8.3
750 – 500 hPa	TransCom	6.6	18.6	18.2	7.6
	Spivakovsky	7.2	20.0	19.9	8.8
	% difference	-8.3%	-7.0%	-8.5%	-13.6%
	Base	5.3	16.8	18.8	10.5
Surface – 750 hPa	TransCom	4.8	14.2	14.6	7.1
	Spivakovsky	4.7	14.4	15.2	7.6
	% difference	-2.1%	-1.4%	-3.9%	-6.6%
	Base	6.0	18.9	22.4	12.8

### 3.1.3 Non-interactive methane chemistry

In the non-interactive chemistry within UKCA, each non-interactive methane tracer reacts with the three prescribed oxidant fields, OH, Cl, and O(<sup>1</sup>D) with the rates specified in Table 3.2, following the TransCom-CH<sub>4</sub> setup [Patra et al., 2011]. Note that these rate constants are identical to the interactive CheST methane chemistry. No products are formed nor are the oxidant fields altered through these chemical reactions, hence the atmospheric oxidative capacity remains constant. In this study, 33 independent tracers have been implemented, each representing methane from a distinct source type and region. The sum of these 33 tracers represents total atmospheric methane as introduced in 3.1. The experiment with the setup described in this section will be referenced ‘ $\Delta\text{OH}$ ’ for the remainder of this thesis.

**Table 3.2** Methane loss reaction rate constants ( $\text{molecules}^{-1} \text{ cm}^3 \text{ s}^{-1}$ ) with the prescribed oxidant fields in the chemistry scheme. The rate constants are taken from Patra et al. [2011] and originate from Sander et al. [2006].

Reactants	Reaction rate constants ( $\text{molecules}^{-1} \text{ cm}^3 \text{ s}^{-1}$ )
OH	$2.45 \times 10^{-12} \exp(-1775 \text{ T}^{-1})$
Cl	$7.30 \times 10^{-12} \exp(-1280 \text{ T}^{-1})$
O( <sup>1</sup> D)	$1.50 \times 10^{-10}$

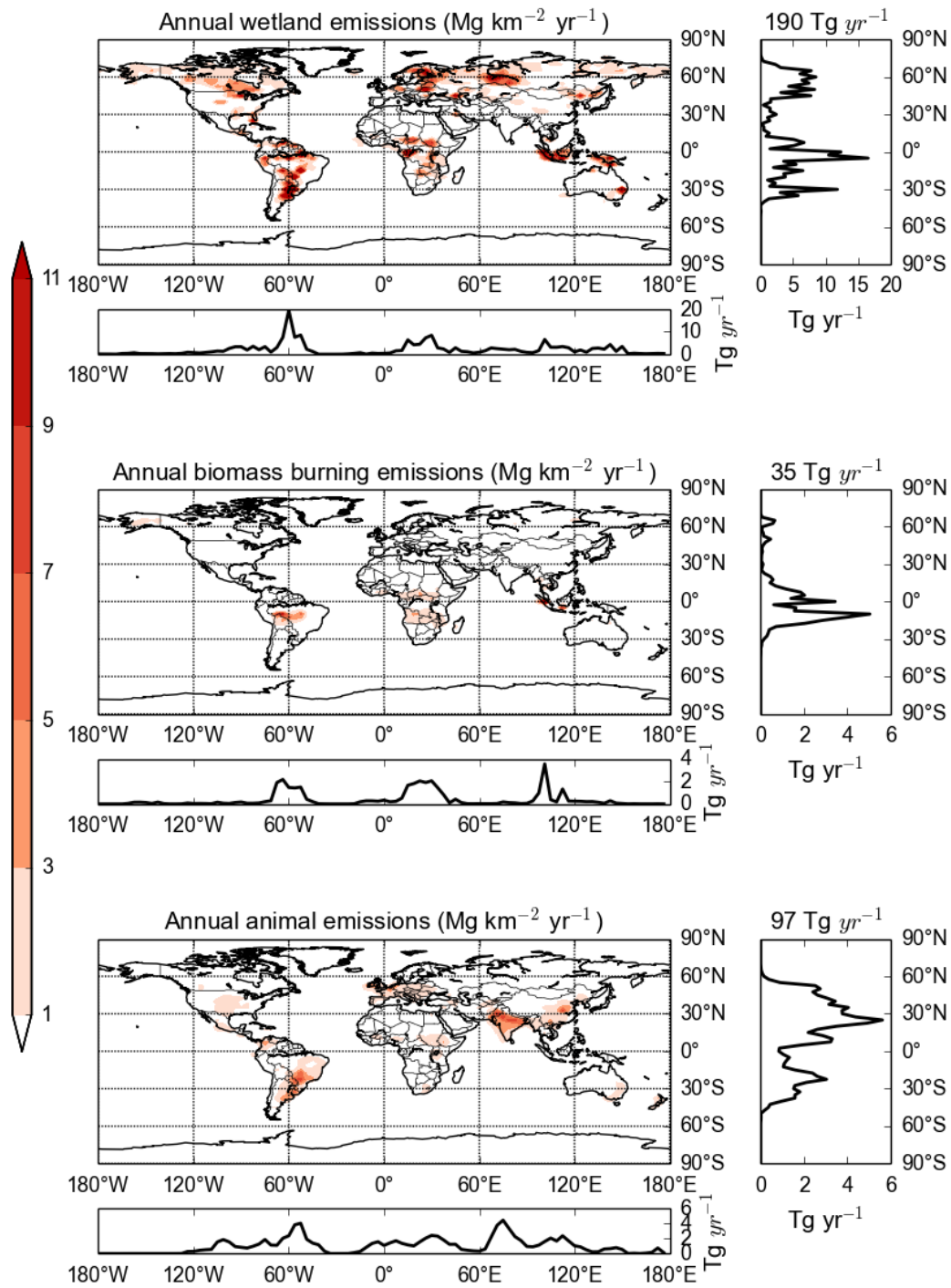
Total  $\Delta\text{OH}$  methane emissions are identical to the emissions for the Base experiment discussed in the previous chapter (section 2.2). In summary, the emissions total 548 Tg(CH<sub>4</sub>) yr<sup>-1</sup> which includes a 25 Tg(CH<sub>4</sub>) yr<sup>-1</sup> soil sink [Fung et al., 1991]. The anthropogenic emissions [EDGAR, EC-JRC/PBL, 2011] total to 322 Tg(CH<sub>4</sub>) yr<sup>-1</sup> with an additional 35 Tg(CH<sub>4</sub>) yr<sup>-1</sup> from biomass burning [van der Werf et al., 2010; Kirschke et al., 2013]. The natural contribution from wetlands [Fung et al., 1991; Patra et al., 2010; Melton et al., 2013], hydrates and termites [Fung et al., 1991] amount to 190 Tg(CH<sub>4</sub>) yr<sup>-1</sup>, 6 Tg(CH<sub>4</sub>) yr<sup>-1</sup> and 20 Tg(CH<sub>4</sub>) yr<sup>-1</sup>, respectively. The methane emissions are split by emission types for individual tracers in this experiment. Coal and gas emissions are combined into one tracer as are waste and all remaining anthropogenic emissions, referred to as coal and waste emissions hereafter, respectively. This means that eight source types can be distinguished in the  $\Delta\text{OH}$  experiment as summarised in Table 3.3. The soil sink (25 Tg(CH<sub>4</sub>) yr<sup>-1</sup>) is applied within the model and distributed amongst the tracers according to their relative contributions in each grid cell of the lowest model level where there is a soil sink.

**Table 3.3** Methane emission source types that can be distinguished in the model setup and their strengths in  $\text{Tg}(\text{CH}_4) \text{ yr}^{-1}$ . Note that the coal source represents the combined strength for coal and gas. The waste source combined the waste emissions with “other anthropogenic” emissions (see chapter 2 for details).

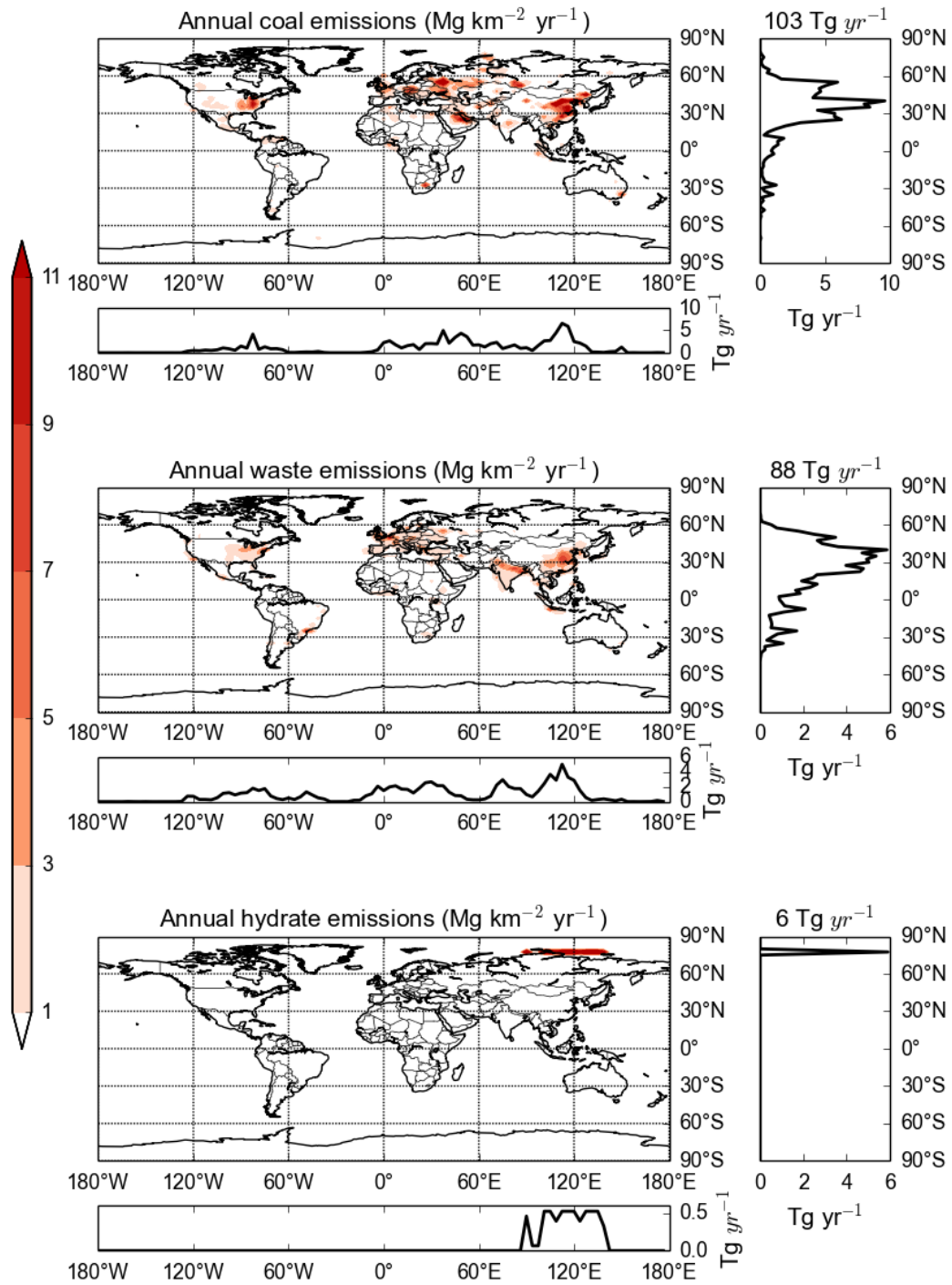
Type	Emissions ( $\text{Tg}(\text{CH}_4) \text{ yr}^{-1}$ )
Wetlands	190
Biomass burning	35
Animals	97
Coal	103
Waste	88
Hydrates	6
Termites	20
Rice	34

Figure 3.4 shows the global distribution and total strength of the annually summed methane emission for these eight source types. Wetland emissions peak in the tropics, mainly from South America, with further contributions from northern latitudes. Termite emissions are evenly distributed across the Southern Tropics while hydrate emissions are located in a narrow band in the Russian Arctic. Biomass burning emissions show a sharp maximum in the tropics with only minimal contribution from high latitude fires. Emissions from coal and waste originate mainly from the Northern Hemisphere while animal emissions have additional contributions from the tropics. These three anthropogenic emission sources are globally distributed across the continents. In contrast, rice emissions are confined to tropical South-East Asia.

In addition to separation by emission source type, five of the eight source type emissions (coal, waste, animals, biomass burning and wetlands) are further split into six emission regions. Hydrates, termites and rice emissions are not further separated as their emissions are already more regionally defined, i.e. high northern Arctic or tropical. This will be discussed in more detail in chapter 4, focusing entirely on exploring the information that can be gained from the individual tracers. This chapter concentrates exclusively on the total atmospheric methane abundance calculated as the sum of all the individual tracers according to equation 3.1.



**Fig. 3.4** Global distribution of the annually summed methane emissions ( $\text{Mg}(\text{CH}_4) \text{ km}^{-2} \text{ yr}^{-1}$ ) for the eight distinct source types included in the model. Compiled as discussed in section 2.2 from Lamarque et al. [2010]; Guenther et al. [1995]; Fung et al. [1991]; van der Werf et al. [2010]; Patra et al. [2010]; EDGAR [EC-JRC/PBL, 2011]; Melton et al. [2013].



**Fig. 3.4 Continued.** Global distribution of the annually summed methane emissions ( $\text{Mg}(\text{CH}_4) \text{ km}^{-2} \text{ yr}^{-1}$ ) for the eight distinct source types included in the model. Compiled as discussed in section 2.2 from Lamarque et al. [2010]; Guenther et al. [1995]; Fung et al. [1991]; van der Werf et al. [2010]; Patra et al. [2010]; EDGAR [EC-JRC/PBL, 2011]; Melton et al. [2013].

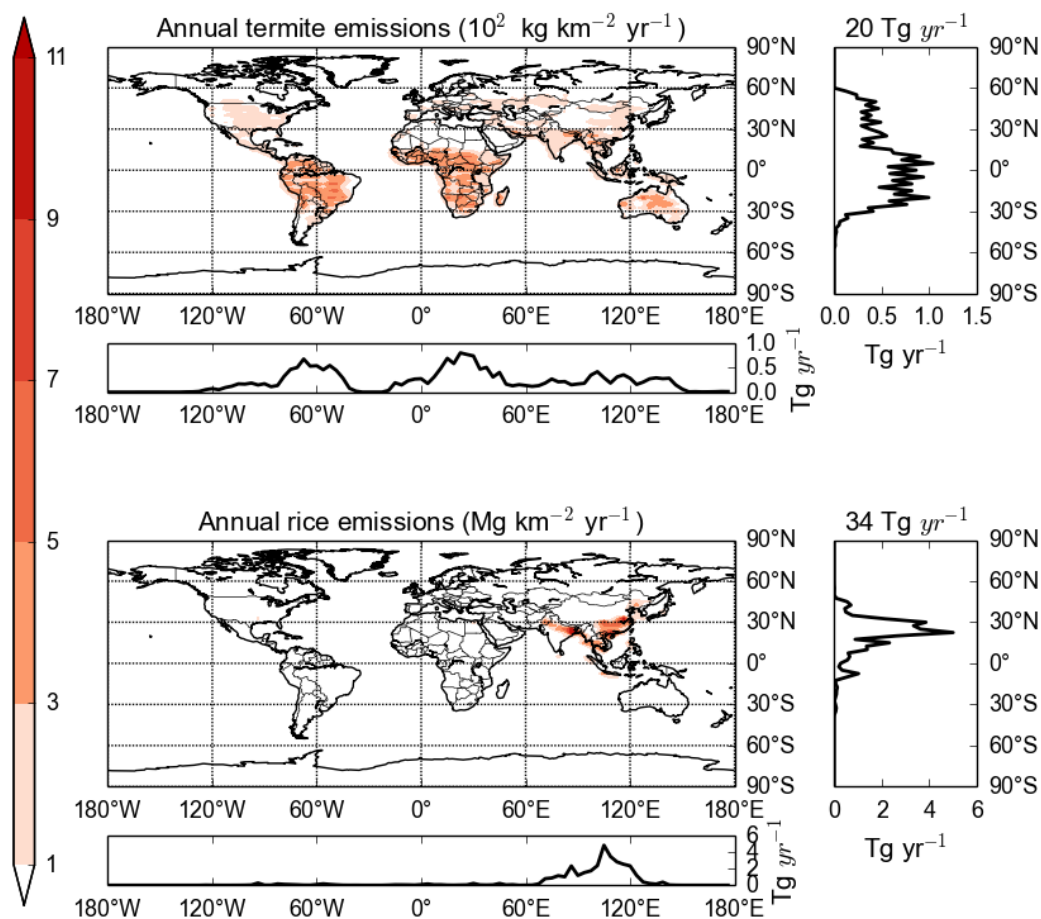


**Fig. 3.4 Continued.** Global distribution of the annually summed methane emissions ( $10^2 \text{ kg}(\text{CH}_4) \text{ km}^{-2} \text{ yr}^{-1}$  and  $\text{Mg}(\text{CH}_4) \text{ km}^{-2} \text{ yr}^{-1}$ ) for the eight distinct source types included in the model. Compiled as discussed in section 2.2 from Lamarque et al. [2010]; Guenther et al. [1995]; Fung et al. [1991]; van der Werf et al. [2010]; Patra et al. [2010]; EDGAR [EC-JRC/PBL, 2011]; Melton et al. [2013].

## 3.2 Evaluation of the $\Delta\text{OH}$ methane chemistry

### 3.2.1 Tropospheric methane

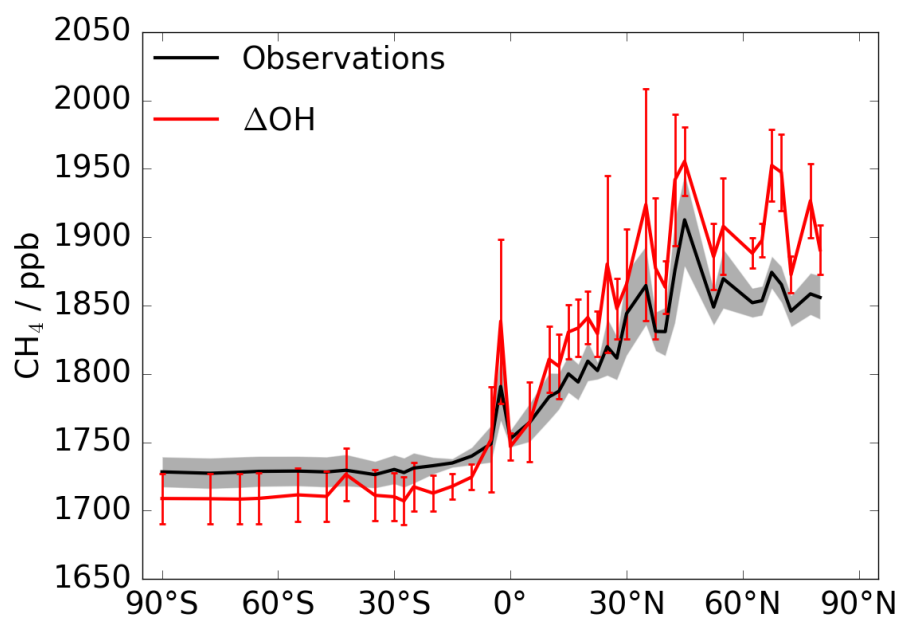
Mean surface  $\Delta\text{OH}$  methane averages to 1818 ppb (sampled in the model grid boxes closest to NOAA surface stations) and matches surface observations (1790 ppb, [Dlugokencky et al., 2016]) well. This suggests that the total methane source strength of  $548 \text{ Tg}(\text{CH}_4) \text{ yr}^{-1}$  is a reasonable estimate for the sink strength prescribed through the oxidant fields. The change in OH field from Base to  $\Delta\text{OH}$  has thus removed the methane low bias of the Base experiment (160 ppb, 9%, chapter 2) and leads to reasonable agreement with observations.

Figure 3.5 shows the latitudinal gradient for observations [Dlugokencky et al., 2016] and  $\Delta\text{OH}$  methane sampled in the model grid boxes closest to the observations. Modelled methane is slightly low biased in the Southern Hemisphere while it is overestimated in the Northern Hemisphere with the model-observation mismatch increasing with northerly latitude. The  $\Delta\text{OH}$  latitudinal methane gradient (148 ppb) is thus overestimated compared to observations (97 ppb) but the model captures the variations in observed methane concentrations well. The sampling of the model in the grid boxes closest to the observations therefore indicates that more local influences on methane (emissions, transport and chemical loss) are reasonably well represented in the model.

In addition, Figure 3.5 highlights that the seasonal amplitude of  $\Delta\text{OH}$  methane is consistently larger than suggested by the observations (shown by the spread at each latitude). In the Southern Hemisphere, methane varies intraannually by 50 ppb. Large seasonal variations can be noted around the equator where changes in atmospheric circulation (e.g. location of the inter tropical convergence zone (ITCZ)) strongly affect methane concentrations. The amplitude of seasonal variations in the Northern Hemisphere exceeds that of the Southern Hemisphere and is much less homogeneous due to the seasonality and strength of methane emissions. This can be seen in the observations, but is more pronounced in the model.

This analysis shows that modelled methane concentrations, sampled at the 66 NOAA sites recording data between January 2000 and December 2005, overestimate the Northern Hemispheric observations, underestimate the Southern Hemispheric observations and exhibit seasonal variations of slightly too great a magnitude. The overestimation of the latitudinal gradient may be caused by a misrepresentation in the emission strength with too high emissions in the Northern Hemisphere and too low emissions in the Southern Hemisphere. Alternatively, or in addition to this, methane loss might be underestimated in the Northern

but overestimated in the Southern Hemisphere. With the bulk of methane emissions located in the Northern Hemisphere, Southern Hemispheric methane is proportionally more affected by transport and sink processes. This may point to the sink strength being biased in this experiment.



**Fig. 3.5** Latitudinal  $\Delta\text{OH}$  methane gradient (red) compared to observations (ppb) [Dlugokencky et al., 2016] (black). The observations are averaged between January 2000 and December 2005. Error bars and shading represent the  $1\sigma$  interval and indicate temporal and spatial variability at each latitude.

Figure 3.6 highlights comparison between modelled methane and observations for sixteen stations from the NOAA observational network [Dlugokencky et al., 2016]. Good agreement can be found at the Southern Hemispheric stations, with correlation higher than  $R^2 = 0.90$  at all stations but Tutuila. The NMBE is small and negative ( $\leq -1\%$ ) for all stations but Mahe Island. The seasonal cycle at Mahe Island, a station in the ITCZ [Dlugokencky et al., 1994a], suggest that Northern Hemispheric methane is high biased resulting in a (small) positive NMBE at this station. Northern Hemispheric  $\Delta\text{OH}$  methane is overestimated at all stations. The smallest NMBE equals 0.9% at Wendover and largest NMBE equals 6.3% at Tae-ahn Peninsula. The correlations between modelled and measured methane in the Northern Hemisphere are mixed, ranging from  $R^2 = 0.0$  at Tae-ahn Peninsula to  $R^2 = 0.94$  at Sary Taukum. Arctic stations Ny-Alesund and Alert correlate reasonably to observations ( $R^2 = 0.75$ ) with the model high bias slightly smaller at Alert than at Ny-Alesund. In contrast,

Pallas shows an even higher bias and no correlation ( $R^2 = 0.31$ ), due to a modelled seasonal minimum earlier than observed and a modelled seasonal maximum later than observed.

The atmospheric  $\Delta$ OH methane burden totals 4844 Tg(CH<sub>4</sub>) which is 519 Tg(CH<sub>4</sub>) higher than the Base methane discussed in the previous chapter. The reduction in tropospheric OH concentrations (-18%) thus resulted in a 12% increase in atmospheric methane burden. The burden for this experiment agrees well with the burden established from the NOAA surface observations following Dlugokencky et al. [1998] and Fung et al. [1991]. They established the relationship that one ppb of surface methane contributes 2.767 Tg(CH<sub>4</sub>) to the atmospheric methane burden, 1790 ppb thus amount to 4886 Tg(CH<sub>4</sub>), which is only 40 Tg(CH<sub>4</sub>) (1%) larger than the burden calculated for this experiment. However, doing the same calculation for surface model data, sampled at the location of the observations, overestimates the burden (5030 Tg(CH<sub>4</sub>), +4%). This may be explained by the low model resolution and thus could be a misrepresentation of the station data when sampling the model. The model – observation mismatch, as seen in Figure 3.6, confirms this explanation.

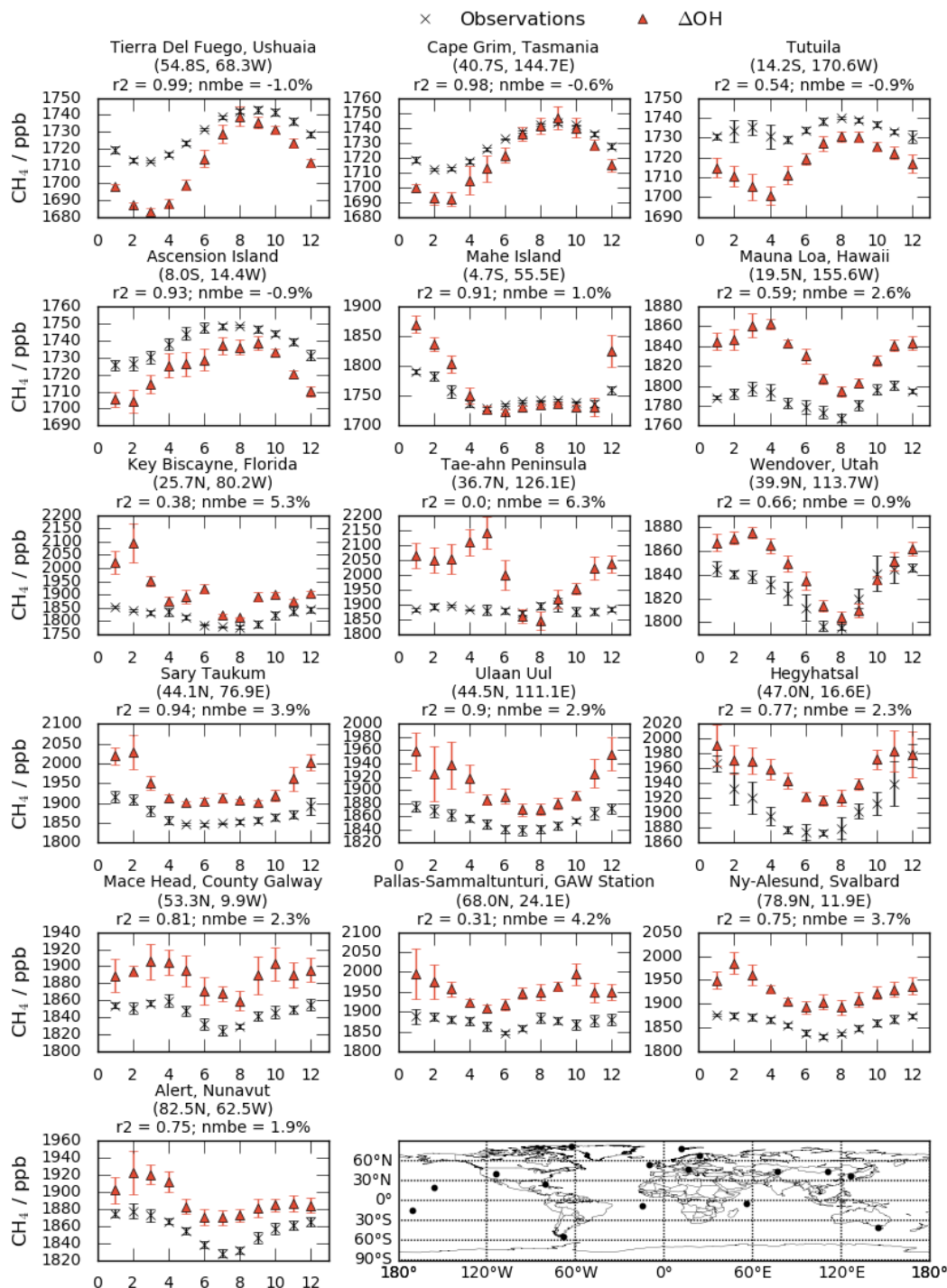


**Fig. 3.6** Comparison of  $\Delta$ OH surface  $\text{CH}_4$  levels with surface measurements (ppb) [Dlugokencky et al., 2016]. The observations are averaged between January 2000 and December 2005. Note the different scale for the individual plots. The map shows the measurement site locations used in this comparison.

### 3.2.2 Methane oxidation

The  $\Delta\text{OH}$  methane lifetime with respect to tropospheric OH loss equals 10.2 years. This is in good agreement with estimates inferred using global OH determined from MCF measurements ( $11.2 \pm 1.3$  years, [Prather et al., 2012]). As can be seen in Figure 3.7, not only does  $\Delta\text{OH}$  follow the ACCMIP model relationship between tropospheric OH abundance and methane lifetime (previously discussed in chapter 2), it is also one of the few models that agrees with methane lifetime and tropospheric OH abundance inferred from observations.

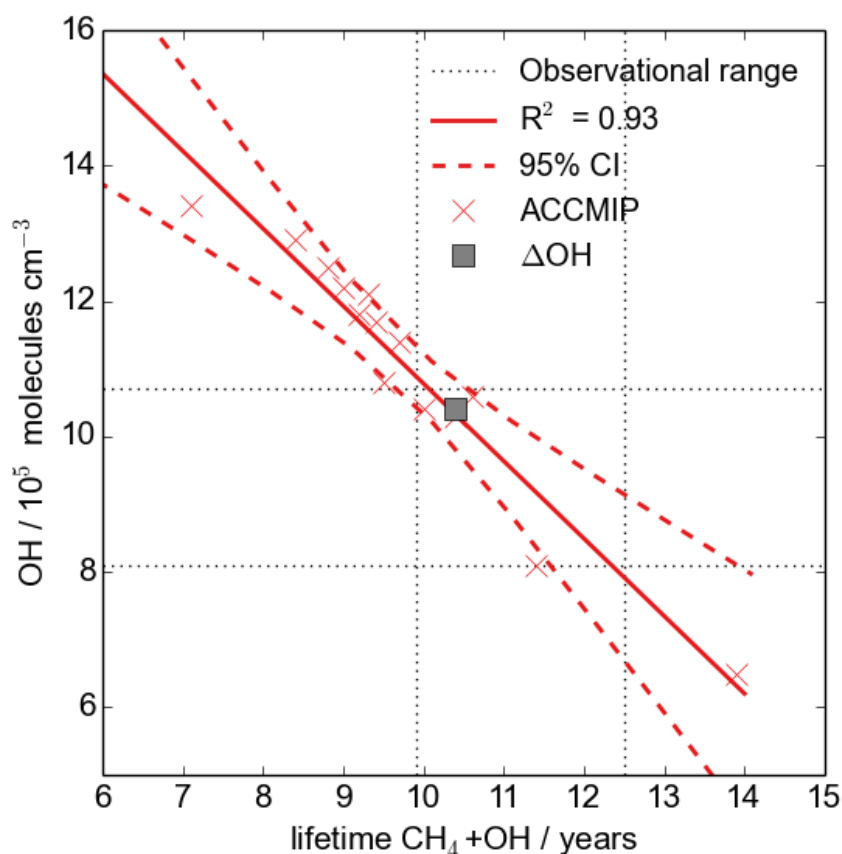


**Fig. 3.7** Relationship between methane lifetime with respect to tropospheric OH loss (years) and tropospheric OH concentrations ( $10^5$  molecules  $\text{cm}^{-3}$ ) for the ACCMIP models [Voulgarakis et al., 2013] (red crosses) and  $\Delta\text{OH}$  (grey square). The observational estimates for the methane lifetime [Prather et al., 2012] and the global mean OH concentrations [Prinn et al., 2001] are indicated by the black dotted lines.

As shown in chapter 2, a reasonable methane lifetime estimate depends on both the atmospheric methane burden and its atmospheric loss, tropospheric OH for the lifetime

presented here. Thus, the  $\Delta\text{OH}$  flux through the reaction of methane with OH is analysed. It is presented in Table 3.4 as a percentage of the total atmospheric flux which amounts to  $473 \text{ Tg}(\text{CH}_4) \text{ yr}^{-1}$ .  $\Delta\text{OH}$  is compared to a published experiment using the unscaled Spivakovsky OH field [Lawrence et al., 2001]; the data presented in that publication is recalculated for tropospheric loss below 250 hPa for this comparison. The table also allows for comparison with the interactive methane flux presented in the previous chapter (Base, last row). For all three experiments, methane loss predominantly (ca. 64%) happens in the tropical troposphere below 500 hPa (30°S to 30°N).

**Table 3.4** Lawrence et al. [2001] analysis of methane loss through reaction with OH. Values are given as percentage of total methane loss. First row:  $\Delta\text{OH}$ ; Second row: Lawrence et al. [2001] calculation using the Spivakovsky OH field, percentage recalculated to a 250 hPa tropopause; Third row: percentage difference between  $\Delta\text{OH}$  and Spivakovsky; Fourth row: Base.

Altitude	Model	90°S – 30°S	30°S – 0°	0° – 30°N	30°N – 90°N
500 – 250 hPa	$\Delta\text{OH}$	1.9	6.6	5.7	2.4
	Lawrence	1.6	6.3	5.4	2.5
	% difference	18.8%	4.8%	9.3%	-4.0%
	Base	1.2	4.7	5.0	2.6
750 – 500 hPa	$\Delta\text{OH}$	3.6	13.6	15.4	6.0
	Lawrence	3.5	16.9	14.7	6.2
	% difference	2.9%	-19.5%	3.4%	-3.2%
	Base	2.4	10.1	12.9	6.6
Surface – 750 hPa	$\Delta\text{OH}$	3.6	16.3	18.0	6.9
	Lawrence	3.1	16.8	15.9	7.1
	% difference	16.1%	-3.0%	13.2%	-2.8%
	Base	3.8	18.0	22.7	10.0

$\Delta\text{OH}$  methane loss is shifted to the northern tropics compared to the Lawrence experiment. A shift to lower altitudes (below 750 hPa) can also be noted. Small differences are apparent in the extra-tropics with a greater (smaller) proportion of methane being lost in the southern (northern) extra-tropics. These differences are however only of little importance as the total methane lost in these extra-tropical regions is minimal. The differences between these two experiments are likely asymmetric due to the scaling of the OH field for the TransCom studies (see above, section 3.1.2). Unfortunately, the absolute fluxes through the reaction of methane and OH cannot be compared as they were not reported by Lawrence et al. [2001].

In comparison to the Base experiment presented in chapter 2 (last row in each subregion), absolute  $\Delta\text{OH}$  tropospheric methane loss is smaller by  $53 \text{ Tg}(\text{CH}_4) \text{ yr}^{-1}$ . Methane loss is

more evenly distributed below 500 hPa for the  $\Delta$ OH experiment while it is concentrated in the region below 750 hPa for the Base experiment.

This analysis shows that reducing tropospheric OH, the predominant chemical sink for atmospheric methane, improved comparison between modelled and observed methane. Global mean surface methane levels and the methane lifetime are well represented in the  $\Delta$ OH experiment. However, methane is overestimated in the Northern and underestimated in the Southern Hemisphere. This might suggest that the North-South gradient in the tropospheric OH field (1.01) is not sufficient to represent the observed latitudinal methane gradient. Alternatively, a redistribution of methane emissions into tropical/Southern Hemispheric regions might improve the gradient. This emission shift will be investigated in chapters 4 and 5.

### **3.3 Non-interactive chemistry impact on the latitudinal gradient**

As outlined above, the  $\Delta$ OH latitudinal methane gradient is overestimated. Questions arise as to whether this is due to the OH field or the non-interactive implementation, as the new chemistry scheme ignores any feedback of methane on OH and itself. An additional experiment has thus been performed in which the Base OH field, presented in the previous chapter and mentioned above, is prescribed in the chemistry scheme introduced in this chapter (i.e. the Base OH is specified and non-interactive). As a reminder, this Base OH field averages to  $12.4 \times 10^5$  molecules  $\text{cm}^{-3}$  in the global troposphere with higher OH concentrations in the Northern than in the Southern Hemisphere. While Base methane concentrations were low biased relative to observations, the latitudinal gradient agreed well with observations. No changes have been made to the methane emissions, resulting in two experiments which differ only in the chemical feedback on OH, i.e. Base(interactive) and Base(non-interactive).

Figure 3.8 indeed shows that the modelled latitudinal gradient is altered when the Base OH field is implemented in the non-interactive chemistry scheme. The latitudinal methane gradient increased from 104 ppb in Base(interactive) to 135 ppb in Base(non-interactive), mainly because of lower Southern Hemispheric methane in Base(non-interactive). This is likely due to the fact that linearising methane chemistry affects the methane loss which is strongest in the tropics. With Southern Hemispheric methane being older than Northern Hemispheric methane, changes in the loss processes impact Southern Hemispheric methane

concentrations more than in the Northern Hemisphere. The overestimation of the methane latitudinal gradient in  $\Delta\text{OH}$  (see above, Figure 3.5) may well result from the absence of the methane feedback.

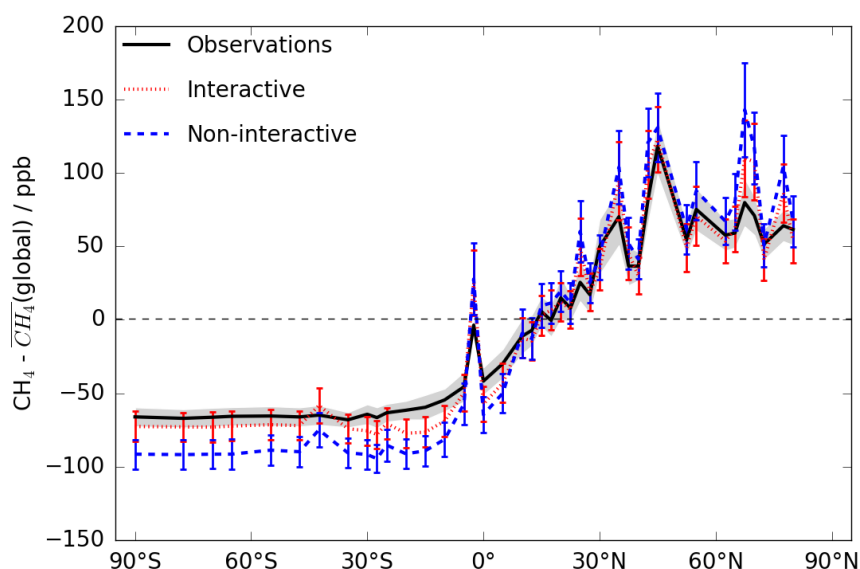


**Fig. 3.8** Latitudinal gradient for Base methane discussed in chapter 2 (interactive, red) and Base(non-interactive) (blue) compared to observations [Dlugokencky et al., 2016] (black), relative to the surface mean (ppb). The observations are averaged between January 2000 and December 2005. Error bars and shading represent the  $1\sigma$  interval and indicate temporal and spatial variability at each latitude.

This section has highlighted that linearising methane chemistry affects the modelled latitudinal methane gradient. Base methane agreed well with the observed latitudinal gradient while the same OH field in the non-interactive chemistry scheme led to an overestimation of the gradient. Time did not allow for further investigation but this analysis might point to a limitation of non-interactive chemistry schemes.

### 3.4 Summary

Modelled methane in the Base scenario (methane emission strength of  $548 \text{ Tg}(\text{CH}_4) \text{ yr}^{-1}$ , chapter 2) was low biased. This can be caused by either (or both) overestimating sink processes or underestimating methane emissions. The oxidant effect on atmospheric methane has been probed in this chapter.

A new model configuration within the UM-UKCA framework has been introduced. This allowed oxidants (OH, Cl, O(<sup>1</sup>D)), to be prescribed which removed methane's chemical self-feedback and rendered methane chemistry linear. The same methane emissions as in the previous chapter were used to simulate atmospheric methane in this new model configuration. While 33 independent methane tracers were simulated, this chapter focused solely on the total atmospheric methane concentration, the sum of all 33 tracers.

Using a published and well trusted OH field inferred from atmospheric observations (TransCom adaption of the Spivakovsky OH field [Spivakovsky et al., 2000; Huijnen et al., 2010; Patra et al., 2011]), absolute levels of modelled methane agreed well with observations. Slight high (low) biases in the Northern (Southern) Hemispheric could be noted, which resulted in an overestimation of the latitudinal methane gradient in the experiment presented in this chapter. The methane lifetime of 10.2 years agreed well with observational estimates. Relatively small changes to atmospheric OH levels (18% reduction in tropospheric concentrations) thus led to large differences in methane concentrations between the experiment discussed in this chapter and the Base experiment presented in chapter 2. This illustrates the sensitivity of atmospheric methane to the coupled methane-OH system. In order to gain more confidence in the OH field, it would be beneficial to model methyl chloroform as its abundance is dominated by the OH sink with little and well known emissions. Constraining the OH sink would help to narrow uncertainties in methane emission estimates.

The last section investigated how the non-interactive chemistry scheme affects the modelled latitudinal methane gradient. The Base OH field which led to good agreement between the modelled and observed latitudinal methane gradient (chapter 2) was implemented into the non-interactive chemistry scheme. This resulted in a latitudinal methane gradient increase much larger than suggested by observations. Any optimisation of non-interactive methane thus needs to be treated with the necessary caution when the results are translated into a more realistic world with chemical feedback.

Nonetheless, non-interactive, linear methane chemistry has many benefits which will be explored in the next chapter. With linear chemistry, many individual tracers can be used to build up the global methane field; 33 were used in the setup presented here. These tracers can be independently scaled from each other after completed simulation allowing different emission scenarios to be assessed. The next chapter shows how these tracers can be used in an optimisation method that improves the modelled latitudinal gradient by effectively redistributing methane emissions.

As mentioned throughout this chapter, the low bias in Base methane concentrations (chapter 2) could also be caused by underestimated methane emissions. This will be analysed in chapter 5 which aims to highlight the sensitivity of atmospheric methane to small emission and oxidant changes.

## 4 | Tagged methane tracer analysis

The previous chapter introduced a model experiment that uses prescribed oxidant fields to investigate atmospheric methane. It was shown that the model represented global methane levels well, but overestimated the latitudinal methane gradient. This non-interactive model setup renders methane chemistry linear and as such allows separate methane tracers to be simulated in parallel. This chapter analyses these individual tracers which represent eight different source types from six geographical regions.

In the first instance the model setup is briefly reintroduced with a focus on the individual tracer methane emissions (section 4.1). In section 4.2, the individual modelled tracer fields are presented and their contributions to atmospheric methane concentrations are discussed. The section analyses the tracers' contributions to the latitudinal gradient and identifies groups of tracers that show distinct features. Section 4.3 then discusses how the latitudinal gradient can be optimised with a linear regression using these canonical tracers. This optimisation scales each individual tracer by a globally uniform parameter. The optimisation can thus be directly linked to the source and region specific emission strengths required for an optimised latitudinal methane gradient because of the linear chemistry. The chapter conclusions are given in section 4.4.

### 4.1 Model setup

#### 4.1.1 Methane tracers

As introduced in chapter 3, 33 independent methane tracers have been implemented in the model which react with prescribed oxidant fields, discussed in detail previously. The sum of these tracers equals total atmospheric methane (equation 3.1, discussed in the previous chapter). In order to gain more detailed information about methane originating from different

source types and regions, the tracers represent eight distinct source types, namely wetlands, biomass burning, animals, coal, waste, hydrates, termites and rice (see Figure 3.4 for the geographical distribution). Apart from hydrates, termites and rice, these source types are further tagged from six emission regions (Figure 4.1). North America (NA), Europe (EU) and Asia (AS) are Northern Hemispheric emission regions (north of 30°N) while South America (SA), Africa (AF) and South & East Asia (SEA) represent tropical (and Southern Hemispheric) emission regions. No further distinction with the Southern Hemisphere has been made as there are only little methane emissions south of 30°S (23 Tg(CH<sub>4</sub>) yr<sup>-1</sup>, 4% of total methane emissions).

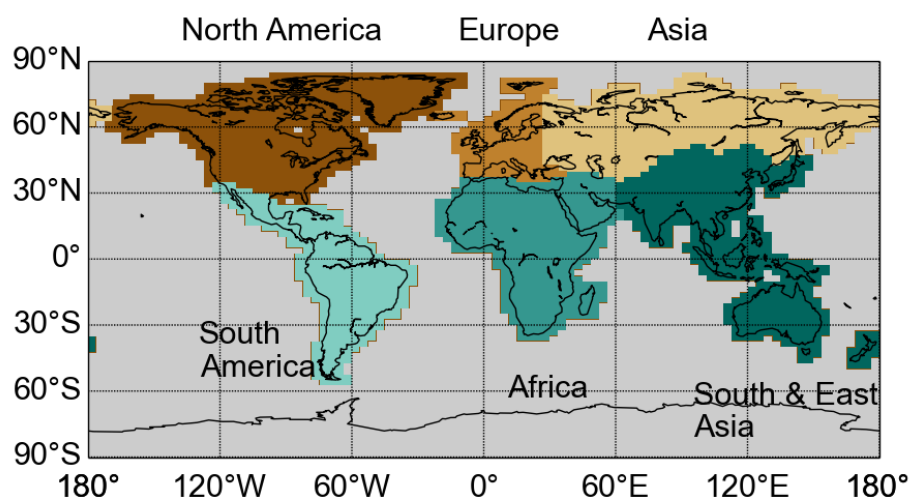


**Fig. 4.1** Map of the six subregions into which the non-interactive methane tracers are separated.

#### 4.1.2 Methane emissions

Methane emissions amount to 548 Tg(CH<sub>4</sub>) yr<sup>-1</sup> which includes a seasonally constant soil sink (25 Tg(CH<sub>4</sub>) yr<sup>-1</sup>). Rice, animal and waste as well as hydrate and termite emissions are also seasonally invariant while methane emissions from coal, biomass burning and wetlands have a distinct seasonal cycles. Table 4.1 shows the annual emission strength of these eight implemented source types in the six different regions. The emissions for hydrates, termites and rice are not regionally tagged in the model, their contribution is thus not split into

the different regions. The soil sink ( $25 \text{ Tg}(\text{CH}_4) \text{ yr}^{-1}$ ) is not included in the table but is applied within the model and distributed amongst the 33 tracers according to their relative contributions in each grid cell of the lowest model level where there is a soil sink.

**Table 4.1** Annually summed methane emissions by source and region in  $\text{Tg}(\text{CH}_4) \text{ yr}^{-1}$ . The numbers may not add up to the totals given due to rounding errors. Note that these emissions amount to  $573 \text{ Tg}(\text{CH}_4) \text{ yr}^{-1}$  as they do not include the soil sink ( $25 \text{ Tg}(\text{CH}_4) \text{ yr}^{-1}$ ) applied fractionally to the tracers within the model. NA: North America, EU: Europe, AS: Asia, SA: South America, AF: Africa, SEA: South & East Asia.

	Global	NA	EU	AS	SA	AF	SEA	Total
Wetlands	-	26.6	9.2	33.8	54.4	29.4	36.6	190.0
Biomass burning	-	1.3	0.1	1.3	10.0	14.3	8.0	35.0
Animals	-	7.3	9.4	4.6	25.8	14.2	35.6	97.0
Coal	-	11.3	8.4	23.7	6.5	17.1	36.3	103.0
Waste	-	10.1	13.3	4.9	9.4	12.8	37.3	88.0
Hydrates	-	-	-	6.0	-	-	-	6.0
Termites	20.0	-	-	-	-	-	-	20.0
Rice	34.0	-	-	-	-	-	-	34.0
<b>Total</b>	<b>54</b>	<b>56.6</b>	<b>40.4</b>	<b>74.3</b>	<b>106.1</b>	<b>87.8</b>	<b>153.8</b>	<b>573.0</b>

## 4.2 Global methane tagged by source and region

As shown in chapter 3, average global tropospheric methane for the  $\Delta\text{OH}$  experiment lies at 1780 ppb (1818 ppb at the surface, section 3.2) which is in good agreement with observations (NOAA, Dlugokencky et al. [2016]). With the 33 independent methane tracers the contribution of eight source types and six regions can be analysed. The contribution of all 33 individual tracers to the tropospheric global annual mean methane concentration is summarised in Table 4.2.

Wetland tracers contribute 593 ppb (33%), biomass burning 107 ppb (6%), animals 300 ppb (17%), coal 322 ppb (18%), waste 272 ppb (15%), hydrates 19 ppb (1%), termites 59 ppb (3%) and rice 103 ppb (6%). As expected these contributions reflect the relative emission source strengths with wetlands being the main contributor followed by coal and gas, animals and waste emissions. Biomass burning, rice, termites and hydrates all contribute less than 10% each and 16% in aggregate to the total.

It is clear from this analysis that European emissions (and thus European tracers) contribute least to atmospheric methane concentrations (130 ppb, 7.2%) while South & East Asian

tracers make the largest contribution (478 ppb, 26.8%). The single largest contributor to atmospheric methane is the South American wetland tracer (171 ppb, 9.3%) which in itself contributes as much as hydrates (20 ppb, 1.1%), termites (59 ppb, 3.3%) and rice (103 ppb, 5.8%) together or global biomass burning (178 ppb, 5.9%). Potential changes to South American wetlands could therefore have the largest impact on atmospheric methane of any individual tracer. This is particularly interesting because analysis of the latitudinal gradient of methane in chapter 3 has highlighted that Southern Hemispheric methane is underestimated relative to observations. Section 4.3 will go into a more detailed analysis.

**Table 4.2** Absolute (a, ppb) and relative (b, %) contribution of all 33 methane tracers to the global tropospheric annual mean methane concentration. The last column and row indicate the methane emission strength by source type and source region, respectively ((a),  $T_g(\text{CH}_4) \text{ yr}^{-1}$  and (b), %). NA: North America, EU: Europe, AS: Asia, SA: South America, AF: Africa, SEA: South & East Asia.

(a)	Global	NA	EU	AS	SA	AF	SEA	Total	Emission
Wetlands	-	84	30	107	171	89	112	593	190
Biomass burning	-	4	0	4	30	43	25	105	35
Animals	-	23	30	14	80	43	110	301	97.0
Coal	-	36	27	77	20	52	114	324	103.0
Waste	-	32	43	16	30	39	116	276	88.0
Hydrates	-	-	-	20	-	-	-	20	6.0
Termites	59	-	-	-	-	-	-	59	20.0
Rice	103	-	-	-	-	-	-	103	34.0
<b>Total</b>	162	178	130	237	331	266	478	1782	
<b>Emission</b>	54.0	56.6	40.4	74.3	106.1	87.8	153.8		573.0

(b)	Global	NA	EU	AS	SA	AF	SEA	Total	Emission
Wetlands	-	4.7	1.7	6.0	9.6	5.0	6.3	33.3	33.2
Biomass burning	-	0.2	0.0	0.2	1.7	2.4	1.4	5.9	6.1
Animals	-	1.3	1.7	0.8	4.5	2.4	6.2	16.9	16.9
Coal	-	2.0	1.5	4.3	1.1	2.9	6.4	18.2	18.0
Waste	-	1.8	2.4	0.9	1.7	2.2	6.5	15.5	15.3
Hydrates	-	-	-	1.1	-	-	-	1.1	1.1
Termites	3.3	-	-	-	-	-	-	3.3	3.5
Rice	5.8	-	-	-	-	-	-	5.8	5.9
<b>Total</b>	9.1	10.0	7.2	13.3	18.6	14.9	26.8	100	
<b>Emission</b>	9.4	9.8	7.0	12.9	18.5	15.3	26.7		100

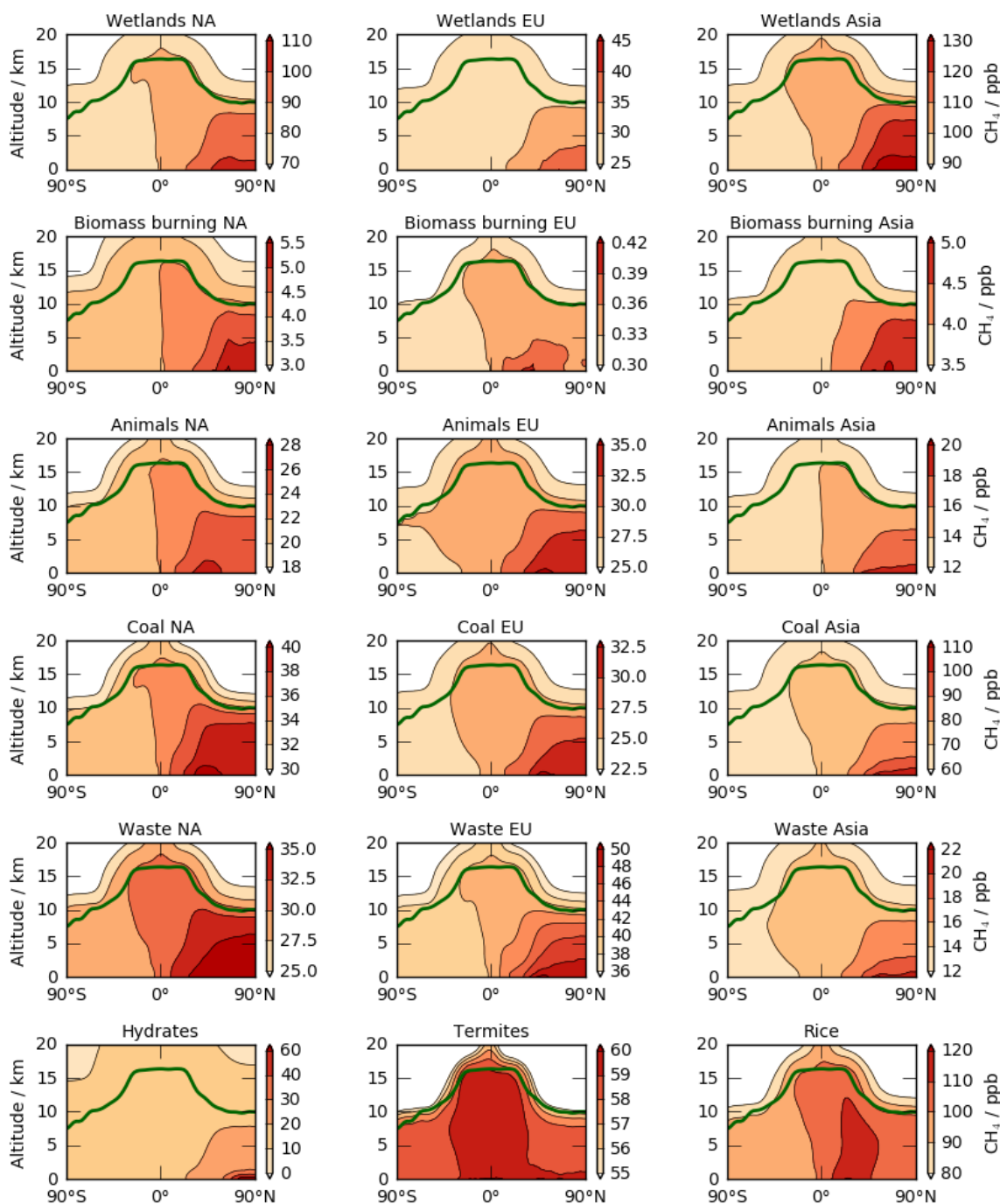
### 4.2.1 Zonally averaged methane tracers

Figure 4.2 shows all 33 zonally averaged annual mean tracer concentrations. All tracers decrease into the stratosphere where they have near identical zonal structures. This is due to the fact that tropospheric air, and thus all methane tracers, enters the stratosphere at roughly the same tropical location before it gets transported into and lost in the stratosphere [Brewer, 1949; Fueglistaler et al., 2005].

The tracers representing methane emitted from the Northern Hemisphere have very similar distributions but, unsurprisingly, show different absolute concentrations. Generally speaking, methane is highest in the lower troposphere in the high northern latitudes and decreases with altitude and into the Southern Hemisphere for wetlands, biomass burning, animals, coal and waste from North America, Europe and Asia.

It can be noted that methane from hydrates is localised at the surface in the high northern latitudes. A sharp vertical gradient is found with hydrate concentrations decreasing to zero in most of the free troposphere. Methane from termites is well mixed throughout the troposphere with only slightly higher concentrations in the tropics because of the uniform emission distributions (see Figure 3.4). The rice tracer shows higher concentrations in the Northern Hemisphere (100 ppb) than in the Southern Hemisphere (80 ppb) with maximum methane concentrations in the northern tropics where the emissions are located.

The tracers emitted from the tropical/Southern Hemispheric regions have dissimilar patterns to those emitted from the Northern Hemisphere. Tracers from South America show higher concentrations in the Southern Hemisphere than in the Northern Hemisphere (wetlands, biomass burning and animals and to a lesser extent waste). The South American coal tracer has highest concentrations in the tropics. The fields for South & East Asian wetlands and biomass burning, as well as African wetlands, animals and waste, also show highest concentrations in the tropics, likely due to the emissions being centered there. The African biomass burning tracer concentrations are slightly larger in the Southern than in the Northern Hemisphere. The other tracers (African coal as well as South & East Asian animals, coal and waste) show larger Northern Hemispheric concentrations.



**Fig. 4.2** Annual mean zonally averaged tracer concentrations (ppb) with source type separated into rows and source region into columns. Note the different scales for the individual graphs. The tropopause is depicted by the solid green line.

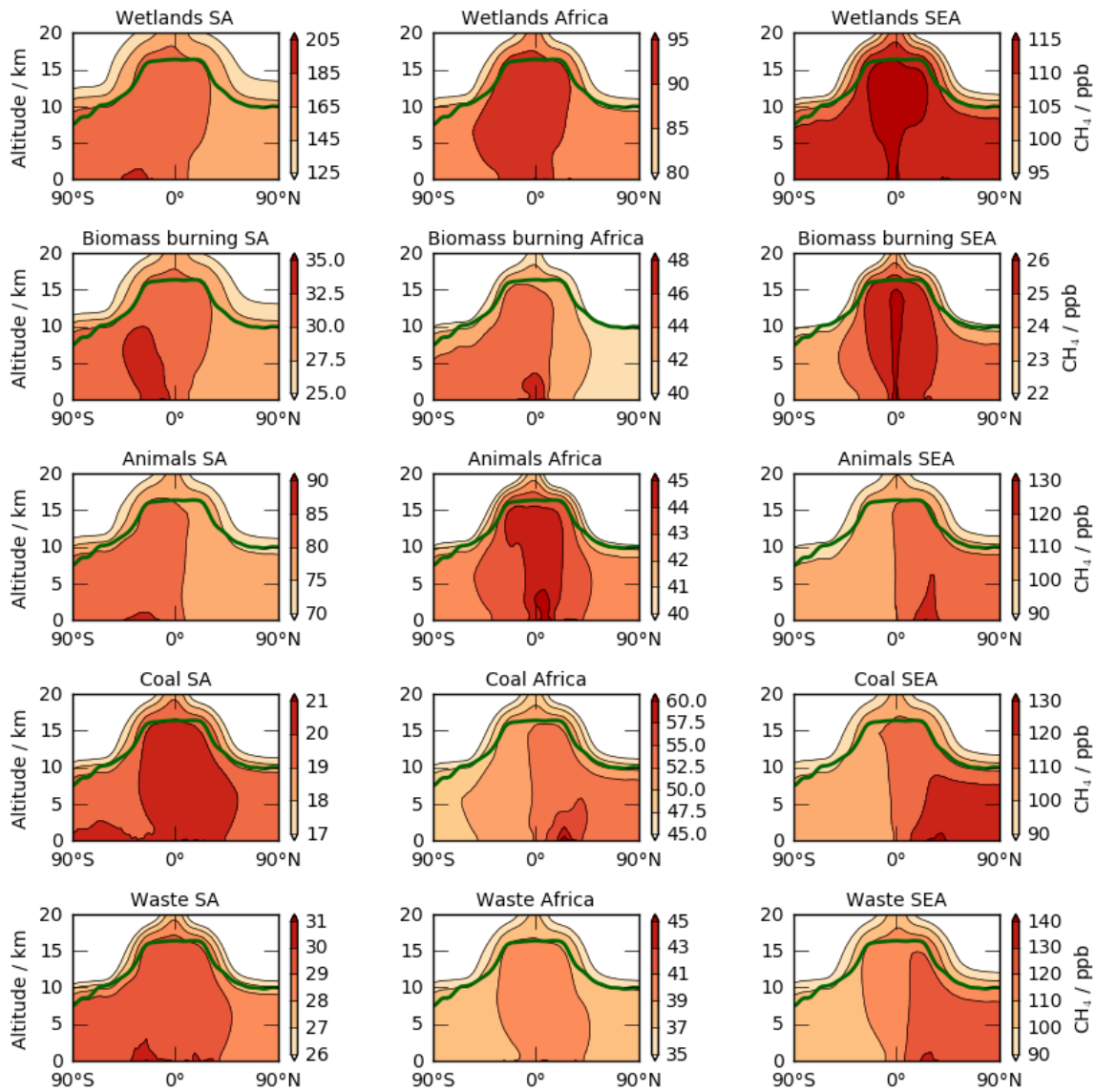


**Fig. 4.2 Continued.** Annual mean zonally averaged tracer concentrations (ppb) with source type separated into rows and source region into columns. Note the different scales for the individual graphs. The tropopause is depicted by the solid green line.

## 4.2.2 Contribution to the latitudinal gradient

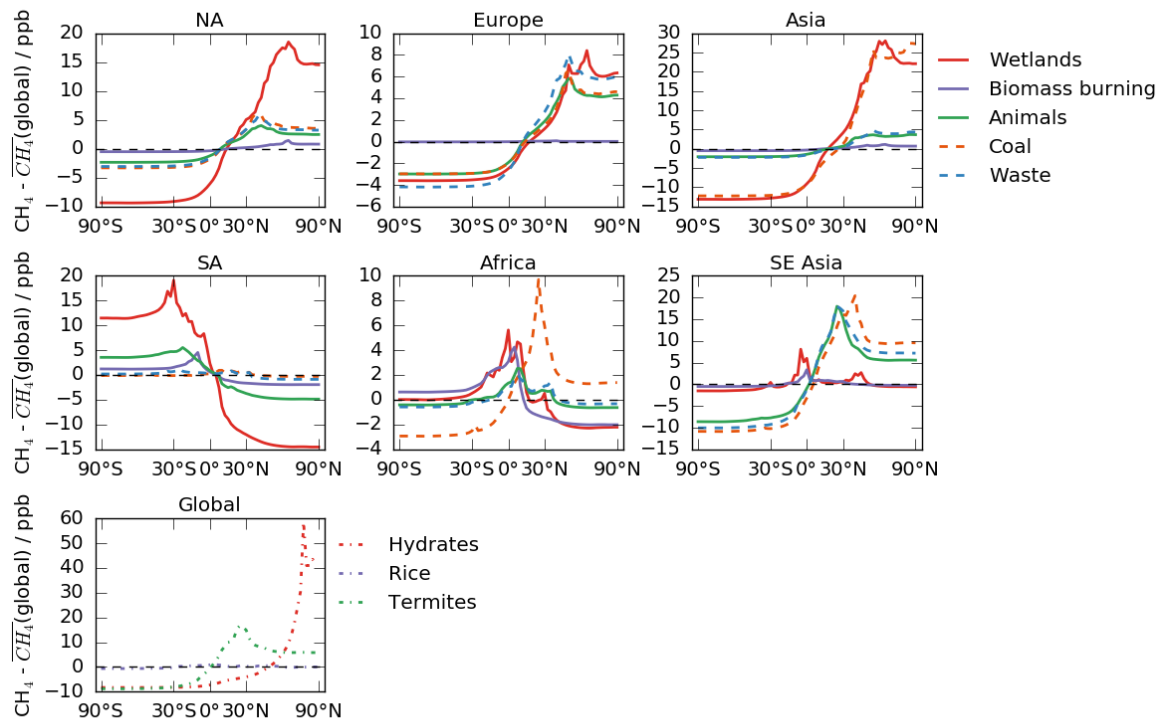
As shown in chapter 3 and mentioned above,  $\Delta\text{OH}$  global mean surface methane agrees well with observations from the NOAA surface network [Dlugokencky et al., 2016]. However, it was also shown that the modelled latitudinal gradient of methane is slightly overestimated with high biases in the Northern and low biases in the Southern Hemisphere (Figure 3.5). Here, the latitudinal gradient of the individual tracers is analysed with the ultimate aim to improve the methane representation in this model setup.

Figure 4.3 shows the latitudinal gradient for all 33 tracers relative to the respective global mean concentrations. To make the figure clearer it is split by region of emission and then shows the source types in different colours. As the hydrate, termite and rice tracers represent global emission fields, they are shown separately. Note that, contrary to the figures shown in the previous chapters, zonally averaged methane is presented and the model is not sampled at observational sites.

The hydrate tracer is associated with the largest latitudinal gradient (70 ppb, minimum to maximum) which is unsurprising because the emissions are highly localised in the high northern latitudes. In contrast, the rice tracer only shows variation of a few ppb with higher methane in the tropics, where the emissions are located. The termite tracer concentrations are higher in the Northern Hemisphere with a sharp increase north of  $10^\circ\text{S}$  and maximising around  $30^\circ\text{N}$ .

Similar patterns can be noted for the Northern Hemispheric tracers. The biomass burning tracers show barely any latitudinal variation which is intuitive as only a total of  $2.7 \text{ Tg}(\text{CH}_4) \text{ yr}^{-1}$  (8%, Table 4.1) gets emitted into these tracers. All other tracers show higher methane concentrations in the Northern Hemisphere. All European tracers, apart from biomass burning, show similar gradients of around 10 ppb (minimum to maximum) with maximum methane around  $40^\circ\text{N}$  (the wetland tracer peaks slightly further north). This magnitude and shape is also noticeable for North America but the wetland tracer here peaks around  $60^\circ\text{N}$  and shows a latitudinal gradient of 30 ppb (minimum to maximum). Over Asia, animal and waste tracers have slightly lower gradients compared to Europe and North America. Furthermore, they peak slightly further north which is linked to this region covering landmass further north than the other two regions. Both wetland and coal have a latitudinal gradient of 40 ppb with maximum methane between  $60^\circ\text{N}$  and  $90^\circ\text{N}$ .

As seen before (Figure 4.2), South American tracers are the only tracers from the tropical (and Southern Hemispheric) regions that show a reversed latitudinal gradient with larger



**Fig. 4.3** Latitudinal gradient for methane concentrations separated by source type and region relative to the respective global mean concentrations (ppb). The gradients for the five source types (wetlands, biomass burning, animals, coal and waste) are shown in different colours with individual graphs for each of the six emission regions (North America, Europe, Asia, South America, Africa and South & East Asia). The gradients for the hydrate, termite and rice tracers are shown in the last graph. Note the different scales for the individual graphs.

methane concentrations in the Southern Hemisphere. The South American wetland tracer has the largest latitudinal gradient of 35 ppb with a peak at 40°S. The shape is similar for the other South American tracers but the amplitude is smaller with 10 ppb for animals and 8 ppb for biomass burning while waste and coal show little latitudinal gradient.

Tracers emitted over Africa mostly maximise in the tropical region with equal methane in the Northern and Southern Hemispheric extra-tropics for animals and waste (3 ppb change in tropics relative to background) but lower methane in the Northern Hemisphere for wetlands and biomass burning (8 ppb minimum to maximum). The African coal tracer is the only tracer with higher Northern Hemispheric methane concentrations maximising around 30°N and showing a minimum to maximum difference of 12 ppb.

South & East Asian wetlands show highest methane concentrations in the tropics (8 ppb higher than in the Southern Hemisphere) and a second lower peak (4 ppb above Southern Hemispheric levels) around 40°N. The biomass burning tracer has a similar structure but a smaller amplitude. South & East Asian coal, animal and waste tracers have similar methane gradients with highest methane concentrations around 40°N and a minimum to maximum difference of 30 ppb. Their shape is similar to the rice tracer, which albeit initialised from a global emission field, has 90% of the emissions in the South & East Asian region.

These differences in the latitudinal gradients of the methane tracers can be used to reflect on the overall latitudinal gradient. As seen before, in order to improve the modelled latitudinal gradient of global methane, Southern Hemispheric methane concentrations are required to be higher and Northern Hemispheric methane concentrations to be lower. This analysis of the tracer latitudinal gradients shows that South American wetlands followed by animals are the most likely candidates for which emission increases would change the Southern Hemispheric methane concentrations. It is more difficult to single out a Northern Hemispheric emission source which would reduce Northern Hemispheric methane concentrations but with coal featuring prominently in the latitudinal gradients this might be an emission to focus on for emission reduction. Section 4.3 introduces a linear regression performed on the data in order to optimise the latitudinal gradient.

## 4.3 Optimising the latitudinal gradient

As outlined in chapter 3 the 33 methane tracers are summed to give the global total methane. This means that they can be scaled independently from each other. Analysis has shown that the latitudinal methane gradient in the  $\Delta\text{OH}$  experiment is overestimated. This section aims to improve this gradient by optimising the modelled data against observations using a local optimisation technique.

### 4.3.1 Linear regression of the tracers

Equation 4.1 denotes mathematically how the modelled total methane concentration  $\hat{y}$  at location  $j$ , dependent on time, latitude, longitude and height, is obtained through a linear combination of modelled methane mixing ratios  $x_{ij}$  multiplied with a global scaling parameter  $p_i$  for each tracer  $i$  (of a total of  $m$  tracers). The scaling parameters  $p_i$  equal one for all tracers

for the results discussed in chapter 3 and above. By changing  $p_i$  the source strength of the tracer  $i$  is altered.

$$\hat{y}_j = \sum_{i=1}^m p_i * x_{ij} \quad (4.1)$$

Due to the linearity in the individually modelled methane tracers and the possibility to scale them, the modelled methane mixing ratios ( $\hat{y}$ ) can be compared and optimised against observations ( $y$ ). Here, the model is optimised against the latitudinal gradient obtained from NOAA surface observations [Dlugokencky et al., 2016] (see Appendix A.3 for more information). The model is sampled at the corresponding model grid boxes to obtain the modelled latitudinal gradient and equation 4.1 is solved. A limited Broyden-Fletcher-Goldfarb-Shanno (BFGS [e.g Nocedal and Wright, 2006]) algorithm is subsequently used to optimise the least square errors (equation 4.2) between the modelled methane concentrations  $\hat{y}$  and the observations  $y$ . This optimisation changes the strength of the parameters  $p_i$  so that  $p_i = \frac{\text{optimised source strength } i}{\text{initial source strength } i}$ .

$$\text{error} = \sum_{j=1}^n (\hat{y}_j - y_j)^2 \quad (4.2)$$

The BFGS algorithm is a local optimisation method. Thus, the optimisation solution might depend on the choice of the initial parameters  $p_i$  which might accidentally form a local minimum. The optimisation (equation 4.2) is therefore calculated 1000 times for different initial parameters  $p_i$ . These initial parameters  $p_i$  are randomly chosen between zero and 10. This ensures that no negative emissions are included but also that the parameters are perturbed from their current state. Physically, a parameter  $p_i$  of the order of 10 does not make sense but perturbing them from their current state increases confidence that the optimisation solution is an overall minimum. The optimised parameters  $p_i$  are required to be greater or equal to zero to ensure that no negative emissions are included in the solutions.

The results of this linear regression do not converge to one solution when all 33 tracers are allowed to be scaled independently. This means that the optimisation method has too many degrees of freedom and that it finds many shallow minima close to each other. This is likely linked to the similar distributions (zonal mean and latitudinal gradient) that many tracers have. The simplicity of the linear regression function is likely unable to distinguish between those tracers that have similar features. Therefore, the solutions of these optimisations cannot be relied upon for a revised source strength. In order to optimise the latitudinal gradient with

the local optimisation technique introduced in this section a different approach is necessary which is discussed in the next section.

### 4.3.2 Regression by category

In section 4.2 it has been shown that the 33 tracers can be grouped by their global distribution (zonal mean and latitudinal gradient) into four categories:

- (I) **Northern Hemispheric tracers:** Tracers with higher methane concentrations in the Northern than in the Southern Hemisphere. All tracers emitted in North America, Europe and Asia as well as hydrates fall into this category, resulting in a total (initial) emission strength for this category of  $171 \text{ Tg}(\text{CH}_4) \text{ yr}^{-1}$ .
- (II) **Southern tropical tracers:** Tracers with higher methane concentrations in the Southern than in the Northern Hemisphere. South American wetlands, biomass burning, animals and waste as well as African biomass burning fall into this category with a total (initial) emission strength of  $114 \text{ Tg}(\text{CH}_4) \text{ yr}^{-1}$ .
- (III) **Tropical tracers:** Tracers with higher methane concentrations in the tropics which fall off into both hemispheres. These tracers are South American coal, African wetlands, animals and waste, South & East Asian wetlands and biomass burning and termites. The total (initial) emission strength for this category equals  $128 \text{ Tg}(\text{CH}_4) \text{ yr}^{-1}$ .
- (IV) **Northern tropical tracers:** Tracers with higher methane concentrations in the northern tropics which fall off towards the north and south. Tracers in this category are African coal, South & East Asian animals, coal and waste and rice with a total (initial) emission source strength of  $160 \text{ Tg}(\text{CH}_4) \text{ yr}^{-1}$ .

For this new optimisation, all tracers that fall into one category have the same scaling parameter  $p_i$  in equation 4.1. Equation 4.2 is then optimised with this new constraint, again for 1000 random initial parameters. These optimisations return one overall solution meaning it is likely that the local minimum found might indeed be the global minimum. Time did not allow further testing by increasing the number of optimisations performed and extending the range of the initial parameters. The present solution is given in Table 4.3. The coefficient of determination ( $R^2$ ) between  $\hat{y}$  and  $y$  for this solution is 0.97. Thus, the modelled (blue) and observed latitudinal gradient show excellent agreement (97 ppb for both) which can be seen in Figure 4.4.

**Table 4.3** Solution of the least square error optimisation for the four tracer categories.

	Category	$p_i$
I	Northern Hemisphere	0.83
II	Southern tropics	1.96
III	Tropics	0.39
IV	Northern tropics	0.98

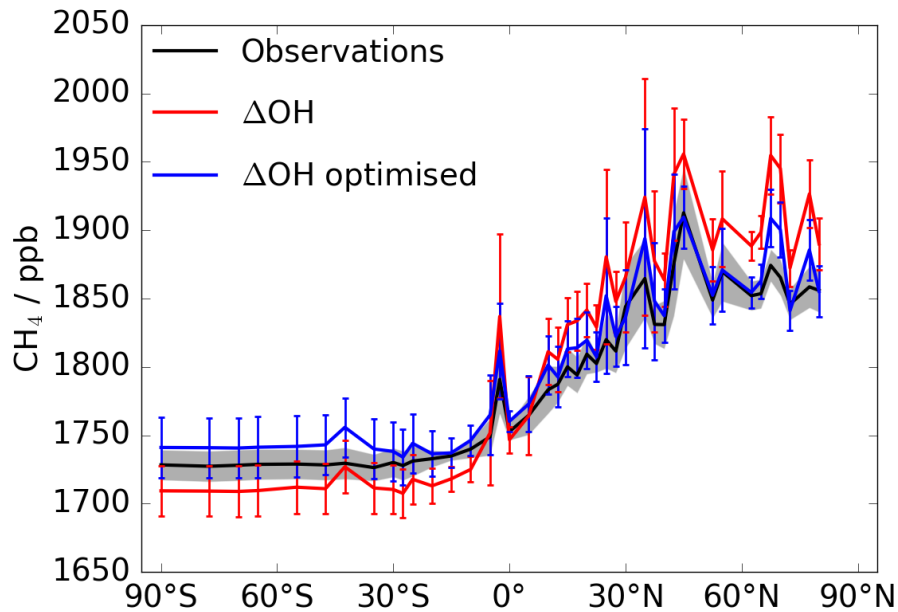


**Fig. 4.4** Latitudinal gradient for  $\Delta\text{OH}$  methane before (red) and after (blue) optimisation compared to observations [Dlugokencky et al., 2016] (black) in ppb. The observations are averaged between January 2000 and December 2005. Error bars and shading represent the  $1\sigma$  interval and indicate temporal and spatial variability at each latitude.

The global emission strength is nearly identical before and after the optimisation at  $573$  and  $572 \text{ Tg}(\text{CH}_4) \text{ yr}^{-1}$ , respectively. This is expected seeing the good agreement of the globally averaged methane concentrations between the model and the observations. Importantly, the optimisation confirms the earlier discussion that a methane emission redistribution into the (southern) tropical regions is necessary to match the latitudinal gradient. The speculation of chapter 3 and the suggestions in section 4.2 are supported by the optimisation results. Table 4.4 highlights that the South American wetland and animal tracers are indeed those with the highest emission change following optimisation making them overall the two largest methane emission contributors globally.

**Table 4.4** Methane emission strength ( $\text{Tg}(\text{CH}_4) \text{ yr}^{-1}$ ) for the 33 tracers before and after the optimisation. The tracers are colour coded according to their category as shown in Table 4.3. Note that the totals may not add up due to rounding errors.

Source	Region	Emission ( $\text{Tg}(\text{CH}_4) \text{ yr}^{-1}$ )	
		Before	After
Wetlands	<i>Total</i>	190	190
	NA	27	22
	EU	9	8
	AS	34	28
	SA	54	107
	AF	29	11
	SEA	37	14
Biomass burning	<i>Total</i>	35	53
	NA	1	1
	EU	0	0
	AS	1	1
	SA	10	20
	AF	14	28
	SEA	8	3
Animals	<i>Total</i>	97	109
	NA	7	6
	EU	9	8
	AS	5	4
	SA	26	51
	AF	14	6
	SEA	36	35
Coal	<i>Total</i>	103	91
	NA	11	9
	EU	8	7
	AS	24	20
	SA	6	3
	AF	17	17
	SEA	36	36
Waste	<i>Total</i>	88	84
	NA	10	8
	EU	13	11
	AS	5	4
	SA	9	19
	AF	13	5
	SEA	37	37
Hydrates		6	5
Termites		20	8
Rice		34	33
<b>Total</b>		<b>573</b>	<b>572</b>

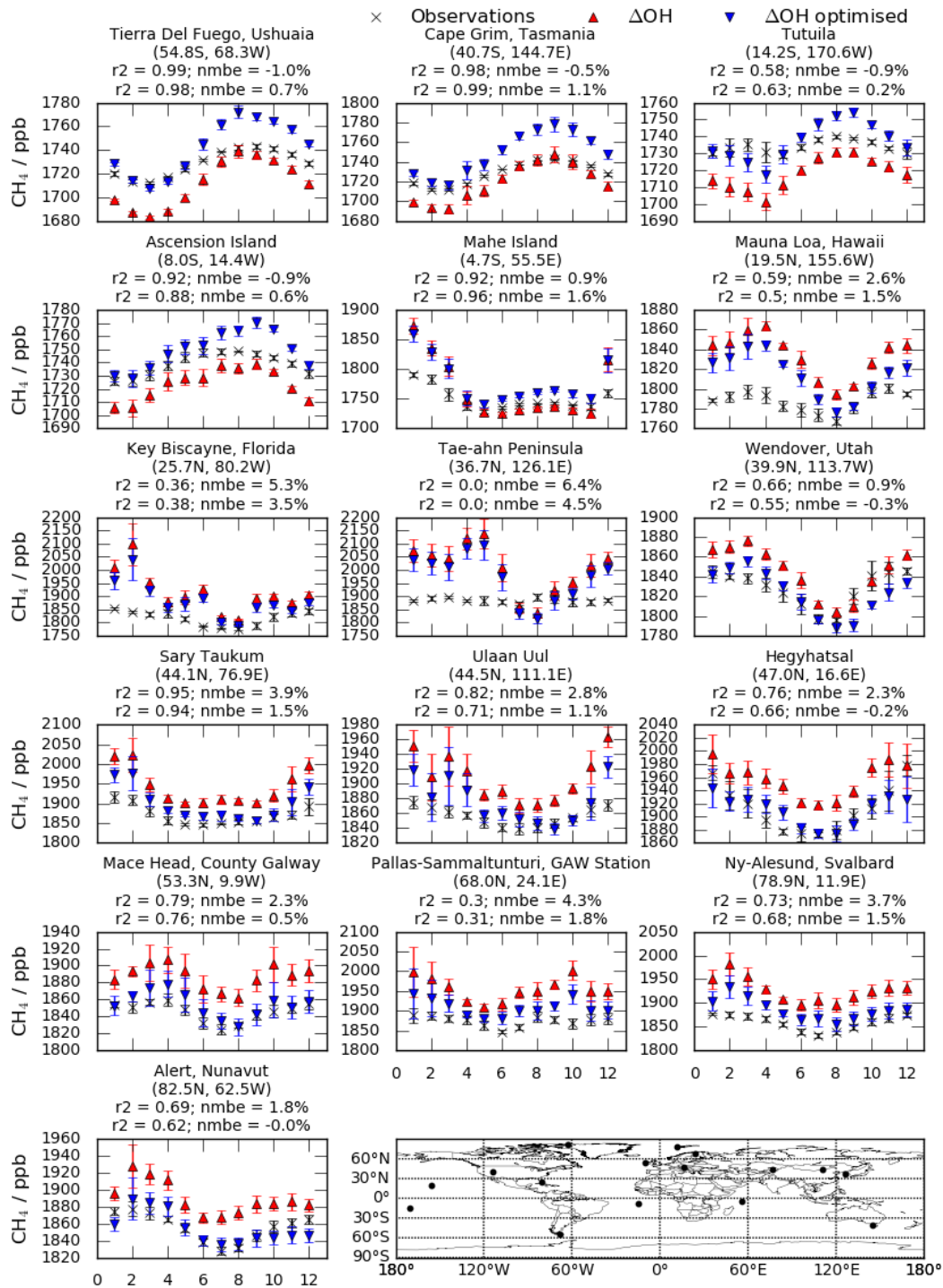


**Fig. 4.5** Comparison of surface methane levels with surface measurements (ppb) [Dlugokencky et al., 2016] (black) before (red) and after (blue) optimisation. The observations are averaged between January 2000 and December 2005. Error bars and shading represent the  $1\sigma$  interval and indicate temporal and spatial variability at each latitude. The map shows the measurement site locations used in this comparison. Note that the first (second) line gives the statistical information before (after) the optimisation.

Figure 4.5 shows the seasonal cycle for surface methane in comparison to surface measurements [Dlugokencky et al., 2016] for  $\Delta\text{OH}$  before (red) and after (blue) the optimisation. The agreement between the model and observations is improved by the optimisation for a number of stations, particularly in the Northern Hemisphere. However, the optimisation technique does not necessarily improve methane concentrations everywhere. This is unsurprising as it was chosen to optimise the latitudinal gradient in the model. Local effects such as the role played by movement of the inter tropical convergence zone at Mahe Island are not considered in the optimisation so such local improvements should not be expected. The example of Mahe Island is chosen as the station changes hemispheric character throughout the year [Dlugokencky et al., 1994a]. It is therefore particularly difficult to improve local methane in the model at that station.

## 4.4 Summary

Methane from the  $\Delta\text{OH}$  experiment introduced in chapter 3 has been analysed further in this chapter. In particular, this chapter explored how the linear chemistry in the prescribed oxidant scheme can be used to gain detailed information on methane from different sources (eight in total) and regions (six). The global distribution of 33 tracers highlighted that South American emissions are the main source of methane for the Southern Hemisphere. Analysis of the latitudinal gradient showed that South American wetlands in particular reduce the North-South gradient in atmospheric methane which was shown to be overestimated relative to observations in the previous chapter. Thus, increases in South American wetlands in particular are expected to improve the model's representation of methane.

The zonal distribution of the 33 tracers identified four distinct tracer types. These four tracer categories are those that show (I) higher Northern Hemispheric concentrations, (II) higher Southern Hemispheric concentrations, (III) highest tropical concentrations and (IV) strong northern tropics preference. This suggests that splitting methane into 33 tracers might not be necessary for future simulations but that a smaller number of tracers is sufficient.

A linear regression was performed with the aim to optimise the latitudinal gradient of  $\Delta\text{OH}$  methane. The optimisation did not converge to a global minimum when all 33 tracers were allowed to be scaled totally independently. Taking advantage of the four tracer categories identified above, the optimisation was constrained to only one scaling factor per category. With a large number of different initial conditions, all optimisation calculations then converged to one overall solution. This optimisation confirmed the overall source

strength of  $573 \text{ Tg}(\text{CH}_4) \text{ yr}^{-1}$  for the  $\Delta\text{OH}$  experiment. However, in order to improve the latitudinal gradient, reductions of Northern Hemispheric emissions and increases in Southern Hemispheric emissions (especially in South America) are required. The dominant role of South American wetlands in determining the latitudinal methane gradient was highlighted throughout this chapter.

Results in this chapter and the two previous chapters suggest that (i) the overall methane emission strength needs to be increased in order to match observations and (ii) that a redistribution of methane emissions into tropical regions is likely beneficial. The next chapter investigates the impact of changing methane emissions on atmospheric methane levels in the interactive model.

A local optimisation method was used to optimise the latitudinal gradient here. The fact that the number of tracers had to be reduced for the linear regression for it to converge to one overall solution might highlight the limitation of this local optimisation method. More involved optimisation techniques, i.e. global techniques (e.g. genetic algorithms), could lead to improved solutions. This was not explored further but could form the basis of a useful further investigation.



## 5 | Probing the atmospheric response to methane emission changes

Modelled methane in chapter 2 (Base) was low biased relative to observations. This can be caused by too large a tropospheric sink (OH) and/or insufficient methane emissions. The effect of different OH fields on atmospheric methane was probed in chapter 3, using a newly developed chemistry scheme with prescribed oxidant fields. The analysis showed that reducing the tropospheric oxidative capacity improved methane levels but that the latitudinal methane gradient was then overestimated ( $\Delta\text{OH}$ ). In chapter 4 the latitudinal gradient of  $\Delta\text{OH}$  methane was optimised with a BFGS-algorithm, and results showed that a redistribution of methane emissions from the Northern Hemisphere into the tropics (South America) dramatically improved the latitudinal gradient.

In this chapter both the methane emission strength and the source distribution are altered and its effect on atmospheric methane assessed. The new emission estimate draws on all analyses presented in the previous chapters, resulting in a redistribution of methane emissions from the northern extra-tropical into tropical regions.

Section 5.1 discusses the geographical distribution of modified methane emissions and their seasonal cycles, highlighting differences to the Base emission scenario. Section 5.2 then quantifies the consequences of this emission change on interactive methane and OH (section 5.3). In section 5.4 an analysis of methane impacts on ozone, CO and  $\text{NO}_x$  is presented highlighting the non-linearity of atmospheric chemistry. The impact on methane levels of altering both the tropospheric OH sink and methane emissions is then discussed in section 5.5 before conclusions are given in section 5.6.

## 5.1 Model setup

The model as outlined in chapter 2 was used with the extended chemistry scheme described in chapter 3. An experiment was performed in which methane emissions were altered, this being the only difference to the Base and  $\Delta\text{OH}$  experiments – these changes are described here.

These additional experiments allow the effect of geographical emission distribution changes upon atmospheric methane to be examined. The data from these experiments will be referred to as  $\Delta\text{ems}$  and  $\Delta(\text{ems}+\text{OH})$ . Table 5.1 summarises the four experiments discussed in this chapter.

**Table 5.1** Experiments to probe the effect of changing methane emissions (strength and geographical distribution), changing OH distributions and (non-)interactive chemistry on atmospheric methane.

	Interactive OH field	Prescribed OH field
Base methane emissions (chapter 2, 3)	Base	$\Delta\text{OH}$
Alternative methane emission estimate	$\Delta\text{ems}$	$\Delta(\text{ems}+\text{OH})$

### 5.1.1 Methane emissions

The methane emissions used in the Base and  $\Delta\text{OH}$  experiments amounted to 548 Tg(CH<sub>4</sub>) yr<sup>-1</sup> with 322 Tg(CH<sub>4</sub>) yr<sup>-1</sup> (59%) from anthropogenic [EC-JRC/PBL, 2011], 35 Tg(CH<sub>4</sub>) yr<sup>-1</sup> (6%) from biomass burning [van der Werf et al., 2010], and 190 Tg(CH<sub>4</sub>) yr<sup>-1</sup> (35%), 6 Tg(CH<sub>4</sub>) yr<sup>-1</sup> (1%) and 20 Tg(CH<sub>4</sub>) yr<sup>-1</sup> (4%) from wetlands [Fung et al., 1991; Patra et al., 2010; Melton et al., 2013], hydrates and termite emissions [Fung et al., 1991], respectively. Furthermore, a soil sink of 25 Tg(CH<sub>4</sub>) yr<sup>-1</sup> (-5%) was included [Fung et al., 1991]. These emissions led to a methane low bias in the Base experiment (chapter 2) by 160 ppb (9%) while the latitudinal gradient sampled in grid boxes closest to measurement stations agreed well with observations [Dlugokencky et al., 2016]). In chapter 3, it was shown that a change in the OH field improved methane concentration but that the latitudinal gradient was overestimated (experiment  $\Delta\text{OH}$ ). Alternatively, the low bias of Base methane may have been caused by

an underestimation of the methane emission strength. Therefore, alternative estimates for methane emissions were examined.

Anthropogenic methane emissions recommended for the Coupled Model Intercomparison Project Phase 5 (CMIP5), at  $275 \text{ Tg}(\text{CH}_4) \text{ yr}^{-1}$ , were found to be lower than the estimate used for Base ( $322 \text{ Tg}(\text{CH}_4) \text{ yr}^{-1}$ ). The CMIP5 emissions therefore result in less emissions into the Northern Hemisphere where the bulk of anthropogenic emissions is located. These CMIP5 emissions, which originate from the database compiled by Lamarque et al. [2010], show no seasonal variation for coal emissions [Gurney et al., 2005] contrary to the Base emissions. As shown in chapter 3, the latitudinal gradient was overestimated for both non-interactive experiments discussed in that chapter, meaning that modelled Northern Hemispheric methane was (relatively) high biased. A reduction in anthropogenic methane from these regions is therefore welcomed for this new experiment and supported by analysis shown in chapter 4. Thus, it was decided to use the CMIP5 anthropogenic emission estimate for the  $\Delta\text{ems}$  experiment.

To be consistent within the experiment, the CMIP5 recommendations were also followed for the biomass burning emissions, which are seasonally varying and originate from the van der Werf et al. [2010] estimate. These biomass burning emissions have effectively the same geographical distribution but a lower strength compared to Base.

However, no recommended CMIP5 emission database exists for natural emissions requiring other data sources for methane emissions from wetlands, hydrates and termites. It was decided to keep the same emissions for hydrate and termites as in the Base experiment [Fung et al., 1991]; there is no work in the literature arguing for a change in these values. Furthermore, the soil sink was removed in the  $\Delta\text{ems}$  experiment. No recommendation for a soil sink is found in the CMIP5 dataset and the soil sink reduces methane emission even further.

With these changes (ignoring soil), methane emissions are reduced compared to the Base experiment. The methane low biased in Base suggests however that the total methane emissions need to be increased in  $\Delta\text{ems}$ . With large uncertainties in the absolute wetland emissions ( $177 - 284 \text{ Tg}(\text{CH}_4) \text{ yr}^{-1}$ , Kirschke et al. [2013]) it was deemed appropriate to increase the wetland flux for  $\Delta\text{ems}$ .

On comparing wetland emissions from the WETCHIMP intercomparison project [Melton et al., 2013], it was decided to make two changes: (i) increasing the tropical wetland flux and

decreasing emissions from boreal wetlands which is supported by findings in chapter 4, and (ii) increasing the overall wetland emission strength.

*(i) Distribution of wetland emissions*

Melton et al. [2013] estimated emissions from wetlands in the northern extra-tropics ( $>35^{\circ}\text{N}$ ) to contribute 27% to the global wetland flux (multi-model mean). In the Base experiment, identical to the TransCom-CH<sub>4</sub> intercomparison project (see chapter 2), this ratio is higher (37%). So, while the geographical distribution of the Fung et al. [1991] wetland estimate was kept for this experiment, the ratio of the boreal to tropical wetland emission strength was altered. Effectively, the wetland methane emissions were shifted from the northern extra-tropics into the tropics. This means that the boreal wetlands (tundra and bogs) were scaled separately from the swamps. This decision is further backed up by the analysis of the latitudinal methane gradient for both non-interactive experiments in chapter 3 and the optimisation introduced in chapter 4.

*(ii) Magnitude of wetland emissions*

The wetland emission strength estimates from the WETCHIMP project [Melton et al., 2013] were studied and it was decided to increase this experiment's emission flux to the ORCHIDEE emission strength which showed the largest overall fluxes of all participating models. Thus, the boreal wetland fluxes (tundra and bogs) were scaled to  $72 \text{ Tg}(\text{CH}_4) \text{ yr}^{-1}$  and the swamp emissions to  $187 \text{ Tg}(\text{CH}_4) \text{ yr}^{-1}$ . This resulted in total methane wetland emissions of  $259 \text{ Tg}(\text{CH}_4) \text{ yr}^{-1}$ , 28% of which come from the northern extra-tropics.

Table 5.2 summarises the methane emissions for Base and  $\Delta\text{ems}$  and highlights the difference between the two estimates. The anthropogenic emissions in  $\Delta\text{ems}$  are 15% lower than in Base while wetland emissions have increased by 36%, their strength nearly equalling the total strength of all anthropogenic emissions in  $\Delta\text{ems}$ . As a result, the total methane emissions are  $37 \text{ Tg}(\text{CH}_4) \text{ yr}^{-1}$  (7%) higher in the  $\Delta\text{ems}$  experiment compared to Base. Mass balance suggests that the global methane concentration in the  $\Delta\text{ems}$  experiment should now be approximately 1816 ppb, following equation 5.1. This would be in good agreement with observations [Dlugokencky et al., 2016]. A 7% methane self-feedback has been included based on the feedback factor calculated for CheST in UKCA [Fuglestedt et al., 1999; Banerjee et al., 2014].

$$[\text{CH}_4] = \frac{585 \text{ Tg}(\text{CH}_4) \text{ yr}^{-1}}{548 \text{ Tg}(\text{CH}_4) \text{ yr}^{-1}} \times 1590 \text{ ppb} \times 1.07 = 1816 \text{ ppb} \quad (5.1)$$

**Table 5.2** Methane emissions in  $\text{Tg}(\text{CH}_4) \text{ yr}^{-1}$  for the  $\Delta\text{ems}$  and Base emission scenarios. The last column indicates the absolute ( $\text{Tg}(\text{CH}_4) \text{ yr}^{-1}$ ) and relative (%) difference between the two estimates ( $\Delta\text{ems} - \text{Base}$ ).

Source	Strength ( $\text{Tg}(\text{CH}_4) \text{ yr}^{-1}$ )		$\Delta\text{ems} - \text{Base}$	
	Base	$\Delta\text{ems}$	( $\text{Tg}(\text{CH}_4) \text{ yr}^{-1}$ )	(%)
Anthropogenic	322	275	-47	-15%
Biomass burning	35	25	-10	-29%
Wetlands	190	259	+69	+36%
Other biogenic	26	26	0	0
Soil sink	-25	0	+25	-100%
Total	548	585	+37	+7%

Figures 5.1 to 5.3 compare the Base and  $\Delta\text{ems}$  emission estimates. Figure 5.1 shows that methane emissions for the  $\Delta\text{ems}$  experiments are lower in the northern mid-latitudes ( $30^\circ\text{N}$  to  $60^\circ\text{N}$ ) compared to Base experiments, while tropical emissions are slightly larger. This is explained by the decreased anthropogenic emissions in the northern mid-latitudes and the increased tropical wetland emissions. The decrease in tropical biomass burning emissions is only  $3 \text{ Tg}(\text{CH}_4) \text{ yr}^{-1}$  and is thus masked by the increased wetland emissions.

Figure 5.2 highlights that changes to the longitudinal distribution of methane emissions are minimal. Anthropogenic emissions decrease nearly everywhere apart from a peak around  $70^\circ\text{E}$  which sees a small increase. Biomass burning emissions are lower globally for  $\Delta\text{ems}$  compared to Base with small increases between  $120^\circ\text{E}$  and  $150^\circ\text{E}$ . The wetland emission total has increased in  $\Delta\text{ems}$ , distributed evenly along the longitudes. Termite and hydrate emissions are not changed.

The seasonality of the methane emission is different for Base and  $\Delta\text{ems}$  (see Figure 5.3). Emissions are slightly lower between November and March for  $\Delta\text{ems}$  which can be linked to the absence of a seasonal cycle for coal and gas emissions while these emissions in the Base experiment maximise and minimise in Northern Hemispheric winter and summer, respectively (section 2.2, Gurney et al. [2005]).

Emissions between March and November are higher for  $\Delta\text{ems}$  compared to Base and a sharper increase in methane emissions can be noted between April and June. This is linked to increased wetland emissions in  $\Delta\text{ems}$ . The biomass burning emission seasonal cycle is less pronounced in  $\Delta\text{ems}$  ( $2 \text{ Tg}(\text{CH}_4) \text{ yr}^{-1}$  difference between minimum and maximum emissions) compared to Base ( $6 \text{ Tg}(\text{CH}_4) \text{ yr}^{-1}$  difference).

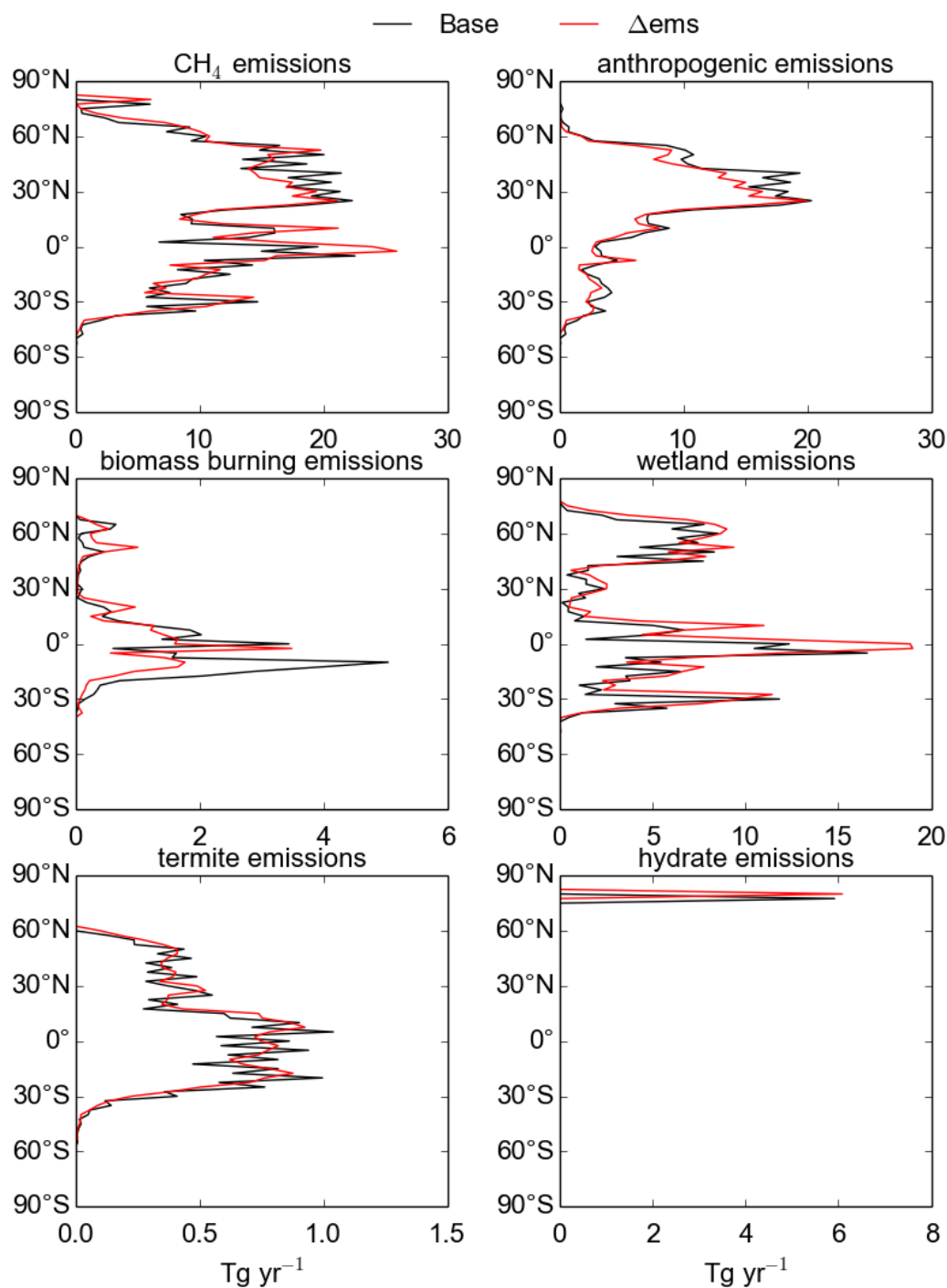


**Fig. 5.1** Comparison of the latitudinal distribution of the  $\Delta\text{ems}$  (red) and Base (black) methane emissions ( $\text{Tg}(\text{CH}_4) \text{ yr}^{-1}$ ). From the top left to the bottom right: Total methane emissions, anthropogenic emissions, biomass burning emissions, wetland emissions, termite emissions and hydrate emissions. Note the different scale for the graphs.

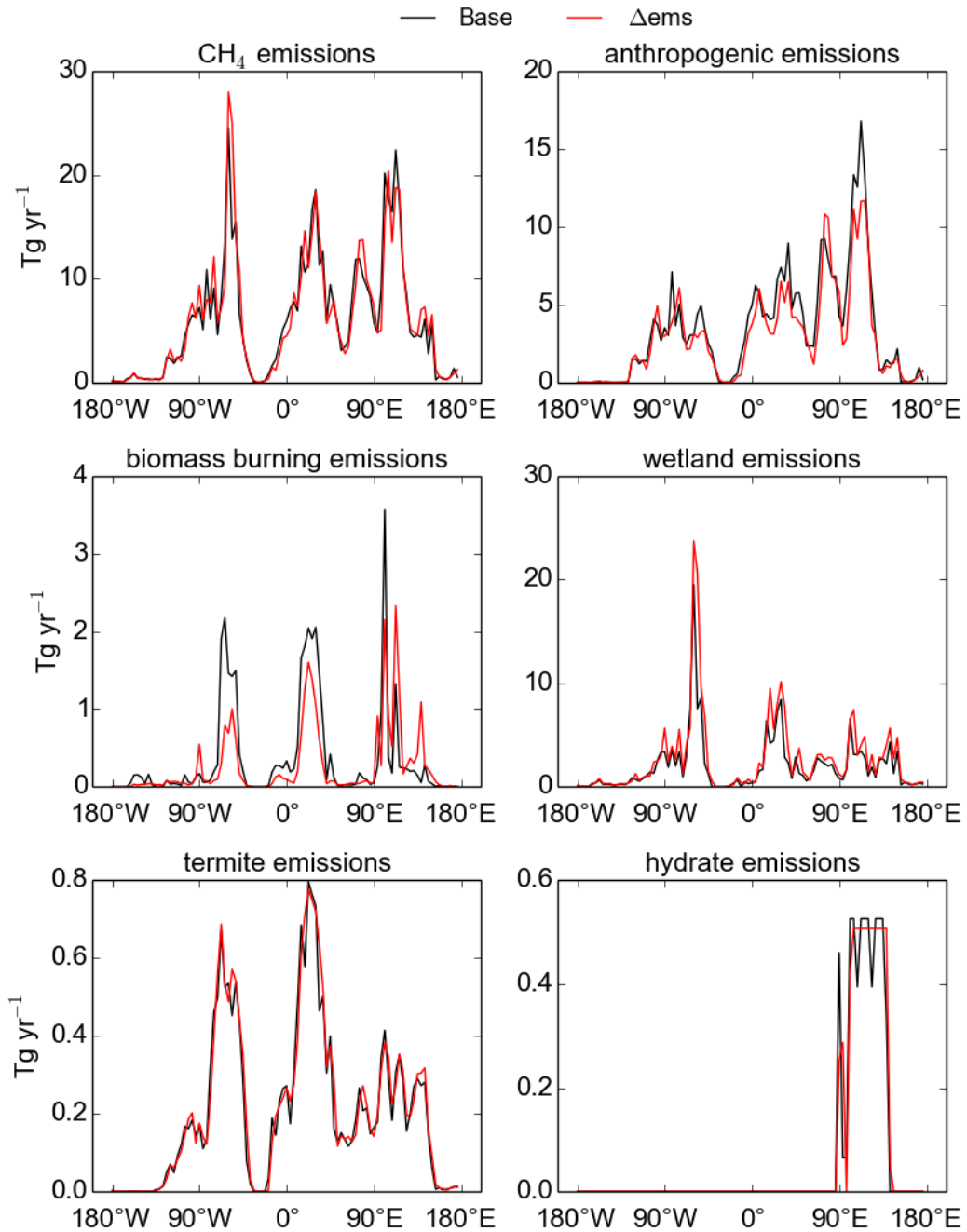


**Fig. 5.2** Comparison of the longitudinal distribution of the  $\Delta$ ems (red) and Base (black) methane emissions (Tg(CH<sub>4</sub>) yr<sup>-1</sup>). From the top left to the bottom right: Total methane emissions, anthropogenic emissions, biomass burning emissions, wetland emissions, termite emissions and hydrate emissions. Note the different scale for the graphs.

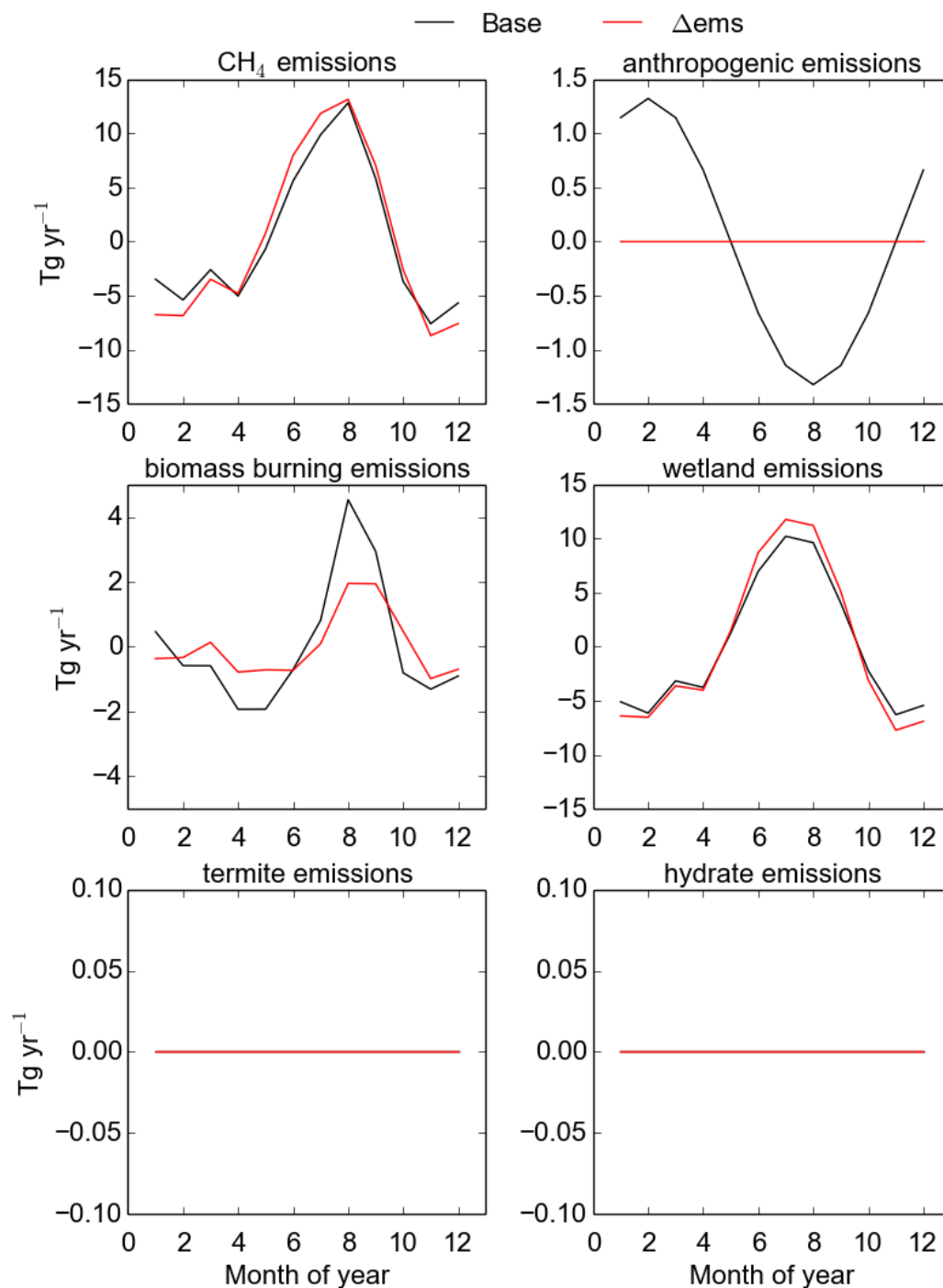


**Fig. 5.3** Comparison of the seasonal cycle of the  $\Delta$ ems (red) and Base (black) methane emissions (Tg(CH<sub>4</sub>) yr<sup>-1</sup>). The graphs show the change in emissions around the annual mean emission. From the top left to the bottom right: Total methane emissions, anthropogenic emissions, biomass burning emissions, wetland emissions, termite emissions and hydrate emissions. Note the different scale for the figures.

## 5.2 Interactive methane

Modelled  $\Delta$ ems methane now shows excellent agreement with NOAA surface flask measurements [Dlugokencky et al., 2016] (averaged between January 2000 and December 2005) which can be seen in Figure 5.4. Also shown on this figure is the latitudinal gradient of methane for the Base experiment discussed in chapter 2. Note that the model is sampled in the grid boxes closest to the surface measurement stations.

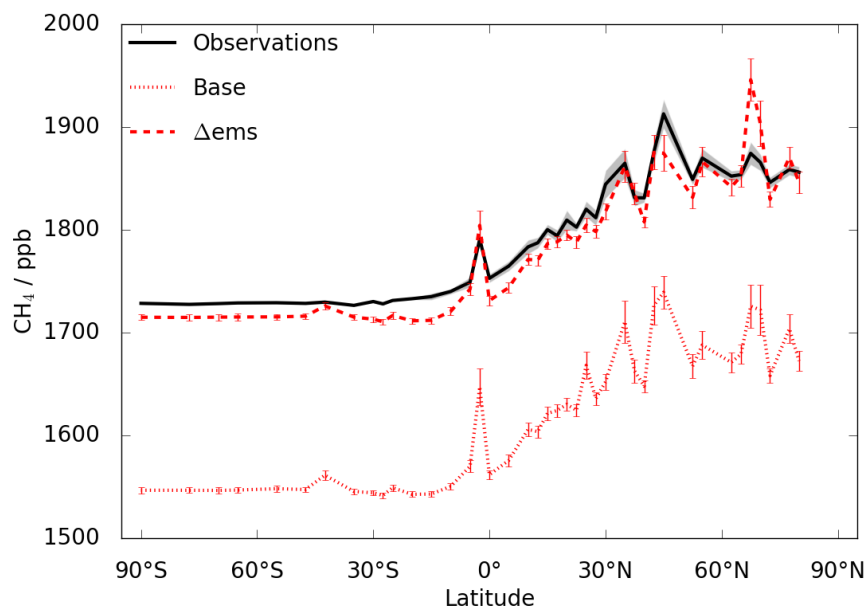


**Fig. 5.4** Latitudinal gradient for  $\Delta$ ems methane (red dashed) and Base methane (red dotted) compared to NOAA surface observations [Dlugokencky et al., 2016] (black). The observations are averaged between January 2000 and December 2005. Error bars and shading represent the  $1\sigma$  interval and indicate temporal and spatial variability at each latitude.

Surface concentrations for  $\Delta$ ems average to 1785 ppb, which is 195 ppb higher than Base methane and agrees extremely well with observations (1780 ppb). This is remarkable as other modelling studies either prescribe methane concentrations or scale their methane concentrations after the simulation to match observations [e.g Dalsøren et al., 2016].  $\Delta$ ems surface methane concentrations are 30 ppb lower than predicted from the emission strength increase (mass balance with a 7% self-feedback, equation 5.1). This difference to the prediction likely originates from the shift of methane emissions towards the tropics. In  $\Delta$ ems more methane is emitted into the sink dominated regions resulting in slightly lower

overall methane concentrations than expected from an emission increase without changing the geographical distribution. Modelled methane reproduces the observed latitudinal gradient of methane well, reflected in a high correlation coefficient between  $\Delta$ ems and observations (similar to the Base latitudinal gradient).

Figure 5.5 shows high correlations between modelled and observed surface methane concentrations at a number of sites located across the globe with small normalised mean bias errors. The observed methane seasonal cycle is especially well captured at remote Southern Hemispheric stations with slight underestimations of absolute methane levels. At Mahe Island, Seychelles, it can be noted that Northern Hemispheric methane (December to April) is high biased in the model while Southern Hemispheric methane (April to November) agrees well with the observations. The Arctic sites Pallas, Ny-Alesund (Zeppelin) and Alert stand out from the general good agreement between modelled and observed methane in the Northern Hemisphere. The seasonal cycle at these stations is not well represented by the model. At Pallas and Ny-Alesund summertime modelled methane increases are too large and too early in the year. This phenomenon was noted by Warwick et al. [2016] who showed that delaying wetland emissions by one month improved the seasonal cycle drastically.

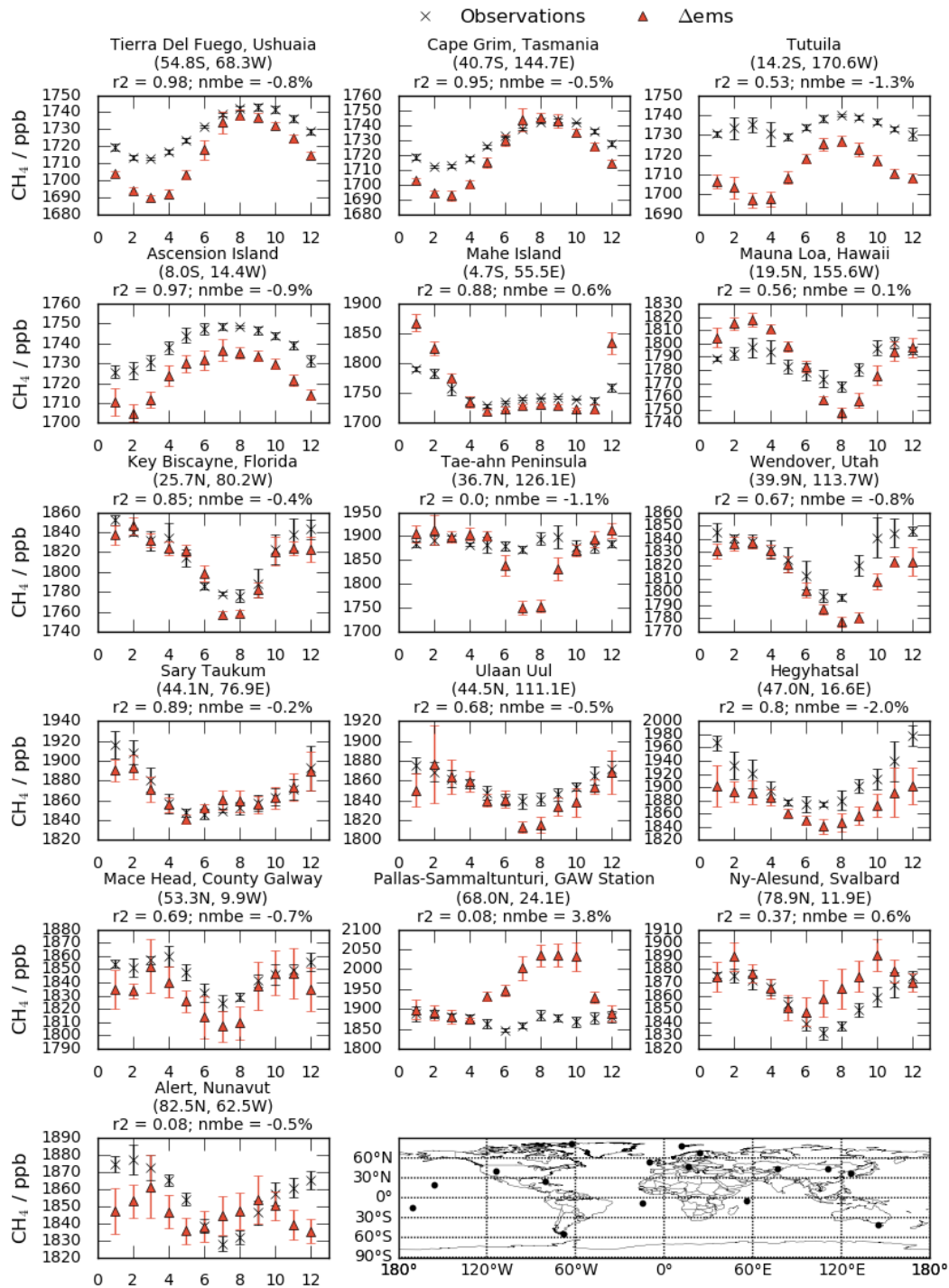


**Fig. 5.5** Comparison of Base surface methane levels with surface measurements (ppb) [Dlugokencky et al., 2016]. The observations are averaged between January 2000 and December 2005. Error bars and shading represent the  $1\sigma$  interval and indicate temporal and spatial variability at each latitude. The map shows the measurement site locations used in this comparison.

Table 5.3 compares some of the key atmospheric variables for methane from the  $\Delta$ ems and the Base experiment. It can be seen that the 7% increase in methane emissions led to an 11% increase in methane concentrations. This increase, greater than a pure mass balance would suggest, highlights the impact of the methane self-feedback on atmospheric levels. This phenomenon has been previously noted in the literature [e.g Isaksen and Hov, 1987; Prather, 1994, 1996; Fuglestedt et al., 1999]. It was also included in the prediction for atmospheric methane levels due to the emission increase in equation 5.1.

**Table 5.3** Comparison of key atmospheric methane variables for Base and  $\Delta$ ems. The last column indicates the percentage difference between  $\Delta$ ems and Base (%).

Key atmospheric variables	Base	$\Delta$ ems	$\Delta$ ems – Base
Tropospheric global mean CH <sub>4</sub> (ppb)	1590	1760	+11%
Atmospheric CH <sub>4</sub> burden (Tg(CH <sub>4</sub> ))	4325	4789	+11%
OH + CH <sub>4</sub> flux (Tg(CH <sub>4</sub> ) yr <sup>-1</sup> )	526	560	+6%
$\tau_{\text{OH} + \text{CH}_4}$ (years)	8.2	8.6	+4%
Tropospheric OH ( $10^5$ molecules cm <sup>-3</sup> )	12.4	12.0	-3%

Table 5.3 shows that the flux through the reaction of methane and OH has increased by 7%. This, coupled with the 11% increase in the atmospheric methane burden results in a 4% increase in the methane lifetime to 8.6 years for the  $\Delta$ ems experiment. This brings the modelled tropospheric lifetime closer to the ACCMIP multi-model mean ( $9.3 \pm 0.9$  years [Voulgarakis et al., 2013]) but it remains outside observational estimates ( $11.2 \pm 1.3$  years [Prather et al., 2012]). Tropospheric OH concentrations are 3% smaller in  $\Delta$ ems compared to Base and will be discussed more in the next section. The  $\Delta$ ems methane lifetime and OH concentration thus still follow the same relationship established from the ACCMIP models (Figure 5.6).

The increase in methane emissions to 585 Tg(CH<sub>4</sub>) yr<sup>-1</sup> and the shift to larger tropical emissions has thus resulted in an excellent model representation of atmospheric methane. The fact that the methane lifetime still does not overlap with observational estimates while the model reproduces the methane distribution well highlights that the lifetime cannot, on its own, be used to evaluate the model's ability to simulate methane. Furthermore, the excellent agreement between modelled and observed methane despite the short methane lifetime and the large hydroxyl radical concentrations (see next section) strengthens the hypothesis of chapter 2, that the model's CO low bias strongly affects (increases) the modelled OH field.

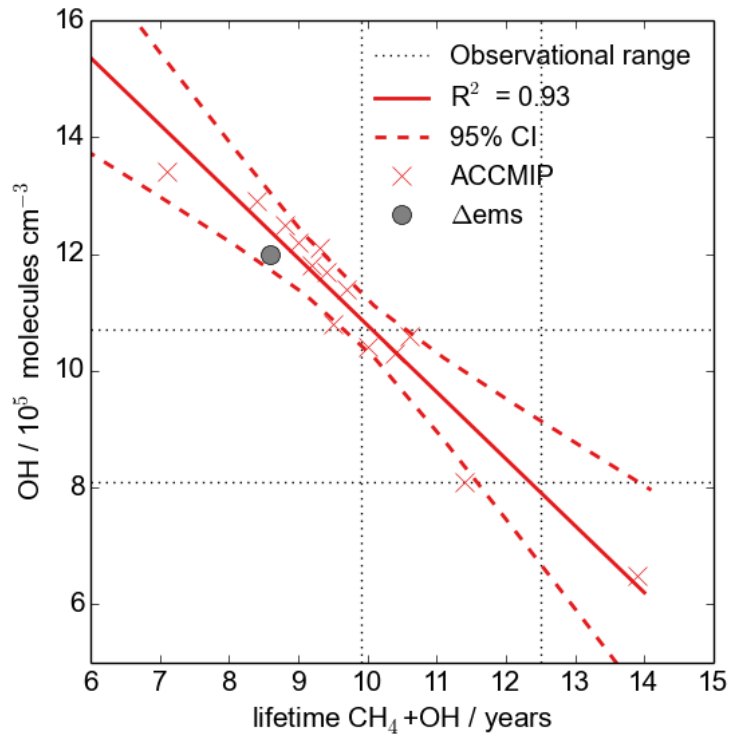


**Fig. 5.6** Relationship between methane lifetime with respect to tropospheric OH loss (years) and tropospheric OH concentrations ( $10^5$  molecules  $\text{cm}^{-3}$ ) for the ACCMIP models [Voulgarakis et al., 2013] (red crosses), Base (grey diamond) and  $\Delta\text{ems}$  (grey circle). The observational estimates for the methane lifetime [Prather et al., 2012] and the global mean OH concentrations [Prinn et al., 2001] are indicated by the black dotted lines.

With the good agreement between modelled and observed methane,  $\Delta\text{ems}$  is suitable as a baseline experiment to investigate future climate impacts on methane and methane's impact on future climate and composition. This will be explored in more detail in the next chapter.

### 5.3 Interactive hydroxyl radical

As mentioned above, the methane emission changes affect tropospheric OH abundance, decreasing the annually averaged (airmass-weighted) tropospheric OH field to  $12.0 \times 10^5$  molecules  $\text{cm}^{-3}$  (3% reduction relative to Base). However, the  $\Delta\text{ems}$  OH field remains larger than estimated from methyl chloroform observations ( $9.4 \pm 1.3 \times 10^5$  molecules  $\text{cm}^{-3}$  [Prinn et al., 2001]).

Table 5.4 summarises annual mean airmass-weighted OH concentrations in the twelve subregions suggested by Lawrence et al. [2001].  $\Delta\text{ems}$  OH is lower throughout the troposphere compared to Base, with the largest relative difference at the surface in the Southern Hemisphere (5%) and the smallest difference in the middle Southern Hemispheric troposphere (750 – 500 hPa, 1.9%). In the tropics,  $\Delta\text{ems}$  OH is ca. 4% lower than Base OH. This is the region with the largest absolute difference, maximising at the surface to  $0.9 \times 10^5$  molecules  $\text{cm}^{-3}$ . In the Northern Hemisphere the differences are largest at the surface and decrease with altitude.

**Table 5.4** Lawrence et al. [2001] analysis of annual mean airmass-weighted [OH] in  $10^5$  molecules  $\text{cm}^{-3}$ . First row:  $\Delta\text{ems}$ ; second row: Base; third row: percentage difference between the  $\Delta\text{ems}$  and the Base OH fields.

Altitude	Interactive model	90°S – 30°S	30°S – 0°	0° – 30°N	30°N – 90°N
500	$\Delta\text{ems}$	4.8	11.6	12.8	8.1
– 250	Base	5.0	12.0	13.2	8.3
hPa	% difference	-4.0%	-3.3%	-3.0%	-2.4%
750	$\Delta\text{ems}$	5.0	16.2	18.1	10.2
– 500	Base	5.3	16.8	18.8	10.5
hPa	% difference	-5.7%	-3.6%	-3.7%	-2.9%
Surface	$\Delta\text{ems}$	5.7	18.1	21.6	12.4
– 750	Base	6.0	18.9	22.4	12.8
hPa	% difference	-5.0%	-4.2%	-3.6%	-3.1%

Figure 5.7 shows the seasonal variation of airmass-weighted OH concentrations in the twelve tropospheric subregions suggested by Lawrence et al. [2001] for Base and  $\Delta\text{ems}$ . The  $\Delta\text{ems}$  OH concentrations are smaller throughout the year in all subregions. The difference is largest in the tropics, maximising between September and November in the Southern Hemisphere. In the Northern Hemisphere the largest differences can be seen in the first half

of the calendar year, likely linked to the different seasonality of the coal and gas methane emissions.

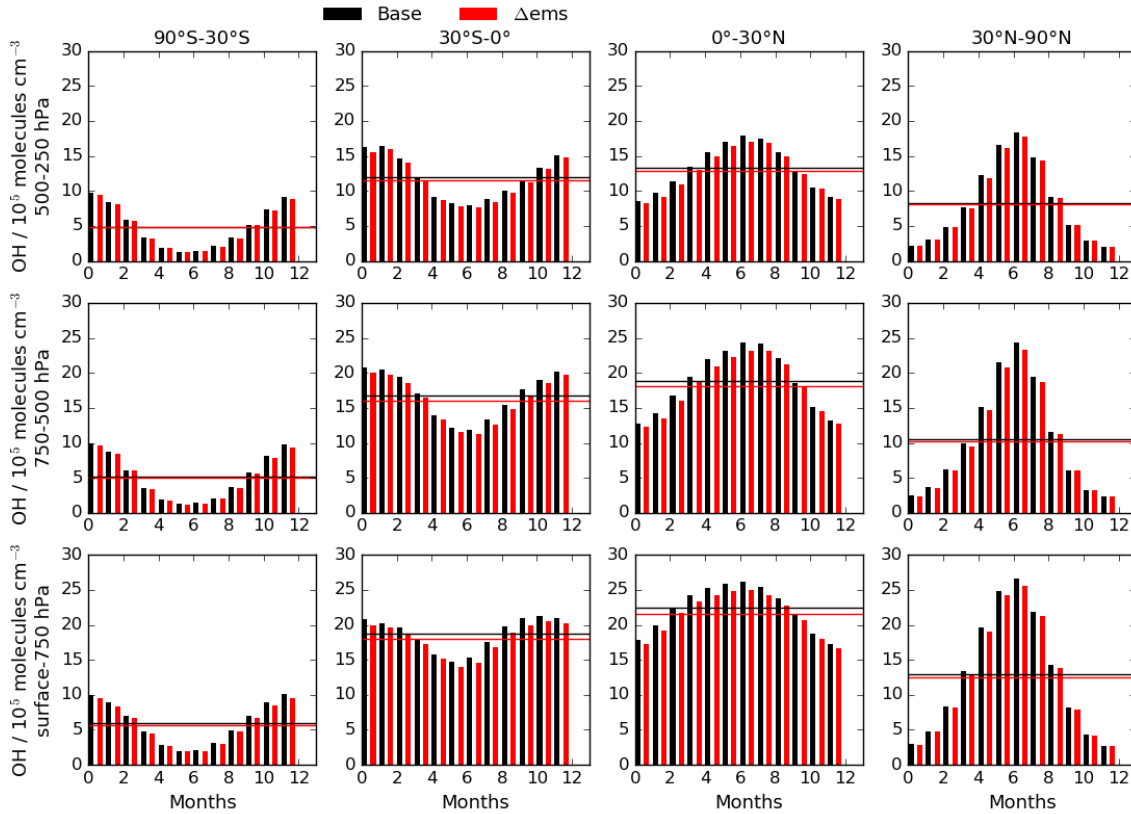


**Fig. 5.7** Comparison of the zonal mean distribution and the seasonal cycle of Base OH (black) and  $\Delta$ ems OH (red) in the twelve atmospheric subregions suggested by Lawrence et al. [2001].

While the methane emission change has improved the model's representation of methane noticeably, the OH decreases in  $\Delta$ ems are small and the OH fields for  $\Delta$ ems and Base show near identical zonal distributions.

## 5.4 Changes to ozone, carbon monoxide and nitrogen oxides

Methane influences OH which in turn influences and is influenced by ozone ( $O_3$ ), carbon monoxide (CO) and the nitrogen oxides ( $NO_x$ ). This section briefly examines differences in these species between the Base and  $\Delta$ ems experiments.

Small but significant (Student's t-test, 95% confidence interval) differences in the annual mean zonally averaged CO fields can be noted (Figure 5.8 (a)). The  $\Delta$ ems CO concentrations exceed those of Base. The absolute differences are largest in the tropics (5 ppb) and decrease into both hemispheres. Overall the CO low bias relative to surface observations [Dlugokencky et al., 2016] is reduced slightly compared to Base (see section 2.3.3, Appendix A.3) with the most noticeable changes at stations at high southern latitudes (not shown).

The differences between the  $\Delta$ ems and Base  $\text{NO}_x$  fields are statistically insignificant in large areas of the troposphere (Figure 5.8 (b)). A small reduction in tropospheric  $\text{NO}_x$  can be noted in the tropical upper troposphere (5 ppt, 2 – 4%) which can be linked to lower OH concentrations in this region for the  $\Delta$ ems experiment, as noted above.

The difference in the ozone fields for the two experiments are statistically insignificant in the high latitudes and small (<1 ppb) in the rest of the troposphere (Figure 5.8 (c)). However, the 7% (37  $\text{Tg}(\text{CH}_4) \text{ yr}^{-1}$ ) increase in methane emissions results in a tropospheric ozone burden increase of 5  $\text{Tg}(\text{O}_3)$  (equivalent of 0.14  $\text{Tg}(\text{O}_3)$  per 1  $\text{Tg}(\text{CH}_4) \text{ yr}^{-1}$  methane emission increase). This is comparable to results presented in Fiore et al. [2008], who gave the range 0.11 – 0.16  $\text{Tg}(\text{O}_3)$  for each 1  $\text{Tg}(\text{CH}_4) \text{ yr}^{-1}$ . Recent and projected methane emissions increases are therefore not only important to understand and mitigate in light of methane's role as a greenhouse gas but also as a precursor gas for air quality.

In conclusion, the small methane emission changes in  $\Delta$ ems (7% increase and shift towards the tropics) do not greatly alter the gross tropospheric composition, i.e. the abundance and distribution of OH, ozone,  $\text{NO}_x$  and CO. However, the ozone increase due to the methane emissions can impact human health and crop yields, which means that methane emission increases should be monitored closely.

While methane does not greatly change  $\text{NO}_x$  and/or CO abundance, changes of similar magnitude to these species are expected to have a larger effect on tropospheric OH and thus tropospheric methane abundance. Increases in  $\text{NO}_x$  emissions will lead to increases in tropospheric OH, in turn acting to decrease tropospheric methane. Increases in CO (and non-methane hydrocarbons such as isoprene) will decrease tropospheric OH levels and thus act to increase tropospheric methane abundance.

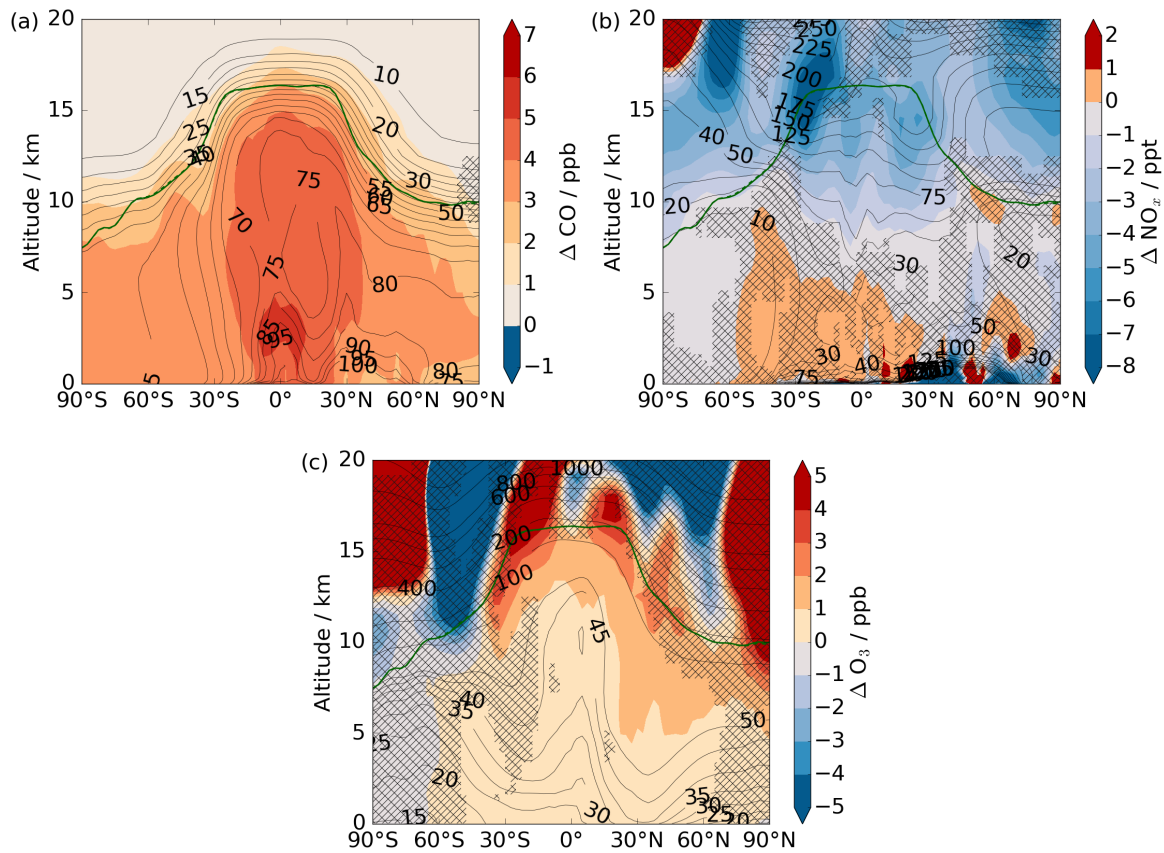


**Fig. 5.8** Absolute changes in annual mean zonally averaged CO (a, ppb),  $\text{NO}_x$  (b, ppt) and ozone (c, ppb) between  $\Delta\text{ems}$  and Base. The contour lines in (b) show the absolute water content for Base (ppm). Hatched areas are not significant at the 95<sup>th</sup> level according to the Student's t-test. The tropopause for the Base experiment is depicted in the solid dark green line. Note the different scales for the graphs.

## 5.5 Non-interactive methane

In chapter 3 it was shown that global mean methane from the  $\Delta\text{OH}$  agreed well with observations [Dlugokencky et al., 2016] while the latitudinal gradient was overestimated. Recall that the TransCom OH field [Patra et al., 2011] is prescribed in  $\Delta\text{OH}$  with a methane emission strength of  $548 \text{ Tg}(\text{CH}_4) \text{ yr}^{-1}$ . In this section the effect of altering the methane emission distribution (and overall emission strength) on non-interactive methane is explored. The TransCom OH field is prescribed as outlined in chapter 3 and the methane emissions described above are used in this new experiment, referred to as  $\Delta(\text{ems}+\text{OH})$ . Keeping the overestimation of the  $\Delta\text{OH}$  methane latitudinal gradient in mind, the question arises whether the  $\Delta(\text{ems}+\text{OH})$  methane latitudinal gradient is affected by the emission shift towards the

tropics. In chapter 4 it was shown that a drastic increase of (predominantly) South American emissions improved the latitudinal gradient immensely.

As discussed in section 5.1, the methane emission strength in the  $\Delta(\text{ems}+\text{OH})$  experiment is 7% higher than in  $\Delta\text{OH}$ . The atmospheric methane abundance in these non-interactive experiments is expected to respond linearly to an emission strength increase. The 7% methane emission increase is thus expected to cause a 7% increase in atmospheric methane abundance. This would result in  $\Delta(\text{ems}+\text{OH})$  methane concentrations being high biased relative to NOAA surface measurements [Dlugokencky et al., 2016] as the global methane abundance in  $\Delta\text{OH}$  was shown to agree well with observations. Surprisingly,  $\Delta(\text{ems}+\text{OH})$  methane concentrations are only 3% higher compared to  $\Delta\text{OH}$  and thus only slightly overestimate methane (Figure 5.9).

**Table 5.5** Comparison of key atmospheric methane variables for the  $\Delta\text{OH}$  and  $\Delta(\text{ems}+\text{OH})$  experiments with the TransCom OH field citePatra2013. The last column indicates the percentage difference between the two estimates ( $\Delta(\text{ems}+\text{OH}) - \Delta\text{ems}$ ).

Atmospheric methane variable	$\Delta\text{OH}$	$\Delta(\text{ems}+\text{OH})$	$\Delta(\text{ems}+\text{OH}) - \Delta\text{ems}$
Surface global mean $\text{CH}_4$ (ppb)	1814	1865	+3%
Atmospheric $\text{CH}_4$ burden (Tg)	4843	5003	+3%
$\text{OH} + \text{CH}_4$ flux ( $\text{Tg}(\text{CH}_4) \text{ yr}^{-1}$ )	466	481	+3%
$[\text{OH}]_{\text{GM}}$ ( $10^5 \text{ molecules cm}^{-3}$ )	10.2	10.2	0%
$\tau_{\text{OH} + \text{CH}_4}$ (years)	10.4	10.4	0%

This somewhat smaller increase in methane abundance is likely due to the methane emissions being redistributed into the tropical regions. As such, more methane gets emitted into the sink-dominated tropics where it is lost quicker. The flux through the reaction of methane and OH has also increased by 3% in the  $\Delta(\text{ems}+\text{OH})$  experiment compared to  $\Delta\text{OH}$  (Table 5.5) which supports this explanation. No change in the methane lifetime can be noted between the  $\Delta\text{OH}$  and  $\Delta(\text{ems}+\text{OH})$  experiments. With a lifetime of 10.2 years the  $\Delta(\text{ems}+\text{OH})$  thus agrees well with observational estimates. In light of the burden differences for the two experiments this shows how the lifetime alone cannot reliably inform how well the model performs in representing methane.

The tropical shift of the methane emissions did not markedly improve the latitudinal methane gradient. The gradient is 142 ppb for the  $\Delta(\text{ems}+\text{OH})$  experiment, compared to 148 ppb for  $\Delta\text{OH}$ , i.e. it is 4% shallower in  $\Delta(\text{ems}+\text{OH})$ . This is still noticeably larger than the observed gradient (95 ppb). Thus, the emission change implemented here did not have a great influence on methane simulated with the prescribed TransCom OH field. Here, contrary

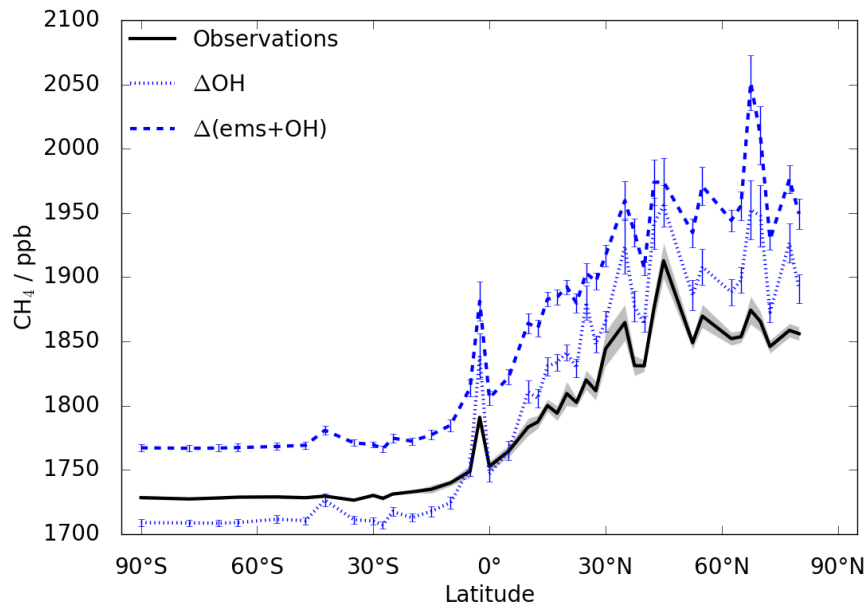


**Fig. 5.9** Latitudinal gradient for  $\Delta(\text{ems}+\text{OH})$  methane (blue dashed) and  $\Delta\text{OH}$  methane (blue dotted) compared to observations [Dlugokencky et al., 2016] (black). Error bars and shading represent the  $1\sigma$  interval and indicate temporal and spatial variability at each latitude.

to the suggestion of the local optimisation technique discussed in chapter 4, the wetland emissions were increased across the three tropical regions and not just in South America. While the strength of South American wetlands was indeed increased, their dampening effect on the latitudinal gradient was cancelled by the emission increases over South-East Asia (and Africa). Further studies of the global distribution of methane emissions and wetlands in particular are necessary to reduce the uncertainty of the results presented here.

In addition to the emission distribution causing the overestimation of the latitudinal gradient, the OH distribution might also be contributing. As discussed in chapter 3, this might point to too little (much) loss in the Northern (Southern) Hemisphere for the TransCom adaption of the Spivakovsky OH field. However, in chapter 3 it was also noted that the latitudinal gradient of a non-interactive simulation with the Base OH field (Base(non-interactive)) was overestimated. As that OH field from the interactive chemistry scheme resulted in a good representation of the interactive methane latitudinal gradient, the repeated overestimation in the prescribed methane chemistry scheme may point to the limitation of that scheme.

## 5.6 Summary

In chapter 2 it was shown that methane emissions of  $548 \text{ Tg}(\text{CH}_4) \text{ yr}^{-1}$  led to a 9% low bias in atmospheric methane concentrations relative to observations but with a good representation of the latitudinal gradient. It was then shown in chapter 3 that reducing the tropospheric OH sink strength improved absolute methane levels but caused an overestimation of the methane latitudinal gradient. This chapter studied the effects of changing the methane emissions on atmospheric composition.

CMIP5 recommendations for the anthropogenic methane emissions were followed as was the estimate for biomass burning emissions. This resulted in a reduction of anthropogenic methane emissions relative to the Base experiment, especially in the Northern Hemisphere. The strengths and distributions of the termite and hydrate emissions were kept identical to the Base experiment. However, the wetland emission flux was increased relative to Base in order to increase the overall methane emission strength. In chapter 2 this was pointed out as a possible way to remove the methane low bias. At the same time, the Base latitudinal gradient was in good agreement with observations. In chapter 4 analysis was presented that suggested that shifting methane emissions from the Northern Hemisphere into the tropics would improve the latitudinal gradient. Particularly South American emissions were shown to decrease the latitudinal gradient. In that chapter it was also shown that a range of tropical emissions affected both hemispheres. For the experiment in this chapter it was deemed reasonable to increase tropical emissions which affect both hemispheres and thus not the latitudinal gradient because the Base experiment showed good agreement with observations. The wetland flux was thus scaled to  $259 \text{ Tg}(\text{CH}_4) \text{ yr}^{-1}$ , a 36% increase relative to Base, using recent estimates from the WETCHIMP project [Melton et al., 2013]. The tropical wetlands (swamps) were increased more than the boreal wetlands (tundra and bogs), bringing their ratio to tropical emissions in line with WETCHIMP estimates (28% of wetland emission from boreal wetlands). Overall, these changes resulted in a 7% increase of the methane emission strength relative to Base.

With this new emission estimate, excellent agreement between modelled and observed methane has been presented showing that the model is able to both capture the latitudinal gradient and absolute methane concentrations. This is particularly worth highlighting as only a limited number of modelling studies use methane emissions instead of concentration boundary conditions. The few studies that use methane emissions often scale their results to match observations [e.g Dalsøren et al., 2016] which has not been done in this chapter.

The methane concentration increase resulted in a small decrease in tropospheric OH levels. However, OH remains larger than suggested by estimates based on methyl chloroform measurements. A small lengthening of the methane lifetime (8.6 years) compared to the Base experiment (8.2 years) could be noted but the lifetime remains slightly low biased relative to observations.

The methane emission change affected tropospheric CO and NO<sub>x</sub> only marginally meaning that CO remained low biased relative to observations. Improving the CO low bias would increase tropospheric OH which could possibly improve the model's representation of the methane lifetime. Including methyl chloroform and methane isotopes in the simulations could help to further constrain the OH field and methane emissions. The 35 Tg(CH<sub>4</sub>) yr<sup>-1</sup> methane emission increase resulted in an increase in the tropospheric ozone burden by 5 Tg. This agrees with previous estimates for the close coupling of tropospheric ozone and methane budgets. It shows how monitoring and mitigating methane emission increases could improve the negative effects of ozone on health and crop yield.

Results were presented which analysed the combined effect of a different tropospheric sink and changed methane emissions on atmospheric methane levels. Surprisingly, the atmospheric burden was found to only increase by 3% and not the expected 7% due to the linear chemistry in this experiment. This has been attributed to methane being emitted into regions where the OH sink is more present. Further experiments assessing the magnitude of this redistribution effect and whether or how it depends on absolute atmospheric methane levels might be important in light of uncertain future emissions. The shift of methane emissions into the tropical regions as implemented has not improved the latitudinal gradient in the Δ(ems+OH) experiment. This highlights the sensitivity of the local optimisation solution from chapter 4 to the exact location of the emissions, i.e. South American wetlands. Analysing the effect of different wetland emission distributions rather than scaling the Fung et al. [1991] estimate might improve the current understanding. This highlights that specifying OH fields is not the ultimate goal when studying atmospheric methane.

The next chapter will investigate how methane abundance changes in a future climate and its sensitivity to future emission scenarios. The model presented in this chapter lends itself well for these sensitivity studies because of the excellent representation of present day atmospheric methane.



## 6 | Probing climate impacts on methane

The previous chapters have all looked at present day climate, assessing the impact of changing methane emissions and methane oxidation on atmospheric methane and other species. In this chapter, the impact of future climate change on atmospheric methane is investigated.

A set of experiments is performed probing the response of methane, and of OH, NO<sub>x</sub>, CO and ozone, to changes in climate and emissions (especially methane emissions). OH is the key tropospheric oxidant. Drivers of tropospheric OH (methane, anthropogenic CO, CO from methane oxidation, etc.) will be analysed highlighting their interdependence. It will be shown that future methane emissions will not only influence atmospheric temperature but also have implications for ozone levels and air quality [e.g. Fiore et al., 2002].

The chapter begins by reintroducing the model and outlining the four experiments analysed in this chapter (section 6.1). Three perturbation experiments are introduced which allow temperature effects and emission impacts (from methane and non-methane emissions) to be distinguished. The section includes a detailed analysis of emission projections for the year 2100. A summary of chapter 5 is presented in section 6.2. Subsequent sections consider the modelled changes resulting from the climate and emission changes. First, in section 6.3, temperature and water vapour changes are presented. Then (section 6.4) methane and OH are discussed. Finally, changes to tropospheric NO<sub>x</sub>, CO and ozone are presented in section 6.5. The chapter concludes in section 6.6.

### 6.1 Model setup

The same model configuration as outlined in chapter 2 is used for the experiments presented in this chapter. Changes have been made to the sea ice and sea surface temperature (SST) fields and anthropogenic surface emissions according to the simulated climate. Three new experiments are compared and contrasted and are summarised in Table 6.1.

**Table 6.1** Summary of the four experiments presented in this chapter probing the atmospheric response to a changing climate. The year 2000 is representative of the present day climate while the year 2100 follows the RCP 8.5 scenario. Note that the Base experiment here is identical to the  $\Delta$ ems experiment in the previous chapter.

Experiment	Climate forcers	Precursor emissions	Anthropogenic methane emissions	Natural methane emissions
Base	2000	2000	2000	2000
$\Delta$ CC	2100	2000	2000	2000
$\Delta$ (CC+methane)	2100	2000	2100	2000
$\Delta$ (CC+ems)	2100	2100	2100	2000

The **Base** experiment used in this chapter is identical to the  $\Delta$ ems experiment discussed in chapter 5. The experiment simulates present day climate (year 2000) with anthropogenic emissions following CMIP5 recommendations [Lamarque et al., 2010]. Methane emissions for this experiment amount to  $585 \text{ Tg}(\text{CH}_4) \text{ yr}^{-1}$ . A detailed breakdown of the individual source contribution was given in chapter 5. This experiment reproduces observed methane concentrations very well, both in terms of global absolute abundance and the latitudinal gradient as discussed in chapter 5.

In the  $\Delta$ CC experiment climate forcers are prescribed for the year 2100 climate according to the RCP 8.5 scenario (representative concentration pathway leading to a  $8.5 \text{ W m}^{-2}$  radiative forcing increase by 2100 relative to preindustrial levels) [Bellouin et al., 2011a; Meinshausen et al., 2011; IPCC, 2013]. These climate forcers are sea ice and SST fields, concentrations of ozone depleting substances (ODS) and greenhouse gas (GHG) concentrations ( $\text{CO}_2$ , methane, nitrous oxide, chlorofluorocarbons and hydrochlorofluorocarbons). These ODS and GHG concentrations for the year 2100 (RCP 8.5 scenario) are prescribed in the radiation scheme only but not imposed in the chemistry scheme. Ozone is passed interactively between the radiation and chemistry scheme. As for Base, methane emissions for this experiment are kept identical to the Base experiment and amount to  $585 \text{ Tg}(\text{CH}_4) \text{ yr}^{-1}$ . All other emissions are also kept at present day levels.

In addition to the changes to the climate forcers in the  $\Delta$ CC experiment, methane emissions for the year 2100 (according to RCP 8.5) [Riahi et al., 2007] are included in the  $\Delta$ (CC+methane) experiment. All other emissions are kept at their year 2000 levels. The total methane emission strength is doubled compared to the present day scenario to  $1170 \text{ Tg}(\text{CH}_4) \text{ yr}^{-1}$ . This is solely due to anthropogenic emission changes, while all natural emissions are kept at the year 2000 levels (see detailed discussion below, Table 6.3). This means

that methane emissions from wetlands amount to 259 Tg(CH<sub>4</sub>) yr<sup>-1</sup>, hydrates to 6 Tg(CH<sub>4</sub>) yr<sup>-1</sup> and termites to 20 Tg(CH<sub>4</sub>) yr<sup>-1</sup>, unchanged from the Base and ΔCC experiments. Climate change would, of course, be expected to change these emissions, but the absolute changes are uncertain. For that reason, the focus is just on changes in the anthropogenic emissions.

In addition to the changes to the climate forcers in the ΔCC experiment and the methane emission changes in Δ(CC+methane), all other anthropogenic emissions are also changed to their projected strength for the year 2100 (RCP 8.5 scenario) [Riahi et al., 2007] in the Δ(CC+ems) experiment. In this scenario surface NO<sub>x</sub> and CO emissions decrease sharply by 33% and 34% respectively, due to stringent mitigation and air quality controls. Other (less abundant) hydrocarbons also decrease except for acetone, isoprene and methanol which increase slightly. Comparison of Δ(CC+methane) and Δ(CC+ems) allows the effect of NO<sub>x</sub> and CO (and other) emissions on tropospheric chemistry to be separated from the effect of methane on OH and ozone levels. The present day (year 2000) and future (year 2100, RCP 8.5) emission strengths for the ten species relevant for the UM-UKCA are summarised in Table 6.2.

Note that the methane concentrations are specified in the radiation scheme according to the simulated climate and not interactively coupled to the chemistry scheme. They are thus identical for ΔCC, Δ(CC+ems) and Δ(CC+methane) experiments and independent of the differences in the chemical fields between these experiments.

**Table 6.2** Annual emissions for species relevant for the UM-UKCA for the years 2000 and 2100 (RCP 8.5 scenario) and their differences [Riahi et al., 2007; Lamarque et al., 2010]. The units are in Tg(species) yr<sup>-1</sup> for all species but C<sub>5</sub>H<sub>8</sub> and CH<sub>3</sub>OH which are in Tg(C) yr<sup>-1</sup>.

Species		Emissions			
		2000	2100 (RCP 8.5)	2100 – 2000	
Nitrogen oxides	NO <sub>x</sub>	138	93	-45	Tg(NO <sub>2</sub> ) yr <sup>-1</sup>
Methane	CH <sub>4</sub>	585	1170	+585	Tg(CH <sub>4</sub> ) yr <sup>-1</sup>
Carbon monoxide	CO	1113	734	-379	Tg(CO) yr <sup>-1</sup>
Formaldehyde	CH <sub>2</sub> O	9	5	-4	Tg(CH <sub>2</sub> O) yr <sup>-1</sup>
Ethane	C <sub>2</sub> H <sub>6</sub>	27	17	-10	Tg(C <sub>2</sub> H <sub>6</sub> ) yr <sup>-1</sup>
Propane	C <sub>3</sub> H <sub>8</sub>	14	8	-6	Tg(C <sub>3</sub> H <sub>8</sub> ) yr <sup>-1</sup>
Acetone	(CH <sub>3</sub> ) <sub>2</sub> CO	46	49	+3	Tg((CH <sub>3</sub> ) <sub>2</sub> CO) yr <sup>-1</sup>
Acetaldehyde	CH <sub>3</sub> CHO	9	6	-3	Tg(CH <sub>3</sub> CHO) yr <sup>-1</sup>
Isoprene	C <sub>5</sub> H <sub>8</sub>	573	580	+7	Tg(C) yr <sup>-1</sup>
Methanol	CH <sub>3</sub> OH	121	129	+8	Tg(C) yr <sup>-1</sup>

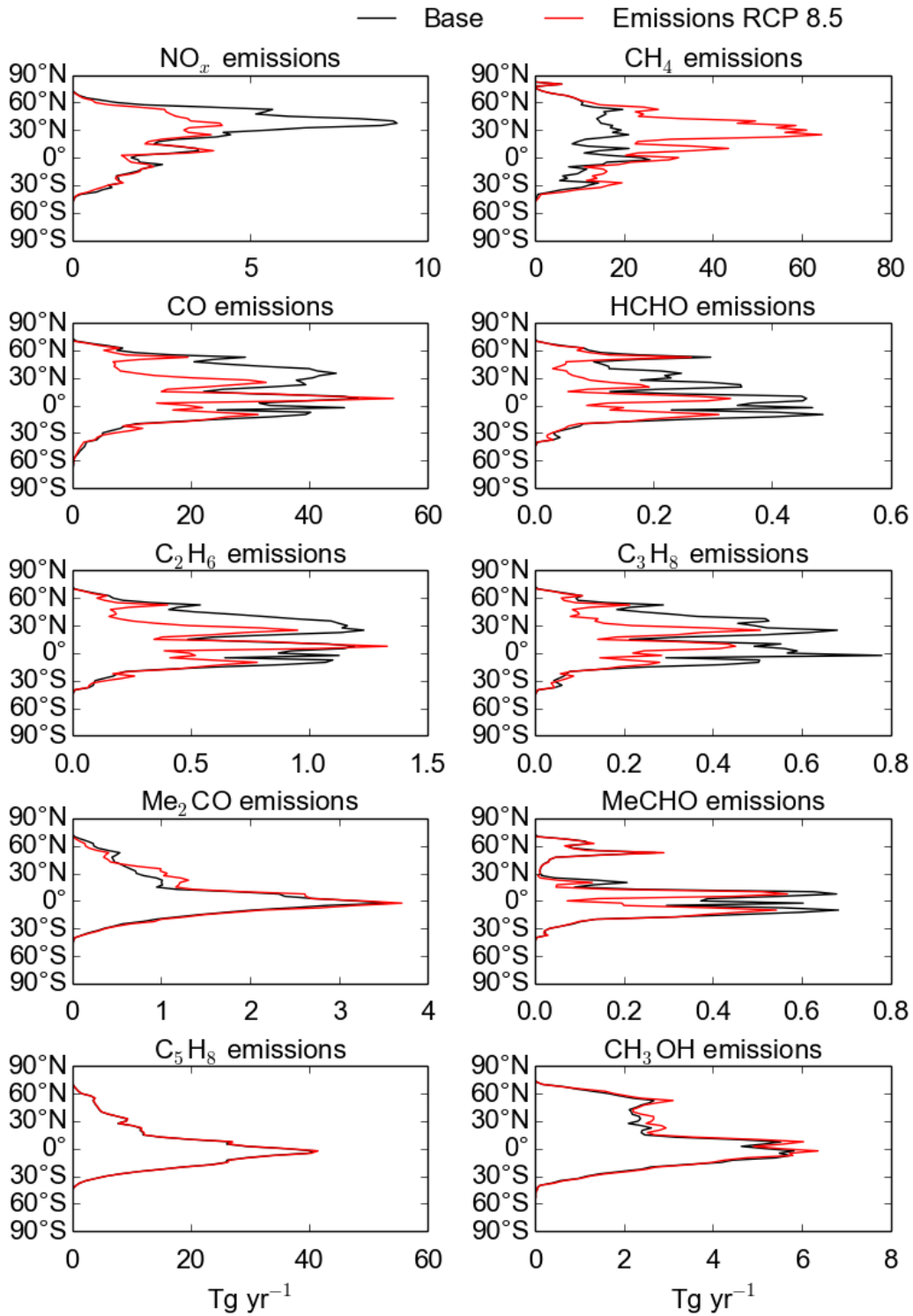


**Fig. 6.1** Comparison of the latitudinal distribution of the year 2100 (RCP 8.5 scenario, red) and Base (black) emissions. From the top left to the bottom right: NO<sub>x</sub>, CH<sub>4</sub>, CO, CH<sub>2</sub>O, C<sub>2</sub>H<sub>6</sub>, C<sub>3</sub>H<sub>8</sub>, (CH<sub>3</sub>)<sub>2</sub>CO, CH<sub>3</sub>CHO, C<sub>5</sub>H<sub>8</sub> and CH<sub>3</sub>OH emissions. The units are in Tg(species) yr<sup>-1</sup> for all species but C<sub>5</sub>H<sub>8</sub> and CH<sub>3</sub>OH which are in Tg(C) yr<sup>-1</sup>. Note the different scales for the graphs.

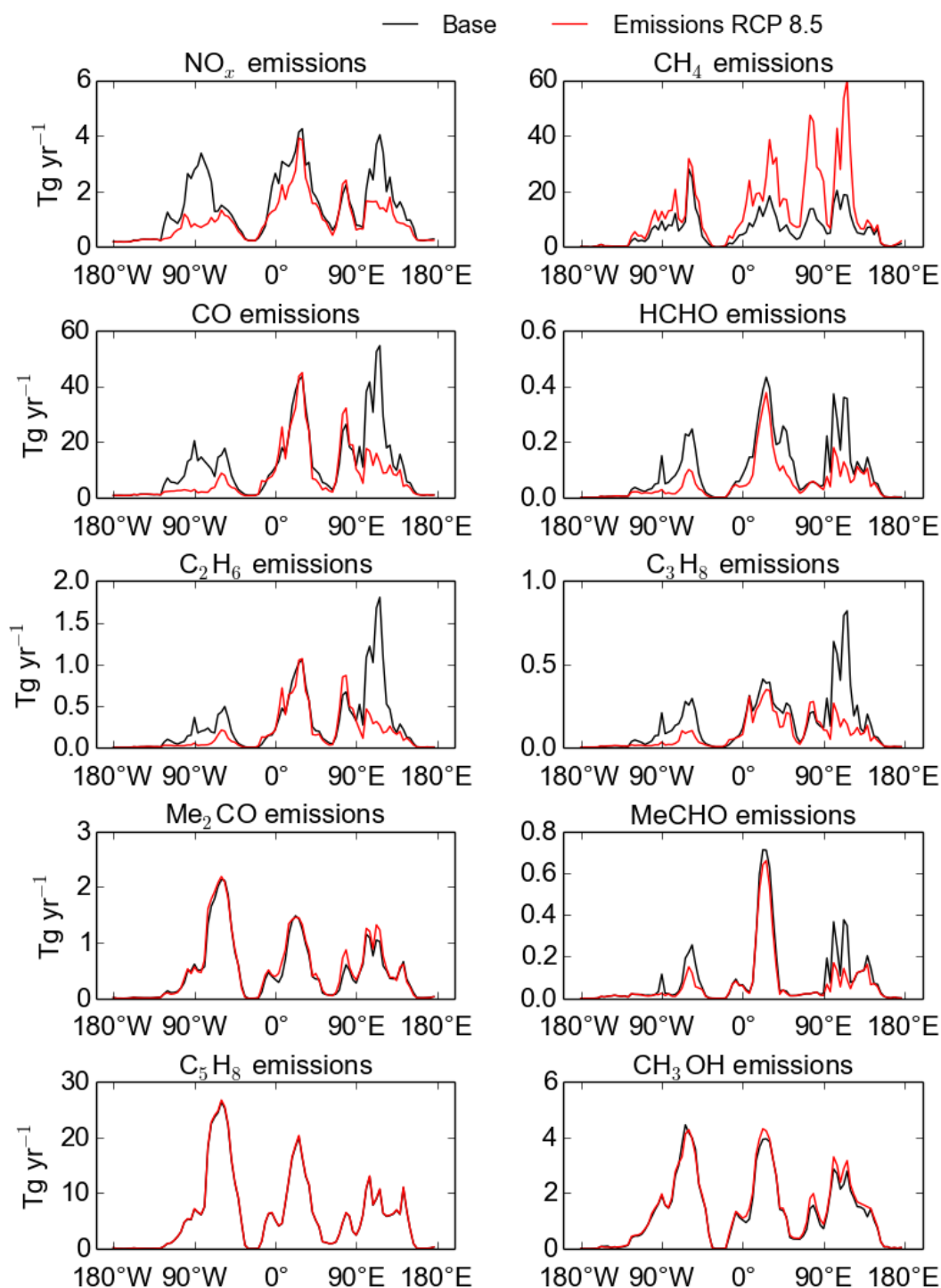


**Fig. 6.2** Comparison of the longitudinal distribution of the year 2100 (RCP 8.5 scenario, red) and Base (black) emissions. From the top left to the bottom right: NO<sub>x</sub>, CH<sub>4</sub>, CO, HCHO, C<sub>2</sub>H<sub>6</sub>, C<sub>3</sub>H<sub>8</sub>, Me<sub>2</sub>CO, MeCHO, C<sub>5</sub>H<sub>8</sub> and CH<sub>3</sub>OH emissions. The units are in Tg(species) yr<sup>-1</sup> for all species but C<sub>5</sub>H<sub>8</sub> and CH<sub>3</sub>OH which are in Tg(C) yr<sup>-1</sup>. Note the different scales for the graphs.

### 6.1.1 Emission changes

Figure 6.1 and Figure 6.2 describe the changes between the year 2000 and year 2100 RCP 8.5 emissions. The emission decreases for  $\text{NO}_x$  in 2100 happen mainly between  $30^\circ\text{N}$  and  $60^\circ\text{N}$  while  $\text{CO}$ ,  $\text{CH}_2\text{O}$ ,  $\text{C}_2\text{H}_6$ ,  $\text{C}_3\text{H}_8$  and  $\text{CH}_3\text{CHO}$  emissions also decrease in the tropics. These six species all show large reductions over the Americas ( $120^\circ\text{W} - 10^\circ\text{W}$ ) and in Asia ( $90^\circ\text{E} - 180^\circ\text{E}$ ). Increases in  $(\text{CH}_3)_2\text{CO}$ , and  $\text{CH}_3\text{OH}$  are evident in the tropics and between  $30^\circ\text{N}$  and  $60^\circ\text{N}$  with an even increase across the longitudes. The increase in methane emissions is discussed in more detail below.

#### Methane emissions changes

Methane emissions double from present day to year 2100 in the RCP 8.5 scenario. The contribution from the different source types can be seen in Table 6.3. As mentioned above, only anthropogenic methane emission increases are included in the scenario with identical distribution and strength for the natural components (wetlands, termites, hydrates). This is highly idealised as biogenic emissions, and wetlands in particular, are expected to respond to changes in climate parameters such as temperature and precipitation [e.g. Walter et al., 2001; Bergamaschi et al., 2007]. However, as temperature and precipitation changes would also affect the distribution of wetlands, a response that cannot be represented in this model version, no change for biogenic emissions is assumed for this sensitivity analysis.

The largest methane emission increases originate from the energy sector, making it the single largest methane emission sector, closely followed by agricultural practices. Wetlands are the third largest emission sector with waste emissions only  $50 \text{ Tg}(\text{CH}_4) \text{ yr}^{-1}$  smaller than wetlands. Emissions from the residential sector contribute only minimally to the total methane emission strength and change little between 2000 and 2100 while methane emissions from biomass burning decrease by 40% by the end of the century.

Figure 6.3 and Figure 6.4 compare the latitudinal and longitudinal distribution of methane emissions for the years 2000 and 2100. Anthropogenic emissions increase across all latitudes but their largest increase is between  $30^\circ\text{N}$  and  $60^\circ\text{N}$ . With biomass burning emission decreases occurring mainly in the tropics ( $30^\circ\text{N} - 30^\circ\text{S}$ ) the overall methane emission increase is predominantly located around  $30^\circ\text{N}$ . Emissions increase at all longitudes but mostly so over Asia ( $90^\circ\text{E} - 180^\circ\text{E}$ ), followed by Europe/Africa ( $10^\circ\text{E} - 90^\circ\text{E}$ ) while emissions over the Americas remain fairly constant ( $120^\circ\text{E} - 10^\circ\text{E}$ ). This last effect is due to biomass burning

**Table 6.3** Annual methane emissions ( $\text{Tg}(\text{CH}_4) \text{ yr}^{-1}$ ) by source type for the year 2000 and 2100 (RCP 8.5 scenario) and their differences in  $\text{Tg}(\text{CH}_4) \text{ yr}^{-1}$  and %.

Methane	Emissions		Difference 2100-2000	
	2000	2100	( $\text{Tg}(\text{CH}_4) \text{ yr}^{-1}$ )	(%)
Agriculture	127	317	190	150%
Energy	71	329	258	363%
Waste	62	208	146	235%
Residential	15	16	1	7%
Biomass burning	25	15	-10	-40%
Wetlands	259	259	0	0%
Termites	20	20	0	0%
Hydrates	6	6	0	0%
Total	585	1170	585	100%

emission reductions over the Americas cancelling the increase in anthropogenic emissions. Anthropogenic emissions increase mostly over Asia, followed by Europe/Africa, then the Americas. In contrast, biomass burning emissions are reduced over the Americas and Asia while they remain fairly constant over Europe/Africa.

The geographical distribution of these emission changes will affect tropospheric OH concentrations. The reduction in CO emissions is likely to lead to increased OH concentrations, especially in the Northern Hemisphere, while  $\text{NO}_x$  emission reductions will reduce the production of ozone and thus OH production. The large increases in methane are likely to have a large impact on tropospheric OH directly as increases in methane lead to increases in the methane loss reaction with OH and thus reduce OH concentrations. Furthermore, more methane oxidation leads to greater CO production which further reduces tropospheric OH. The next sections aim to look at the effect of climate change and emission changes separately, and in combination, on tropospheric chemistry.

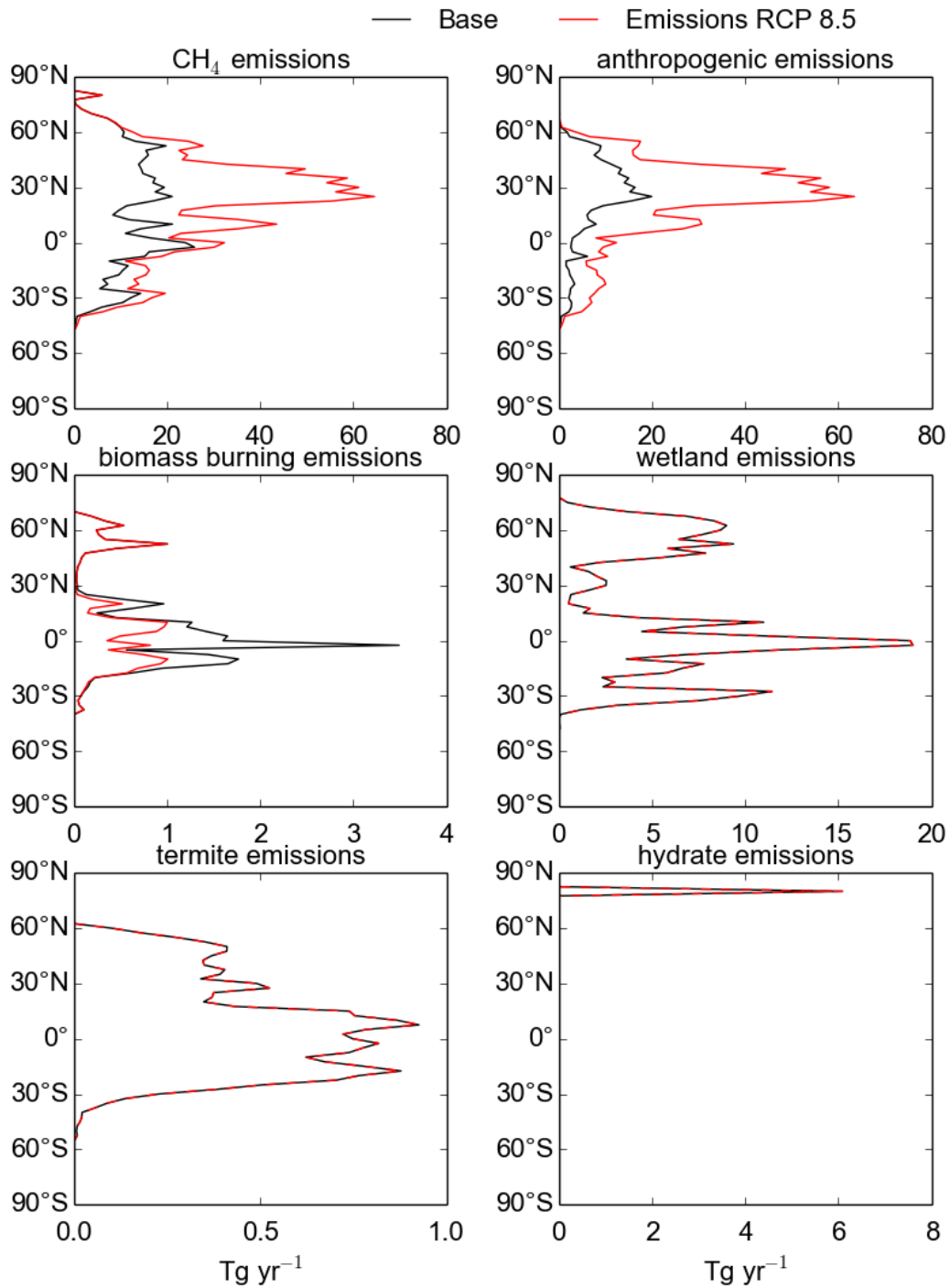


**Fig. 6.3** Comparison of the latitudinal distribution of the year 2100 (RCP 8.5 scenario, red) and Base (black) methane emissions (Tg(CH<sub>4</sub>) yr<sup>-1</sup>). From the top left to the bottom right: Total methane emissions, anthropogenic emissions, biomass burning emissions, wetland emissions, termite emissions and hydrate emissions. Note the different scales for the graphs.

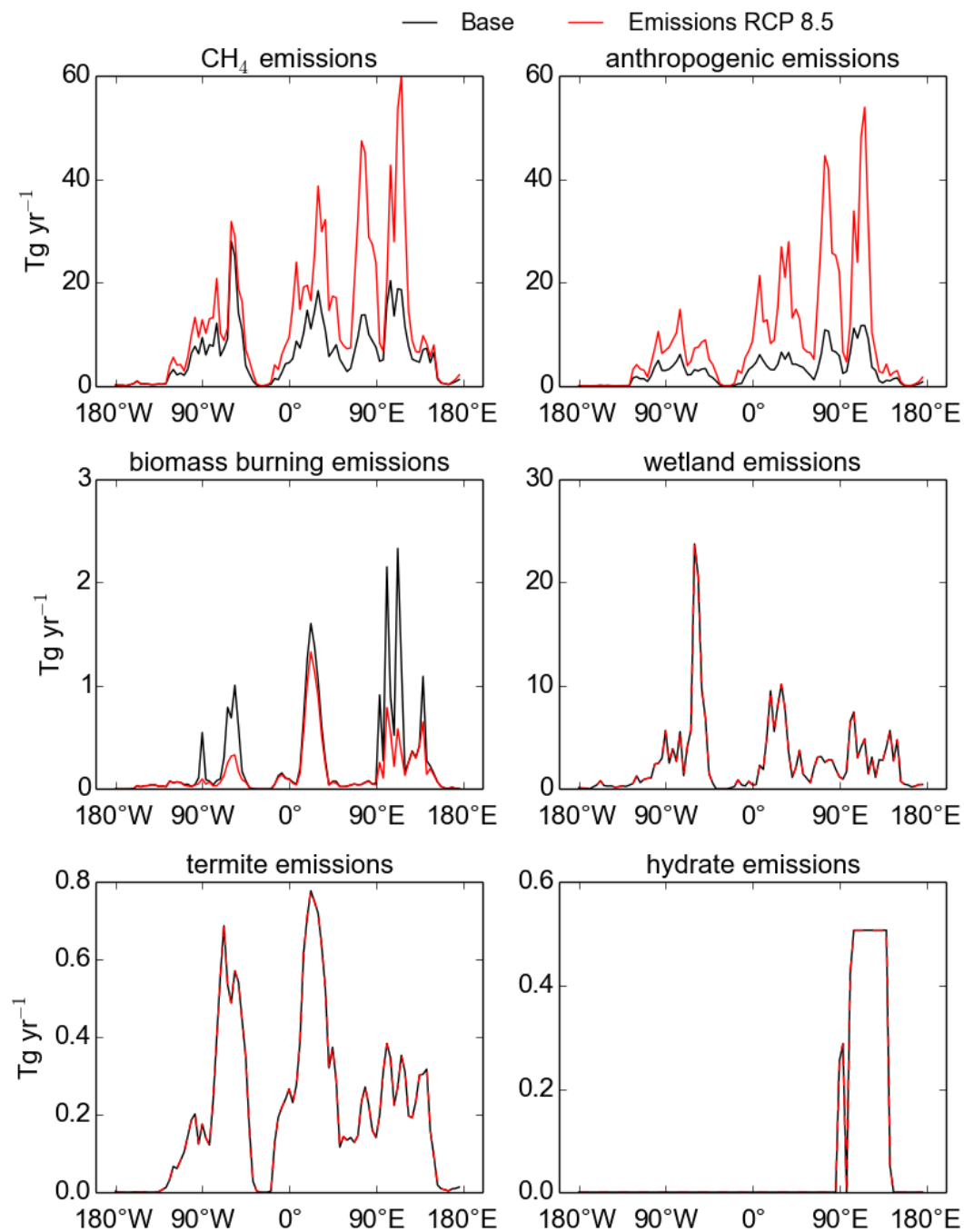


**Fig. 6.4** Comparison of the longitudinal distribution of the year 2100 (RCP 8.5, scenario, red) and Base (black) methane emissions (Tg(CH<sub>4</sub>) yr<sup>-1</sup>). From the top left to the bottom right: Total methane emissions, anthropogenic emissions, biomass burning emissions, wetland emissions, termite emissions and hydrate emissions. Note the different scales for the graphs.

## 6.2 Present day

This section briefly summarises results from the previous chapter in order to allow for more detailed analysis of the climate change experiments discussed in the next sections. As outlined in chapter 5,  $\Delta$ ems, i.e. this chapter's Base experiment, agrees extremely well with surface observations for methane, both in absolute magnitude and for the latitudinal gradient. The Base model has a methane lifetime with respect to tropospheric loss via OH of 8.6 years which agrees well with other chemistry climate models ( $9.3 \pm 0.9$  years [Voulgarakis et al., 2013]) but is short relative to observational estimates ( $11.2 \pm 1.3$  years [Prather et al., 2012]). This has been linked to a large tropospheric OH field in Base which averages (airmass-weighted) globally to  $12.0 \times 10^5$  molecules  $\text{cm}^{-3}$ , larger than suggested by methyl chloroform measurements ( $9.4 \pm 1.3 \times 10^5$  molecules  $\text{cm}^{-3}$  [e.g. Prinn et al., 2001]).

In addition to this, CO was found to be low biased relative to observations globally, but more so in the Northern Hemisphere which may be linked to insufficient emissions and/or too strong a tropospheric sink [e.g. Strode et al., 2015]. Tropospheric  $\text{NO}_x$  agreed reasonably well with aircraft observations with model high biases at the surface. These might be linked to low biases in surface ozone found in the Northern Hemisphere. Tropical ozone is high relative to ozone sonde data which might lead to increased tropical OH production.

The Base tropospheric ozone burden is 336 Tg( $\text{O}_3$ ) which is in good agreement with recent multi-model studies ( $334 \pm 39$  Tg( $\text{O}_3$ ) [Stevenson et al., 2006] and  $339 \pm 23$  Tg( $\text{O}_3$ ) [Young et al., 2013]). The ozone burden is slightly larger than that for the Base experiment in Banerjee et al. [2014] (Base(lbc), 326 Tg( $\text{O}_3$ )). The methane boundary condition being the only difference between these two models (emissions here compared to a concentration boundary condition for Banerjee et al. [2014]), it can be concluded that the ozone burden difference is a direct result from the methane differences in these two experiments.

The next sections analyse in detail the effect on the troposphere of changing the climate forcers and emissions under a future climate scenario.

## 6.3 Temperature and water vapour changes

As expected, the future climate according to the RCP 8.5 scenario leads to annual mean zonally averaged tropospheric temperature increases (Figure 6.5). This increase amounts to more than 10 K in the tropical upper troposphere and at the surface in the high northern

latitudes. The temperature increase is less pronounced in the southern high latitudes and smallest at the surface in the tropics. Temperature changes are expected to affect the chemical loss of methane through the reaction with OH as the reaction rate constant ( $2.45 \times 10^{-12} \exp(-1775 T^{-1})$  molecules $^{-1}$  cm $^3$  s $^{-1}$  [Sander et al., 2011]) is strongly temperature dependent. Figure 6.5 also shows the uplifting of the tropopause under future climate.

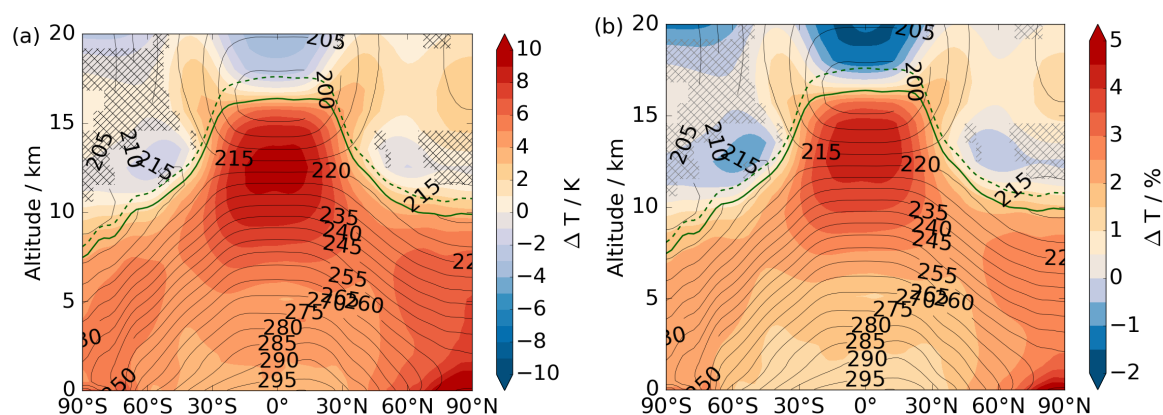


**Fig. 6.5** Absolute (a, K) and relative (b, %) changes in annual mean zonally averaged temperature ( $\Delta CC - \text{Base}$ ). The contour lines in (b) show the absolute temperature for Base (K). Hatched areas are not significant at the 95<sup>th</sup> level according to the Student's t-test. The tropopause for the Base ( $\Delta CC$ ) experiment is depicted in the solid (dashed) dark green line.

The tropospheric water content increases under a future climate as the atmosphere can hold more water vapour at higher temperatures. The largest relative increase in water vapour (>200%) is found in the tropical upper troposphere where temperature differences are greatest. However, because water vapour abundance is largest close to the (tropical) surface, this is where the absolute differences are greatest (14,000 ppm). These changes in water vapour impact methane chemistry through an increase in OH production via the reaction  $\text{H}_2\text{O} + \text{O}(^1\text{D})$  (see chapter 1, reaction 1.6). In a simple scheme, OH concentrations are proportional to the square root of water vapour content according to this reaction.

The temperature and atmospheric water content in  $\Delta(\text{CC}+\text{methane})$  and  $\Delta(\text{CC}+\text{ems})$  are not statistically different to  $\Delta\text{CC}$ . This is expected given that the same GHG concentrations (apart from interactive ozone) are prescribed in the radiation scheme for the three experiments. Thus, temperatures in  $\Delta(\text{CC}+\text{methane})$  and  $\Delta(\text{CC}+\text{ems})$  are 5 to 10 K higher relative to Base with most the largest changes in the tropical upper troposphere and the Arctic. Water abundance is greater in  $\Delta(\text{CC}+\text{methane})$  and  $\Delta(\text{CC}+\text{ems})$  than in Base with the largest relative changes happening in the tropical upper troposphere, as seen for  $\Delta\text{CC}$ . Changing the

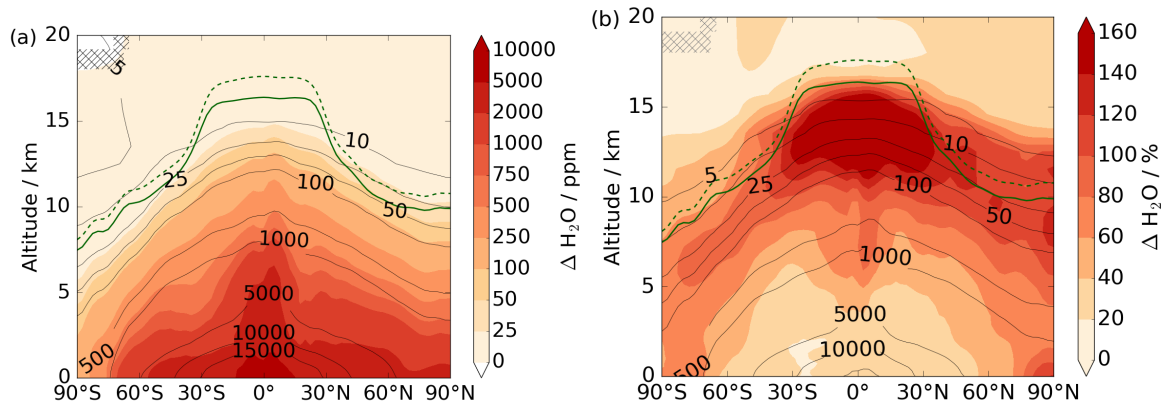


**Fig. 6.6** Absolute (a, ppm) and relative (b, %) changes in annual mean zonally averaged atmospheric water content ( $\Delta\text{CC} - \text{Base}$ ). The contour lines in (b) show the absolute water content for Base (ppm). Hatched areas are not significant at the 95<sup>th</sup> level according to the Student's t-test. The tropopause for the Base ( $\Delta\text{CC}$ ) experiment is depicted in the solid (dashed) dark green line.

anthropogenic surface emissions in addition to the climate does not affect the atmospheric temperature and water abundance significantly but affects tropospheric composition which will be addressed next.

The next sections aim to investigate the composition changes and their drivers of the  $\Delta\text{CC}$ ,  $\Delta(\text{CC}+\text{ems})$  and  $\Delta(\text{CC}+\text{methane})$  experiments. Initially tropospheric OH and methane abundance will be assessed (section 6.4). These changes will be linked to tropospheric  $\text{CO}$ ,  $\text{NO}_x$  and ozone in section 6.5. In both cases temperature and water vapour effects will be discussed first ( $\Delta\text{CC}$ ) followed by an investigation of the impact of methane and other anthropogenic emission changes ( $\Delta(\text{CC}+\text{methane})$  and  $\Delta(\text{CC}+\text{ems})$ ).

## 6.4 Changes to tropospheric OH and methane

The temperature and water vapour changes affect tropospheric OH concentrations and therefore, indirectly, methane. This section aims to highlight the effect of the OH changes on atmospheric methane. The large impact of the projected emission changes on tropospheric composition are explored.

### 6.4.1 $\Delta$ CC

#### OH

The  $\Delta$ CC globally averaged (airmass-weighted) tropospheric OH concentration indeed increases to  $15.9 \times 10^5$  molecules  $\text{cm}^{-3}$  which is  $3.8 \times 10^5$  molecules  $\text{cm}^{-3}$  (30%) greater than Base OH. This increase is linked to the higher tropospheric water content in  $\Delta$ CC (Figure 6.6) which leads to increased production of OH. Recall that the water vapour increase reaches 200% and that a simple chemical scheme would suggest that OH concentrations are proportional to the square root of water vapour concentrations. Increases in lightning  $\text{NO}_x$  emissions in  $\Delta$ CC,  $10.6 \text{ Tg(N) yr}^{-1}$  compared to  $6.6 \text{ Tg(N) yr}^{-1}$  in Base, also contribute to higher OH levels in the upper tropical troposphere by enhancing ozone in that region. The OH increases are largest in the tropics, exceeding 50%, and are fairly symmetric around the equator (Figure 6.7). The OH increases are thus most noticeable in regions of the tropical lower and middle troposphere where methane loss is believed to be highest [Bloss et al., 2005]. They are thus likely to impact the atmospheric methane abundance. The increase in tropospheric OH due to climate change modelled here is expected and has been noted previously [e.g. John et al., 2012; Morgenstern et al., 2013].

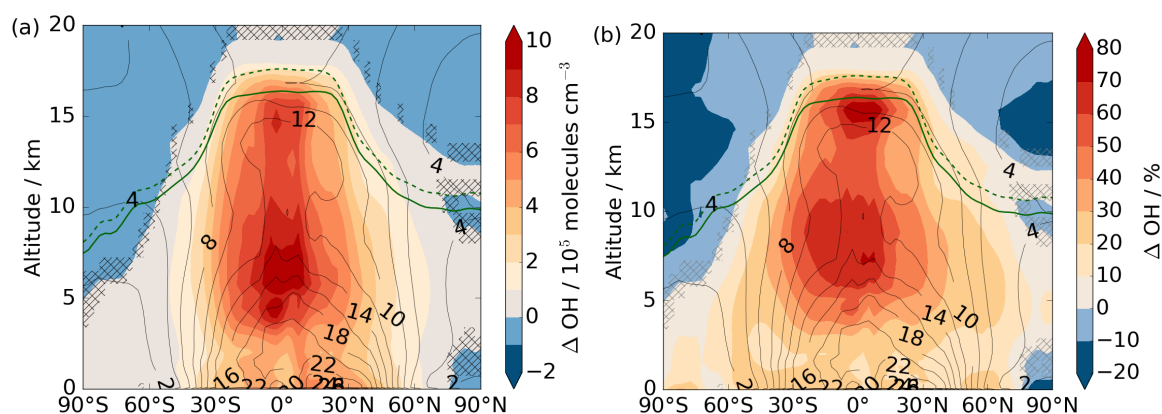


**Fig. 6.7** Absolute (a,  $10^5$  molecules  $\text{cm}^{-3}$ ) and relative (b, %) changes in annual mean zonally averaged OH ( $\Delta$ CC – Base). The contour lines show the absolute OH concentrations for Base ( $10^5$  molecules  $\text{cm}^{-3}$ ). The tropopause for the Base ( $\Delta$ CC) experiment is depicted in the solid (dashed) dark green line. Hatched areas are not significant at the 95<sup>th</sup> level according to the Student's t-test.

Figure 6.8 compares the seasonality of the Base (black) and  $\Delta$ CC (red) OH fields for the tropospheric (solid lines) as well as Northern (dashed) and Southern (dotted) Hemispheric averages. Tropospheric OH increases in  $\Delta$ CC are of the same magnitude throughout the year

in both hemispheres. The differences from the Base field are slightly larger in the respective summer months of the Northern and Southern Hemispheres which cancel when considering the whole troposphere. The fact that the OH changes are symmetric about the equator points to a globally uniform change in water vapour, the major OH precursor, as the source for the OH increases.

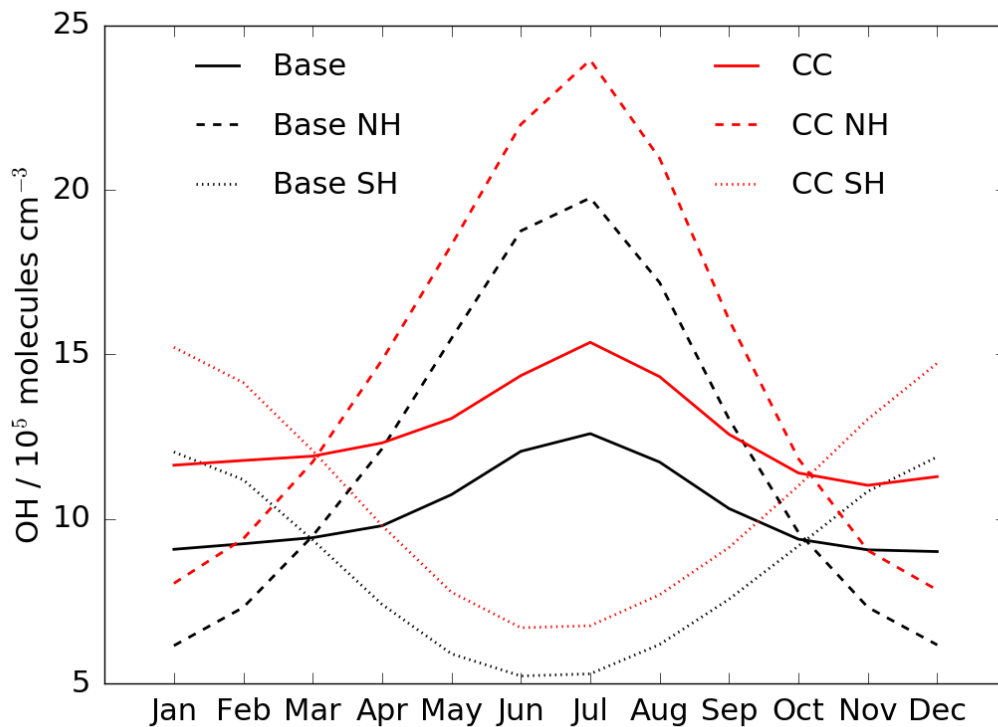


**Fig. 6.8** Seasonal variation in tropospheric Base OH concentrations ( $10^5 \text{ molecules cm}^{-3}$ ) in red and  $\Delta\text{CC}$  OH in black. The solid lines represent global, dotted lines Southern Hemispheric (SH) and dashed lines Northern Hemispheric (NH) OH concentrations.

The OH increase presented here (30%) is larger than the equivalent increase in the experiments with a lower boundary concentration for methane (20%, for the  $\Delta(\text{CC8.5+ODS})$  experiment [Banerjee et al., 2014, 2016, calculated separately]). This difference can be explained by the different methane burdens in the two experiments. The methane burden in  $\Delta(\text{CC8.5+ODS})$  is dominated by the lower boundary condition for methane which effectively fixes tropospheric methane concentrations at 1.75 ppm (present day levels). In the  $\Delta\text{CC}$  experiment, with a flux boundary condition, methane concentrations are allowed to respond to the tropospheric OH changes. Higher OH concentrations therefore reduce tropospheric

methane which in turn leads to higher OH concentrations, a phenomenon not included in the study by Banerjee et al. [2014].

## Methane

The OH increase in the  $\Delta$ CC experiment (warmer climate but present day emissions) leads, indeed, to a reduction in atmospheric methane. Methane concentrations decrease in most parts of the troposphere by 500 ppb (30%) with slightly more decreases at the Arctic surface (530 ppb) and in the tropical troposphere (510 ppb) than in the free troposphere. The decrease in the tropics is larger because most methane is lost in this region (Figure 6.9).

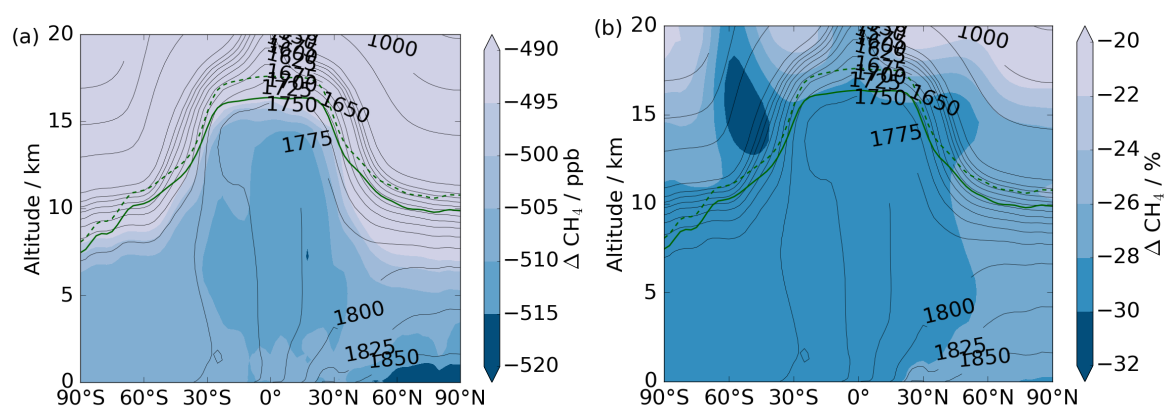


**Fig. 6.9** Absolute (a, ppb) and relative (b, %) changes in annual mean zonal averaged methane ( $\Delta$ CC – Base). The contour lines in (b) show the absolute methane concentrations for Base (ppb). The tropopause for the Base ( $\Delta$ CC) experiment is depicted in the solid (dashed) dark green line.

The total atmospheric methane burden for  $\Delta$ CC amounts to 3421 Tg(CH<sub>4</sub>) which is 1368 Tg(CH<sub>4</sub>) (29%) smaller than the Base burden. Despite the burden reduction, the absolute flux through the reaction between methane and OH in  $\Delta$ CC remains as high as in Base (568 Tg(CH<sub>4</sub>) yr<sup>-1</sup> and 560 Tg(CH<sub>4</sub>) yr<sup>-1</sup>, respectively). This means a higher proportion of methane is lost through this reaction which is due to the high tropospheric OH concentrations discussed above. The burden reduction and the high flux of methane loss with tropospheric OH will be related to the methane lifetime with respect to loss with tropospheric OH. In  $\Delta$ CC, the methane lifetime is reduced to 6.0 years, 2.5 years (30%) shorter than the Base lifetime. The methane lifetime in  $\Delta$ (CC8.5+ODS) [Banerjee et al., 2014, 2016] only shortens by 1.9 years (20%) to 7.4 years which is consistent with the smaller OH increase relative to the present day in that experiment compared to  $\Delta$ CC (see above). While the methane abundance

remains constant in  $\Delta(\text{CC8.5+ODS})$ , the methane flux through the reaction of methane and OH is increased. This leads to the reduced lifetime in that experiment.

Table 6.4 shows the percentage of the global tropospheric methane loss through the reaction with OH in each of the twelve subregions suggested by Lawrence et al. [2001]. Relatively, more methane is lost at higher altitudes in the  $\Delta\text{CC}$  than in the Base experiment; compare the reduction from 22.6% to 20.9% and the increase from 12.9% to 13.8% for the Base and  $\Delta\text{CC}$  experiments at the surface and in the mid-troposphere in the northern tropics ( $0^\circ - 30^\circ\text{N}$ ), respectively. This results from the large increase in tropospheric OH in the tropical middle to upper troposphere in  $\Delta\text{CC}$  (Figure 6.7).

**Table 6.4** Lawrence et al. [2001] analysis of tropospheric methane loss through the reaction with OH. Values are given as percentage of global tropospheric methane loss to 250 hPa. First row: OH from  $\Delta\text{CC}$ ; second row: OH from Base; third row:  $\Delta\text{CC} - \text{Base}$  (%).

Altitude	Model	$90^\circ\text{S} - 30^\circ\text{S}$	$30^\circ\text{S} - 0^\circ$	$0^\circ - 30^\circ\text{N}$	$30^\circ\text{N} - 90^\circ\text{N}$
500	$\Delta\text{CC}$	1.3	5.3	6.0	3.0
- 250	Base	1.2	4.7	5.0	2.6
hPa	% difference	+8.3%	+12.8%	-20.0%	+15.4%
750	$\Delta\text{CC}$	2.4	11.9	13.8	6.4
- 500	Base	2.5	10.1	12.9	6.6
hPa	% difference	-4.0%	-17.8%	+7.0%	-3.0%
Surface	$\Delta\text{CC}$	3.4	16.4	20.9	9.2
- 750	Base	3.8	17.9	22.6	10.0
hPa	% difference	-10.5%	-8.4%	-7.5%	-8.0%

## 6.4.2 $\Delta(\text{CC+methane})$ and $\Delta(\text{CC+ems})$

### Methane

Methane emissions are doubled to  $1170 \text{ Tg}(\text{CH}_4) \text{ yr}^{-1}$  in the  $\Delta(\text{CC+methane})$  and  $\Delta(\text{CC+ems})$  experiments with the increase solely coming from anthropogenic emissions (section 6.1.1). Large methane differences relative to Base and  $\Delta\text{CC}$  are thus expected in both experiments. Recall that all anthropogenic emissions ( $\text{CO}$ ,  $\text{NO}_x$ , etc., as well as methane) change to their projected strengths in 2100 in  $\Delta(\text{CC+ems})$  while only methane emissions are altered in  $\Delta(\text{CC+methane})$ . This methane emission increase significantly influences the tropospheric oxidative capacity by reducing tropospheric OH, acting in the opposite direction to climate change (increased OH due to lightning  $\text{NO}_x$  emission and tropospheric water vapour increases).

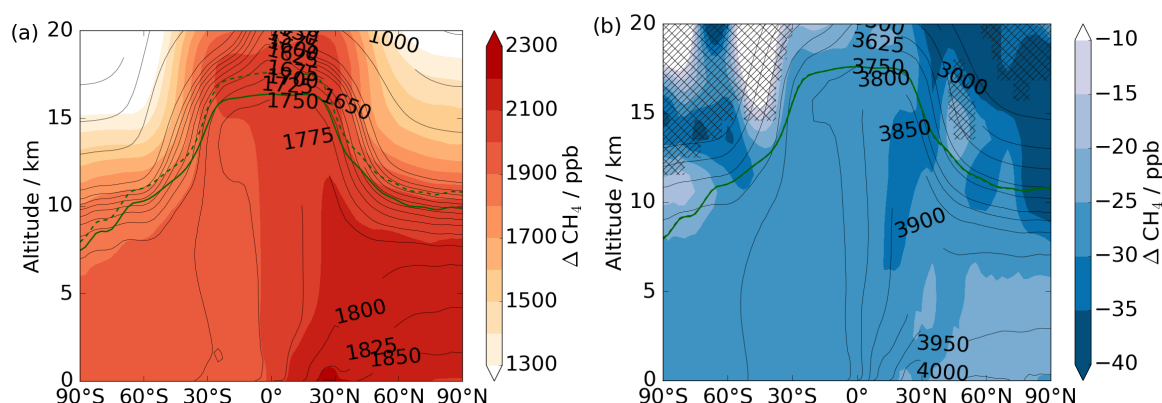


**Fig. 6.10** Changes in annual mean zonally averaged methane concentrations (ppb). (a)  $\Delta(\text{CC}+\text{methane}) - \text{Base}$ ; the contour lines show the absolute methane concentrations for Base (ppb); the tropopause for the Base ( $\Delta(\text{CC}+\text{methane})$ ) experiment is depicted in the solid (dashed) dark green line. (b)  $\Delta(\text{CC}+\text{ems}) - \Delta(\text{CC}+\text{methane})$ ; the contour lines show absolute methane for  $\Delta(\text{CC}+\text{methane})$  (ppb); the tropopause for the  $\Delta(\text{CC}+\text{methane})$  experiment is depicted in the solid dark green line. Hatched areas are not significant at the 95<sup>th</sup> level according to the Student's t-test. Note the different scales for the graphs.

Doubling methane emissions has increased the atmospheric methane burden to 10,336 Tg( $\text{CH}_4$ ) in the  $\Delta(\text{CC}+\text{methane})$  experiment. This is 5547 Tg( $\text{CH}_4$ ) (116%) larger than in Base and 6915 Tg( $\text{CH}_4$ ) (202%) larger than in  $\Delta\text{CC}$ . The increase shows a small latitudinal gradient being larger in the Northern than in the Southern Hemisphere (Figure 6.10 (a)). In the  $\Delta(\text{CC}+\text{ems})$  experiment, atmospheric methane abundance is 76 Tg( $\text{CH}_4$ ) (1%) lower than in  $\Delta(\text{CC}+\text{methane})$  which is fairly uniformly distributed throughout the troposphere (Figure 6.10 (b)). The largest methane increase in the  $\Delta(\text{CC}+\text{methane})$  and  $\Delta(\text{CC}+\text{ems})$  experiments is found in the lowermost troposphere between the equator and 60°N, coincident with the largest methane emission increases in this region.

Globally averaged tropospheric methane concentrations in  $\Delta(\text{CC}+\text{ems})$ , which incorporates all recommended forcings according to the RCP 8.5 scenario, are 3746 ppb. This is in excellent agreement with CMIP5 recommended harmonised methane concentrations for the year 2100 according to RCP 8.5 (3750 ppb, available at <http://www.iiasa.ac.at/web-apps/tnt/RcpDb>, Taylor et al. [2009] and Meinshausen et al. [2011]) The methane lifetime with respect to tropospheric OH loss increased from 6.0 years in  $\Delta\text{CC}$  to 9.2 years for the  $\Delta(\text{CC}+\text{methane})$  and  $\Delta(\text{CC}+\text{ems})$  experiments. The  $\Delta(\text{CC}+\text{ems})$  lifetime lies at the lower end of the ACCMIP multi-model lifetime estimate for the year 2100 ( $10.5 \pm 1.6$  years [Voulgarakis et al., 2013]).

The similarity in the methane burden, and methane loss, in the  $\Delta(\text{CC}+\text{methane})$  and  $\Delta(\text{CC}+\text{ems})$  experiments is expected as the atmospheric abundance is largely dominated by methane emissions, identical in both experiments. The small differences between the two experiments are due to differences in the respective OH fields linked to tropospheric  $\text{CO}$ ,  $\text{NO}_x$  and ozone abundance (which will be discussed in section 6.5).

## OH

The OH fields in  $\Delta(\text{CC}+\text{methane})$  and  $\Delta(\text{CC}+\text{ems})$  are affected by the higher methane concentrations in these experiments. OH is expected to be lower than for the  $\Delta\text{CC}$  experiment due to the increased loss reaction through methane (and  $\text{CO}$ , see below).

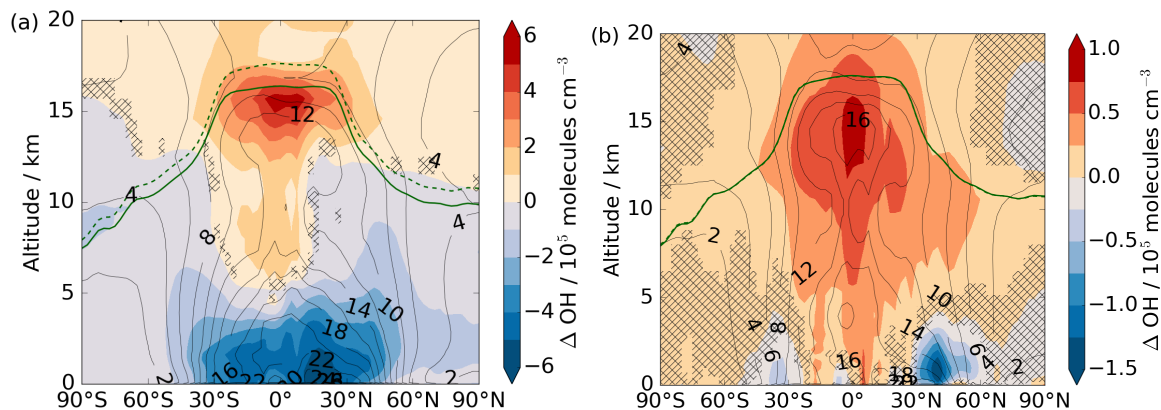


**Fig. 6.11** Changes in annual mean zonally averaged OH concentrations ( $10^5$  molecules  $\text{cm}^{-3}$ ). (a)  $\Delta(\text{CC}+\text{methane}) - \text{Base}$ ; the contour lines show the absolute OH concentrations for Base ( $10^5$  molecules  $\text{cm}^{-3}$ ); the tropopause for the Base ( $\Delta(\text{CC}+\text{methane})$ ) experiment is depicted in the solid (dashed) dark green line. (b)  $\Delta(\text{CC}+\text{ems}) - \Delta(\text{CC}+\text{methane})$ ; the contour lines show the absolute OH concentrations for  $\Delta(\text{CC}+\text{methane})$  ( $10^5$  molecules  $\text{cm}^{-3}$ ); the tropopause for the  $\Delta(\text{CC}+\text{methane})$  experiment is depicted in the solid dark green line. Hatched areas are not significant at the 95<sup>th</sup> level according to the Student's t-test. Note the different scales for the graphs.

Indeed, tropospheric OH concentrations are substantially reduced in  $\Delta(\text{CC}+\text{methane})$  and  $\Delta(\text{CC}+\text{ems})$ , at  $10.5 \times 10^5$  and  $10.6 \times 10^5$  molecules  $\text{cm}^{-3}$  (tropospheric airmass-weighted average), respectively. OH concentrations in the  $\Delta(\text{CC}+\text{ems})$  experiment are thus  $1.4 \times 10^5$  molecules  $\text{cm}^{-3}$  (12%) smaller than the Base OH concentrations. Thus, the anthropogenic emission changes (methane and other species) outweigh the climate induced OH increases leading to a 32% decrease in tropospheric OH compared to the  $\Delta\text{CC}$  experiment. The North-South gradient of the OH field remains the same for all simulations discussed in this

chapter, with higher OH concentrations in the Northern than in the Southern Hemisphere (North-South gradient of 1.3). The OH decrease noted in  $\Delta(\text{CC+ems})$  also agrees well with the corresponding ACCMIP multi-model average OH decrease of  $11 \pm 8\%$  relative to present day [Voulgarakis et al., 2013].

While the global mean OH abundance decreases, a dipole pattern can be noted in the zonally averaged picture (Figure 6.11 (a)). As in the  $\Delta\text{CC}$  experiment, tropical  $\Delta(\text{CC+methane})$  OH increases in the middle to upper troposphere relative to Base. Increases in lightning  $\text{NO}_x$  emissions in this region due to the climate induced circulation changes lead to higher ozone levels and thus greater OH production (see section 6.5). This tropical upper tropospheric OH increase is in contrast to a reduction in OH concentrations in the lowest 5 km of the troposphere (-10 – -40% from the tropics to poles). This decrease is largest in the tropics with absolute levels being  $6 \times 10^5$  molecules  $\text{cm}^{-3}$  smaller compared to Base. The OH reduction is attributed to increased sinks for tropical OH close to the surface, by reaction with methane and CO.

Small differences can be noted in the OH zonal mean distribution for the  $\Delta(\text{CC+methane})$  and  $\Delta(\text{CC+ems})$  experiments (Figure 6.11 (b)).  $\Delta(\text{CC+ems})$  tropical upper tropospheric OH is  $1 \times 10^5$  molecules  $\text{cm}^{-3}$  higher while OH decreases at the surface between  $30^\circ\text{N}$  and  $60^\circ\text{N}$  ( $2 \times 10^5$  molecules  $\text{cm}^{-3}$ ). These surface changes are likely linked to the differences in the modelled  $\text{NO}_x$ , CO and ozone fields for these two experiments (see below).

In summary, increased tropospheric temperatures lead to a higher tropospheric water vapour content which is reflected in higher tropospheric OH abundance for the  $\Delta\text{CC}$  experiment (present day emissions). The large tropospheric OH sink (30% greater than Base) causes methane concentrations to decrease by 30% and results in a shorter methane lifetime, as seen in previous studies [John et al., 2012; Morgenstern et al., 2013; Banerjee et al., 2014, 2016]. Doubling methane emissions in the  $\Delta(\text{CC+methane})$  and  $\Delta(\text{CC+ems})$  experiments doubles the atmospheric methane burden (actually 116% and 114%, respectively). The OH fields for these two experiments are similar in their global strength (12% lower than Base and 32% lower than  $\Delta\text{CC}$ ). However the  $\Delta(\text{CC+ems})$  OH field is slightly lower in the Northern Hemisphere and higher in the tropics compared to  $\Delta(\text{CC+methane})$ . This is linked to CO,  $\text{NO}_x$  and ozone abundance differences in the two experiments which will be discussed below.

## 6.5 Changes to other key tropospheric species

This section aims to investigate further the drivers of the tropospheric OH change to gain more understanding of the interactions between temperature/water vapour, methane and CO, NO<sub>x</sub> and ozone. The large OH and methane changes discussed in the previous section both influence, and are influenced by, the tropospheric CO, NO<sub>x</sub> and ozone abundance which will be discussed here. First, the effect of temperature changes alone on tropospheric composition will be discussed followed by the emission influences.

### 6.5.1 ΔCC

#### CO

The increase in tropospheric OH in ΔCC (section 6.4.1) not only causes methane to decrease but also leads to decreases in tropospheric CO (Figure 6.12, top row). These decreases are largest in the tropics (25 ppb, 25%) and are less pronounced in the extra-tropics of both hemispheres. While CO in the Northern Hemisphere shows larger decreases on an absolute level, the relative CO decreases in the Southern Hemisphere are larger. The increase in CO at the tropical tropopause is linked to the upwards shift of the tropopause under future climate. With negligible CO concentrations in the stratosphere, the increase is over a small background and therefore not particularly important.

#### NO<sub>x</sub>

Tropospheric ΔCC NO<sub>x</sub> levels (Figure 6.12, middle row) increase in the tropics, especially in the upper tropical troposphere and lower stratosphere where the increase amounts to 100 ppt (80%). This increase is linked to lightning NO<sub>x</sub> emissions which equal 10.6 Tg(N) yr<sup>-1</sup> in the ΔCC experiment, 4.0 Tg(N) yr<sup>-1</sup> (61%) greater than in Base. Lightning NO<sub>x</sub> is closely linked to convection which increases in a warmer (Figure 6.5), moister (Figure 6.6) climate and the depth of which is affected by the higher tropopause [e.g Zeng and Pyle, 2003; Young et al., 2013]. The values reported here are comparable to the corresponding experiments presented in Banerjee et al. [2014] and slightly larger than the ACCMIP multi-model mean [Voulgarakis et al., 2013]. Increased lightning NO<sub>x</sub> emissions lead to increased ozone production in the upper tropical troposphere which produces more OH in this region. The tropical OH increase noted in Figure 6.7 can thus be attributed to the lightning NO<sub>x</sub> emissions.

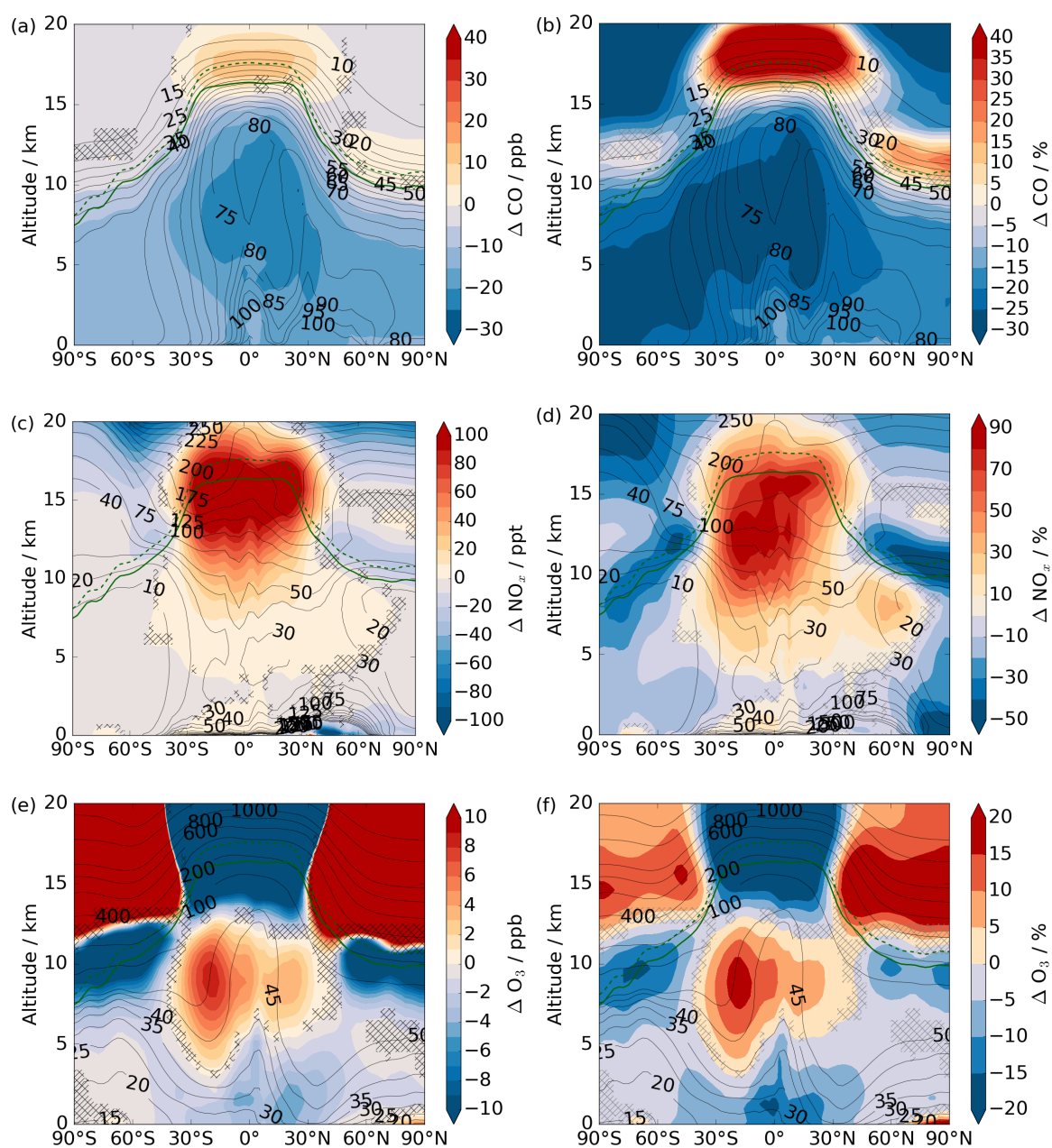


**Fig. 6.12** Changes in annual mean zonally averaged CO (a and b, top row, ppb), NO<sub>x</sub> (c and d, middle row, ppt) and ozone (e and f, bottom row, ppb) between  $\Delta\text{CC}$  and Base. The second column shows percentage changes. The contour lines in all graphs represent the absolute levels for the Base experiment. Hatched areas are not significant at the 95th level according to the Student's t-test. The tropopause for the Base ( $\Delta\text{CC}$ ) experiment is depicted in the solid (dashed) dark green line. Note the different scales for the graphs.

## Ozone

Ozone changes in  $\Delta$ CC show large spatial variability (Figure 6.12, bottom row). Ozone mixing ratios increase in the mid to upper tropical troposphere while lower tropical stratospheric ozone is reduced in  $\Delta$ CC. The stratospheric response is consistent with the strengthening of the overturning Brewer Dobson Circulation under climate change [e.g. Butchart et al., 2006]. Increases in tropospheric tropical ozone are larger to the south (8 ppb, 15%) than to the north of the equator (4 ppb, 5%). This ozone increase in the tropical upper troposphere follows the increased  $\text{NO}_x$  levels in this region, fuelling ozone production leading to increased OH (Figure 6.7). Increased transport from ozone rich stratospheric air into the troposphere also contributes to the higher ozone levels here [e.g Butchart et al., 2006]. Tropical surface ozone and free tropospheric ozone in both hemispheres are reduced in  $\Delta$ CC likely because of higher atmospheric water vapour in these regions (Figure 6.6) driving ozone loss (and formation of OH) [e.g. Brasseur et al., 2006]. In contrast, surface ozone in the high northern latitudes is increased by 20%.

Overall, the tropospheric ozone burden increases from 336 Tg( $\text{O}_3$ ) in Base to 353 Tg( $\text{O}_3$ ) in  $\Delta$ CC (see Table 6.5 below which gives the ozone burden for all four experiments discussed in this chapter). This increase of 17 Tg( $\text{O}_3$ ) is much smaller than the values reported in Banerjee et al. [2014] for the equivalent experiments (70 Tg( $\text{O}_3$ )). Banerjee et al. [2014] performed an offline calculation aimed to represent the OH feedback on methane. They estimated that the methane adjustment, i.e. methane responding to the changed tropospheric OH levels, lowers the tropospheric ozone burden by 13 Tg( $\text{O}_3$ ) for the RCP 8.5 scenario to a net 57 Tg( $\text{O}_3$ ) increase relative to present day levels. This is still much larger than the ozone burden change estimated here. These differences highlight the sensitivity and thus importance of moving from concentration boundary conditions to flux boundary conditions in chemistry climate models.

In summary for this section, higher tropospheric temperatures increase tropospheric water vapour which leads to higher OH concentrations. These high OH concentrations lead, in turn, to methane and CO reductions which further enhance the OH increase.  $\text{NO}_x$  concentrations increase due to lightning emission increases in the tropical upper troposphere where OH production is subsequently enhanced leading to ozone increases in this region. Overall, the tropospheric ozone burden increases under a future climate but the lightning  $\text{NO}_x$  effect (leading to increases in ozone) is buffered by reduced methane concentrations and higher water vapour which reduce ozone production [e.g. Brasseur et al., 2006], especially in the lower troposphere. The next section will explore how projected anthropogenic emission

changes influence CO, NO<sub>x</sub> and ozone and how they interact with their climate-induced changes.

### 6.5.2 $\Delta(\text{CC+ems})$ and $\Delta(\text{CC+methane})$

In addition to the changing climate in the  $\Delta\text{CC}$  experiment, (anthropogenic) emissions are changed in the  $\Delta(\text{CC+methane})$  and  $\Delta(\text{CC+ems})$  experiments. Only methane emissions are altered in the  $\Delta(\text{CC+methane})$  experiment, doubling to 1170 Tg(CH<sub>4</sub>) yr<sup>-1</sup> for the year 2100 according to RCP 8.5 scenario. In contrast, all UKCA emission species such as NO<sub>x</sub>, methane and CO (see Table 6.2 for details) follow their projected emission strength in  $\Delta(\text{CC+ems})$ . This section explores how CO, NO<sub>x</sub> and ozone concentrations change in these two experiments.

#### CO

Large CO increases can be noted in  $\Delta(\text{CC+methane})$  relative to Base throughout the troposphere (Figure 6.13 (a)). The largest increases can be found in the lower tropical troposphere and at the tropical tropopause (50 ppb). These increases are due to increased CO production following the methane oxidation with the much higher methane abundance in  $\Delta(\text{CC+methane})$ .

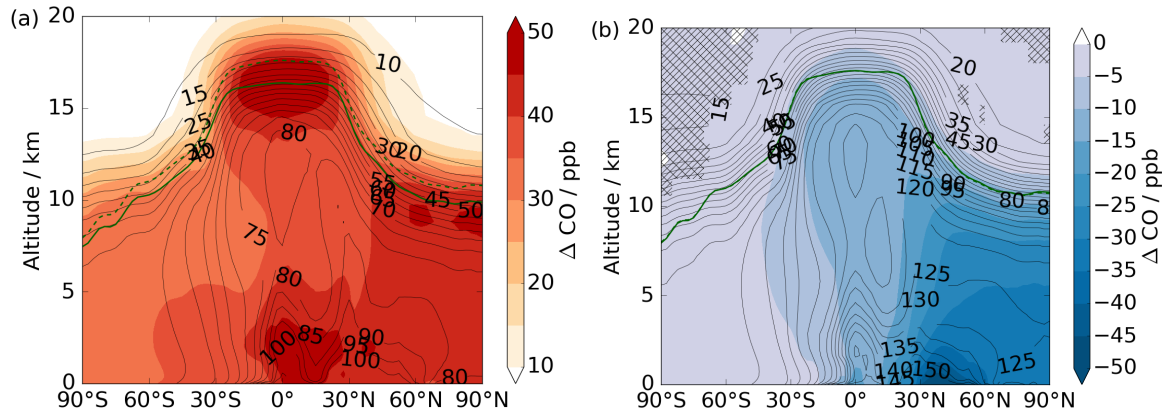


**Fig. 6.13** Changes in annual mean zonally averaged CO concentrations (ppb). (a)  $\Delta(\text{CC}+\text{methane}) - \text{Base}$ ; the contour lines show the absolute CO levels for Base (ppb); the tropopause for the Base ( $\Delta(\text{CC}+\text{methane})$ ) experiment is depicted in the solid (dashed) dark green line. (b)  $\Delta(\text{CC}+\text{ems}) - \Delta(\text{CC}+\text{methane})$ ; the contour lines show the absolute CO levels for  $\Delta(\text{CC}+\text{methane})$  (ppb); the tropopause for  $\Delta(\text{CC}+\text{methane})$  is depicted in the solid dark green line. Hatched areas are not significant at the 95<sup>th</sup> level according to the Student's t-test. Note the different scales for the graphs.

In the  $\Delta(\text{CC}+\text{ems})$  experiment surface CO emissions are decreased by  $379 \text{ Tg}(\text{CO}) \text{ yr}^{-1}$  (35%, see Table 6.2). These emission decreases act in the opposite direction to the chemical CO production noted in  $\Delta(\text{CC}+\text{methane})$ , resulting in CO concentration decreases in the Northern Hemisphere, especially between  $30^\circ\text{N}$  and  $60^\circ\text{N}$ , in  $\Delta(\text{CC}+\text{ems})$  relative to  $\Delta(\text{CC}+\text{methane})$  (Figure 6.13 (b)). This CO difference between  $\Delta(\text{CC}+\text{methane})$  and  $\Delta(\text{CC}+\text{ems})$  highlights the effect of emission decreases on atmospheric CO levels. It shows how CO emission changes counteract the chemical CO production increase following methane loss, particularly in the Northern Hemisphere where the CO emissions are predominantly located. Clearly there is a large range of possible future emission scenarios for methane and CO. The balance between possible methane emission increases and CO decreases will have a profound impact on the tropospheric oxidising capacity (see below).

## **NO<sub>x</sub>**

There is an increase in  $\Delta(\text{CC}+\text{methane})$  NO<sub>x</sub> concentrations in the tropical troposphere, with the largest increases occurring in the upper troposphere (Figure 6.14 (a)). As discussed above, the NO<sub>x</sub> increase is linked to increased lightning NO<sub>x</sub> emissions ( $10.7 \text{ Tg}(\text{N}) \text{ yr}^{-1}$  in  $\Delta(\text{CC}+\text{methane})$  compared to  $6.60 \text{ Tg}(\text{N}) \text{ yr}^{-1}$  in Base). These increases in NO<sub>x</sub> lead to higher ozone production (Figure 6.15 (a)) and thus influence the tropospheric OH abundance.

Northern Hemispheric surface  $\text{NO}_x$  decreases in  $\Delta(\text{CC}+\text{methane})$  are likely due to higher hydrocarbon concentrations (e.g. methane and CO) reacting with  $\text{NO}_x$ .

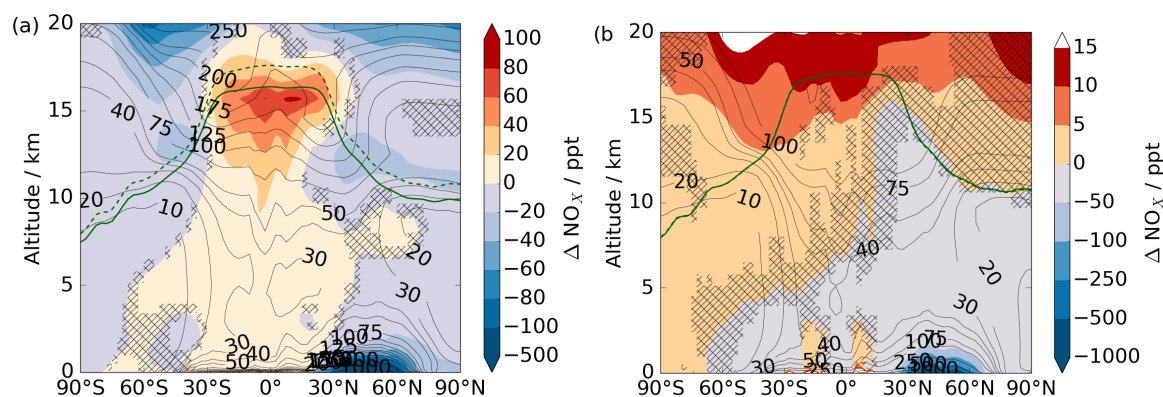


**Fig. 6.14** Changes in annual mean zonally averaged  $\text{NO}_x$  concentrations (ppt). (a)  $\Delta(\text{CC}+\text{methane}) - \text{Base}$ ; the contour lines show the absolute  $\text{NO}_x$  levels for Base (ppt); the tropopause for the Base ( $\Delta(\text{CC}+\text{methane})$ ) experiment is depicted in the solid (dashed) dark green line. (b)  $\Delta(\text{CC}+\text{ems}) - \Delta(\text{CC}+\text{methane})$ ; the contour lines show the absolute  $\text{NO}_x$  levels for  $\Delta(\text{CC}+\text{methane})$  (ppt); the tropopause for  $\Delta(\text{CC}+\text{methane})$  is depicted in the solid dark green line. Hatched areas are not significant at the 95<sup>th</sup> level according to the Student's t-test. Note the different scales for the graphs.

Tropospheric  $\text{NO}_x$  is similar in the  $\Delta(\text{CC}+\text{ems})$  and  $\Delta(\text{CC}+\text{methane})$  experiments. Differences occur around the  $\text{NO}_x$  emission region in the Northern Hemisphere where  $\Delta(\text{CC}+\text{ems})$   $\text{NO}_x$  concentrations are lower than in  $\Delta(\text{CC}+\text{methane})$  (Figure 6.14 (b)). Overall, the surface emissions of  $\text{NO}_x$  decrease in the future (see Table 6.2). These surface  $\text{NO}_x$  decreases in  $\Delta(\text{CC}+\text{ems})$  relative to  $\Delta(\text{CC}+\text{methane})$  can likely explain the tropospheric OH differences in these regions noted above (Figure 6.11 (b)). This surface  $\text{NO}_x$  concentration decrease influences surface ozone levels, as discussed next.

## Ozone

Tropospheric ozone is higher in  $\Delta(\text{CC}+\text{methane})$  relative to Base throughout the troposphere (Figure 6.15 (a)). The largest increases (up to 18 ppb) are in the upper troposphere around 30°S and 30°N. Stratospheric circulation changes are thought to lead to increased downward transport from the stratosphere [e.g Butchart et al., 2006]. Furthermore, increased ozone production is expected due to increases in lightning  $\text{NO}_x$  emissions. Increased chemical ozone loss due to higher water vapour in this region [e.g. Brasseur et al., 2006] and surface

$\text{NO}_x$  emission reductions (especially in the Northern Hemisphere) lead to a decrease in net ozone production.

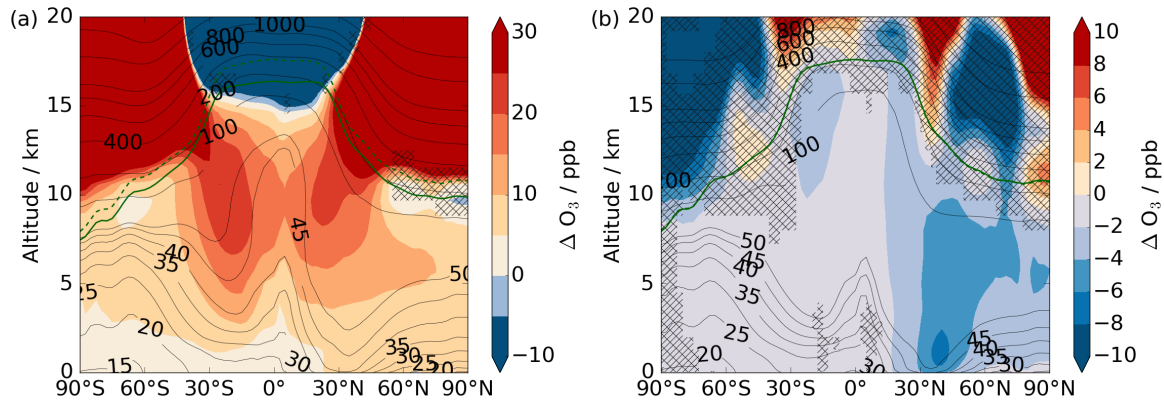


**Fig. 6.15** Changes in annual mean zonally averaged ozone (ppb) for  $\Delta(\text{CC+ems}) - \text{Base}$  (a) and  $\Delta(\text{CC+methane}) - \Delta(\text{CC+ems})$  (b). The contour lines in all graphs represent the absolute levels for the Base (a) or  $\Delta(\text{CC+ems})$  (b) experiment. Hatched areas are not significant at the 95<sup>th</sup> level according to the Student's t-test. The tropopause for the Base ( $\Delta(\text{CC+ems})$ ) experiment is depicted in the solid dark green line. Note the different scales for the graphs.

Figure 6.15 (b) highlights the ozone difference due to CO,  $\text{NO}_x$  and other surface emission decreases projected under RCP 8.5. While the Southern Hemispheric ozone differences are small between the  $\Delta(\text{CC+methane})$  and  $\Delta(\text{CC+ems})$ , differences can be noted in the Northern Hemisphere. There, decreased ozone concentrations can be noted in  $\Delta(\text{CC+ems})$ , especially between 30°N and 60°N which is due to the lower  $\text{NO}_x$  and CO surface emissions in the  $\Delta(\text{CC+ems})$  experiment. Figure 6.15 (b) thus describes the impact of anthropogenic ozone precursor emissions on tropospheric ozone and highlights the benefits of air pollution mitigation.

The ozone burden for all four experiments discussed in this chapter and, for comparison, the ACCMIP multi-model mean estimates [Young et al., 2013] is shown in Table 6.5. The total tropospheric ozone burden increases by 91 Tg( $\text{O}_3$ ) to 427 Tg( $\text{O}_3$ ) in the  $\Delta(\text{CC+ems})$  experiment relative to Base. This is slightly higher than the ACCMIP multi-model mean ( $60 \pm 22$  Tg( $\text{O}_3$ )) [Young et al., 2013]. The tropospheric ozone increase will have implications for human health and crop yield as noted in numerous studies [e.g. Fiore et al., 2015; Monks et al., 2015; von Schneidemesser et al., 2015].

The ozone burden difference between  $\Delta(\text{CC+ems})$  and Base is a result of different drivers of tropospheric ozone, such as a changing climate and precursor emission changes. With the

**Table 6.5** Tropospheric ozone burden ( $\text{Tg}(\text{O}_3)$ ) for the four climate change experiments presented in this chapter and their difference to the Base experiment. For comparison purposes the ACCMIP multi-model estimates for the present day and the year 2100 are included [Young et al., 2013].

Experiment	Burden ( $\text{Tg}(\text{O}_3)$ )	Difference to Base ( $\text{Tg}(\text{O}_3)$ )
Base	336	–
$\Delta\text{CC}$	353	17
$\Delta(\text{CC}+\text{ems})$	427	91
$\Delta(\text{CC}+\text{methane})$	443	107
ACCMIP Base	$337 \pm 23$	–
ACCMIP $\text{CC}+\text{ems}$	$395 \pm 36$	$60 \pm 22$

experiments presented in this chapter the different contributions to the ozone burden changes can be distinguished. This is shown in Figure 6.16.

The ozone burden changes in the  $\Delta\text{CC}$  experiment relative to Base can be attributed to climate driven ozone changes. These are, for instance, ozone production from increased lightning  $\text{NO}_x$  emissions and increased transport from the stratosphere but also increased ozone loss due to higher tropospheric water vapour content. The ozone burden change associated to these climate forcings amounts to a net ozone increase of 17  $\text{Tg}(\text{O}_3)$  in the  $\Delta\text{CC}$  experiment relative to Base as discussed above, shown in green in Figure 6.16.

The  $\Delta(\text{CC}+\text{methane})$  ozone burden is 107  $\text{Tg}(\text{O}_3)$  higher than the Base ozone burden of which 17  $\text{Tg}(\text{O}_3)$  can be attributed to the changing climate (green) assuming the effects are linearly additive. Thus, the doubling of methane emissions in the  $\Delta(\text{CC}+\text{methane})$  experiment results in a 90  $\text{Tg}(\text{O}_3)$  ozone burden increase shown in orange in Figure 6.16. This corresponds to a 0.15  $\text{Tg}(\text{O}_3)$  ozone burden increase per one  $\text{Tg}(\text{CH}_4) \text{ yr}^{-1}$  methane emission increase, similar to the value noted in chapter 5 and within the range given in Fiore et al. [2008].

The  $\Delta(\text{CC}+\text{methane})$  ozone burden is 16  $\text{Tg}(\text{O}_3)$  higher than the  $\Delta(\text{CC}+\text{ems})$  burden. It can thus be concluded that the decrease in anthropogenic surface emissions of  $\text{NO}_x$  and CO (and others) cause tropospheric ozone to decrease by 16  $\text{Tg}(\text{O}_3)$  shown in hatched blue in Figure 6.16.

Methane is therefore the dominant driver of the tropospheric ozone burden increase in the experiments presented here and uncertainties in methane emissions have large influences on future air quality. This supports numerous previous studies which call for methane emission

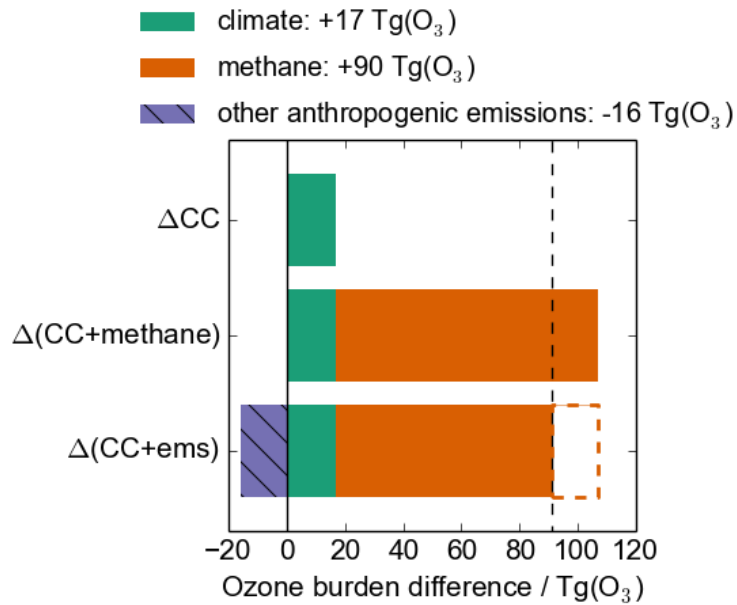


**Fig. 6.16** Contribution to the ozone burden difference between the future climate simulations and Base. Ozone changes due to climate changes (e.g. circulation) are shown in green, ozone changes due to increased methane emissions in orange and ozone changes due to other anthropogenic surface emissions in hatched blue.

mitigation strategies to reduce the future ozone burden [e.g. Fiore et al., 2008; Wild et al., 2012; Morgenstern et al., 2013; Stevenson et al., 2013; Voulgarakis et al., 2013].

Sections 6.3 and 6.4 have shown that changes in climate and, hence, temperature and water vapour, as well as changes in methane emissions all have an important influence on methane and OH. In this section, changes in the concentrations of other gases (ozone, NO<sub>x</sub> and CO) which also have an important coupling to methane and OH have been explored. Increases in methane abundance under a future climate led to tropospheric CO increases following methane oxidation despite CO surface emission decreases. Furthermore, the doubling of methane emissions drastically increased the tropospheric ozone burden highlighting the tight coupling between the species and the importance of methane mitigation for tackling climate change and air quality problems.

## 6.6 Summary

This chapter has investigated the tropospheric composition in a projected future climate. Three experiments were compared to a present day scenario which was identical to the  $\Delta$ ems experiment presented in chapter 5, referenced as ‘Base’ in this chapter. The present day Base experiment showed excellent agreement between modelled and observed surface methane concentrations. The modelled methane lifetime with respect to tropospheric OH loss (8.6 years) agreed well with the ACCMIP multi-model mean ( $9.3 \pm 0.9$  years [Voulgarakis et al., 2013]) but was short compared to observational estimates ( $11.2 \pm 1.3$  years [Prather et al., 2012]). Small CO, ozone and NO<sub>x</sub> model biases were highlighted but were comparable to other chemistry-climate models. The Base tropospheric ozone burden of 336 Tg(O<sub>3</sub>) was in good agreement with recent multi-model studies ( $334 \pm 39$  Tg(O<sub>3</sub>) [Stevenson et al., 2006] and  $339 \pm 23$  Tg(O<sub>3</sub>) [Young et al., 2013]).

The future climate perturbation experiments presented in this chapter simulated the year 2100 according to the RCP 8.5 scenario with identical climate forcings (SSTs, sea ice, ozone depleting substance concentrations and greenhouse gas concentrations in the radiation code). Three different emission scenarios were simulated with these perturbation experiments:

- $\Delta$ CC: present day emissions were imposed, identical to those in the Base
- $\Delta$ (CC+methane): only the methane emission strength was perturbed according to the future scenario while all other emissions were kept identical to the Base experiment
- $\Delta$ (CC+ems): all anthropogenic (NO<sub>x</sub>, CO, methane etc.) emissions followed the RCP 8.5 projections

These three experiments showed similar increases in tropospheric water vapour due to the warmer climate.

In the  $\Delta\text{CC}$  experiment, i.e. climate change only, the increased water vapour content (and lightning  $\text{NO}_x$  induced OH production) led to a 30% increase relative to the present day Base experiment in globally averaged (airmass-weighted) tropospheric OH concentrations to  $15.9 \times 10^5$  molecules  $\text{cm}^{-3}$ . This OH increase decreased tropospheric methane concentrations by 30% compared to the Base experiment throughout the troposphere.  $\text{NO}_x$  concentration increases were noted in the tropical upper troposphere and attributed to lightning  $\text{NO}_x$  emission increases because of more convection in a warmer, moister climate. These higher  $\text{NO}_x$  concentrations caused increased tropospheric ozone production in this region leading to enhanced OH concentrations as noted above. These upper tropospheric  $\text{NO}_x$  increases were of the same magnitude in all three climate change experiments.

The doubling of methane emissions in the  $\Delta(\text{CC}+\text{ems})$  and  $\Delta(\text{CC}+\text{methane})$  experiments led to a slightly more than doubled atmospheric methane burden. Methane increased throughout the troposphere but the increases were greater in the Northern Hemisphere where the bulk of the emissions was located. This large methane burden increase in the  $\Delta(\text{CC}+\text{ems})$  and  $\Delta(\text{CC}+\text{methane})$  experiments reduced the tropospheric OH sink to  $10.6 \times 10^5$  molecules  $\text{cm}^{-3}$  (airmass-weighted). This was 13% smaller than Base OH and agreed well with the ACCMIP multi-model mean for the year 2100 [Voulgarakis et al., 2013]. The OH reduction was found mainly in the lower troposphere where high methane and CO concentrations in the  $\Delta(\text{CC}+\text{methane})$  and  $\Delta(\text{CC}+\text{ems})$  experiments fuelled OH loss. The lightning  $\text{NO}_x$  emission induced increase in upper tropospheric OH was still seen in these experiments but overall this effect was smaller than the surface OH reduction.

Reduced tropospheric CO concentrations were found in  $\Delta\text{CC}$ . This was attributed to the combined effect of a large OH sink in the moister climate modelled here and reduced chemical production because of lower methane concentrations in this experiment. In contrast, CO concentrations increased throughout the troposphere in the  $\Delta(\text{CC}+\text{methane})$  experiment with larger increases in the Northern Hemisphere. This was due to increased chemical production following methane loss with the higher methane concentrations in this experiment. In the  $\Delta(\text{CC}+\text{ems})$  experiment surface CO emissions were reduced according to the RCP 8.5 scenario. This counteracted the CO production noted in the  $\Delta(\text{CC}+\text{methane})$  experiment in the Northern Hemisphere where the bulk of emissions were located. However, overall CO production following methane oxidation outweighed this CO reduction due to CO emission changes.

In the  $\Delta\text{CC}$  experiment ozone decreased at the surface and in the extra-tropical free troposphere due to increased ozone loss because of higher water vapour concentrations. This decrease was outweighed by ozone production from increased lightning  $\text{NO}_x$  emissions in the tropical upper troposphere, with additional contribution from transport downwards from the stratosphere. Overall, the tropospheric ozone burden increased by 17  $\text{Tg}(\text{O}_3)$  in the  $\Delta\text{CC}$  experiment. Projected decreases in surface  $\text{NO}_x$  and CO emissions according to RCP 8.5 acted to reduce the tropospheric ozone burden by 16  $\text{Tg}(\text{O}_3)$  showing the benefits of air pollution mitigation. Doubling methane emissions showed the largest overall impact on the tropospheric ozone burden. In the  $\Delta(\text{CC}+\text{methane})$  experiment 90  $\text{Tg}(\text{O}_3)$  of the ozone burden increase could be attributed to the methane concentration increase (0.15  $\text{Tg}(\text{O}_3)$  ozone burden increase per one  $\text{Tg}(\text{CH}_4) \text{ yr}^{-1}$  methane emission increase).

These results highlight the importance of mitigating methane emissions, not only to mitigate climate change but also to improve air quality. Understanding the tropospheric OH budget, and the interactions of OH with a range of atmospheric species, remains a major research challenge.

# 7 | Conclusions and future work

## 7.1 Conclusions

This thesis has presented analyses from a modelling study of atmospheric methane with the Unified Model coupled to the United Kingdom Chemistry and Aerosol submodel (UM-UKCA). The impacts of a changing tropospheric methane sink and changing methane emissions were investigated. A revised methane emission map was established that led to excellent agreement with observations and the atmospheric composition response to projected climate changes was analysed.

The chemistry-climate model used in this thesis differed from other modelling studies through its use of a methane emission flux boundary condition instead of a concentration boundary condition. This is closer to the ‘real’ world but computationally more expensive. Methane’s relatively long lifetime requires long spin-up times and often leads to trends in modelled methane concentrations [e.g. Stevenson et al., 2013]. Here, spin-up times were reduced by continuously extrapolating methane concentrations, effectively nudging them to their stable levels.

A new chemistry scheme was developed and implemented into UKCA. Oxidants were prescribed removing methane’s chemical self-feedback and rendering methane chemistry linear. This new non-interactive chemistry scheme allowed the effect of different estimates for global OH (concentrations and distribution) on atmospheric methane to be analysed. Interactive and non-interactive methane chemistry were simulated in parallel. Methane emissions and OH concentrations could thus be perturbed and their effects on atmospheric methane could be separated.

An initial methane emission map was created based on recent emission estimates with a global source strength of  $548 \text{ Tg}(\text{CH}_4) \text{ yr}^{-1}$ . Interactively simulated methane was low biased relative to observations (9%) while good agreement was achieved for the latitudinal gradient.

Global interactively modelled tropospheric OH was greater than suggested by estimates based on methyl chloroform measurements and had a larger North-South gradient. Analysis suggested that this might be linked to biases in interactively modelled NO<sub>x</sub>, CO and ozone as well as methane. Thus, in order to improve interactively modelled methane emission increases and/or alterations to the OH sink were required.

An OH field based on observations was therefore prescribed in the non-interactive chemistry scheme. This allowed the effect of lower global OH concentrations (18% reduction) and equal amounts of OH in the Northern and Southern Hemisphere on non-interactive methane to be assessed. This led to much improved global methane concentrations which were in good agreement with observations. However, the latitudinal methane gradient was overestimated. Analysis suggested that methane emissions be redistributed into the tropics which was subsequently backed by a local optimisation on a multi-variate linear regression. Increases in tropical methane emissions, in particular South American wetlands, were identified as key regions to improve the global representation of atmospheric methane.

Thus, new experiments were conducted in which methane emissions from the Northern Hemisphere (north of 30°N) were shifted into the (southern) tropics. The global methane emission strength was increased to 585 Tg(CH<sub>4</sub>) yr<sup>-1</sup> (+7%), a strength increase supported by prior analyses. These emission estimates resulted in excellent modelled methane agreement with observations both for global average methane concentrations and the latitudinal gradient. This is impressive as those few modelling studies that use methane emissions often resort to scaling methane concentration to match observations [e.g. Dalsøren et al., 2016]. Scaling the methane abundance, however, neglects methane's impact on other chemical species, such as ozone, which can then not be fully represented in the model.

The necessity of incorporating methane emissions into global models was highlighted with experiments assessing methane emission effects on future atmospheric composition. These experiments demonstrated methane's crucial role in determining the future atmospheric oxidative capacity and its impact on future air quality. These results confirm the importance of mitigating methane emissions, not only from a climate warming point of view but also in light of air quality issues. Uncertainties associated with methane projections are of particular importance seeing methane's direct and indirect chemical (e.g. CO and ozone) and radiative effects.

The newly developed non-interactive chemistry scheme is useful, as shown in this thesis, to investigate impacts of different emission regions and source types on global methane. Results can be used to optimise emission maps and non-interactive chemistry schemes are

computationally less expensive than interactive ones. However, the chemical self-feedback of methane cannot be considered. Thus, matching observations well with a non-interactive chemistry scheme cannot represent the ‘real’ world as well as interactive chemistry models. This is especially important as the non-interactive chemistry scheme was shown to impact the latitudinal methane gradient. Thus, ultimately, modelling interactive chemistry is necessary to further understanding of atmospheric methane chemistry and methane trends.

Results presented in this thesis illustrated the sensitivity of atmospheric methane to the coupled methane-OH system. Using different approaches to determine the drivers of the model-observation mismatch allowed a new methane emission map to be devised. A small emission increase and an emission shift to tropical region drastically improved modelled methane and had impacts on other species such as ozone. This highlighted that replacing the methane concentration boundary condition with methane emissions in a chemistry-climate model was not only feasible but necessary to gauge the full impact of methane on atmospheric composition.

## 7.2 Future work

This thesis has investigated the strong coupling between methane and the hydroxyl radical. The sensitivity of atmospheric methane abundance to small methane source and sink changes highlights the importance of understanding the methane budget. It is essential to reduce uncertainties regarding methane’s source strength and distribution as well as to improve understanding of the global OH field. In this section some ideas for further work are outlined.

The UM-UKCA version used for the experiments in this thesis (vn. 7.3) has a relatively coarse horizontal resolution. A newer model version with a higher resolution and improved dynamical representation might improve the representation of atmospheric methane and other chemical species in the model. A better representation of the stratospheric age of air has been shown in these newer versions which would improve the stratospheric representation of methane [Hardiman et al., 2015]. This can in turn affect tropospheric methane through stratospheric to tropospheric transport [e.g Saad et al., 2016].

### **Improving the understanding of tropospheric OH**

The analysis has highlighted the discrepancy of the model’s OH field compared with observational based estimates and its high sensitivity to future changes. Further investigating the

drivers of tropospheric OH could reduce the uncertainty in atmospheric methane associated with the OH distribution and improve modelled OH. It is proposed to include methyl chloroform in the model presented in this thesis as done, for instance, in Warwick et al. [2016] and the TransCom-CH<sub>4</sub> studies [Patra et al., 2011]. This compound provides constraints on the global OH field as its atmospheric loss is dominated by OH and its emissions are near to zero and well monitored [e.g. Patra et al., 2014; Prinn et al., 2005; Holmes et al., 2013]. Comparing modelled methyl chloroform to observations would furthermore allow conclusions about the model's (interhemispheric) transport.

Additionally, further investigations of the model's CO, NO<sub>x</sub> and ozone biases are necessary as pointed out in numerous previous studies [e.g. Naik et al., 2013; Strode et al., 2015; Young et al., 2013; Stevenson et al., 2013]. Reducing these biases (and intermodel spread) would increase the confidence in the model's OH field and likely improve comparison to OH estimates based on observations. Nicely et al. [2017] showed in a study of eight CTMs that ozone and CO differences between models affect the methane lifetime differences between these models by 0.3 and 0.23 years, respectively. They estimated ozone and CO to be the third and fourth most important causes for lifetime differences (after model mechanistic differences and ozone photolysis). Improving the model's representation for these species is therefore an important scientific goal to reconcile modelled OH with observations.

### **Modelling isotopic methane**

Analysis presented in this thesis was entirely based on the total methane abundance. While methane in the non-interactive experiments was tagged by source region and type no information was included regarding its isotopic composition. As outlined in the introduction (chapter 1) methane emission sources have distinct isotopic signatures [e.g. Fisher et al., 2006; Schwietzke et al., 2016]. Modelling isotopic methane and comparison to isotopic measurements would provide a further important constraint on the methane emission distribution and strength [e.g. Warwick et al., 2016].

The tropospheric chlorine sink has previously been shown to affect the isotopic ratio of tropospheric methane [e.g. Allan et al., 2007]. Attempts to constrain tropospheric chlorine are ongoing [e.g. Hossaini et al., 2016a]. Modelling isotopes could therefore be used to investigate and improve the tropospheric chlorine sink and further the scientific understanding of its role in methane oxidation.

Isotopic measurements have been used in attributing the recent methane increase to biogenic emissions [Nisbet et al., 2016; Schaefer et al., 2016]. It is not currently well established whether the biogenic emission increase is attributed to wetland emissions or agricultural practices (rice and animals). All experiments presented in this thesis were performed in a free running climate model. The model's meteorology can also be nudged to observations (see Telford et al. [2013] for details). With nudged experiments specific meteorological patterns can be recreated allowing for more detailed comparison with observations. Combining this with isotopic modelling (and measurements) will prove valuable for furthering understanding of interannual variability in methane emissions.

### **Uncertainty in wetland emissions**

This thesis did not explore the model's sensitivity to changes in the wetland distribution. Large uncertainties are linked to wetland emissions and their geographical distribution [e.g. Kirschke et al., 2013; Melton et al., 2013; Warwick et al., 2016] and the sensitivity of the latitudinal methane gradient to the source distribution was highlighted in this thesis. Studying the impact of different estimates within one model could potentially constrain these estimates. Different wetland emission estimates could be simulated in parallel with the newly developed non-interactive chemistry scheme. Comparing differing estimates, such as those from Melton et al. [2013], within the same model framework could lead to more constraints on the overall wetland methane source strength.

Additionally, it has been shown that wetland extent and emissions are sensitive to temperature, precipitation and CO<sub>2</sub> as well as meteorological changes [Warwick et al., 2002; Bloom et al., 2010; Ringeval et al., 2010, 2011; van Groenigen et al., 2011; Yvon-Durocher et al., 2014]. This is of particular importance when attributing recent observed changes in global methane as outlined in the introduction (chapter 1) but also in light of future climate change. Future methane emission changes from natural sources such as wetlands have not been taken into account in the experiments presented in this thesis. Wetland emissions could, for instance, be scaled with a Q10 fit representing future temperatures [e.g. Meng et al., 2012]. The Q10 fit approximates the relationship between methane wetland emissions and soil temperature. However, emissions would still remain uncoupled to other modelled processes known to affect not only the emission strength but also the wetland distribution, such as those mentioned above. The next section therefore briefly outlines model changes that could lead to a better representation of these processes.

### **Process based modelling of wetland emissions**

Throughout this thesis, emissions were imposed via external climatological emission fields independent of any processes in the model. However, as eluded to above, wetland emissions depend on atmospheric factors such as temperatures and precipitation. Process based modelling of wetland emissions, e.g. with the Joint UK Land Environment Simulator (JULES) (<https://jules.jchmr.org/>), could therefore improve the representation of wetland methane emissions in the model. In JULES methane emissions from wetlands (methanogenesis) are calculated as a function of soil moisture, soil carbon content and temperature [e.g. McNorton et al., 2016b; Clark et al., 2011]. Process based modelling could therefore not only capture interannual wetland emission variability but also allow for feedbacks between climate and emissions.

Current efforts in the modelling community are focused on creating full Earth system models (ESMs), i.e. models that resolve and couple atmospheric, soil and ocean processes (<http://www.jwcrp.org.uk/research-activity/ukesm.asp>). This will allow a comprehensive analysis of climate and composition change drivers and could reduce uncertainties inherent in emission inputs. Hopcroft et al. [2017] used an ESM to assess drivers of the differences between the last glacial maximum and pre-industrial methane concentrations. They found that, with current understanding of the relevant processes for methane emission, methane concentrations at the last glacial maximum were overestimated. Further work is therefore necessary to understand present day methane variability and to estimate future (natural) methane emissions.

### **Methane's radiative impacts**

This thesis has shown that methane changes tropospheric ozone as well as OH and CO abundances. This has implications for the atmospheric oxidative capacity and further work is necessary to determine the drivers of future chemistry and the composition sensitivity to (methane) emissions. The ozone increase attributed to methane emission increases not only has implications for air quality but also impacts the radiative forcing [e.g. Fiore et al., 2015]. Methane also indirectly impacts stratospheric water vapour and CO<sub>2</sub> concentrations [e.g. Revell et al., 2016] which themselves also affect Earth's radiative balance [e.g. Myhre et al., 2013]. These effects were not assessed in this thesis but warrant further investigation. Furthermore, Etminan et al. [2016] have recently proposed to increase methane's radiative forcing which would impact climate.

# References

- Allan, W., Lowe, D. C., and Cainey, J. M. (2001a). Active chlorine in the remote marine boundary layer: Modeling anomalous measurements of  $\delta^{13}\text{C}$  in methane. *Geophysical Research Letters*, 28(17):3239–3242.
- Allan, W., Lowe, D. C., Gomez, A. J., Struthers, H., and Brailsford, G. W. (2005). Interannual variation of  $\delta^{13}\text{C}$  in tropospheric methane: Implications for a possible atomic chlorine sink in the marine boundary layer. *Journal of Geophysical Research*, 110(D11):D11306.
- Allan, W., Manning, M. R., Lassey, K. R., Lowe, D. C., and Gomez, A. J. (2001b). Modeling the variation of  $\delta^{13}\text{C}$  in atmospheric methane: Phase ellipses and the kinetic isotope effect. *Global Biogeochemical Cycles*, 15(2):467–481.
- Allan, W., Struthers, H., and Lowe, D. C. (2007). Methane carbon isotope effects caused by atomic chlorine in the marine boundary layer: Global model results compared with Southern Hemisphere measurements. *Journal of Geophysical Research*, 112(D4):D04306.
- Archibald, A. T., Levine, J. G., Abraham, N. L., Cooke, M. C., Edwards, P. M., Heard, D. E., Jenkin, M. E., Karunaharan, A., Pike, R. C., Monks, P. S., Shallcross, D. E., Telford, P. J., Whalley, L. K., and Pyle, J. A. (2011). Impacts of HO<sub>x</sub> regeneration and recycling in the oxidation of isoprene: Consequences for the composition of past, present and future atmospheres. *Geophysical Research Letters*, 38(L5):L05804.
- Bândă, N., Krol, M., van Weele, M., Van Noije, T., Le Sager, P., and Röckmann, T. (2016). Can we explain the observed methane variability after the Mount Pinatubo eruption? *Atmospheric Chemistry and Physics*, 16(1):195–214.
- Banerjee, A., Archibald, A. T., Maycock, A. C., Telford, P., Abraham, N. L., Yang, X., Braesicke, P., and Pyle, J. A. (2014). Lightning NO<sub>x</sub>, a key chemistry-climate interaction: impacts of future climate change and consequences for tropospheric oxidising capacity. *Atmospheric Chemistry and Physics*, 14(18):9871–9881.
- Banerjee, A., Maycock, A. C., Archibald, A. T., Abraham, N. L., Telford, P., Braesicke, P., and Pyle, J. A. (2016). Drivers of changes in stratospheric and tropospheric ozone between year 2000 and 2100. *Atmospheric Chemistry and Physics*, 16(5):2727–2746.
- Bekki, S., Law, K. S., and Pyle, J. A. (1994). Effects of ozone depletion on atmospheric CH<sub>4</sub> and CO concentrations. *Nature*, 371(6498):595–597.

- Bellouin, N., Collins, W. J., Culverwell, I. D., Halloran, P. R., Hardiman, S. C., Hinton, T. J., Jones, C. D., McDonald, R. E., McLaren, A. J., O'Connor, F. M., Roberts, M. J., Rodriguez, J. M., Woodward, S., Best, M. J., Brooks, M. E., Brown, A. R., Butchart, N., Dearden, C., Derbyshire, S. H., Dharssi, I., Doutriaux-Boucher, M., Edwards, J. M., Falloon, P. D., Gedney, N., Gray, L. J., Hewitt, H. T., Hobson, M., Huddleston, M. R., Hughes, J., Ineson, S., Ingram, W. J., James, P. M., Johns, T. C., Johnson, C. E., Jones, A., Jones, C. P., Joshi, M. M., Keen, A. B., Liddicoat, S., Lock, A. P., Maidens, A. V., Manners, J. C., Milton, S. F., Rae, J. G. L., Ridley, J. K., Sellar, A., Senior, C. A., Totterdell, I. J., Verhoef, A., Vidale, P. L., and Wiltshire, A. (2011a). The HadGEM2 family of Met Office Unified Model climate configurations. *Geoscientific Model Development*, 4(3):723–757.
- Bellouin, N., Rae, J., Jones, A., Johnson, C., Haywood, J., and Boucher, O. (2011b). Aerosol forcing in the Climate Model Intercomparison Project (CMIP5) simulations by HadGEM2-ES and the role of ammonium nitrate. *Journal of Geophysical Research*, 116(D20):D20206.
- Berchet, A., Bousquet, P., Pison, I., Locatelli, R., Chevallier, F., Paris, J. D., Dlugokencky, E. J., Laurila, T., Hatakka, J., Viisanen, Y., Worthy, D. E. J., Nisbet, E. G., Fisher, R. E., France, J. L., Lowry, D., and Ivakhov, V. (2015). Atmospheric constraints on the methane emissions from the East Siberian Shelf. *Atmospheric Chemistry and Physics Discussions*, 15(18):25477–25501.
- Bergamaschi, P., Frankenberg, C., Meirink, J. F., Krol, M., Dentener, F., Wagner, T., Platt, U., Kaplan, J. O., Körner, S., Heimann, M., Dlugokencky, E. J., and Goede, A. (2007). Satellite cartography of atmospheric methane from SCIAMACHY on board ENVISAT: 2. Evaluation based on inverse model simulations. *Journal of Geophysical Research*, 112(D2):D02304.
- Bergamaschi, P., Houweling, S., Segers, A., Krol, M., Frankenberg, C., Scheepmaker, R. A., Dlugokencky, E. J., Wofsy, S. C., Kort, E. A., Sweeney, C., Schuck, T., Brenninkmeijer, C., Chen, H., Beck, V., and Gerbig, C. (2013). Atmospheric CH<sub>4</sub> in the first decade of the 21st century: Inverse modeling analysis using SCIAMACHY satellite retrievals and NOAA surface measurements. *Journal of Geophysical Research: Atmospheres*, 118(13):7350–7369.
- Bloom, A. A., Palmer, P. I., Fraser, A., Reay, D. S., and Frankenberg, C. (2010). Large-Scale Controls of Methanogenesis Inferred from Methane and Gravity Spaceborne Data. *Science*, 327(5963):322–325.
- Bloss, W. J., Evans, M. J., Lee, J. D., Sommariva, R., Heard, D. E., and Pilling, M. J. (2005). The oxidative capacity of the troposphere: Coupling of field measurements of OH and a global chemistry transport model. *Faraday Discussions*, 130:425.
- Bousquet, P., Ciais, P., Miller, J. B., Dlugokencky, E. J., Hauglustaine, D. A., Prigent, C., Van der Werf, G. R., Peylin, P., Brunke, E.-G., Carouge, C., Langenfelds, R. L., Lathière, J., Papa, F., Ramonet, M., Schmidt, M., Steele, L. P., Tyler, S. C., and White, J. (2006). Contribution of anthropogenic and natural sources to atmospheric methane variability. *Nature*, 443(7110):439–443.

- Bousquet, P., Hauglustaine, D. A., Peylin, P., Carouge, C., and Ciais, P. (2005). Two decades of OH variability as inferred by an inversion of atmospheric transport and chemistry of methyl chloroform. *Atmospheric Chemistry and Physics*, 5(10):2635–2656.
- Brasseur, G. P., Schultz, M., Granier, C., Saunois, M., Diehl, T., Botzet, M., Roeckner, E., and Walters, S. (2006). Impact of Climate Change on the Future Chemical Composition of the Global Troposphere. *Journal of Climate*, 19(16):3932–3951.
- Brewer, A. W. (1949). Evidence for a world circulation provided by the measurements of helium and water vapour distribution in the stratosphere. *Quarterly Journal of the Royal Meteorological Society*, 75(326):351–363.
- Butchart, N., Scaife, A. A., Bourqui, M., de Grandpré, J., Hare, S. H. E., Kettleborough, J., Langematz, U., Manzini, E., Sassi, F., Shibata, K., Shindell, D., and Sigmond, M. (2006). Simulations of anthropogenic change in the strength of the Brewer–Dobson circulation. *Climate Dynamics*, 27(7-8):727–741.
- Carver, G. D., Brown, P. D., and Wild, O. (1997). The ASAD atmospheric chemistry integration package and chemical reaction database. *Computer Physics Communications*, 105(2):197–215.
- Christensen, T. R., Panikov, N., Mastepanov, M., Joabsson, A., Öquist, M., Sommerkorn, M., Reynaud, S., and Svensson, B. (2003). Biotic controls on CO<sub>2</sub>, and CH<sub>4</sub> exchange in wetlands - a closed environment study. *Biogeochemistry*, 64(3):337–354.
- Ciais, P., Sabine, C., Bala, G., Bopp, L., Brovkin, V., Canadell, J., Chhabra, A., DeFries, R., Galloway, J., Heimann, M., Jones, C., Le Quéré, C., Myneni, R. B., Piao, S., Thornton, P., Myneni, R. B., Piao, S., Thornton, P., Le Quere, C., Myneni, R. B., Piao, S., Thornton, P., Le Quere, C., Myneni, R. B., Piao, S., and Thornton, P. (2013). Carbon and Other Biogeochemical Cycles. In Stocker, T., Qin, D., Plattner, G.-K., Tignor, M., Allen, S., Boschung, J., Nauels, A., Xia, Y., Bex, V., and Midgley, P., editors, *Climate Change 2013: The Physical Science Basis. Contribution of Working Group I to the Fifth Assessment Report of the Intergovernmental Panel on Climate Change 2013: The Physical Science Basis. Contribution of Working Group I to the Fifth Assesse*, chapter 6. Cambridge University Press, Cambridge, United Kingdom and New York, NY, USA.
- Cicerone, R. J. and Oremland, R. S. (1988). Biogeochemical Aspects Of Atmospheric Methane. *Global Biogeochemical Cycles*, 2(4):299–327.
- Clark, D. B., Mercado, L. M., Sitch, S., Jones, C. D., Gedney, N., Best, M. J., Pryor, M., Rooney, G. G., Essery, R. L. H., Blyth, E., Boucher, O., Harding, R. J., Huntingford, C., and Cox, P. M. (2011). The Joint UK Land Environment Simulator (JULES), model description – Part 2: Carbon fluxes and vegetation dynamics. *Geoscientific Model Development*, 4(3):701–722.
- Cracknell, A. P. (1994). Radiative Forcing of Climate Change , IPCC Emission Scenarios. pages 1–33.
- Craig, H. (1957). Isotopic standards for carbon and oxygen and correction factors for mass-spectrometric analysis of carbon dioxide. *Geochimica et Cosmochimica Acta*, 12:133–149.

- Dalsøren, S. B., Myhre, C. L., Myhre, G., Gomez-Pelaez, A. J., Søvde, O. A., Isaksen, I. S. A., Weiss, R. F., and Harth, C. M. (2016). Atmospheric methane evolution the last 40 years. *Atmospheric Chemistry and Physics*, 16(5):3099–3126.
- Davies, T., Cullen, M. J. P., Malcolm, A. J., Mawson, M. H., Staniforth, A., White, A. A., and Wood, N. (2005). A new dynamical core for the Met Office's global and regional modelling of the atmosphere. *Quarterly Journal of the Royal Meteorological Society*, 131(608):1759–1782.
- Dlugokencky, E. J., Dutton, E. G., Novelli, P. C., Tans, P. P., Masarie, K. A., Lantz, K. O., and Madronich, S. (1996). Changes in CH<sub>4</sub> and CO growth rates after the eruption of Mt. Pinatubo and their link with changes in tropical tropospheric UV flux. *Geophysical Research Letters*, 23(20):2761–2764.
- Dlugokencky, E. J., Houweling, S., Bruhwiler, L., Masarie, K. A., Lang, P. M., Miller, J. B., and Tans, P. P. (2003). Atmospheric methane levels off: Temporary pause or a new steady-state? *Geophysical Research Letters*, 30(19):1992.
- Dlugokencky, E. J., Lang, P. M., Crotwell, A. M., Mund, J. W., Crotwell, M. J., and Thoning, K. W. (2016). Atmospheric Methane Dry Air Mole Fractions from the NOAA ESRL Carbon Cycle Cooperative Global Air Sampling Network, 1983-2015, Version: 2016-07-07.
- Dlugokencky, E. J., Masarie, K. A., Lang, P. M., Tans, P. P., and Steele, L. P. (1994a). A dramatic decrease in the growth rate of atmospheric methane in the northern hemisphere during 1992. *Geophysical Research Letters*, 21(1):45–48.
- Dlugokencky, E. J., Masarie, K. A., Lang, P. M., and Tans, P. P. (1998). Continuing decline in the growth rate of the atmospheric methane burden. *Nature*, 393(6684):447–450.
- Dlugokencky, E. J., Nisbet, E. G., Fisher, R., and Lowry, D. (2011). Global atmospheric methane: budget, changes and dangers. *Philosophical Transactions of the Royal Society A: Mathematical, Physical and Engineering Sciences*, 369(1943):2058–72.
- Dlugokencky, E. J., Steele, L. P., Lang, P. M., and Masarie, K. A. (1994b). The growth rate and distribution of atmospheric methane. *Journal of Geophysical Research*, 99(94):17021–17043.
- EC-JRC/PBL (2011). Emission Database for Global Atmospheric Research (EDGAR), release version 4.2.
- Ehhalt, D., Prather, M., Dentener, F., Derwent, R., Dlugokencky, E., Holland, E., Isaksen, I., Katima, J., Kirchhoff, V., Matson, P., Midgley, P., and Wang, M. (2001). Atmospheric Chemistry and Greenhouse Gases. In Houghton, J., Ding, Y., Griggs, D., Noguer, M., van der Linden, P., Dai, X., Maskell, K., and Johnson, C., editors, *Climate Change 2001: The Scientific Basis. Third Assessment Report of the Intergovernmental Panel on Climate Change*, chapter 4. Cambridge University Press, Cambridge, United Kingdom and New York, NY, USA.

- Emmons, L. K., Hauglustaine, D. A., Müller, J. F., Carroll, M. A., Brasseur, G. P., Brunner, D., Staehelin, J., Thouret, V., and Marenco, A. (2000). Data composites of airborne observations of tropospheric ozone and its precursors. *Journal of Geophysical Research*, 105:20497.
- Etheridge, D. M., Steele, L. P., Francey, R. J., and Langenfelds, R. L. (1998). Atmospheric methane between 1000 A. D. and present: Evidence of anthropogenic emissions and climatic variability. *Journal of Geophysical Research*, 103(D13):15979–15993.
- Etiopie, G., Lassey, K. R., Klusman, R. W., and Boschi, E. (2008). Reappraisal of the fossil methane budget and related emission from geologic sources. *Geophysical Research Letters*, 35(9):L09307.
- Etminan, M., Myhre, G., Highwood, E. J., and Shine, K. P. (2016). Radiative forcing of carbon dioxide, methane, and nitrous oxide: A significant revision of the methane radiative forcing. *Geophysical Research Letters*, pages 614–623.
- Fiore, A. M., Jacob, D. J., Field, B. D., Streets, D. G., Fernandes, S. D., and Jang, C. (2002). Linking ozone pollution and climate change: The case for controlling methane. *Geophysical Research Letters*, 29(19):25–1–25–4.
- Fiore, A. M., Naik, V., and Leibensperger, E. M. (2015). Air Quality and Climate Connections. *Journal of the Air & Waste Management Association*, 65(6):645–685.
- Fiore, A. M., West, J. J., Horowitz, L. W., Naik, V., and Schwarzkopf, M. D. (2008). Characterizing the tropospheric ozone response to methane emission controls and the benefits to climate and air quality. *Journal of Geophysical Research*, 113(D8):D08307.
- Fisher, R., Lowry, D., Wilkin, O., Sriskantharajah, S., and Nisbet, E. G. (2006). High-precision, automated stable isotope analysis of atmospheric methane and carbon dioxide using continuous-flow isotope-ratio mass spectrometry. *Rapid Communications in Mass Spectrometry*, 20(2):200–208.
- Fisher, R. E., Sriskantharajah, S., Lowry, D., Lanoisellé, M., Fowler, C. M. R., James, R. H., Hermansen, O., Lund Myhre, C., Stohl, A., Greinert, J., Nisbet-Jones, P. B. R., Mienert, J., and Nisbet, E. G. (2011). Arctic methane sources: Isotopic evidence for atmospheric inputs. *Geophysical Research Letters*, 38(21):n/a–n/a.
- Fueglistaler, S., Bonazzola, M., Haynes, P. H., and Peter, T. (2005). Stratospheric water vapor predicted from the Lagrangian temperature history of air entering the stratosphere in the tropics. *Journal of Geophysical Research D: Atmospheres*, 110(8):1–10.
- Fuglestedt, J., Berntsen, T., Isaksen, I., Mao, H., Liang, X.-Z., and Wang, W.-C. (1999). Climatic forcing of nitrogen oxides through changes in tropospheric ozone and methane; global 3D model studies. *Atmospheric Environment*, 33:961–977.
- Fung, I., John, J., Lerner, J., Matfhevs, E., Prather, M., Steele, L. P., and Fraser, P. J. (1991). Three-Dimensional Model Synthesis of the Global Methane Cycle. *Journal of Geophysical Research*, 96(D7):13033–13065.

- Ghosh, A., Patra, P. K., Ishijima, K., Umezawa, T., Ito, A., Etheridge, D. M., Sugawara, S., Kawamura, K., Miller, J. B., Dlugokencky, E. J., Krummel, P. B., Fraser, P. J., Steele, L. P., Langenfelds, R. L., Trudinger, C. M., White, J. W. C., Vaughn, B., Saeki, T., Aoki, S., and Nakazawa, T. (2015). Variations in global methane sources and sinks during 1910–2010. *Atmospheric Chemistry and Physics*, 15(5):2595–2612.
- Giannakopoulos, C., Chipperfield, M. P., Law, K. S., and Pyle, J. A. (1999). Validation and intercomparison of wet and dry deposition schemes using 210 Pb in a global three-dimensional off-line chemical transport model. *Journal of Geophysical Research: Atmospheres*, 104(D19):23761–23784.
- Guenther, A., Hewitt, C. N., Erickson, D., Fall, R., Geron, C., Graedel, T., Harley, P., Klinger, L., Lerdau, M., McKay, W. A., Pierce, T., Scholes, B., Steinbrecher, R., Tallamraju, R., Taylor, J., and Zimmerman, P. (1995). A global model of natural volatile organic compound emissions. *Journal of Geophysical Research*, 100(D5):8873.
- Gurney, K. R., Chen, Y.-H., Maki, T., Kawa, S. R., Andrews, A., and Zhu, Z. (2005). Sensitivity of atmospheric CO<sub>2</sub> inversions to seasonal and interannual variations in fossil fuel emissions. *Journal of Geophysical Research*, 110(D10):D10308.
- Hardiman, S. C., Boutle, I. A., Bushell, A. C., Butchart, N., Cullen, M. J. P., Field, P. R., Furtado, K., Manners, J. C., Milton, S. F., Morcrette, C., O'Connor, F. M., Shipway, B. J., Smith, C., Walters, D. N., Willett, M. R., Williams, K. D., Wood, N., Lukeabraham, N., Keeble, J., Maycock, A. C., Thuburn, J., and Woodhouse, M. T. (2015). Processes controlling tropical tropopause temperature and stratospheric water vapor in climate models. *Journal of Climate*, 28(16):6516–6535.
- Hewitt, H. T., Copesey, D., Culverwell, I. D., Harris, C. M., Hill, R. S. R., Keen, A. B., McLaren, A. J., and Hunke, E. C. (2011). Design and implementation of the infrastructure of HadGEM3: the next-generation Met Office climate modelling system. *Geoscientific Model Development*, 4(2):223–253.
- Holmes, C. D., Prather, M. J., Søvde, O. A., and Myhre, G. (2013). Future methane, hydroxyl, and their uncertainties: key climate and emission parameters for future predictions. *Atmospheric Chemistry and Physics*, 13(1):285–302.
- Hopcroft, P. O., Valdes, P. J., O'Connor, F. M., Kaplan, J. O., and Beerling, D. J. (2017). Understanding the glacial methane cycle. *Nature Communications*, 8:14383.
- Hossaini, R., Chipperfield, M. P., Saiz-Lopez, A., Fernandez, R., Monks, S., Feng, W., Brauer, P., and von Glasow, R. (2016a). A global model of tropospheric chlorine chemistry: Organic versus inorganic sources and impact on methane oxidation. *Journal of Geophysical Research: Atmospheres*, 121(23):14,271–14,297.
- Hossaini, R., Patra, P. K., Leeson, A. A., Krysztofiak, G., Abraham, N. L., Andrews, S. J., Archibald, A. T., Aschmann, J., Atlas, E. L., Belikov, D. A., Bönisch, H., Carpenter, L. J., Dhomse, S., Dorf, M., Engel, A., Feng, W., Fuhlbrügge, S., Griffiths, P. T., Harris, N. R. P., Hommel, R., Keber, T., Krüger, K., Lennartz, S. T., Maksyutov, S., Mantle, H., Mills, G. P., Miller, B., Montzka, S. A., Moore, F., Navarro, M. A., Oram, D. E., Pfeilsticker, K., Pyle, J. A., Quack, B., Robinson, A. D., Saikawa, E., Saiz-Lopez, A., Sala, S., Sinnhuber, B.-M., Taguchi, S., Tegtmeier, S., Lidster, R. T., Wilson, C., and Ziska, F. (2016b). A multi-model

- intercomparison of halogenated very short-lived substances (TransCom-VSLS): linking oceanic emissions and tropospheric transport for a reconciled estimate of the stratospheric source gas injection of bromine. *Atmospheric Chemistry and Physics*, 16(14):9163–9187.
- Huijnen, V., Williams, J., van Weele, M., van Noije, T., Krol, M., Dentener, F., Segers, A., Houweling, S., Peters, W., de Laat, J., Boersma, F., Bergamaschi, P., van Velthoven, P., Le Sager, P., Eskes, H., Alkemade, F., Scheele, R., Nédélec, P., and Pätz, H.-W. (2010). The global chemistry transport model TM5: description and evaluation of the tropospheric chemistry version 3.0. *Geoscientific Model Development*, 3(2):445–473.
- IPCC (2013). *Climate Change 2013: The Physical Science Basis. Contribution of Working Group I to the Fifth Assessment Report of the Intergovernmental Panel on Climate Change*. Cambridge University Press, Cambridge, United Kingdom and New York, NY, USA, Cambridge.
- Isaksen, I. S. A. and Hov, Ø. (1987). Calculation of trends in the tropospheric concentration of O<sub>3</sub>, OH, CO, CH<sub>4</sub> and NO<sub>x</sub>. *Tellus B*, 39B(3):271–285.
- John, J. G., Fiore, A. M., Naik, V., Horowitz, L. W., and Dunne, J. P. (2012). Climate versus emission drivers of methane lifetime against loss by tropospheric OH from 1860–2100. *Atmospheric Chemistry and Physics*, 12(24):12021–12036.
- Kaplan, J. O. (2002). Wetlands at the Last Glacial Maximum: Distribution and methane emissions. *Geophysical Research Letters*, 29(6):3–1–3–4.
- Kay, J. E., L'Ecuyer, T., Gettelman, A., Stephens, G., and O'Dell, C. (2008). The contribution of cloud and radiation anomalies to the 2007 Arctic sea ice extent minimum. *Geophysical Research Letters*, 35(8):L08503.
- Kirschke, S., Bousquet, P., Ciais, P., Saunoy, M., Canadell, J. G., Dlugokencky, E. J., Bergamaschi, P., Bergmann, D., Blake, D. R., Bruhwiler, L., Cameron-Smith, P., Castaldi, S., Chevallier, F., Feng, L., Fraser, A., Heimann, M., Hodson, E. L., Houweling, S., Josse, B., Fraser, P. J., Krummel, P. B., Lamarque, J.-F., Langenfelds, R. L., Le Quéré, C., Naik, V., O'Doherty, S., Palmer, P. I., Pison, I., Plummer, D., Poulter, B., Prinn, R. G., Rigby, M., Ringeval, B., Santini, M., Schmidt, M., Shindell, D. T., Simpson, I. J., Spahni, R., Steele, L. P., Strode, S. A., Sudo, K., Szopa, S., van der Werf, G. R., Voulgarakis, A., van Weele, M., Weiss, R. F., Williams, J. E., and Zeng, G. (2013). Three decades of global methane sources and sinks. *Nature Geoscience*, 6(10):813–823.
- Krol, M. and Lelieveld, J. (2003). Can the variability in tropospheric OH be deduced from measurements of 1,1,1-trichloroethane (methyl chloroform)? *Journal of Geophysical Research: Atmospheres*, 108(D3):n/a–n/a.
- Lamarque, J.-F., Bond, T. C., Eyring, V., Granier, C., Heil, A., Klimont, Z., Lee, D., Liousse, C., Mieville, A., Owen, B., Schultz, M. G., Shindell, D., Smith, S. J., Stehfest, E., Van Aardenne, J., Cooper, O. R., Kainuma, M., Mahowald, N., McConnell, J. R., Naik, V., Riahi, K., and van Vuuren, D. P. (2010). Historical (1850–2000) gridded anthropogenic and biomass burning emissions of reactive gases and aerosols: methodology and application. *Atmospheric Chemistry and Physics*, 10(15):7017–7039.

- Lamarque, J.-F., Shindell, D. T., Josse, B., Young, P. J., Cionni, I., Eyring, V., Bergmann, D., Cameron-Smith, P., Collins, W. J., Doherty, R., Dalsoren, S., Faluvegi, G., Folberth, G., Ghan, S. J., Horowitz, L. W., Lee, Y. H., MacKenzie, I. A., Nagashima, T., Naik, V., Plummer, D., Righi, M., Rumbold, S. T., Schulz, M., Skeie, R. B., Stevenson, D. S., Strode, S., Sudo, K., Szopa, S., Voulgarakis, A., and Zeng, G. (2013). The Atmospheric Chemistry and Climate Model Intercomparison Project (ACCMIP): overview and description of models, simulations and climate diagnostics. *Geoscientific Model Development*, 6(1):179–206.
- Lawrence, M. G., Jöckel, P., and von Kuhlmann, R. (2001). What does the global mean OH concentration tell us? *Atmospheric Chemistry and Physics*, 1(1):37–49.
- Lelieveld, J., Brenninkmeijer, C. A. M., Joeckel, P., Isaksen, I. S. A., Krol, M. C., Mak, J. E., Dlugokencky, E. J., Montzka, S. A., Novelli, P. C., Peters, W., and Tans P. P. (2006). New Directions: Watching over tropospheric hydroxyl (OH). *Atmospheric Environment*, 40(29):5741–5743.
- Mattey, D., Fisher, R., Atkinson, T., Latin, J.-P., Durrell, R., Ainsworth, M., Lowry, D., and Fairchild, I. (2013). Methane in underground air in Gibraltar karst. *Earth and Planetary Science Letters*, 374:71–80.
- McCormick, M. P. and Veiga, R. E. (1992). SAGE II measurements of early Pinatubo aerosols. *Geophysical Research Letters*, 19(2):155–158.
- McNorton, J., Chipperfield, M. P., Gloor, M., Wilson, C., Feng, W., Hayman, G. D., Rigby, M., Krummel, P. B., O’Doherty, S., Prinn, R. G., Weiss, R. F., Young, D., Dlugokencky, E., and Montzka, S. A. (2016a). Role of OH variability in the stalling of the global atmospheric CH<sub>4</sub> growth rate from 1999 to 2006. *Atmospheric Chemistry and Physics*, 16(12):7943–7956.
- McNorton, J., Gloor, E., Wilson, C., Hayman, G. D., Gedney, N., Comyn-Platt, E., Marthews, T., Parker, R. J., Boesch, H., and Chipperfield, M. P. (2016b). Role of regional wetland emissions in atmospheric methane variability. *Geophysical Research Letters*, 43(21):11,433–11,444.
- Meinshausen, M., Smith, S. J., Calvin, K., Daniel, J. S., Kainuma, M. L. T., Lamarque, J.-F., Matsumoto, K., Montzka, S. A., Raper, S. C. B., Riahi, K., Thomson, A., Velders, G. J. M., and van Vuuren, D. P. (2011). The RCP greenhouse gas concentrations and their extensions from 1765 to 2300. *Climatic Change*, 109(1-2):213–241.
- Melton, J. R., Wania, R., Hodson, E. L., Poulter, B., Ringeval, B., Spahni, R., Bohn, T., Avis, C. A., Beerling, D. J., Chen, G., Eliseev, A. V., Denisov, S. N., Hopcroft, P. O., Lettenmaier, D. P., Riley, W. J., Singarayer, J. S., Subin, Z. M., Tian, H., Zürcher, S., Brovkin, V., van Bodegom, P. M., Kleinen, T., Yu, Z. C., and Kaplan, J. O. (2013). Present state of global wetland extent and wetland methane modelling: conclusions from a model inter-comparison project (WETCHIMP). *Biogeosciences*, 10(2):753–788.
- Meng, L., Hess, P., Mahowald, N., Yavitt, J., Riley, W., Subin, Z., Lawrence, D., Swenson, S., Jauhiainen, J., and Fuka, D. (2012). Sensitivity of wetland methane emissions to model assumptions: application and model testing against site observations. *Biogeosciences*, 9(7):2793–2819.

- Monks, P. S., Archibald, A. T., Colette, A., Cooper, O., Coyle, M., Derwent, R., Fowler, D., Granier, C., Law, K. S., Mills, G. E., Stevenson, D. S., Tarasova, O., Thouret, V., von Schneidmesser, E., Sommariva, R., Wild, O., and Williams, M. L. (2015). Tropospheric ozone and its precursors from the urban to the global scale from air quality to short-lived climate forcer. *Atmospheric Chemistry and Physics*, 15(15):8889–8973.
- Montzka, S. A., Dlugokencky, E. J., and Butler, J. H. (2011a). Non-CO<sub>2</sub> greenhouse gases and climate change. *Nature*, 476(7358):43–50.
- Montzka, S. A., Krol, M., Dlugokencky, E., Hall, B., Jockel, P., and Lelieveld, J. (2011b). Small Interannual Variability of Global Atmospheric Hydroxyl. *Science*, 331(6013):67–69.
- Montzka, S. A., Spivakovsky, C. M., Butler, J. H., Elkins, J. W., Lock, L. T., and Mondeel, D. J. (2000). New Observational Constraints for Atmospheric Hydroxyl on Global and Hemispheric Scales. *Science*, 288(5465):500–503.
- Morgenstern, O., Braesicke, P., O'Connor, F. M., Bushell, A. C., Johnson, C. E., Osprey, S. M., and Pyle, J. A. (2009). Evaluation of the new UKCA climate-composition model – Part 1: The stratosphere. *Geoscientific Model Development*, 2(1):43–57.
- Morgenstern, O., Zeng, G., Abraham, N. L., Telford, P. J., Braesicke, P., Pyle, J. A., Hardiman, S. C., O'Connor, F. M., and Johnson, C. E. (2013). Impacts of climate change, ozone recovery, and increasing methane on surface ozone and the tropospheric oxidizing capacity. *Journal of Geophysical Research: Atmospheres*, 118(2):1028–1041.
- Myhre, C. L., Ferré, B., Platt, S. M., Silyakova, A., Hermansen, O., Allen, G., Pisso, I., Schmidbauer, N., Stohl, A., Pitt, J., Jansson, P., Greinert, J., Percival, C., Fjaeraa, A. M., O'Shea, S. J., Gallagher, M., Le Breton, M., Bower, K. N., Bauguitte, S. J. B., Dalsøren, S., Vadakkepuliambatta, S., Fisher, R. E., Nisbet, E. G., Lowry, D., Myhre, G., Pyle, J. A., Cain, M., and Mienert, J. (2016). Extensive release of methane from Arctic seabed west of Svalbard during summer 2014 does not influence the atmosphere. *Geophysical Research Letters*, 43(9):4624–4631.
- Myhre, G., Shindell, D., Breon, F.-M., Collins, W., Fuglestedt, J., Huang, J., Koch, D., Lamarque, J.-F., Lee, D., Mendoza, B., Nakajima, T., Robock, A., Stephens, G., Takemura, T., and Zhang, H. (2013). Anthropogenic and Natural Radiative Forcing. In Stocker, T., Qin, D., Plattner, G.-K., Tignor, M., Allen, S., Boschung, J., Nauels, A., Xia, Y., Bex, V., and Midgley, P., editors, *Climate Change 2013: The Physical Science Basis. Contribution of Working Group I to the Fifth Assessment Report of the Intergovernmental Panel on Climate Change*, chapter 8. Cambridge University Press, Cambridge, United Kingdom and New York, NY, USA.
- Naik, V., Voulgarakis, A., Fiore, A. M., Horowitz, L. W., Lamarque, J.-F., Lin, M., Prather, M. J., Young, P. J., Bergmann, D., Cameron-Smith, P. J., Cionni, I., Collins, W. J., Dalsøren, S. B., Doherty, R., Eyring, V., Faluvegi, G., Folberth, G. A., Josse, B., Lee, Y. H., MacKenzie, I. A., Nagashima, T., van Noije, T. P. C., Plummer, D. A., Righi, M., Rumbold, S. T., Skeie, R., Shindell, D. T., Stevenson, D. S., Strode, S., Sudo, K., Szopa, S., and Zeng, G. (2013). Preindustrial to present-day changes in tropospheric hydroxyl radical and methane lifetime from the Atmospheric Chemistry and Climate Model Intercomparison Project (ACCMIP). *Atmospheric Chemistry and Physics*, 13(10):5277–5298.

- Nicely, J. M., Salawitch, R. J., Canty, T., Anderson, D. C., Arnold, S. R., Chipperfield, M. P., Emmons, L. K., Flemming, J., Huijnen, V., Kinnison, D. E., Lamarque, J.-f., Mao, J., Monks, S. A., Steenrod, S. D., Tilmes, S., and Turquety, S. (2017). Quantifying the causes of differences in tropospheric OH within global models. *Journal of Geophysical Research: Atmospheres*, 122:1–25.
- Nisbet, E. G., Dlugokencky, E. J., Manning, M. R., Lowry, D., Fisher, R. E., France, J. L., Michel, S. E., Miller, J. B., White, J. W. C., Vaughn, B., Bousquet, P., Pyle, J. A., Warwick, N. J., Cain, M., Brownlow, R., Zazzeri, G., Lanoisellé, M., Manning, A. C., Gloor, E., Worthy, D. E. J., Brunke, E.-G., Labuschagne, C., Wolff, E. W., and Ganesan, A. L. (2016). Rising atmospheric methane: 2007–2014 growth and isotopic shift. *Global Biogeochemical Cycles*, 30(9):1356–1370.
- Nocedal, J. and Wright, S. (2006). *Numerical Optimization*. Springer Series in Operations Research and Financial Engineering. Springer New York.
- O'Connor, F. M., Boucher, O., Gedney, N., Jones, C. D., Folberth, G. A., Coppel, R., Friedlingstein, P., Collins, W. J., Chappellaz, J., Ridley, J., and Johnson, C. E. (2010). Possible role of wetlands, permafrost, and methane hydrates in the methane cycle under future climate change: A review. *Reviews of Geophysics*, 48(4):RG4005.
- O'Connor, F. M., Johnson, C. E., Morgenstern, O., Abraham, N. L., Braesicke, P., Dalvi, M., Folberth, G. A., Sanderson, M. G., Telford, P. J., Voulgarakis, A., Young, P. J., Zeng, G., Collins, W. J., and Pyle, J. A. (2014). Evaluation of the new UKCA climate-composition model – Part 2: The Troposphere. *Geoscientific Model Development*, 7(1):41–91.
- Patra, P., Houweling, S., Krol, M., Bousquet, P., and Jacob, D. (2010). Protocol for TransCom CH4 intercomparison. 2009(November 2009).
- Patra, P. K., Houweling, S., Krol, M., Bousquet, P., Belikov, D., Bergmann, D., Bian, H., Cameron-Smith, P., Chipperfield, M. P., Corbin, K., Fortems-Cheiney, A., Fraser, A., Gloor, E., Hess, P., Ito, A., Kawa, S. R., Law, R. M., Loh, Z., Maksyutov, S., Meng, L., Palmer, P. I., Prinn, R. G., Rigby, M., Saito, R., and Wilson, C. (2011). TransCom model simulations of CH4 and related species: linking transport, surface flux and chemical loss with CH4 variability in the troposphere and lower stratosphere. *Atmospheric Chemistry and Physics*, 11(24):12813–12837.
- Patra, P. K., Krol, M. C., Montzka, S. A., Arnold, T., Atlas, E. L., Lintner, B. R., Stephens, B. B., Xiang, B., Elkins, J. W., Fraser, P. J., Ghosh, A., Hints, E. J., Hurst, D. F., Ishijima, K., Krummel, P. B., Miller, B. R., Miyazaki, K., Moore, F. L., Mühle, J., O'Doherty, S., Prinn, R. G., Steele, L. P., Takigawa, M., Wang, H. J., Weiss, R. F., Wofsy, S. C., and Young, D. (2014). Observational evidence for interhemispheric hydroxyl-radical parity. *Nature*, 513(7517):219–223.
- Petit, J. R., Jouzel, J., Raynaud, D., Barkov, N. I., Barnola, J.-M., Basile, I., Bender, M., Chappellaz, J., Davis, M., Delaygue, G., Delmotte, M., Kotlyakov, V. M., Legrand, M., Lipenkov, V. Y., Lorius, C., Pépin, L., Ritz, C., Saltzman, E., and Stievenard, M. (1999). Climate and atmospheric history of the past 420,000 years from the Vostok ice core, Antarctica. *Nature*, 399(6735):429–436.

- Pisso, I., Myhre, C. L., Platt, S. M., Eckhardt, S., Hermansen, O., Schmidbauer, N., Mienert, J., Vadakkepuliambatta, S., Bauguitte, S., Pitt, J., Allen, G., Bower, K. N., O'Shea, S., Gallagher, M. W., Percival, C. J., Pyle, J., Cain, M., and Stohl, A. (2016). Constraints on oceanic methane emissions west of Svalbard from atmospheric in situ measurements and Lagrangian transport modeling. *Journal of Geophysical Research: Atmospheres*, pages 188–200.
- Prather, M. J. (1994). Lifetimes and eigenstates in atmospheric chemistry. *Geophysical Research Letters*, 21(9):801–804.
- Prather, M. J. (1996). Time scales in atmospheric chemistry: Theory, GWPs for CH<sub>4</sub> and CO, and runaway growth. *Geophysical Research Letters*, 23(19):2597–2600.
- Prather, M. J., Holmes, C. D., and Hsu, J. (2012). Reactive greenhouse gas scenarios: Systematic exploration of uncertainties and the role of atmospheric chemistry. *Geophysical Research Letters*, 39(9):n/a–n/a.
- Price, C. and Rind, D. (1994). Modeling Global Lightning Distributions in a General Circulation Model. *Monthly Weather Review*, 122(8):1930–1939.
- Prinn, R. G. and Huang, J. (2001). Comment on “Global OH trend inferred from methylchloroform measurements” by Maarten Krol et al. *Journal of Geophysical Research: Atmospheres*, 106(D19):23151–23157.
- Prinn, R. G., Huang, J., Weiss, R. F., Cunnold, D. M., Fraser, P. J., Simmonds, P. G., McCulloch, A., Harth, C., Reimann, S., Salameh, P., O'Doherty, S., Wang, R. H. J., Porter, L. W., Miller, B. R., and Krummel, P. B. (2005). Evidence for variability of atmospheric hydroxyl radicals over the past quarter century. *Geophysical Research Letters*, 32(7):n/a–n/a.
- Prinn, R. G., Huang, J., Weiss, R. F., Cunnold, D. M., Fraser, P. J., Simmonds, P. G., McCulloch, A., Harth, C., Salameh, P., O'Doherty, S., Wang, R. H. J., Porter, L., and Miller, B. R. (2001). Evidence for Substantial Variations of Atmospheric Hydroxyl Radicals in the Past Two Decades. *Science*, 292(5523):1882–1888.
- Prinn, R. G., Weiss, R. F., Miller, B. R., Huang, J., Alyea, F. N., Cunnold, D. M., Fraser, P. J., Hartley, D. E., and Simmonds, P. G. (1995). Atmospheric Trends and Lifetime of CH<sub>3</sub>CCl<sub>3</sub> and Global OH Concentrations. *Science*, 269(5221):187–192.
- Rayner, N. A., Parker, D. E., Horton, E. B., Folland, C. K., Alexander, L. V., Rowell, D. P., Kent, E. C., and Kaplan, A. (2003). Global analyses of sea surface temperature, sea ice, and night marine air temperature since the late nineteenth century. *Journal of Geophysical Research*, 108(D14):4407.
- Revell, L. E., Stenke, A., Rozanov, E., Ball, W., Lossow, S., and Peter, T. (2016). The role of methane in projections of 21st century stratospheric water vapour. *Atmospheric Chemistry and Physics*, 16(20):13067–13080.
- Riahi, K., Grübler, A., and Nakicenovic, N. (2007). Scenarios of long-term socio-economic and environmental development under climate stabilization. *Technological Forecasting and Social Change*, 74(7):887–935.

- Rigby, M., Prinn, R., Fraser, P., Simmonds, P., Langenfelds, R., Huang, J., Cunnold, D., Steele, L., Krummel, P., Weiss, R., O'Doherty, S., Salameh, P., Wang, H., Harth, C., Mühle, J., and Porter, L. (2008). Renewed growth of atmospheric methane. *Geophysical Research Letters*, 35(22):L22805.
- Ringeval, B., de Noblet-Ducoudré, N., Ciais, P., Bousquet, P., Prigent, C., Papa, F., and Rossow, W. B. (2010). An attempt to quantify the impact of changes in wetland extent on methane emissions on the seasonal and interannual time scales. *Global Biogeochemical Cycles*, 24(2):n/a–n/a.
- Ringeval, B., Friedlingstein, P., Koven, C., Ciais, P., de Noblet-Ducoudré, N., Decharme, B., and Cadule, P. (2011). Climate-CH<sub>4</sub> feedback from wetlands and its interaction with the climate-CO<sub>2</sub> feedback. *Biogeosciences*, 8(8):2137–2157.
- Saad, K. M., Wunch, D., Deutscher, N. M., Griffith, D. W. T., Hase, F., De Mazière, M., Notholt, J., Pollard, D. F., Roehl, C. M., Schneider, M., Sussmann, R., Warneke, T., and Wennberg, P. O. (2016). Seasonal variability of stratospheric methane: implications for constraining tropospheric methane budgets using total column observations. *Atmospheric Chemistry and Physics*, 16(21):14003–14024.
- Sander, S. P., Friedl, R. R., Barker, J. R., Golden, D. M., Kurylo, M. J., Wine, P. H., Abbatt, J. P. D., Burkholder, J. B., Kolb, C. E., Moortgat, G. K., Huie, R. E., and Orkin, V. L. (2011). Chemical Kinetics and Photochemical Data for Use in Atmospheric Studies Evaluation No. 17. Technical report, Jet Propulsion Laboratory, California Institute of Technology, Pasadena, CA.
- Sander, S. P., Friedl, R. R., Golden, D. M., Kurylo, M. J., Moortgat, G. K., Keller-Rudek, H., Wine, P. H., Ravishankara, A. R., Kolb, C. E., Molina, M. J., Finlayson-Pitts, B. J., Huie, R. E., and Orkin, V. L. (2006). Chemical Kinetics and Photochemical Data for Use in Atmospheric Studies Evaluation No. 15. Technical report, Jet Propulsion Laboratory, California Institute of Technology, Pasadena, CA.
- Saueressig, G., Crowley, J. N., Bergamaschi, P., Brühl, C., Brenninkmeijer, C. M., and Fischer, H. (2001). Carbon 13 and D kinetic isotope effects in the reactions of CH<sub>4</sub> with O(1D) and OH: New laboratory measurements and their implications for the isotopic composition of stratospheric methane. *Journal of Geophysical Research: Atmospheres*, 106(D19):23127–23138.
- Saunois, M., Bousquet, P., Poulter, B., Peregón, A., Ciais, P., Canadell, J. G., Dlugokencky, E. J., Etiope, G., Bastviken, D., Houweling, S., Janssens-Maenhout, G., Tubiello, F. N., Castaldi, S., Jackson, R. B., Alexe, M., Arora, V. K., Beerling, D. J., Bergamaschi, P., Blake, D. R., Brailsford, G., Brovkin, V., Bruhwiler, L., Crevoisier, C., Crill, P., Covey, K., Curry, C., Frankenberg, C., Gedney, N., Höglund-Isaksson, L., Ishizawa, M., Ito, A., Joos, F., Kim, H.-S., Kleinen, T., Krummel, P., Lamarque, J.-F., Langenfelds, R., Locatelli, R., Machida, T., Maksyutov, S., McDonald, K. C., Marshall, J., Melton, J. R., Morino, I., Naik, V., O'Doherty, S., Parmentier, F.-J. W., Patra, P. K., Peng, C., Peng, S., Peters, G. P., Pison, I., Prigent, C., Prinn, R., Ramonet, M., Riley, W. J., Saito, M., Santini, M., Schroeder, R., Simpson, I. J., Spahni, R., Steele, P., Takizawa, A., Thornton, B. F., Tian, H., Tohjima, Y., Viovy, N., Voulgarakis, A., van Weele, M., van der Werf, G. R., Weiss, R., Wiedinmyer, C., Wilton, D. J., Wiltshire, A., Worthy, D., Wunch, D., Xu, X., Yoshida, Y.,

- Zhang, B., Zhang, Z., and Zhu, Q. (2016). The global methane budget 2000–2012. *Earth System Science Data*, 8(2):697–751.
- Schaefer, H., Fletcher, S. E. M., Veidt, C., Lassey, K. R., Brailsford, G. W., Bromley, T. M., Dlugokencky, E. J., Michel, S. E., Miller, J. B., Levin, I., Lowe, D. C., Martin, R. J., Vaughn, B. H., and White, J. W. C. (2016). A 21st-century shift from fossil-fuel to biogenic methane emissions indicated by  $^{13}\text{C}\text{H}_4$ . *Science*, 352(6281):80–84.
- Schwietzke, S., Sherwood, O. A., Bruhwiler, L. M. P., Miller, J. B., Etiope, G., Dlugokencky, E. J., Michel, S. E., Arling, V. A., Vaughn, B. H., White, J. W. C., and Tans, P. P. (2016). Upward revision of global fossil fuel methane emissions based on isotope database. *Nature*, 538(7623):88–91.
- Shakhova, N., Semiletov, I., Leifer, I., Sergienko, V., Salyuk, A., Kosmach, D., Chernykh, D., Stubbs, C., Nicolsky, D., Tumskey, V., and Gustafsson, Ö. (2013). Ebullition and storm-induced methane release from the East Siberian Arctic Shelf. *Nature Geoscience*, 7(1):64–70.
- Shakhova, N., Semiletov, I., Salyuk, A., Yusupov, V., Kosmach, D., and Gustafsson, O. (2010). Extensive Methane Venting to the Atmosphere from Sediments of the East Siberian Arctic Shelf. *Science*, 327(5970):1246–1250.
- Solomon, S., Qin, D., Manning, Z., Chen, Z., Marquis, M., Averyt, K. B., Tignor, M. M. B., Miller, H. L., Manning, M. R., Marquis, M., Averyt, K. B., Tignor, M. M. B., LeRoy Miller Jr., H., and Chen, Z. (2007). *Climate Change 2007: The Physical Basis, Contribution of Working Group I to the Fourth Assessment Report of the Intergovernmental Panel on Climate Change*. Technical report.
- Spivakovsky, C. M., Logan, J. A., Montzka, S. A., Balkanski, Y. J., Foreman-Fowler, M., Jones, D. B. A., Horowitz, L. W., Fusco, A. C., Brenninkmeijer, C. A. M., Prather, M. J., Wofsy, S. C., and McElroy, M. B. (2000). Three-dimensional climatological distribution of tropospheric OH: Update and evaluation. *Journal of Geophysical Research: Atmospheres*, 105(D7):8931–8980.
- Stevenson, D. S., Dentener, F. J., Schultz, M. G., Ellingsen, K., van Noije, T. P. C., Wild, O., Zeng, G., Amann, M., Atherton, C. S., Bell, N., Bergmann, D. J., Bey, I., Butler, T., Cofala, J., Collins, W. J., Derwent, R. G., Doherty, R. M., Drevet, J., Eskes, H. J., Fiore, A. M., Gauss, M., Hauglustaine, D. A., Horowitz, L. W., Isaksen, I. S. A., Krol, M. C., Lamarque, J.-F., Lawrence, M. G., Montanaro, V., Müller, J.-F., Pitari, G., Prather, M. J., Pyle, J. A., Rast, S., Rodriguez, J. M., Sanderson, M. G., Savage, N. H., Shindell, D. T., Strahan, S. E., Sudo, K., and Szopa, S. (2006). Multimodel ensemble simulations of present-day and near-future tropospheric ozone. *Journal of Geophysical Research*, 111(D8):D08301.
- Stevenson, D. S., Young, P. J., Naik, V., Lamarque, J.-F., Shindell, D. T., Voulgarakis, A., Skeie, R. B., Dalsoren, S. B., Myhre, G., Berntsen, T. K., Folberth, G. A., Rumbold, S. T., Collins, W. J., MacKenzie, I. A., Doherty, R. M., Zeng, G., van Noije, T. P. C., Strunk, A., Bergmann, D., Cameron-Smith, P., Plummer, D. A., Strode, S. A., Horowitz, L., Lee, Y. H., Szopa, S., Sudo, K., Nagashima, T., Josse, B., Cionni, I., Righi, M., Eyring, V., Conley, A., Bowman, K. W., Wild, O., and Archibald, A. (2013). Tropospheric ozone changes, radiative forcing and attribution to emissions in the Atmospheric Chemistry and

- Climate Model Intercomparison Project (ACCMIP). *Atmospheric Chemistry and Physics*, 13(6):3063–3085.
- Strode, S. A., Duncan, B. N., Yegorova, E. A., Kouatchou, J., Ziemke, J. R., and Douglass, A. R. (2015). Implications of carbon monoxide bias for methane lifetime and atmospheric composition in chemistry climate models. *Atmospheric Chemistry and Physics*, 15(20):11789–11805.
- Taylor, K. E. (2001). Summarizing multiple aspects of model performance in a single diagram. *Journal of Geophysical Research: Atmospheres*, 106(D7):7183–7192.
- Taylor, K. E., Stouffer, R. J., and Meehl, G. A. (2009). An Overview of CMIP5 and the Experiment Design. *Bulletin of the American Meteorological Society*, 93(4):485–498.
- Telford, P., Lathi re, J., Abraham, N., Archibald, A., Braesicke, P., Johnson, C., Morgenstern, O., O’Connor, F., Pike, R., Wild, O., Young, P., Beerling, D., Hewitt, C., and Pyle, J. (2011). Effects of Climate-induced Changes in Isoprene Emissions after the eruption of Mount Pinatubo. *Procedia Environmental Sciences*, 6:199–205.
- Telford, P. J., Abraham, N. L., Archibald, A. T., Braesicke, P., Dalvi, M., Morgenstern, O., O’Connor, F. M., Richards, N. A. D., and Pyle, J. A. (2013). Implementation of the Fast-JX Photolysis scheme (v6.4) into the UKCA component of the MetUM chemistry-climate model (v7.3). *Geoscientific Model Development*, 6(1):161–177.
- Tilmes, S., Lamarque, J., Emmons, L. K., Conley, A., Schultz, M. G., Saunio, M., Thouret, V., Thompson, A. M., Oltmans, S. J., Johnson, B., and Tarasick, D. (2012). Technical Note: Ozone sonde climatology between 1995 and 2011: description, evaluation and applications. *Atmospheric Chemistry and Physics*, 12(16):7475–7497.
- van der Werf, G. R., Randerson, J. T., Giglio, L., Collatz, G. J., Kasibhatla, P. S., and Arellano, A. F. (2006). Interannual variability in global biomass burning emissions from 1997 to 2004. *Atmospheric Chemistry and Physics*, 6(11):3423–3441.
- van der Werf, G. R., Randerson, J. T., Giglio, L., Collatz, G. J., Mu, M., Kasibhatla, P. S., Morton, D. C., DeFries, R. S., Jin, Y., and van Leeuwen, T. T. (2010). Global fire emissions and the contribution of deforestation, savanna, forest, agricultural, and peat fires (1997–2009). *Atmospheric Chemistry and Physics*, 10(23):11707–11735.
- van Groenigen, K. K. J., Osenberg, C. C. W., and Hungate, B. A. B. (2011). Increased soil emissions of potent greenhouse gases under increased atmospheric CO<sub>2</sub>. *Nature*, 475(7355):214–216.
- von Schneidemesser, E., Monks, P. S., Allan, J. D., Bruhwiler, L., Forster, P., Fowler, D., Lauer, A., Morgan, W. T., Paasonen, P., Righi, M., Sindelarova, K., and Sutton, M. A. (2015). Chemistry and the Linkages between Air Quality and Climate Change. *Chemical Reviews*, 115(10):3856–3897.
- Voulgarakis, A., Naik, V., Lamarque, J.-F., Shindell, D. T., Young, P. J., Prather, M. J., Wild, O., Field, R. D., Bergmann, D., Cameron-Smith, P., Cionni, I., Collins, W. J., Dals ren, S. B., Doherty, R. M., Eyring, V., Faluvegi, G., Folberth, G. A., Horowitz, L. W., Josse, B., MacKenzie, I. A., Nagashima, T., Plummer, D. A., Righi, M., Rumbold, S. T., Stevenson,

- D. S., Strode, S. A., Sudo, K., Szopa, S., and Zeng, G. (2013). Analysis of present day and future OH and methane lifetime in the ACCMIP simulations. *Atmospheric Chemistry and Physics*, 13(5):2563–2587.
- Walter, B. P., Heimann, M., and Matthews, E. (2001). Modeling modern methane emissions from natural wetlands: 1. Model description and results. *Journal of Geophysical Research: Atmospheres*, 106(D24):34189–34206.
- Warwick, N. J. (2003). *Global Modelling of Atmospheric Methane and Methyl Bromide*. PhD thesis, University of Cambridge.
- Warwick, N. J., Bekki, S., Law, K. S., Nisbet, E. G., and Pyle, J. A. (2002). The impact of meteorology on the interannual growth rate of atmospheric methane. *Geophysical Research Letters*, 29(20):8–1–8–4.
- Warwick, N. J., Cain, M. L., Fisher, R., France, J. L., Lowry, D., Michel, S. E., Nisbet, E. G., Vaughn, B. H., White, J. W. C., and Pyle, J. A. (2016). Using  $\delta^{13}\text{C}\text{-CH}_4$  and  $\delta\text{D}\text{-CH}_4$  to constrain Arctic methane emissions. *Atmospheric Chemistry and Physics*, 16(23):14891–14908.
- Warwick, N. J., Pyle, J. A., Carver, G. D., Yang, X., Savage, N. H., O'Connor, F. M., and Cox, R. A. (2006). Global modeling of biogenic bromocarbons. *Journal of Geophysical Research*, 111(D24):D24305.
- Wesely, M. L. (1989). Parameterization of surface resistances to gaseous dry deposition in regional-scale numerical models. *Atmospheric Environment (1967)*, 23(6):1293–1304.
- Westbrook, G. K., Thatcher, K. E., Rohling, E. J., Piotrowski, A. M., Pällike, H., Osborne, A. H., Nisbet, E. G., Minshull, T. A., Lanoisellé, M., James, R. H., Hühnerbach, V., Green, D., Fisher, R. E., Crocker, A. J., Chabert, A., Bolton, C., Beszczynska-Möller, A., Berndt, C., and Aquilina, A. (2009). Escape of methane gas from the seabed along the West Spitsbergen continental margin. *Geophysical Research Letters*, 36(15).
- Whiticar, M. and Schaefer, H. (2007). Constraining past global tropospheric methane budgets with carbon and hydrogen isotope ratios in ice. *Philosophical Transactions of the Royal Society A: Mathematical, Physical and Engineering Sciences*, 365(1856):1793–1828.
- WHO (2003). Health Aspects of Air Pollution with Particulate Matter, Ozone and Nitrogen Dioxide. *Report on a WHO Working Group Bonn, Germany 13–15 January 2003*, (January):98.
- Wild, O. (2007). Modelling the global tropospheric ozone budget: exploring the variability in current models. *Atmospheric Chemistry and Physics*, 7(10):2643–2660.
- Wild, O., Fiore, A. M., Shindell, D. T., Doherty, R. M., Collins, W. J., Dentener, F. J., Schultz, M. G., Gong, S., MacKenzie, I. A., Zeng, G., Hess, P., Duncan, B. N., Bergmann, D. J., Szopa, S., Jonson, J. E., Keating, T. J., and Zuber, A. (2012). Modelling future changes in surface ozone: a parameterized approach. *Atmospheric Chemistry and Physics*, 12(4):2037–2054.
- Wolff, E. W. (2014). Palaeoclimate: Climate in phase. *Nature Geoscience*, 7(6):397–398.

- Worden, J., Jiang, Z., Jones, D. B. A., Alvarado, M., Bowman, K., Frankenberg, C., Kort, E. A., Kulawik, S. S., Lee, M., Liu, J., Payne, V., Wecht, K., and Worden, H. (2013). El Niño, the 2006 Indonesian peat fires, and the distribution of atmospheric methane. *Geophysical Research Letters*, 40(18):4938–4943.
- Young, P. J., Archibald, A. T., Bowman, K. W., Lamarque, J.-F., Naik, V., Stevenson, D. S., Tilmes, S., Voulgarakis, A., Wild, O., Bergmann, D., Cameron-Smith, P., Cionni, I., Collins, W. J., Dalsøren, S. B., Doherty, R. M., Eyring, V., Faluvegi, G., Horowitz, L. W., Josse, B., Lee, Y. H., MacKenzie, I. A., Nagashima, T., Plummer, D. A., Righi, M., Rumbold, S. T., Skeie, R. B., Shindell, D. T., Strode, S. A., Sudo, K., Szopa, S., and Zeng, G. (2013). Pre-industrial to end 21st century projections of tropospheric ozone from the Atmospheric Chemistry and Climate Model Intercomparison Project (ACCMIP). *Atmospheric Chemistry and Physics*, 13(4):2063–2090.
- Yvon-Durocher, G., Allen, A. P., Bastviken, D., Conrad, R., Gudas, C., St-Pierre, A., Thanh-Duc, N., and del Giorgio, P. A. (2014). Methane fluxes show consistent temperature dependence across microbial to ecosystem scales. *Nature*, 507(7493):488–491.
- Zeng, G. and Pyle, J. A. (2003). Changes in tropospheric ozone between 2000 and 2100 modeled in a chemistry-climate model. *Geophysical Research Letters*, 30(7):1–4.
- Zhang, Y. (2008). Online-coupled meteorology and chemistry models: history, current status, and outlook. *Atmospheric Chemistry and Physics*, 8(11):2895–2932.

# A | Observations

The model data in this thesis is compared to a range of observations. As the same observational data is referenced multiple times they will be presented in this section. First, the ozone sonde data compiled by Tilmes et al. [2012] is outlined. Then, three ozone surface observational networks in the Northern Hemisphere will be introduced. This is followed by a brief description of the NOAA/ESRL GMD surface network from which both CO and methane observations are used throughout this thesis. The section concludes with the data composites made by Emmons et al. [2000] for aircraft observations for NO<sub>x</sub> and CO.

## A.1 Ozone sonde data

Tilmes et al. [2012] compiled a global ozone climatology using 42 stations with ozone sonde data covering the period between 1995 and 2011 with at least 12 soundings per year. Twelve regions were defined (Table A.1) for which the ozone sonde data is representative. Modelled data is averaged over the whole of each of these regions. This may introduce some bias in the comparison as some regions are only validated against few measurements while many data points go into the model average. This will be especially noticeable at the surface. In this thesis modelled data is compared to this ozone sonde climatology at four different altitudes (900 hPa, 700 hPa, 500 hPa and 250 hPa).

**Table A.1** Region over which the ozone sonde data are averaged according to [Tilmes et al., 2012]

Region	Latitudes	Longitudes
South Pole	80°N – 60°N	60°W – 60°E
Southern Mid-latitudes	60°S – 40°S	135°E – 175°E
West Pacific/East Indian Ocean	25°S – 25°N	90°E – 135°W
equatorial Americas	25°S – 25°N	90°W – 45°W
Atlantic/Africa	25°S – 25°N	45°W – 45°E
NH Subtropics	20°N – 30°N	90°E – 135°W
Eastern US	30°N – 40°N	90°W – 60°W
Japan	30°N – 40°N	110°E – 150°E
Western Europe	40°N – 55°N	10°W – 35°E
Canada	45°N – 65°N	135°W – 35°W
NH Polar West	60°N – 80°N	45°W – 45°E
NH Polar East	70°N – 80°N	135°W – 35°W

## A.2 Ozone surface observations

Surface ozone observations are obtained from the Clean Air Status and Trends Network (CASTNET, <https://www.epa.gov/castnet>), the European Monitoring and Evaluation Programme (EMEP, <http://www.emep.int>), the Japan Meteorological Agency and Japanese Ministry of the Environment. The hourly observations are averaged into monthly means before comparison with the model. The observations are averaged into seven regions the boundaries of which are given in Table A.2.

**Table A.2** Ozone surface regions over which observations and modelled data are averaged for comparison.

Region	Longitude	Latitude
West US	25°N – 50°N	125°W – 90°W
North East US	37°N – 50°N	90°W – 64°W
South East US	25°N – 37°N	90°W – 64°W
North Europe	50°N – 70°N	10°W – 33°E
Central Europe	40°N – 50°N	10°W – 33°E
South Europe	30°N – 40°N	10°W – 33°E
Japan	24°N – 45°N	123°W – 155°E

### **A.3 Methane and carbon monoxide surface observations**

Modelled methane and CO are compared to surface flask measurements from the NOAA Earth System Research Laboratory – Global Monitoring Division ([Dlugokencky et al., 2016]). Surface flask measurements were analysed in Boulder, Colorado and averaged into monthly mean files. Data for the years 2000 to 2005 (inclusive) are downloaded and averaged into a climatology for all available stations in order to minimise the influence of specific meteorological conditions on the measurements. This climatology was then used for comparison with the modelled data presented in this dissertation which was sampled in the grid box of each measurement station.

There are 66 stations that measured methane and CO between 2000 and 2005. Of these 64 are identical while two stations only measured methane and two others only measured CO. Their geographical distribution is shown in Figure A.1 and their locations can be found in Table A.3. Throughout this thesis seasonal cycles are shown for 16 measurement stations for both methane and CO. These stations are highlighted in bold in Table A.3. Note that the Ny-Alesund station is often referenced as Zeppelin.

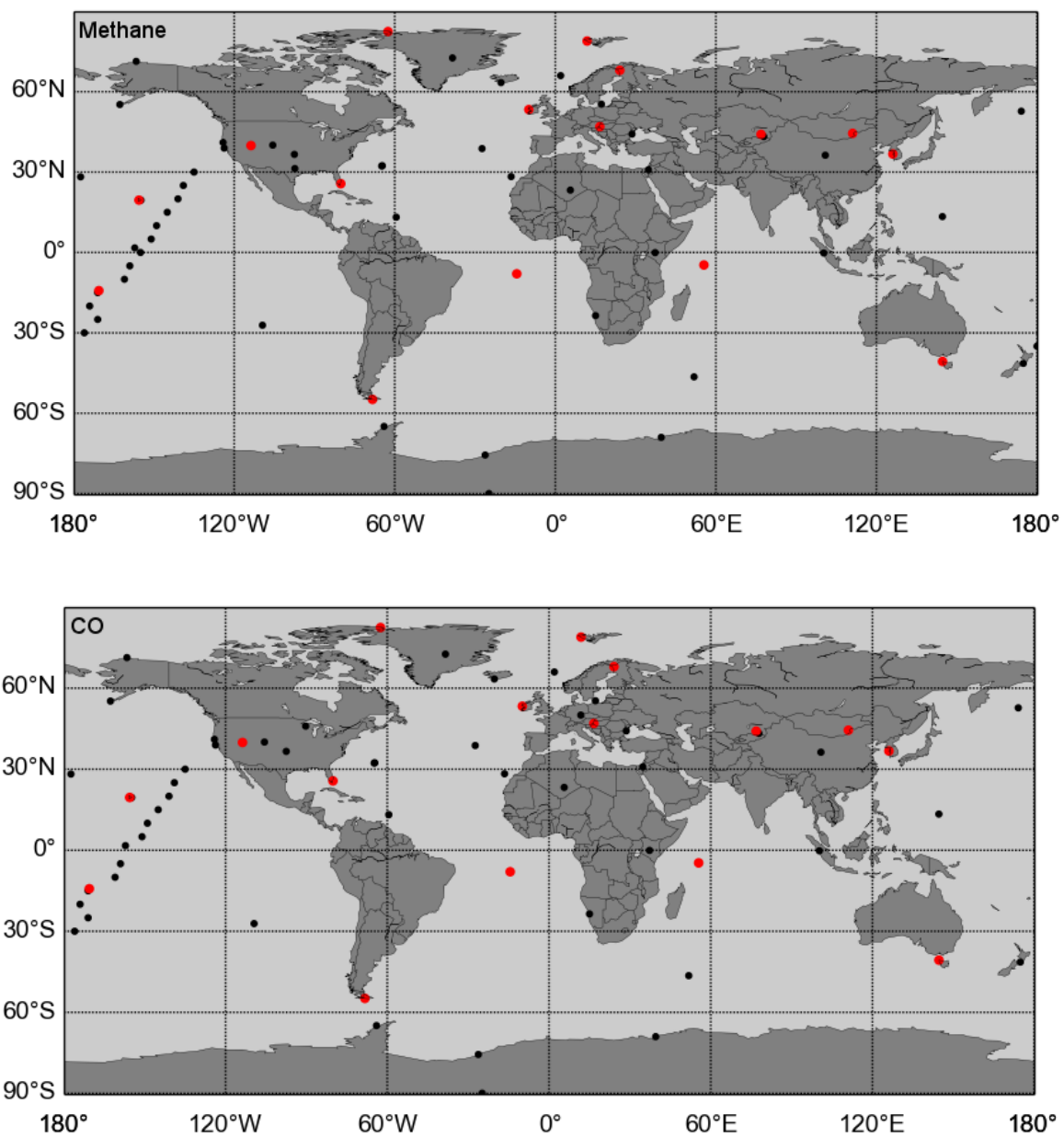


**Fig. A.1** Geographical location of NOAA surface methane (top) and CO (bottom) measurement stations measuring between January 2000 and December 2005. Stations shown in red are those for which seasonal cycles are shown in this thesis.

**Table A.3** NOAA surface station network [Dlugokencky et al., 2016]. Seasonal cycles for the stations in bold are shown throughout this thesis.

Code	Name	Country	Latitude	Longitude
spo	South Pole, Antarctica	United States	90.0°S	24.8°W
hba	Halley Station, Antarctica	United Kingdom	75.6°S	26.2°W
syo	Syowa Station, Antarctica	Japan	69.0°S	39.6°E
psa	Palmer Station, Antarctica	United States	64.9°S	64.0°W
<b>tdf</b>	<b>Tierra Del Fuego, Ushuaia</b>	<b>Argentina</b>	<b>54.8°S</b>	<b>68.3°W</b>
crz	Crozet Island	France	45.4°S	51.8°E
<b>cgo</b>	<b>Cape Grim, Tasmania</b>	<b>Australia</b>	<b>40.7°S</b>	<b>144.7°E</b>
bhd	Baring Head Station	New Zealand	41.4°S	174.9°E
pocs35*	Pacific Ocean (35 S)	/	35.0°S	180.0°E
pocs30	Pacific Ocean (30 S)	/	30.0°S	176.0°W
eic	Easter Island	Chile	109.4°S	109.4°W
nmb	Gobabeb	Namibia	15.0°S	15.0°E
pocs25	Pacific Ocean (25 S)	/	25.0°S	171.0°W
pocs20	Pacific Ocean (20 S)	/	20.0°S	174.0°W
pocs15	Pacific Ocean (15 S)	/	15.0°S	171.0°W
<b>smo</b>	<b>Tutuila</b>	<b>American Samoa</b>	<b>14.2°S</b>	<b>170.6°W</b>
pocs10	Pacific Ocean (10 S)	/	10.0°S	161.0°W
<b>asc</b>	<b>Ascension Island</b>	<b>United Kingdom</b>	<b>8.0°S</b>	<b>14.4°W</b>
<b>sey</b>	<b>Mahe Island</b>	<b>Seychelles</b>	<b>4.7°S</b>	<b>55.5°E</b>
pocs05	Pacific Ocean (5 S)	/	5.0°S	159.0°W
mkn	Mt. Kenya	Kenya	0°	37.3°W
bkt	Bukit Kototabang	Indonesia	0.2°S	100.3°E
pocn00*	Pacific Ocean (0 N)	/	0°	155.0°W
chr	Christmas Island	Republic of Kiribati	1.7°N	157.2°E
pocn05	Pacific Ocean (5 N)	/	5.0°N	151.0°W

\* only for methane comparison

\*\* only for CO comparison

**Table A.3** NOAA surface station network [Dlugokencky et al., 2016]. Seasonal cycles for the stations in bold are shown throughout this thesis.

Code	Name	Country	Latitude	Longitude
pocn10	Pacific Ocean (10 N)	/	10.°N	149.0°W
gmi	Mariana Islands	Guam	13.4°N	155.7°E
rpb	Ragged Point	Barbados	13.2°N	59.4°W
pocn15	Pacific Ocean (15 N)	/	15.0°N	145°W
kum	Cape Kumukahi, Hawaii	United States	19.5°N	154.8°W
<b>mlo</b>	<b>Mauna Loa, Hawaii</b>	<b>United States</b>	<b>19.5°N</b>	<b>155.6°W</b>
pocn20	Pacific Ocean (20 N)	/	20.0°N	141°W
ask	Assekrem	Algeria	5.6°N	5.6°E
pocn25	Pacific Ocean (25 N)	/	25.0°N	139°W
<b>key</b>	<b>Key Biscayne, Florida</b>	<b>United States</b>	<b>25.7°N</b>	<b>80.2°W</b>
mid	Sand Island, Midway	United States	28.2°N	177.4°W
izo	Izana, Tenerife, Canary Islands	Spain	28.3°N	16.5°W
wis	WIS Station, Negev Desert	Israel	30.9°N	34.8°E
pocn30	Pacific Ocean (30 N)	/	30.0°N	135°W
wkt	Moody, Texas	United States	31.3°N	97.3°W
bmw	Tudor Hill, Bermuda	United Kingdom	32.3°N	64.9°W
bme	St. Davids Head, Bermuda	United Kingdom	36.4°N	64.6°W
wlg	Mt. Waliguan	Peoples Republic of China	36.3°N	100.9°E
<b>tap</b>	<b>Tae-ahn Peninsula</b>	<b>Republic of Korea</b>	<b>36.6°N</b>	<b>126.1°E</b>
sgp	Southern Great Plains, Oklahoma	United States	36.6°N	97.5°W
pta	Point Arena, California	United States	39.0°N	123.7°W
<b>uta</b>	<b>Wendover, Utah</b>	<b>United States</b>	<b>39.9°N</b>	<b>113.7°W</b>
azr	Terceira Island, Azores	Portugal	38.8°N	27.4°W
thd	Trinidad Head, California	United States	41.1°N	124.2°W
nwr	Niwot Ridge, Colorado	United States	40.1°N	105.6°W

\* only for methane comparison

\*\* only for CO comparison

**Table A.3** NOAA surface station network [Dlugokencky et al., 2016]. Seasonal cycles for the stations in bold are shown throughout this thesis.

Code	Name	Country	Latitude	Longitude
bsc	Black Sea, Constanta	Romania	44.2°N	28.7°E
kzm	Plateau Assy	Kazakhstan	43.3°N	77.9°E
<b>kzd</b>	<b>Sary Taukum</b>	<b>Kazakhstan</b>	<b>44.1°N</b>	<b>76.9°E</b>
<b>uum</b>	<b>Ulaan Uul</b>	<b>Mongolia</b>	<b>44.5°N</b>	<b>111.1°E</b>
<b>hun</b>	<b>Hegyhatsal</b>	<b>Hungary</b>	<b>47.0°N</b>	<b>16.7°E</b>
lef**	Park Falls, Wisconsin	United States	45.9°N	90.3°W
oxk**	Ochsenkopf	Germany	50.0°N	11.9°E
shm	Shemya Island, Alaska	United States	52.7°N	174.1°E
<b>mhd</b>	<b>Mace Head, County Galway</b>	<b>Ireland</b>	<b>53.3°N</b>	<b>9.9°W</b>
bal	Baltic Sea	Poland	55.4°N	17.2°E
cba	Cold Bay, Alaska	United States	55.2°N	162.7°W
ice	Storhofdi, Vestmannaeyjar	Iceland	64.4°N	20.3°W
stm	Ocean Station M	Norway	66.0°N	2°E
<b>pal</b>	<b>Pallas-Sammaltunturi, GAW Station</b>	<b>Finland</b>	<b>68.0°N</b>	<b>24.1°E</b>
brw	Barrow, Alaska	United States	71.3°N	156.6°W
sum	Summit	Greenland	82.6°N	38.4°W
<b>zep</b>	<b>Ny-Alesund, Svalbard</b>	<b>Norway and Sweden</b>	<b>78.9°N</b>	<b>11.9°E</b>
<b>alt</b>	<b>Alert, Nunavut</b>	<b>Canada</b>	<b>82.5°N</b>	<b>62.5°W</b>

\* only for methane comparison

\*\* only for CO comparison

## A.4 NO<sub>x</sub> and CO aircraft observations

Emmons et al. [2000] have aggregated a number of aircraft observations important for ozone photochemistry from the 1980s and 1990s. Vertical profiles exist for defined campaign regions (10° to 20° degree boxes) and 1 km vertical resolution with statistical information about the observations. Due to the nature of campaigns (short time coverage, limited repeats),

they advised in their paper to use the median distribution for each region in order to minimise the influence of plume pollution. This advice is followed in this thesis with error bars representing the interquartile range of the observations. Model data are averaged over the campaign regions as are the (climatological) months of the campaign dates.

Even though the campaigns used for the data composites do not technically overlap with the period modelled in this thesis (2000), the dataset is used to probe the model's vertical distribution of CO and NO<sub>x</sub>. Model data are averaged over the campaign regions and are probed during the campaign months. It should be noted that the composites are created based on aircraft observations, which are by nature sparse in temporal and spatial coverage. The relatively coarse resolution of the model thus cannot be expected to represent point measurements well.

Figure A.2 shows the regions over which the aircraft campaign data (and thus the model data) are averaged. It can be noted that more regions exist for CO than for NO<sub>x</sub> measurements.

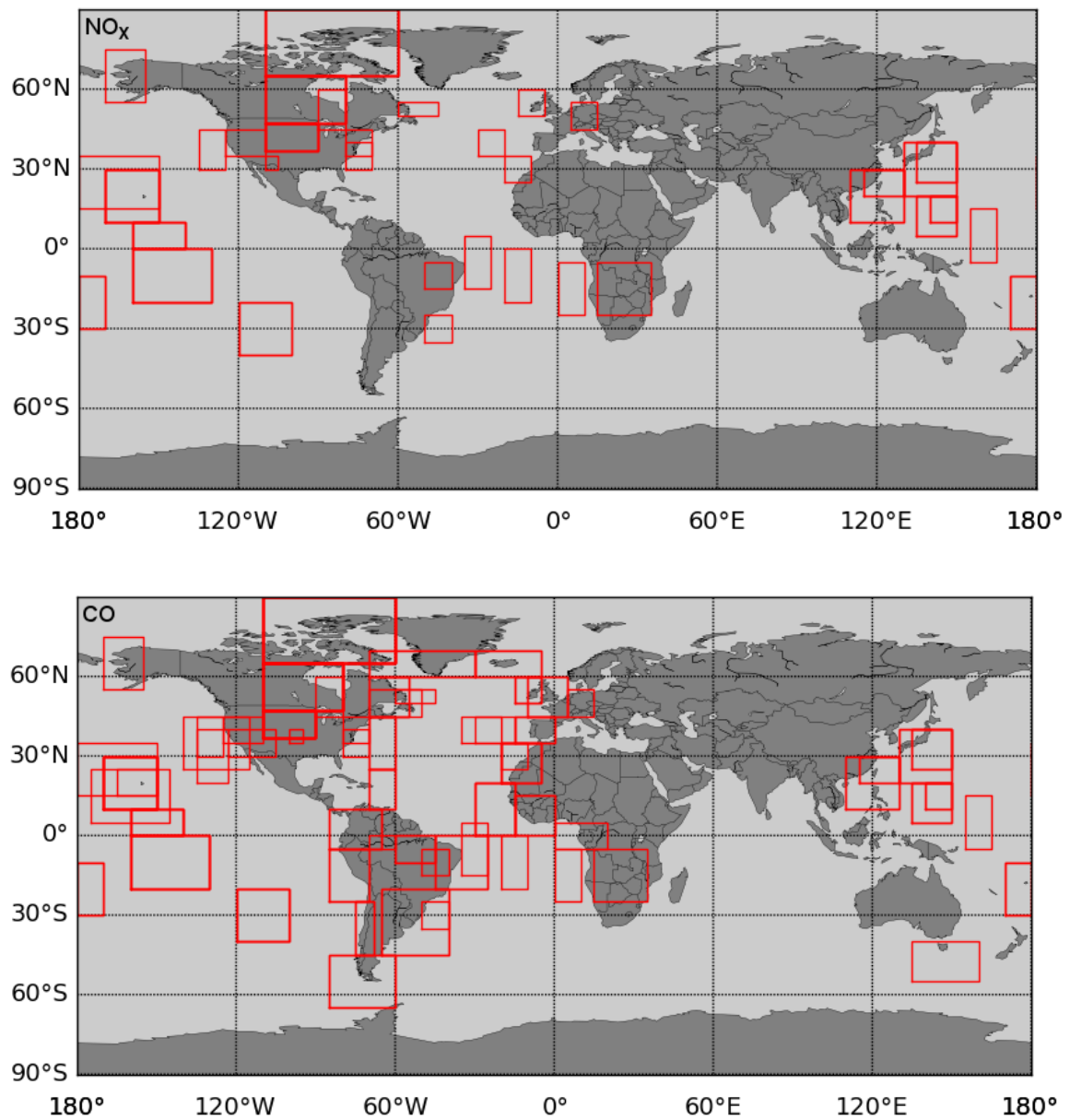


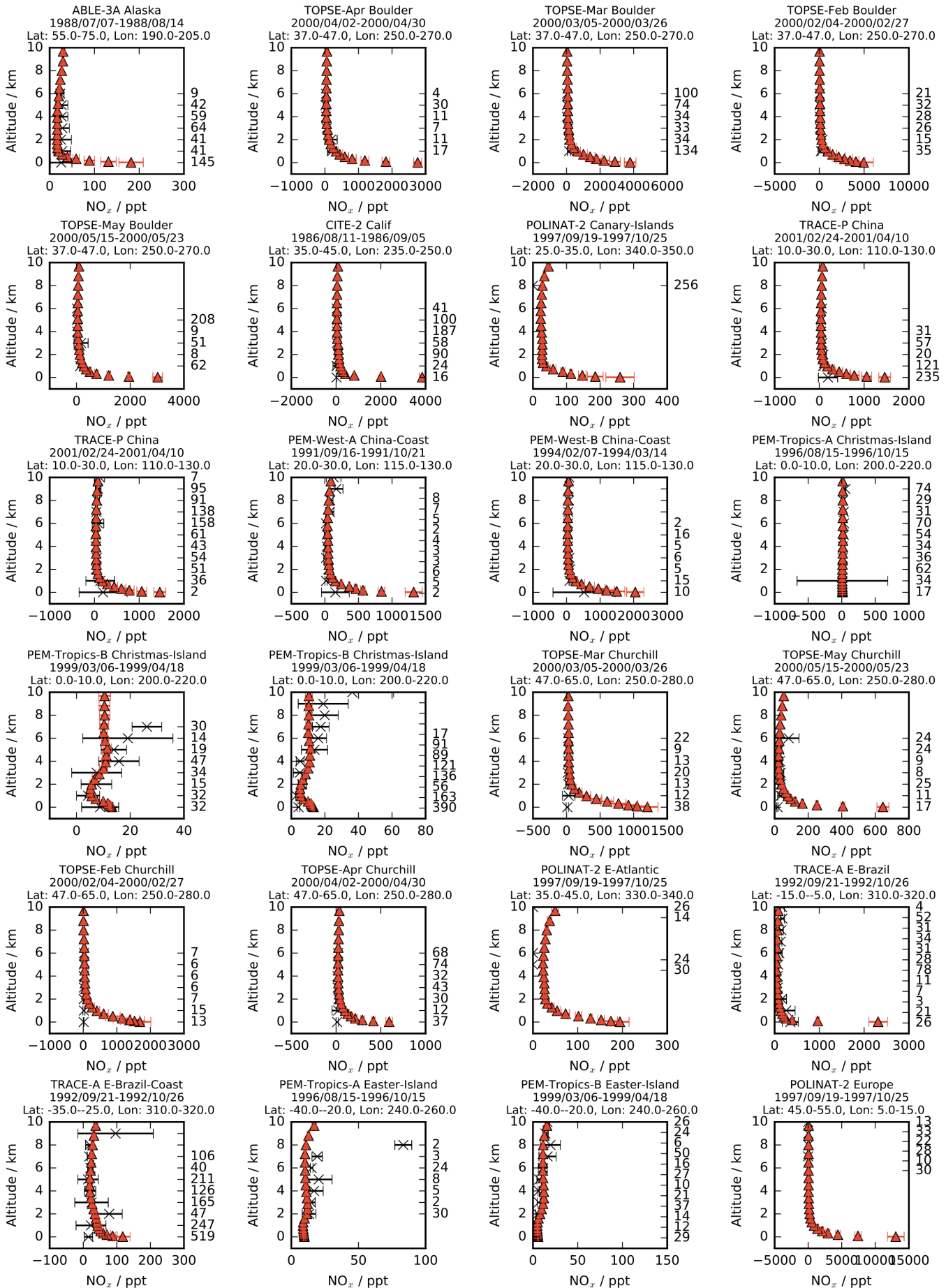
**Fig. A.2** Geographical distribution of the aircraft campaign regions for NO<sub>x</sub> (top) and CO (bottom) as defined in Emmons et al. [2000].



## **B** |

**Fig. B.1** Vertical profiles of tropospheric  $\text{NO}_x$  concentrations for the Base model (chapter 2) in red compared to aircraft observation composites [Emmons et al., 2000] (ppt).

× Emmons    ▲ Base





× Emmons    ▲ Base

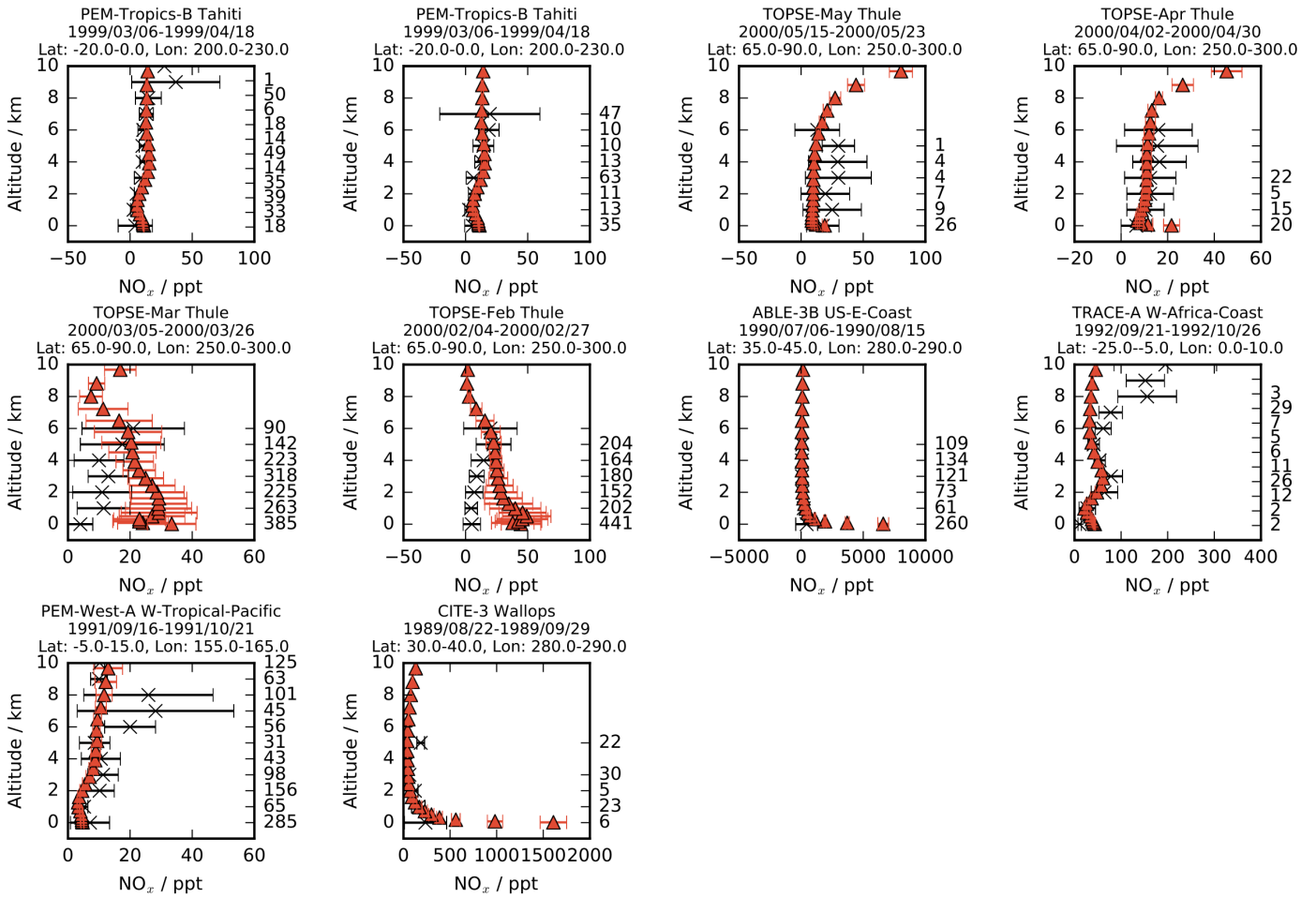
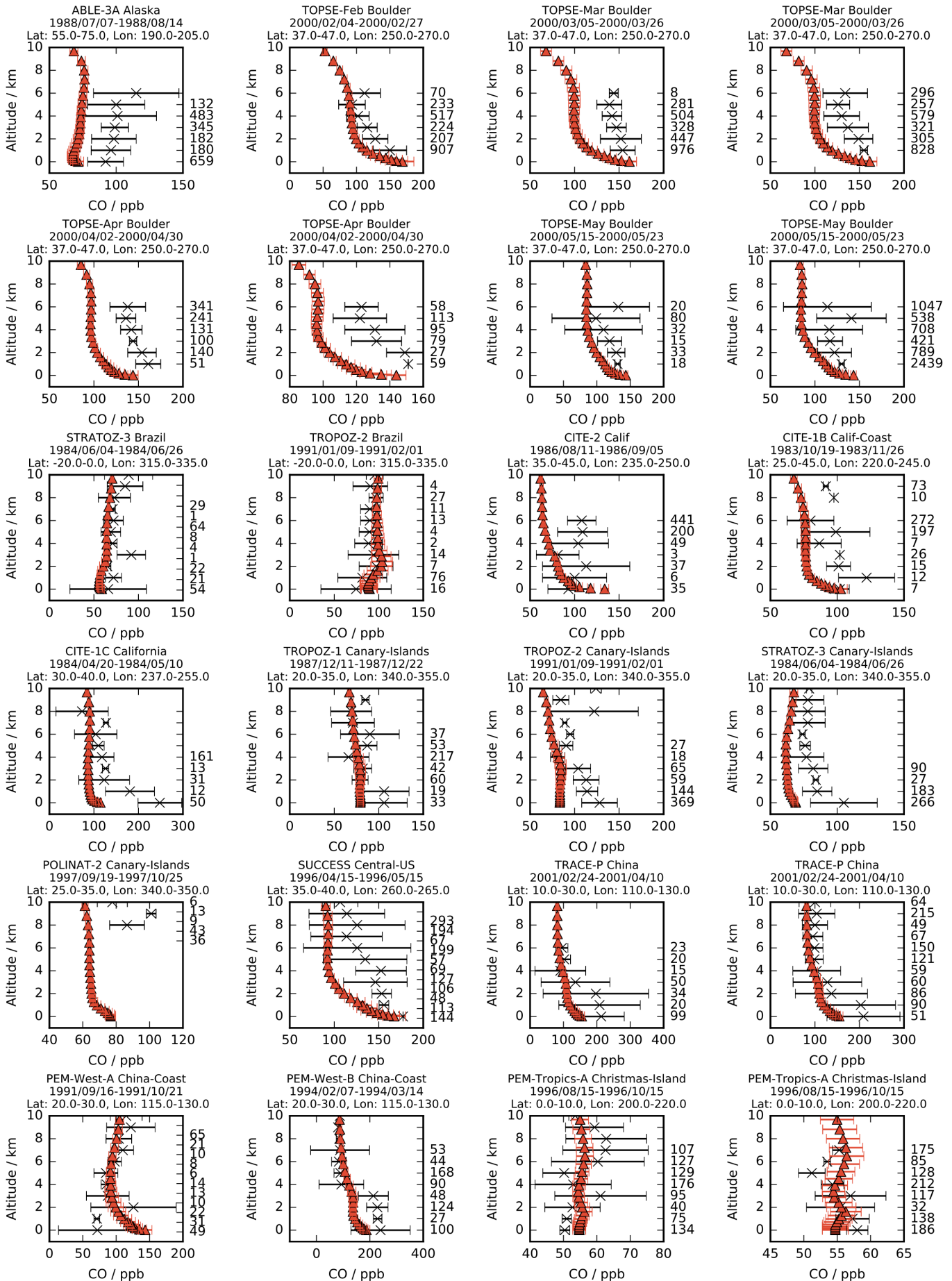
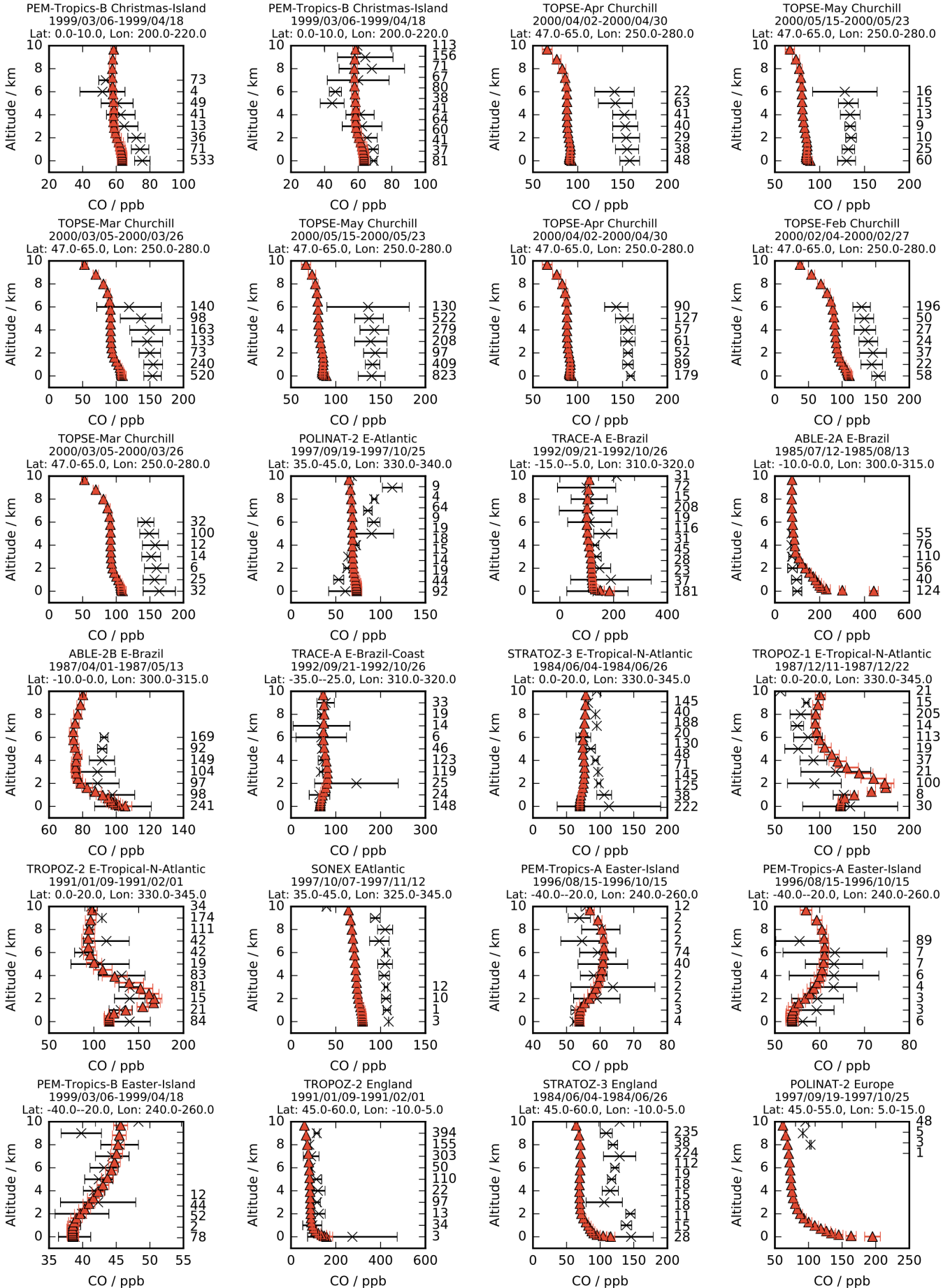


**Fig. B.2** Vertical profiles of tropospheric CO concentrations for the Base model (chapter 2) in red compared to aircraft observation composites [Emmons et al., 2000] (ppb).

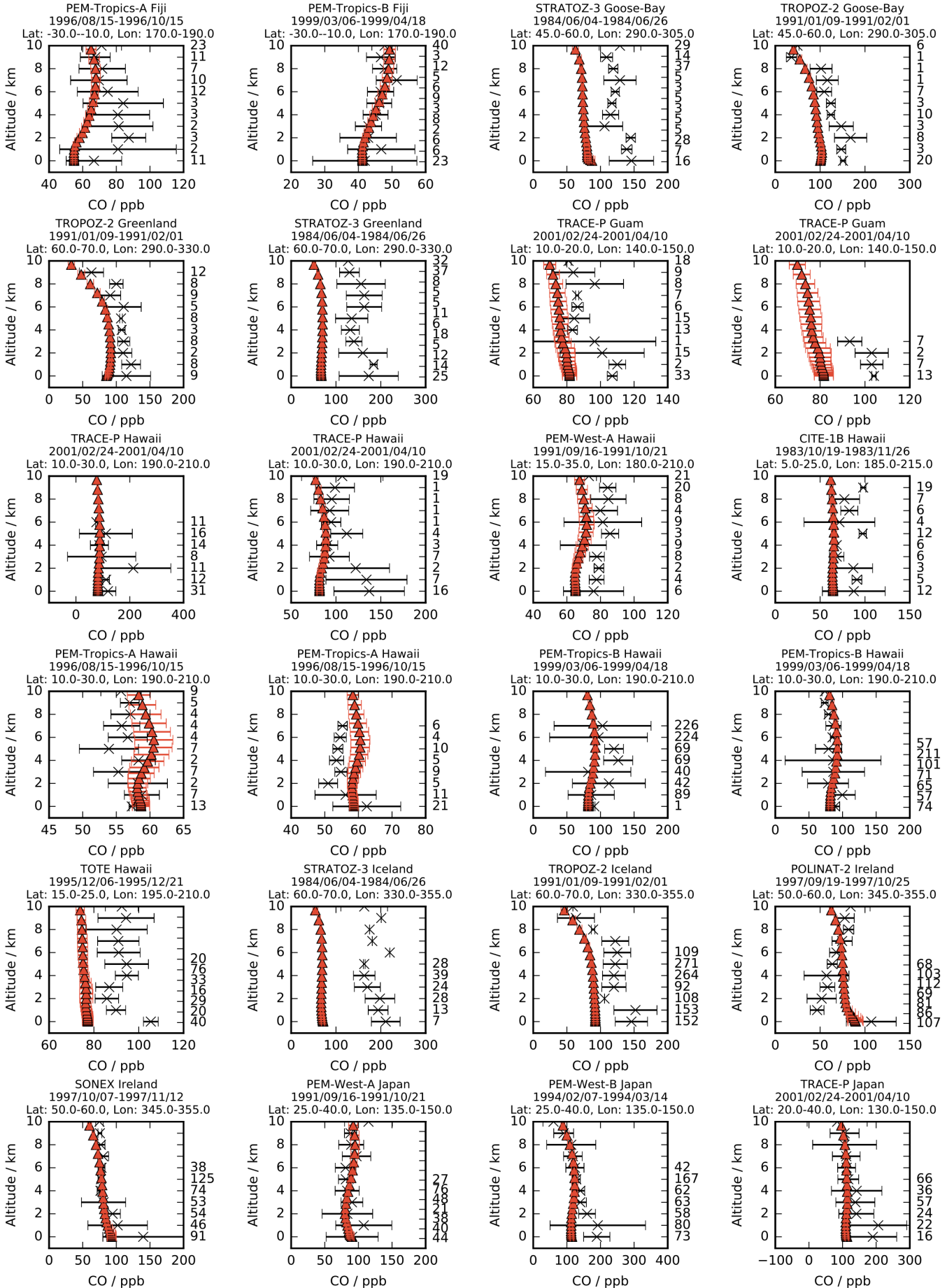
× Emmons    ▲ Base



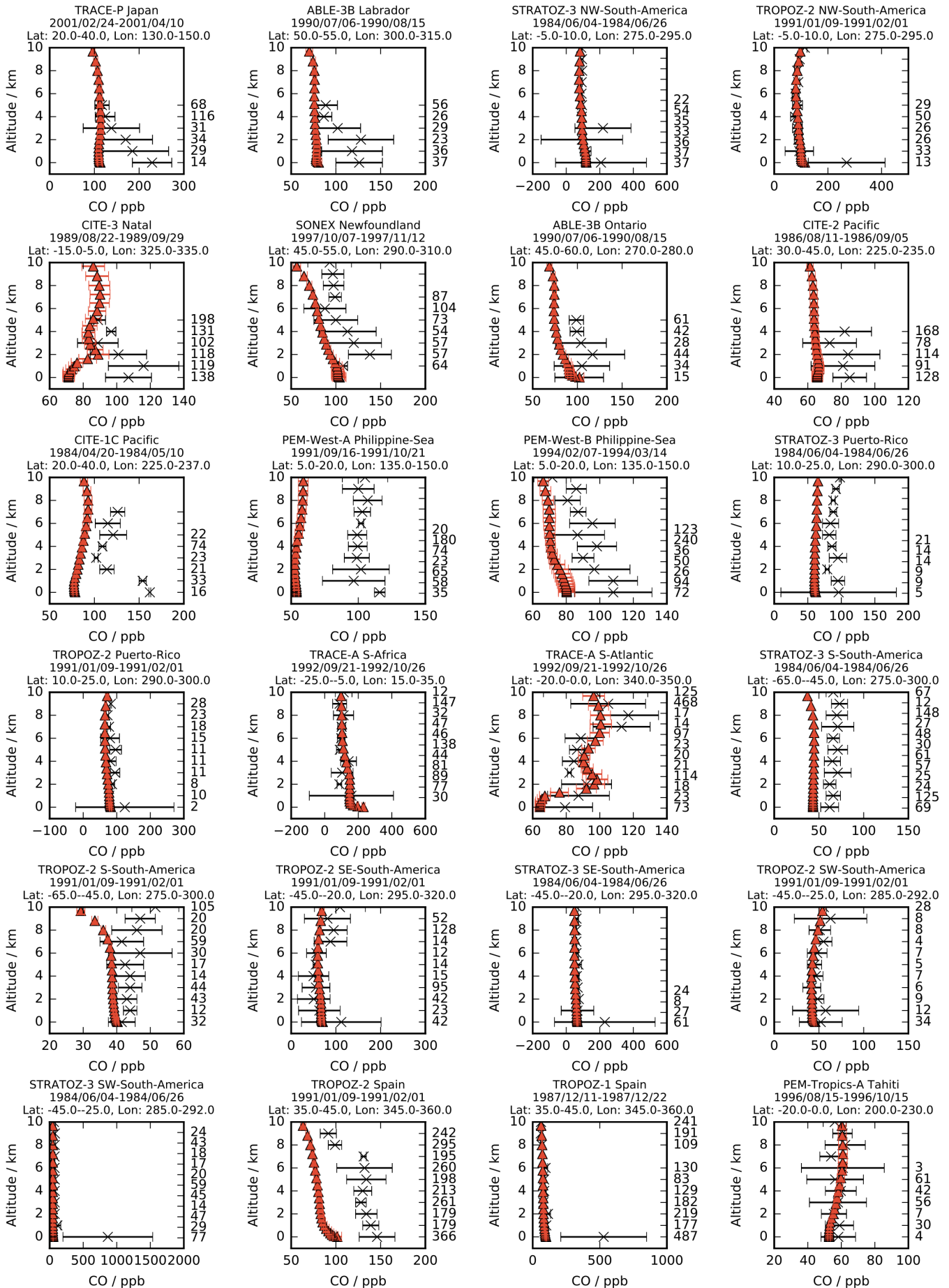
× Emmons    ▲ Base



× Emmons    ▲ Base



× Emmons    ▲ Base



× Emmons    ▲ Base

